UNIVERSITY OF CALIFORNIA

Santa Barbara

Mechanical properties of confined mussel-inspired materials

A dissertation submitted in partial satisfaction of the

requirements for the degree Doctor of Philosophy

in Chemical Engineering

by

George Dowley Degen

Committee in charge:

Professor Joan-Emma Shea, Co-chair

Professor Angela Pitenis, Co-chair

Professor Bradley Chmelka

Professor Song-I Han, Co-chair

Professor Matthew Helgeson

Professor J. Herbert Waite

June 2021

The dissertation of George Dowley Degen is approved.

_____

Bradley Chmelka

_____

Song-I Han

_____

Matthew Helgeson

_____

J. Herbert Waite

_____

Angela Pitenis, Committee Co-Chair

_____

Joan-Emma Shea, Committee Co-Chair

June 2021

ACKNOWLEDGEMENTS

UCSB is a collaborative place, and I have been fortunate to work with a fantastic network of professors. To my advisors, Professors Joan-Emma Shea, Angela Pitenis, and Jacob Israelachvili, and my collaborators, Professors Herb Waite, Alison Butler, and Brad Chmelka, thank you for your support and guidance.

To my friends in science and running, thank you for the fun times in lab and on the bluffs. We have now dispersed across the country and around the world, and I look forward to years of traveling to visit. St. Elmo, from the first inappropriate joke, I knew we would get along. Thank you for hours of cycling and fierce debate.

To my family, I will be sad to leave California, but happy to be closer to you. Grandma, thank you for all the research discussions. Mibs, I am so glad you visited Santa Barbara—I loved seeing the city through your eyes.

Jenny, I cannot imagine my PhD without you. Walking dogs, beach days, runs, and meals in the office, it was all wonderful. Next stop, Boston!

VITA OF GEORGE DOWLEY DEGEN
June 2021

EDUCATION

Bachelor of Science in Chemical Engineering, Minor in Computer Science, Carnegie Mellon University, May 2015 (with University and College Honors)

Doctor of Philosophy in Chemical Engineering, University of California, Santa Barbara, June 2021

PROFESSIONAL EMPLOYMENT

Summer 2012: Research Experience for Undergraduates. Department of Chemical and Biological Engineering, University of Wisconsin, Madison. Advisor: Prof. Brian Pfleger.

Summer 2013: Research Experience for Undergraduates. Department of Chemical and Biological Engineering, University of Colorado, Boulder. Advisor: Prof. Ryan Gill.

2013: Undergraduate Research. Department of Chemical Engineering, Carnegie Mellon University. Advisor: Prof. Aditya Khair.

Summer 2014: Summer Undergraduate Laboratory Internship Program. Argonne National Laboratory. Advisor: Dr. Meltem Urgun-Demirtas.

2014-2015: Undergraduate Research. Department of Chemical Engineering, Carnegie Mellon University. Advisor: Prof. Kathryn Whitehead.

2015: Undergraduate Research. Department of Chemical Engineering, Carnegie Mellon University. Advisor: Prof. B. Erik Ydstie.

Summer 2015: Undergraduate Research Opportunities Program. RWTH Aachen University. Advisor: Prof. Ahmed Ismail.

2015-2021: Graduate Research. Department of Chemical Engineering, University of California, Santa Barbara. Advisors: Prof. Jacob Israelachvili, Prof. Joan-Emma Shea, Prof. Angela Pitenis.

PUBLICATIONS

GD Degen*, J Chen, AL Chau, LK Månsson, AA Pitenis, “Poroelasticity of highly confined hydrogel films measured with a surface forces apparatus.” Soft Matter 2020, 16, 8096–8100.

WR Wonderly, TR Cristiani, KC Cunha, GD Degen, JE Shea*, JH Waite*, “Dueling backbones: comparing peptoid and peptide analogues of a mussel adhesive protein.” Macromolecules 2020, 53 (16), 6767–6779.

AL Chau, J Rosas, GD Degen, LK Månsson, J Chen, E Valois, AA Pitenis*, "Aqueous surface gels as low friction interfaces to mitigate implant-associated inflammation." J. Mater. Chem. B 2020, 8, 6782–6791.

GD Degen, PR Stow, RB Lewis, RC Andresen Eguiluz, E Valois, K Kristiansen, A Butler*, JN Israelachvili, "Impact of molecular architecture and adsorption density on adhesion of mussel-inspired surface primers with catechol-cation synergy." J. Am. Chem. Soc. 2019, 141 (47), 18673–18681.

GD Degen*, TR Cristiani, N Cadirov, RC Andresen Eguiluz, K Kristiansen, AA Pitenis, JN Israelachvili, "Surface damage influences the JKR contact mechanics of glassy low-molecular-weight polystyrene films." Langmuir 2019, 35 (48), 15674–15680.

HA Dobbs†, GD Degen†, ZJ Berkson, K Kristiansen, AM Schrader, T Oey, GN Sant, BF Chmelka*, JN Israelachvili, "Electrochemically enhanced dissolution of silica and alumina in alkaline environments." Langmuir 2019, 35 (48), 15651–15660.

K Kristiansen†*, SH Donaldson Jr.†, ZJ Berkson, J Scott, R Su, X Banquy, DW Lee, HB de Aguiar, JD McGraw, GD Degen, JN Israelachvili, "Multimodal miniature surface forces apparatus (μSFA) for interfacial science measurements." Langmuir 2019, 35 (48), 15500–15514

SM Hart, GD Degen, JM Urueña, PP Levings, WG Sawyer, AA Pitenis*, "Friction-induced apoptosis." Tribology Letters 2019, 67, 82.

RI Zeitoun, AD Garst, GD Degen, G Pines, TJ Mansell, TY Glebes, NR Boyle, RT Gill*, "Multiplexed tracking of combinatorial genomic mutations in engineered cell populations." Nature Biotechnology 2015, 33 (6), 631–637.

SE Feicht, GD Degen, AS Khair*, "Moving ion fronts in mixed ionic-electronic conducting polymer films." AIChE Journal 2015, 61 (4), 1447–1454.

AWARDS

UC Santa Barbara University Award of Distinction (2021)
Lindau Nobel Laureate Interdisciplinary Meeting, University of California Delegate (2021)
UC President's Dissertation Year Fellowship (2020-2021)
NSF Graduate Research Fellowship (2017-2020)
STLE Early Career Award (2020)
UCSB Chemical Engineering Schlinger Fellowship (2019)
CSP Technologies Teacher-Scholar Fellowship (2019)
1st Place, UCSB Grad Slam (2019)
Best Oral Presentation, UCSB Chemical Engineering Graduate Student Symposium (2019)
UCSB MRL Education Programs Outstanding K-12 Volunteer Award (2019)
Opportunity Award, MechBio Symposium, Irvine, CA (2018)

ABSTRACT

Mechanical properties of confined mussel-inspired materials

by

George Dowley Degen

There is currently a need for improved adhesives for medical and marine applications, primarily because the presence of water severely undermines adhesion. Due to their robust adhesion under water, marine mussels have been widely studied as inspirations for the design of wet adhesives. However, development of mussel-inspired materials has historically over-emphasized the importance of the catechol functionality in mussel adhesion. This thesis demonstrates that the mechanical properties of mussel-inspired materials, including adhesion, cohesion, and stiffness, result from a range of factors beyond the presence of catechols. By investigating model systems spanning multiple length scales, this work reveals the importance of failure mode, binding group density, and electrostatic interactions on interfacial adhesion of mussel-inspired surface primers and peptides at the atomic scale. Interactions between thin films of pressure sensitive adhesives and polymers are shown to depend on film composition which is influenced by solvent-induced structural rearrangement and contact-induced damage. The mechanical properties of micro-scale hydrogel films are shown to be dictated by fluid flow through the polymer network. By providing a better understanding of mussel adhesion, this work seeks to guide the design of new mussel-inspired materials for diverse applications.

I. Introduction

There is a need for improved adhesives for wet conditions including marine and physiological environments. Aqueous electrolyte solutions are particularly challenging for adhesives because water and salt interfere with the ability of most existing adhesives to bind to surfaces. Most notably, tightly bound hydration layers on surfaces discourage molecular contact by adhesives, van der Waals forces are significantly reduced under water, and ions in solution screen electrostatic interactions and compete with adhesives for binding sites on charged surfaces.[1] As a result, adhesive that are effective in dry conditions often fail to stick to wet surfaces.

Despite the challenges that water poses to adhesion, marine mussels readily adhere to almost any surface, allowing them to live in the turbulent intertidal zone of the ocean. To adhere to a surface, mussels create adhesive plaques attached to the surface, each connected to the body of the mussel by a collagenous thread. Mussels fabricate a collection of plaques and threads called the byssus.[2] Byssal adhesion results from phenomena occurring over multiple length scales, from nanometers to millimeters, including interfacial adhesion, cohesion and energy dissipation within the plaque and thread, reliable and rapid processing from liquid precursors, and favorable geometry for controlled load translation and detachment. While mussel-inspired materials leveraging aspects of these properties have been developed,[3] the many aspects of mussel adhesion are still not fully understood. Further improvements in mussel inspired materials require a deeper understanding of the mechanical properties of these materials at many length scales.

Many features of mussel adhesion and mussel-inspired materials involve high levels of confinement, where the width of the contact region greatly exceeds the film thickness. Highly

confined films appear at interfaces between the adhesive and the substrate, where the width of the interfacial region is often nanometers. Confinement is also relevant to thin films of mussel-inspired materials tens to hundreds of nanometers in thickness such as pressure sensitive adhesives, where the mechanical properties of the film are sensitive to film heterogeneity induced by the deposition mode or damage to the film. Even in materials as thick as tens of microns, the contact geometry can result in high levels of confinement.

This thesis describes research on aspects of mussel adhesion occurring over the nano- to micro-scale and high levels of confinement. The robust adhesion of mussel foot proteins to many surfaces prompted research on the nano-scale interfacial mechanics of small molecules and peptides containing catechols and cationic amines (Chapters 2 and 3). In addition to establishing an adhesive interface, mussel proteins also participate in strong cohesive interactions that strengthen the plaque. To investigate the factors influencing cohesion in polyphenolic polymers, synthetic pressure sensitive adhesives and industrial polymers were studied (Chapters 4 and 5). Finally, fluid-filled polymer networks are important for mussel adhesion, both in the coacervate-filled gel architecture of the plaque[4] and the soft, hydrated coating of the thread.[5] The mechanics of micro-scale fluid-filled networks was investigated using a synthetic hydrogel model system (Chapter 6). Collectively, these studies will inform the rational design of new, mussel-inspired materials for diverse applications.

II. The influence of charged groups on adhesion and cohesion of catecholic surface primers

A. Background

Marine mussels fasten themselves to surfaces under water using adhesive proteins.[2] The most adhesive mussel foot proteins (mfps) are rich in the catecholic amino acid 3,4-dihydroxyphenylalanine (Dopa),[6,7] which is derived from tyrosine by post-translational modification. Dopa has been shown to facilitate adhesion through diverse intermolecular interactions,[8] giving mfps the ability to adhere to diverse organic and inorganic surfaces. [6,9,10] As a result, Dopa and other catechols have been incorporated into many synthetic wet adhesives.[3,11]

Due to the large proportion of cationic residues, most commonly lysine, paired with Dopa in the most adhesive interfacial mussel protein (Mfp-5),[6,12] it has been hypothesized that both these residues are important for adhesion. Furthermore, other compounds containing catechol and cationic functionalities have been shown to adhere to many surfaces. Polydopamine, formed from the polymerization and self-assembly of oxidized dopamine,[13–16] adheres to a wide variety of materials and has been proposed for many applications.[17] Other adhesives containing catechol and cationic functionalities include catechol-chitosan[18–20] and catechol-poly(ethylenimine),[21,22] among others.[23,24] Molecules containing Dopa and other catechols adhere to apatite[25] and metal oxide[26] surfaces found in bone and implant materials, and have

been shown to be biocompatible,[3] making them attractive alternatives to existing medical adhesives, many of which are ineffective[27,28] or cytotoxic.[29–31]

Despite widespread scientific and applications-based research on materials containing catechol functionalities,[3] specific adhesion mechanisms of these materials have only recently begun to be explored.[32] It has been demonstrated that adhesives incorporating catechol and cationic amine functionalities bind more strongly to muscovite mica in saline solutions than adhesives incorporating either catechols or cations alone,[33] a cooperative effect known as catechol-cation synergy. The adjacent pairing of Dopa and lysine in the Mfp-5 sequence[12] has prompted speculation that intramolecular proximity of catechol and cationic functionalities may be necessary for adhesion, and that an intramolecular cut-off distance may exist beyond which catechol-cation synergy no longer operates.[34] A recent study showed that the order of catechol and cationic functionalities impacts the single-molecule pull-off force,[35] supporting the hypothesis that direct adjacency of catechol and cationic functionalities may enhance adhesion. However, until now no study has directly explored the impact of intramolecular spacing on catechol-cation synergy.

Here, we present adhesion measurements of films of siderophore analog surface primers with systematically varying intramolecular spacing between catechol and cationic amine functionalities. We show that the pull-off force mediated by the siderophore analogs depends critically on the adsorption density and confirm that catechol-cation synergy enables adhesion. Surprisingly, the results demonstrate that direct intramolecular adjacency between catechol and cationic functionalities is not necessary for catechol-cation synergy and suggest that no intramolecular cut-off distance between these functionalities exists for which catechol-cation synergy will be abolished. To explain the results, we propose a mechanism for catechol-cation

synergy based on electrostatically driven adsorption and support this mechanism with a qualitative model.

B. Experimental Section

We synthesized a suite of seven siderophore analogs, synthetic mimics of bacterial iron chelators called siderophores.[36] Each analog has a central tris(2-aminoethyl)amine (Tren) scaffold with three identical peptide arms. Here, each peptide arm contained glycine and lysine and were capped with either the catechol 2,3-dihydroxybenzoyl (2,3-DHBA) or benzoyl functionality (Figure 2.1). The intramolecular spacing between 2,3-DHBA and lysine in the peptide arms was varied by changing the peptide sequence. Three of the analogs were isomers: Tren(GGK-Cat)$_3$, Tren(GKG-Cat)$_3$, and Tren(KGG-Cat)$_3$. Tren denotes the tris(2-aminoethyl)amine scaffold, G and K denote glycine and lysine, respectively, and Cat denotes 2,3-DHBA. Siderophore analogs with even greater catechol-cation spacing (Tren(KGGG-Cat)$_3$ and Tren(KGGGGGG-Cat)$_3$), cationic amines but without catechols (Tren(GGK-Benz)$_3$), and only catechols (Tren(GGG-Cat)$_3$) were also synthesized. Additional details on materials, synthesis, and molecular characterization are included in Appendix 1. Analogs were dissolved at 1 mM in an aqueous salt solution (50 mM acetic acid, 150 mM KNO_3, pH = 3.3), chosen to mimic physiological ionic strengths but avoid catechol oxidation by maintaining an acidic pH.

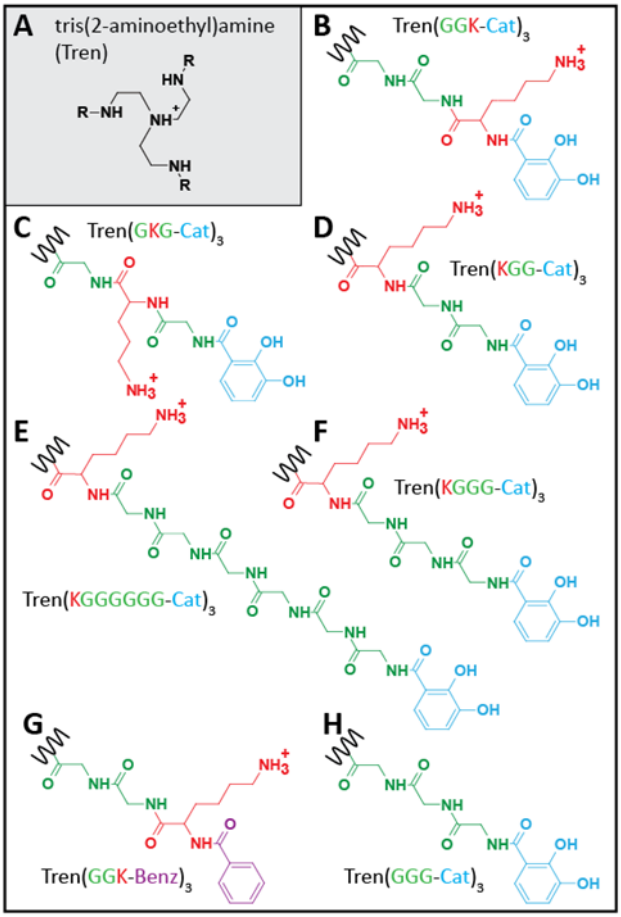

Figure 2.1. The suite of siderophore analogs investigated. (A) Tris(2-aminoethyl)amine (Tren) scaffold. R-groups are shown in (B)-(H). The intramolecular distance between 2,3-DHBA and lysine is varied in (B) Tren(GGK-Cat)$_3$, (C) Tren(GKG-Cat)$_3$, (D) Tren(KGG-Cat)$_3$, (E) Tren(KGGGGGG-Cat)$_3$, and (F) Tren(KGGG-Cat)$_3$. Analogs containing lysine without 2,3-DHBA, (G) Tren(GGK-Benz)$_3$, and 2,3-DHBA without lysine, (H) Tren(GGG-Cat)$_3$ were also synthesized.

Adhesion measurements were performed using a surface forces apparatus (SFA) model SFA2000 (SurForce, LLC), described in detail in Appendix 2. In the SFA, freshly cleaved muscovite mica surfaces were arranged in a crossed cylinder geometry. All experiments were performed at a constant temperature. Siderophore analogs were deposited via adsorption from solution into films on either one (asymmetric deposition) or both (symmetric deposition) mica surfaces. For asymmetric deposition, 50 µL of 400 µM siderophore analog solution was injected onto one of the mica surfaces and incubated for at least 60 min. The surface was then rinsed before adhesion measurements. For symmetric deposition, siderophore analog solution was injected into a capillary meniscus between both surfaces (final concentration 90-667 µM). The surfaces were incubated for at least 60 min and were not rinsed before adhesion measurements.

Adhesion measurements were performed with the mica surfaces bridged by a capillary meniscus of ~50 µL salt solution (50 mM acetic acid, 150 mM KNO_3, pH = 3.3) at a constant temperature (T = 22 ± 1 °C). Normal force (F) and surface separation distance (D) were measured during cycles of i) approach and compression, ii) waiting at maximum compression (t_{wait}), and iii) separation and jump from contact were performed at constant approach and separation velocities. Measured forces were normalized by the average radius of curvature of the surfaces (R). Pull-off force ($-F_{ad}/R$) was calculated from the distance that the surfaces jumped from contact during separation corresponding to the most negative force measured during separation. Pull-off force did not depend on separation velocity (V_{out} = 2-10 nm/s) (Figure A2.1) nor maximum compression (F/R = 9-108 mN/m). We use the term "pull-off" instead of "adhesion" because the force required to separate the mica surfaces can correspond to adhesive failure at the film-mica interface, cohesive failure at the film-film interface, or a

combination of the two failure modes. The separation distance during compression of the surfaces at which the force exceeded 1 mN/m was denoted the onset of interaction (D_{onset}). The surface separation distance measured at maximum compression was denoted compressed film thickness (D_t). The change in film thickness after waiting at maximum compression (ΔD_t) was reported as the difference between compressed film thicknesses measured before and after waiting at maximum compression. Error bars correspond to the standard deviation, with an additional contribution to the error in D_t for 6 of the data points from measuring D_t relative to the D_t measured in salt solution. To characterize film coverage, atomic force microscopy (AFM) imaging was performed on mica immersed in salt solution (50 mM acetic acid, 150 mM KNO_3, pH = 3.3) with an MFP-3D Bio AFM (Asylum Research, Goleta, CA), described in Appendix 3.

C. Results and Discussion

We used a surface forces apparatus (SFA) to directly test whether intramolecular proximity is necessary for catechol-cation synergy by measuring the adhesion to mica of siderophore analogs with systematically varying spacing between catechol and cationic amine functionalities. In adhesion measurements, two failure modes can contribute to the measured pull-off force: adhesive failure (separation at the film-mica interface) and cohesive failure (separation at the film-film interface). When adhesive failure occurs , the pull-off force corresponds to intermolecular interactions between siderophore analogs and mica, which can include bidentate hydrogen bonds and coordinate covalent bonds.[2] When cohesive failure occurs, the pull-off force corresponds to intermolecular interaction between siderophore analogs adsorbed on each mica surface, which can include hydrogen bonds, hydrophobic interactions, and cation-pi interactions.[2] Catechol-cation synergy refers to cooperative binding

of molecules to a substrate. Therefore, to assess the impact of molecular structure on catechol-cation synergy, it is necessary to measure pull-off forces corresponding to adhesive failure. For the case of molecularly smooth mica surfaces (Figure A3.1), a monolayer film between the surfaces guarantees adhesive failure because each siderophore analog within the monolayer can bind to both mica surfaces, and therefore separation must occur at the film-mica interface. Below, we establish the deposition conditions resulting in a monolayer of siderophore analogs between the surfaces, and therefore adhesive failure. We then confirm that catechol-cation synergy occurs and discuss the impact of intramolecular catechol-cation spacing on the synergy.

Compression and separation of films of siderophore analogs in an SFA enabled measurement of pull-off force (F_{ad}/R), onset of interaction (D_{onset}), and compressed film thickness (D_t). Figure 2.2 shows representative plots of normal force (F/R) vs. surface separation distance (D) measured for films of Tren(GGK-Cat)$_3$, Tren(GKG-Cat)$_3$, and Tren(KGG-Cat)$_3$. Each plot corresponds to an experiment conducted using a single pair of mica surfaces. First, bare mica surfaces were compressed and separated in salt solution (black circles). Next, a film of siderophore analogs was deposited onto one of the mica surfaces via asymmetric deposition, followed by compression and separation of the surfaces (red circles). Finally, analogs were deposited symmetrically onto both surfaces, and the surfaces were again compressed and separated (blue circles). Open circles correspond to approach and compression of the surfaces; closed circles correspond to separation and jump from contact. In each plot, F_{ad}/R, D_t, and D_{onset} are indicated.

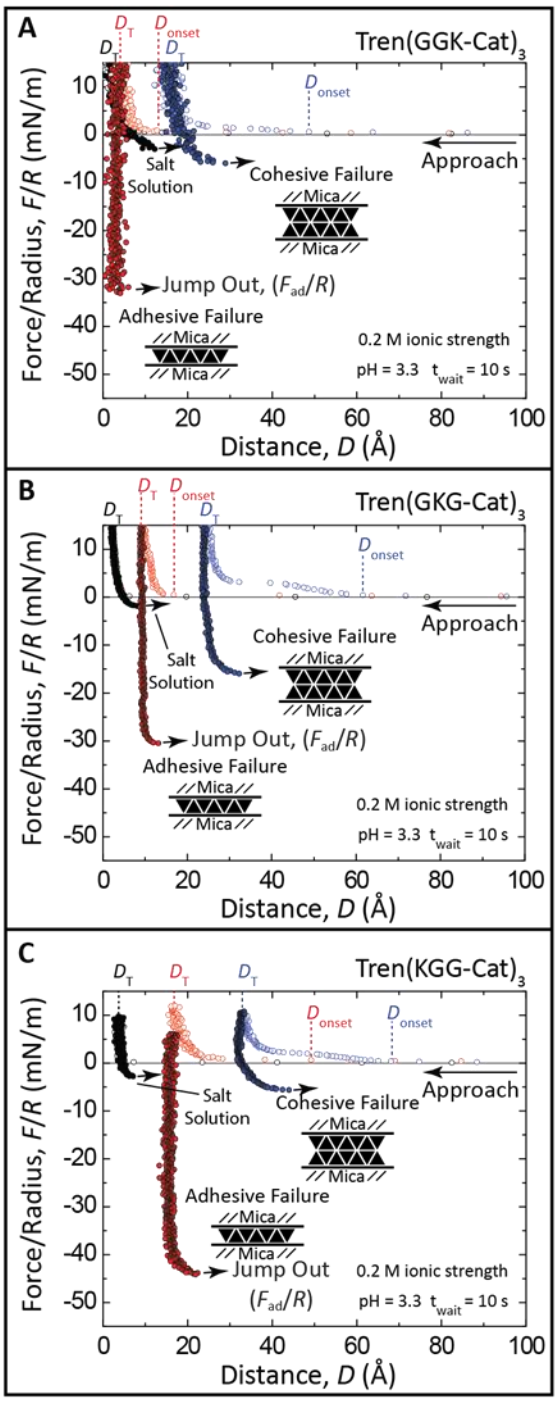

Figure 2.2. Plots of normal force (F/R) vs. separation distance (D) for bare mica surfaces (black circles) and after asymmetric (red circles) and symmetric (blue circles) depositions of (A) Tren(GGK-Cat)$_3$, (B) Tren(GKG-Cat)$_3$, and (C) Tren(KGG-Cat)$_3$. Open circles show approach and compression of the surfaces; closed circles show separation and jump from contact.

Pull-off force, onset of interaction, and contact time dependence measured during compression and separation of films of siderophore analogs depended on the compressed film thickness. Figure 2.3 shows plots of pull-off force ($-F_{ad}/R$) as a function of compressed film thickness (D_t). For each analog, D_t < 10 Å corresponds to low pull-off force. Pull-off force is maximized at D_t = 10 Å, and the maximum pull-off forces mediated by each analog are not statistically significantly different ($\alpha = .05$) (Figure A2.2). As D_t increases 10 Å, pull-off force decreases. Interestingly, the analog with the greatest separation between catechol and cationic functionalities (Tren(KGG-Cat)$_3$) mediates larger pull-off forces than Tren(GKG-Cat)$_3$ and Tren(GGK-Cat)$_3$ for 15 Å < D_t < 20 Å, discussed later.

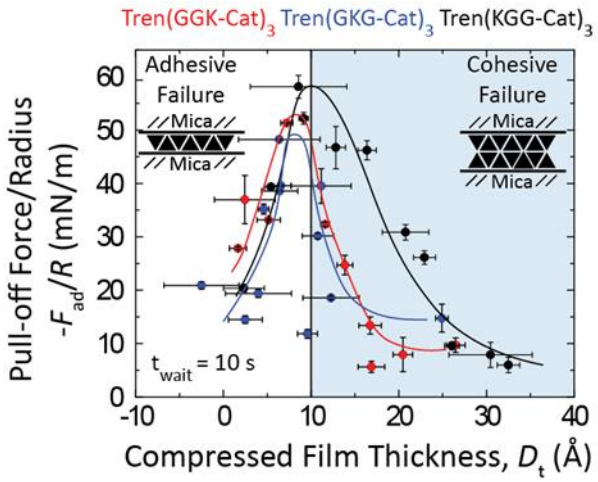

Figure 2.3. Plots of pull-off force ($-F_{ad}/R$) vs. compressed film thickness (D_t) for Tren(GGK-Cat)$_3$ (red circles), Tren(GKG-Cat)$_3$ (blue circles), and Tren(KGG-Cat)$_3$ (black circles). Lines are included to guide the eye.

The compressed film thickness corresponding to maximum pull-off force (D_t = 10 Å) also corresponds to a discontinuous increase in the onset of interaction (D_{onset}). Figure 2.4 shows plots of D_{onset} as a function of D_t. As D_t increases from 0 to 10 Å, D_{onset} increases from 5 to 15 Å. At D_t = 10 Å, D_{onset} increases discontinuously from 15 to 40 Å. As D_t increases further from 10 to 30 Å, D_{onset} increases from 40 to 60 Å. D_t = 10 Å also corresponds to a minimum increase in pull-off force with increased contact time. Figure 2.5A shows pull-off force for t_{wait} = 60 min ($F_{t = 60\ min}$), normalized by pull-off force for t_{wait} = 10 s ($F_{t = 10\ s}$), as a function of D_t. For all analogs, increased contact time generally results in increased pull-off force ($F_{t = 60\ min}/F_{t = 60\ min} \geq 1$). However, the increase in pull-off force is minimized for D_t = 10 Å ($F_{t = 60\ min}/F_{t = 10\ s}$ = 1.0). Increased contact time also decreases D_t. Figure 2.5B shows the change in compressed film thickness ΔD_t as a function of D_t measured before the wait time. Open circles correspond to short waiting times (t_{wait} = 10 s) for which D_t did not decrease (ΔD_t = 0). In contrast, closed circles correspond to longer contact times (t_{wait} = 60 min) and decreases in D_t ($\Delta D_t > 0$), with the largest decreases occurring for D_t > 10 Å.

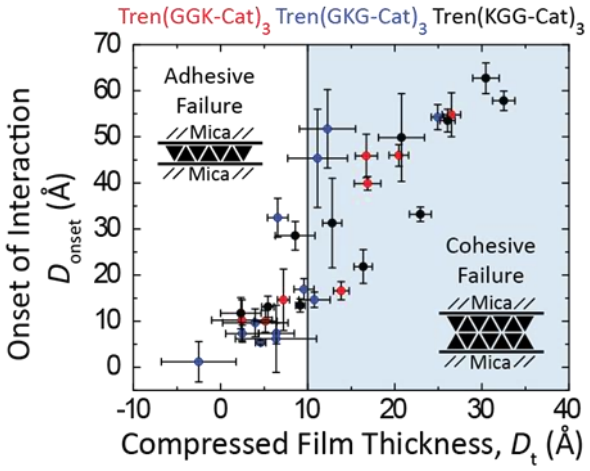

Figure 2.4. Plots of onset of interaction (D_{onset}) vs. compressed film thickness (D_t) for Tren(GGK-Cat)$_3$ (red circles), Tren(GKG-Cat)$_3$ (blue circles), and Tren(KGG-Cat)$_3$ (black circles).

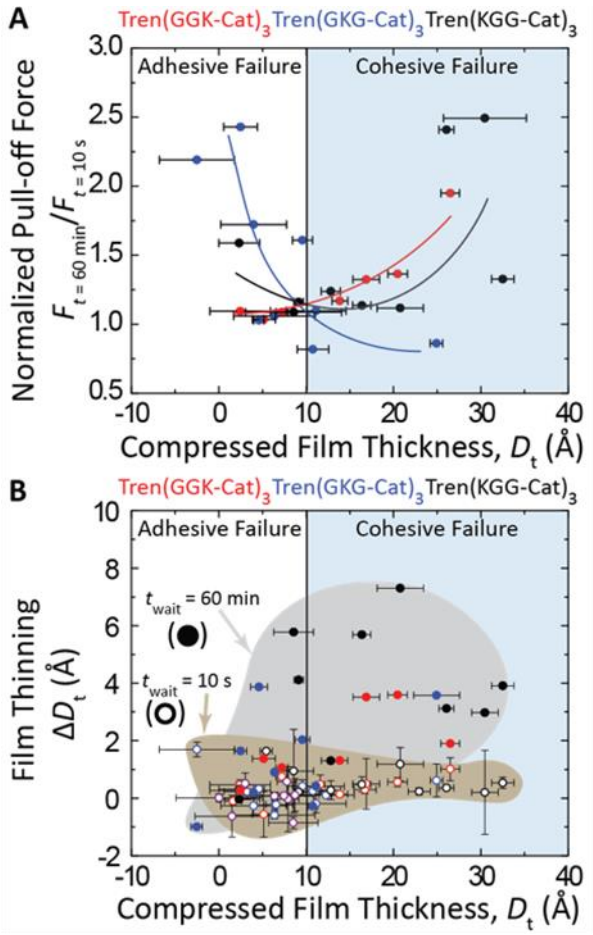

Figure 2.5. (A) Plots of normalized pull-off force ($F_{t\ =\ 60\ min}/F_{t\ =\ 10\ s}$) vs. compressed film thickness (D_t) for Tren(GGK-Cat)$_3$ (red circles), Tren(GKG-Cat)$_3$ (blue circles), and Tren(KGG-Cat)$_3$ (black circles). Lines are included to guide the eye. (B) Corresponding plots of change in film thickness (ΔD_t) vs. D_t for t_{wait} = 10 s (open circles) and t_{wait} = 60 min (closed circles).

As shown above, the maximum pull-off force, discontinuous increase in the onset of interaction, and minimum increase in pull-off force with waiting time all occur for the same compressed film thickness (D_t = 10 Å). Taken together, the relationships between these quantities suggest that this film thickness corresponds to a monolayer of siderophore analogs between the surfaces. For D_t > 10 Å, a transition occurs from a single monolayer between the mica surfaces to two monolayers, one on each mica surface. This transition results in a corresponding transition from adhesive failure to cohesive failure. For reference, Figure 2.6 shows a schematic diagram of mica surfaces before and after asymmetric or symmetric deposition of siderophore analogs at different surface densities. Panels i. and iv. show mica surfaces prior to deposition of siderophore analogs. Panels ii., iii, v. and vi. show single monolayers between the surfaces and adhesive failure. Panel vii. shows a monolayer on each surface and cohesive failure. Below, we relate our results to a transition from adhesive failure to cohesive failure and interpret measured pull-off forces in the context of catechol-cation synergy.

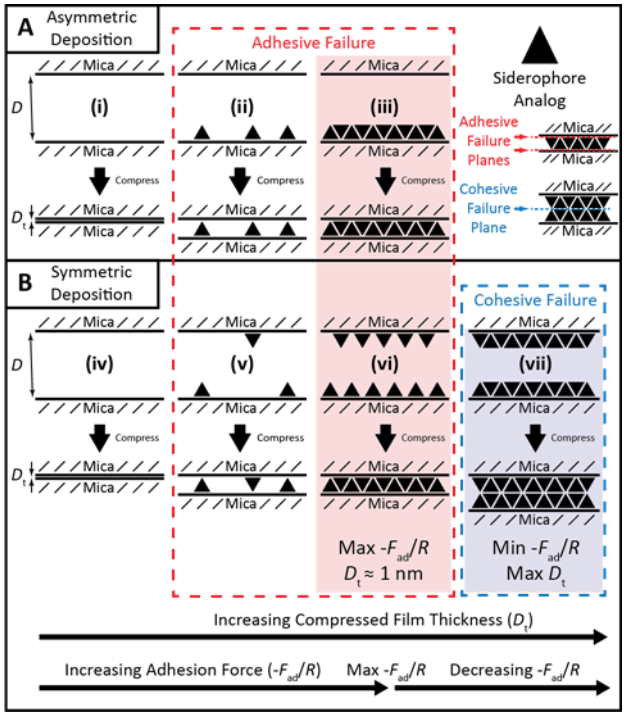

Figure 2.6. A transition from one monolayer (adhesive failure) to two monolayers (cohesive failure) decreases pull-off force ($-F_{ad}/R$) and increases compressed film thickness (D_t). (A) Asymmetric deposition of siderophore analogs on a single surface yields adhesive failure, shown in (ii) and (iii). (B) Symmetric deposition of siderophore analogs on both surfaces results in either adhesive failure shown in (v) and (vi) or cohesive failure shown in (vii). (ii) and (v) show configurations with the same pull-off force; configurations with maximum pull-off force are shown in (iii) and (vi). Bare mica surfaces before deposition of siderophore analogs are shown in (i) and (iv).

We attribute the low pull-of force and onset of interaction for D_t < 10 Å to a sparse monolayer between the mica surfaces. A sparse monolayer contains relatively few siderophore analog molecules binding to both surfaces, and therefore is expected to mediate a low pull-off force, consistent with the data shown in Figure 2.3. A sparse monolayer between the surfaces can be established by either asymmetric deposition (Figure 2.6 ii.) or symmetric deposition (Figure 2.6 v.) with a low concentration of siderophore analogs in solution. We note that waiting at maximum compression results in disproportionate increases in the pull-off force mediated by Tren(GKG-Cat)$_3$ relative to the other analogs for D_t < 10 Å (Figure 2.5A, blue circles). Separation of the glycine residues in Tren(GKG-Cat)$_3$ may reduce the conformational flexibility and inhibit initial binding to both mica surfaces. Time in contact may enable rearrangement and binding to both mica surfaces of individual Tren(GKG-Cat)$_3$ molecules, thus increasing the pull-off force.

The maximum pull-off force and minimum increase in pull-off force with waiting time occur for D_t = 10 Å, suggesting that this film thickness corresponds to a single densely packed monolayer between the surfaces. The ability of siderophore analogs to form films of varying density was confirmed with AFM imaging—increasing the concentration of siderophore analogs in solution during incubation increases the density of the film on the mica surface (Figure A3.2). Like a sparse monolayer, a densely packed monolayer can result from asymmetric deposition of siderophore analogs onto one of the surfaces (Figure 2.6 iii.), or from symmetric deposition of a sparse monolayer of analogs onto both surfaces (Figure 2.6 vi.). When these sparse monolayers are brought into contact, they combine to form a densely packed monolayer. Regardless of the deposition method, a densely packed monolayer is expected to maximize the number of siderophore analogs binding to both mica surfaces and

therefore maximize the pull-off force, consistent with the data shown in Figure 2.3. The minimum increase in pull-off force with waiting time also occurs at D_t = 10 Å, providing additional evidence that this compressed film thickness corresponds to a densely packed monolayer. Dense packing of analogs on a surface and a corresponding low surface area per molecule may prevent functional groups in each molecule from binding to the surface, leaving the groups free to bind to the adjacent surface upon contact. Therefore, increased contact time does not change the distribution of functionalities binding to each surface and pull-off force remains constant.

The discontinuous increase in onset of interaction for $D_t > 10$ Å indicates a transition from a single densely packed monolayer to two monolayers between the surfaces. With a monolayer on each surface, repulsive forces begin when the films on each surface contact each other. This distance (D_{onset} = 40 Å) is slightly more than double the onset of interaction for a single densely packed monolayer (D_{onset} = 15 Å), consistent with a transition from one to two monolayers. The largest compressed film thickness (D_t = 30 Å) corresponds to D_{onset} = 60 Å. This value is larger than would be expected for symmetric densely packed monolayers, suggesting that additional siderophore analogs can adsorb onto the monolayers on each surface. However, no evidence of an adsorbed layer beyond a monolayer is seen after asymmetric deposition, suggesting that the siderophore analogs loosely adsorb to the monolayer and are removed during the rinsing associated with asymmetric deposition. We note that D_t is not expected to increase discontinuously during a transition from one to two monolayers because D_t depends on the adsorption density of the monolayers. A densely packed monolayer is expected to have a larger D_t than a sparse monolayer because individual molecules occupy less area on the surface and therefore extend further into solution. Similar

behavior is also seen in adsorbed surfactant monolayers.[37] As a result, the discontinuous increase in D_{onset} reveals the transition from one to two monolayers in a way that D_t does not.

The decreasing pull-off force with increasing film thickness for D_t > 10 Å provides additional evidence of a transition from a single densely packed monolayer to two monolayers between the surfaces by indicating a transition from adhesive failure to cohesive failure. An adhesive system is expected to fail at the weakest interface. If the film-film interface were stronger than the film-mica interface, adhesive failure would continue to occur at the film-mica interface, regardless of the value of D_t. In that case, pull-off force would not decrease with increasing D_t. Here, the pull-off force decreases with increasing D_t, suggesting a transition from adhesive to cohesive failure. We propose that as the monolayers on each surface become more densely packed, peptide arms on siderophore analogs in each monolayer become unable to penetrate the adjacent monolayer and therefore fail to bind to both mica surfaces. Instead, pull-off forces correspond to cohesive failure and interactions between analogs in opposite films (Figure 2.6 vii.). The decrease in molecular interdigitation with increasing film density is analogous to the behavior of polymer brushes used for antibiofouling surfaces: increasing polymer grafting density decreases the ability of small peptide adhesives to penetrate the brush layer and bind to the underlying substrate.[38] Consistent with this interpretation, the highest incubation concentration of siderophore analogs during symmetric deposition resulted in the lowest pull-off forces (Figure A2.3). We note that when a bare mica surface is brought into contact with a monolayer of siderophore analogs on the opposite surface (as occurs after asymmetric deposition), siderophore analogs may transfer from one surface to the other upon separation of the surfaces, ultimately resulting

in the same distribution of siderophore analogs on each surface as the symmetric deposition configuration shown in Figure 2.6 vi.

The increase in pull-off force and decrease in film thickness with waiting time for $D_t > 10$ Å suggest a partial transition from cohesive failure to adhesive failure. We attribute this transition to interdigitation of siderophore analogs in monolayers on each surface. Here, interdigitation refers to peptide arms of the siderophore analogs penetrating the opposite film and binding to the underlying mica surface. Increasing the fraction of individual siderophore analogs binding to both mica surfaces results in an increased ratio of adhesive failure to cohesive failure, and consequently an increased pull-off force. Interdigitation likely also results in partial coalescence of the two films, consistent with the decrease in film thickness ($\Delta D_t > 0$) after increased waiting time reported in Figure 2.5B for $D_t > 10$ Å.

As stated above, Tren(KGG-Cat)$_3$, mediated larger pull-off forces than Tren(GKG-Cat)$_3$ and Tren(GGK-Cat)$_3$ for 15 Å < D_t < 20 Å (Figure 2.3). The increased pull-off force at these film thicknesses suggests that the glycine residues in Tren(KGG-Cat)$_3$ give the catechols independent mobility from the surface-bound lysines,[39] enabling them to penetrate the film on the adjacent mica surface and bind to both mica surfaces. Films of Tren(KGG-Cat)$_3$ also show the largest increases in pull-off force ($F_{t = 60\ min}/F_{t = 10\ s} > 1$) and decreases in film thickness (ΔD_t), consistent with increased mobility of catechol functionalities. Alternatively, because the lysine residues of Tren(KGG-Cat)$_3$ are close to the cationic Tren core, positive charge is localized at the center of the molecule. This localized charge density may enhance intermolecular cation-pi interactions and strengthen cohesion between symmetric monolayers, consistent with recent studies demonstrating the importance of cation-pi interactions in the adhesion and cohesion of materials containing catechol and cationic functionalities.[40,41] Under

this interpretation, the low pull-off force mediated by Tren(GGK-Cat)$_3$ at D_t = 30 Å suggests that the monolayers become sufficiently densely packed to bury the charged groups and inhibit cation-pi interactions between adjacent films.

To confirm that catechol-cation synergy was occurring, we measured forces mediated by siderophore analogs with cationic amines but without catechols (Tren(GGK-Benz)$_3$, Figure 2.1G) and forces mediated by analogs with only catechol functionalities (Tren(GGG-Cat)$_3$, Figure 2.1H), with representative force-distance plots shown in Figures A2.4 and A2.6. Consistent with previous studies,[33,34] these molecules mediated much lower pull-off forces than siderophore analogs containing catechol and cationic amine functionalities. Films of Tren(GGK-Benz)$_3$ showed a >50% decrease in pull-off forces relative to Tren(GGK-Cat)$_3$ (Figure A2.2). The pull-off force likely results from adhesive electrostatic interactions between pendant cationic amines and the mica surfaces and cohesive hydrophobic and cation-pi interactions. Films of Tren(GGK-Benz)$_3$ also exhibited long-range repulsion on compression that decreased over sequential compression and separation cycles, indicating rearrangement of adsorbed aggregates. Properties of films of Tren(GGK-Benz)$_3$ are described in Figure A2.5. Tren(GGG-Cat)$_3$ showed no evidence of adsorption in the SFA after a 5-h incubation, with onset of interaction, compressed film thickness, and pull-off force remaining identical to the values measured for bare mica surfaces in salt solution. Over 144 h, pull-off force progressively decreased from ~3 mN/m (mica-mica adhesion in salt solution) to zero as the compressed film thickness increased from <1 nm to 50 nm. These changes indicate the adsorption of multilayer aggregates on the mica surfaces, likely driven by electrostatic attraction between the cationic Tren scaffold and the negatively charged mica. The presence of adsorbed aggregates after 24- and 48-h incubations of Tren(GGG-Cat)$_3$ on mica was

confirmed with AFM (Figure A3.3). Pull-off force mediated by the aggregates depends on the separation velocity (Figure A2.6), suggesting that the aggregates are weakly associated and that the pull-off force results from energy dissipation. The delayed adsorption of Tren(GGG-Cat)$_3$ (over hours rather than minutes) suggests that cationic amines of the lysine residues drive adsorption onto the mica surface. Therefore, hydrogen bonds (involving the catechol functionalities or the peptide backbones of each arm of the siderophore analogs), electrostatic interactions involving the Tren core, and non-specific van der Waals interactions are insufficient to drive rapid adsorption of siderophore analogs into monolayers on the mica.

Above, we demonstrate the two criteria necessary for confirming the presence of catechol-cation synergy. We identify pull-off forces corresponding to a monolayer of siderophore analogs, therefore guaranteeing adhesive failure. We then show that siderophore analogs with catechol and cationic amine functionalities mediate significantly larger adhesion than analogs with either catechols or cationic amines alone. Importantly, the molecular weight and density of catechol and cationic amine functionalities were the same for Tren(GGK-Cat)$_3$, Tren(GKG-Cat)$_3$, and Tren(KGG-Cat)$_3$. Since molecular weight[42] and density of binding functionalities[34] influence the adsorption and adhesion of small molecules, keeping these quantities constant enables direct comparison of the adhesion forces to assess the impact of intramolecular spacing on catechol-cation synergy. Surprisingly, increasing the intramolecular catechol-cation spacing by up to two glycine residues does not abolish catechol-cation synergy—Tren(GGK-Cat)$_3$, Tren(GKG-Cat)$_3$, and Tren(KGG-Cat)$_3$ all mediate the same maximum pull-off force (Figure A2.2). Therefore, direct intramolecular proximity is not necessary for catechol-cation synergy.

To further explore the impact of catechol-cation spacing on adhesion, we synthesized siderophore analogs with three and six glycine residues separating 2,3-DHBA and lysine, Tren(KGGG-Cat)$_3$ and Tren(KGGGGGG-Cat)$_3$, respectively. As expected, both molecules mediate substantial pull-off forces despite the increased catechol-cation spacing (Figures A2.7-A2.10). However, the pull-off forces were lower than the pull-off forces for Tren(GGK-Cat)$_3$, Tren(GKG-Cat)$_3$, and Tren(KGG-Cat)$_3$. Figure 2.7 shows a plot of pull-off force vs. molecular weight for various siderophore analogs containing catechol and cationic amine functionalities. The adhesion of Tren(K-Cat)$_3$ reported in a previous study[33] remains the highest of all the siderophore analogs studied thus far due to its relatively low molecular weight and correspondingly large catechol-cation density. As molecular weight increases, pull-off force monotonically decreases, which we attribute to the decreasing density of catechol functionalities within each molecule. The gradually decreasing pull-off force due to decreasing binding group density is fundamentally different from an abrupt decrease in pull-off force at some intramolecular cut-off distance that abolishes catechol-cation synergy. Since adhesion force decreases gradually with catechol-cation spacing up to a spacing of six glycine residues, our results suggest that no such cut-off distance exists, and that further increases in catechol-cation spacing will continue to gradually decrease the adhesion force even as catechol-cation synergy persists.

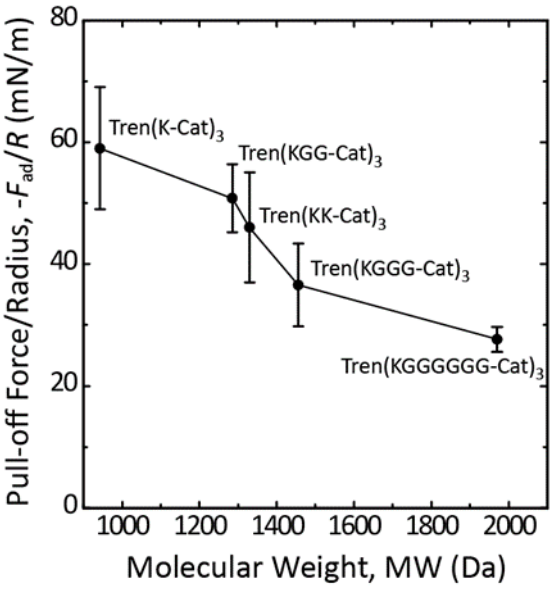

Figure 2.7. Plot of pull-off force (-F_{ad}/R) for t_{wait} = 10 s vs. molecular weight (MW) for siderophore analogs containing catechol and cationic amine functionalities. Data for Tren(K-Cat)$_3$ (t_{wait} = 2 min) and Tren(KK-Cat)$_3$ (t_{wait} = 10 min) reproduced previous publications.[33,34] Lines included to guide the eye.

The results also suggest that the simultaneous detachment of catechol and cationic functionalities from the surface does not contribute to catechol-cation synergy in our experiments. Detachment order has been proposed to contribute to catechol-cation synergy in single-molecule adhesion studies, where the pulling geometry is precisely determined.[35] Unlike single-molecule studies, our experiments involve ~10^8 siderophore analog molecules binding to mica (assuming each analog occupies 1 nm^2 on the mica surface) and a distribution of binding geometries. For example, the adjacent glycine residues in the peptide arms of Tren(KGG-Cat)$_3$ are expected to give conformational flexibility to the molecule[39] and consequently enable a range of distances between surface-bound catechol and cationic amine functionalities in a single siderophore analog arm. For the case where the catechol and cationic amine bind to the mica surface in close proximity (<1 nm), the cationic amine is expected to detach first during adhesive failure due to geometric considerations. For the case where the catechol and cationic amine bind relatively far apart on the mica (~2 nm), simultaneous detachment is possible. However, such distant binding is unlikely for entropic reasons, and therefore sequential catechol-cation detachment from the mica is expected to occur for the majority of Tren(KGG-Cat)$_3$ molecules in the contact area. In contrast, simultaneous detachment of catechol and cationic functionalities from the mica surface is more likely for Tren(GGK-Cat)$_3$ due to the intramolecular adjacency of those functionalities. If detachment order were necessary for catechol-cation synergy in our experiments, Tren(GGK-Cat)$_3$ would be expected to mediate larger adhesion forces than Tren(KGG-Cat)$_3$. Since Tren(GGK-Cat)$_3$, Tren(GKG-Cat)$_3$, and Tren(KGG-Cat)$_3$ mediate the same adhesion forces, we conclude that detachment order of catechol and cationic amine functionalities does not contribute to catechol-cation synergy in this work.

Based on our results, we propose the following mechanism for catechol-cation adhesion synergy: pendant cationic amines of the siderophore analogs exchange with adsorbed cations on the mica surface and drive adsorption onto the mica, enabling subsequent binding of catechols to the mica. With a monolayer of siderophore analogs on the surface, the effective concentration of catechols within 1 nm of the surface is ~3 M, much greater than the bulk siderophore analog concentration (90-667 μM). This effective catechol concentration is calculated assuming that siderophore analogs bind to every negative charge on the mica lattice (1 e^- per 0.5 nm^2). We suggest that the increased concentration of catechols near the mica surface increases the probability of catechols replacing surface-bound cations and binding to the mica.

To justify our mechanism for catechol-cation synergy we developed a qualitative model based on Bell Theory[43] to predict the lifetime and fractional surface coverage of cationic species adsorbed on the mica surface, further described in Appendix 4. The model predicts that siderophore analogs can adsorb to mica solely via their cationic amines. While the assumptions made in the derivation of the model preclude quantitative comparison with experiments, the predictions are qualitatively consistent with our experimental results showing that siderophore analogs lacking cationic functionalities do not adsorb into adhesive monolayers on mica in an aqueous electrolyte solution. As such, the role of cations in catechol-cation synergy is to drive adsorption onto negatively charged surfaces and enable subsequent binding of catechol functionalities. The cooperative effect operates irrespective of the intramolecular catechol-cation spacing. This result is surprising given that the majority of catechols in the most adhesive interfacial mussel protein are located directly adjacent to

cationic amines and raises a fundamental biological question about the evolutionary pressure(s) responsible for this residue distribution.

D. Conclusions

This chapter explores the effect of intramolecular separation of catechol and cationic functionalities on adhesion mediated by monolayers of siderophore analog surface primers. Our results demonstrate that the pull-off force required to separate mica surfaces depends critically on the siderophore analog adsorption density, highlighting the importance of failure mode on adhesive performance. Furthermore, direct intramolecular adjacency of catechol and cationic amine functionalities is not necessary for catechol-cation synergy. Instead, increasing the intramolecular catechol-cation spacing in an adhesive by the addition of non-binding domains progressively reduces adhesion due to the reduced density of binding groups. In sum, the results presented here explain the synergistic binding of catechol and cationic functionalities and suggest that the density of binding groups, rather than the intramolecular arrangement of those groups, should be prioritized when designing adhesives for binding to negatively charged surfaces in saline environments.

III. The molecular context of Dopa influences peptide adsorption and adhesion

A. Background

Despite the widespread interest in polyphenolic adhesives, the adhesion mechanisms of these materials are not fully understood. Recent research suggests that the adhesion of catechols can be enhanced by neighboring cationic functionalities,[33] which may explain the frequent pairing of Dopa and lysine in the adhesive proteins of at least two mussel species.[12,44] However, while many studies demonstrate binding synergy between catecholic and cationic functionalities,[34,35,45–50] others find that pairing these functionalities yields no benefit to adhesion,[51,52] or even decreases adhesion.[40,53] Furthermore, although hydrogen bonds have been proposed to contribute to mussel adhesion,[54–56] some simulations show few hydrogen bonds between Dopa residues from adhesive peptides and mica.[57,58] Recent studies demonstrate that Dopa and other aromatic residues enhance electrostatic interactions between charged residues and surfaces,[58,59] suggesting that Dopa does not always directly participate in adhesion. These disparate results highlight the importance of understanding molecular adhesion mechanisms for the rational design of mussel-inspired adhesives.

Simulations have been increasingly used to investigate the conformations and adhesion mechanisms of catecholic materials.[57,58,60–63] Because most of the characterization of the adhesion of mussel proteins has been performed with a surface forces apparatus (SFA), comparing simulations to complementary SFA experiments is desirable, yet few such studies have been reported.[57,61] Furthermore, while most studies investigate materials that are highly charged and hydrophilic, a prominent mussel foot protein mfp-3 *slow* (mfp-3s), contains few

positive charges and is relatively hydrophobic.[64] Also, only half of the many tyrosine residues in mfp-3s are converted to Dopa, in contrast with the extensive modification of tyrosine to Dopa in other mussel adhesive proteins.[12,65] Understanding the effect of conversion of tyrosine to Dopa in sparsely charged, hydrophobic materials remains an open research area.

Here, we use force measurements and simulations to investigate binding mechanisms of peptide derivatives of mfp-3s. Adhesion measurements in a surface forces apparatus demonstrate that peptides containing Dopa adsorb into adhesive monolayers on mica in an aqueous electrolyte solution, while peptides containing tyrosine adsorb in weakly adhesive clusters. Molecular dynamics simulations highlight the importance of positive charges for peptide adsorption to mica. Simulations of mfp-3s peptide adsorption on silica, self-assembled monolayers, and a lipid bilayer, coupled with the experimental and computational results on mica surfaces, collectively suggest that the molecular context of Dopa—the nature of the surrounding residues and the target surface—dictates adsorption and adhesion, with implications for the design of mussel-inspired adhesives.

B. Experimental Section

Surface Forces Apparatus Adhesion Measurements: A previously designed[66] peptide derivative of the mussel adhesive protein mfp-3 slow (mfp-3S), was commercially ordered with unmodified termini (GenScript). Tyrosine residues were enzymatically modified to Dopa using mushroom tyrosinase.[67] Peptides containing tyrosine and Dopa were denoted mfp-3s-pep-Tyr and mfp-3s-pep-Dopa, respectively (Figure 3.1A). Adhesion measurements were performed with a surface forces apparatus (SFA2000, SurForce LLC), described in detail in Appendix 5. In the SFA, mica surfaces were arranged in a crossed-cylinder geometry, locally equivalent to a sphere of radius R contacting a flat surface.[1] Peptides were deposited from

solution (250 mM KNO_3, 100 mM acetic acid, pH 3) onto both surfaces. All experiments were conducted with a capillary meniscus of the same solution between the surfaces. Solution conditions were chosen to match a previous study of the same peptides.[61] A schematic of the SFA experimental configuration is shown in Figure 3.1B. To measure adhesion, the surfaces were compressed and separated by translating the base of a double cantilever spring bearing one of the surfaces at constant velocity v = 2-12 nm/s. Deflections of the spring yielded the normal force F between the surfaces, which was normalized by the average radius of curvature R of the surfaces. The surfaces were compressed to a maximum compression of 100 mN/m. After waiting at maximum compression (t_{dwell} = 10 s or 60 min), the surfaces were separated. The tensile force F_{ad} before the surfaces jumped out of contact was converted into an adhesion energy per area between flat surfaces according to the DMT theory,[68] $E_{\mathrm{ad}} = -F_{\mathrm{ad}}/2\pi R$, described further in Appendix 5.

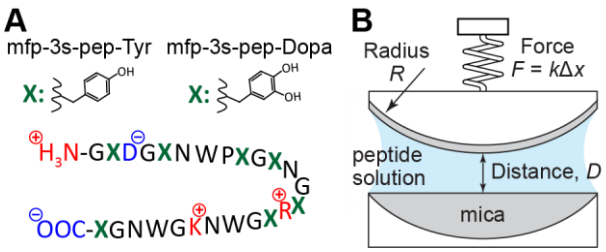

Figure 3.1. (A) The sequence of the mussel-derived peptides used in this work. The letter X represents either the tyrosine residues in mfp-3s-pep-Tyr or the Dopa residues in mfp-3s-pep-Dopa. (B) Schematic of the surface forces apparatus crossed cylinder configuration.

Molecular Dynamics Simulations—System Parameters, Structures, and Equilibration: Each system consisted of a peptide molecule in a cubic simulation box (5.2 *x* 5.2 *x* 5.2 nm^3 for systems in bulk water and 8 x 8 x 8 nm^3 for mica systems) explicitly solvated with SPC water molecules[69] and 1 Cl^- ion for neutral charge. Peptide secondary structures were deduced from the three most dominant mfp-3s-pep-Dopa states observed in earlier work[61], and Dopa residues were converted back to Tyr residues, when applicable, to create mfp-3s-pep-Tyr structures. The simulations were performed using GROMACS 2018[70] and the GROMOS 53A6 force field,[71] however duplicate simulations were also carried out using the AMBER03* force field for proteins[72,73] and TIP3P water[74] in order to mitigate biases from a singular force field. Partial charge assignments for the catechol hydroxyl groups were based on earlier calculations[75]. After solvation, steepest descent energy minimization was carried out for 5,000-100,000 steps, or until a tolerance of 750 kJ/mol/nm was achieved. Simulations were then slowly heated to 300 K for 5 ns using the velocity-rescaling[76] thermostat and a 1 ps time constant. The positions of heavy atoms in the peptide were initially restrained using a force of 1,000 kJ/mol nm^2 in all directions, and under an NVT ensemble with periodic boundary conditions in the *x*, *y* and *z* directions. Peptide hydrogen bonds were constrained using the LINCS method[77] while water bonds were constrained using the SETTLE algorithm.[78] A leapfrog algorithm[79] was also used to integrate the equations of motion with a time step of 2 femtoseconds. In addition, Particle Mesh Ewald (PME) summation[80] was used to treat long-range electrostatic interactions beyond a cutoff radius of 1.0 nm in Fourier space while short-range electrostatics and van der Waals interactions were tabulated in direct space. A Verlet[81] cut-off scheme was used for neighbor searching, with non-bonded pairs updated every 10 steps. After temperature and volume equilibration, an unrestrained 20 ns NPT simulation was

performed to equilibrate the pressure of the system using a Berendsen barostat[82] coupled isotropically (in all dimensions) at 1 bar. A time constant of 0.5 ps and isothermal compressibility of 4.5×10^{-5} bar^{-1} was used in each bulk water simulation.

For systems containing mica, a mica model[83] consisting of a single layer of *muscovite-2M$_1$* ($KAl_2(Si_3Al)O_{10}(OH)_2$) was placed in the simulation box and modeled with parameters from the INTERFACE force field.[84] The mica surface contained 5,120 atoms and was treated as an infinite molecule than spanned the *x*- and *y*-dimensions of the simulation box. During equilibration, heavy atoms were restrained on the surface while light atoms (i.e., hydrogen) were free to move. The negatively charged mica surface was neutralized using 255 K^+ ions resulting in a net neutral system. During NPT equilibration, a semi-isotropic Berendsen barostat was used with no compressibility in the *x*- and *y*-dimensions and aqueous compressibility (4.5×10^{-5} bar^{-1}) in the *z*-dimension to maintain the presence of a surface. Initial peptide structures in the vicinity of mica were taken from the final states deduced from bulk REMD simulations, described in detail below.

Replica-Exchange Molecular Dynamics (REMD) Simulations: The coordinates and velocities obtained from the last frame of each NPT simulation were used to create replicas for each REMD simulation (50 replicas using the GROMOS force field and 70 replicas using the AMBER03* force field). Each replica was heated to a target temperature over 20 ns at constant volume (NVT ensemble). The temperatures ranged roughly from 295-500 K for bulk simulations and 295-470 K for mica-containing simulations. Production REMD simulations were then performed for 400 ns (bulk simulations) or 500 ns (mica simulations) using the Nose-Hoover thermostat[76] with a 1 ps time constant. The average exchange rate between adjacent replicas was approximately 25%, optimized from the initial 10 ns of the REMD

simulation. Exchanges between replicas were attempted every 3 ps. The first 100 ns of the production run was discarded to ensure adequate equilibration of each replica, while the analyses described in this study were limited only to subsequent times in the production run. The cutoff radii used in the simulations were 1.2 nm for the short-range electrostatics and van der Waals interactions.

Umbrella Sampling Simulations: The most dominant structures in REMD simulations were used as the initial peptide structures for umbrella sampling simulations. Peptides bound to mica were then pulled away from or pushed toward the mica to sample both attractive and repulsive potential of mean force (PMF). In instances where the peptide was pulled away from a surface not explored with REMD simulations, the peptide was added to bulk solution at least 1 nm above the new interface and allowed to diffuse and/or bind to the interface for 20 ns, with parameters similar to those described earlier. Upon binding, the peptide was pulled away or pushed toward the surface as described for the mica simulations. Peptides were pulled/pushed with a force of 5000 kJ/mol/nm^2 at a rate of 1 nm/ns until they traversed a net distance of 2-4 nm. Replicas were tabulated every 0.1 nm, yielding an ensemble of about 20-40 replicas. Following collection of the ensemble, we harmonically constrained the peptide in each position and collected energetics for 70 ns using a Nose-Hoover thermostat[76] and 1 ps time constant. We utilized the weighted-histogram analysis method (WHAM) to calculate the free energy of adhesion to each interface, providing a quantitative binding affinity to multiple interfaces. A POPC membrane consisting of 512 lipids was also generated for the umbrella sampling simulations using the CHARMM-GUI web interface (http://www.charmm-gui.org), which was equilibrated at 300 K for 100 ns using the AMBER03 force field.

Simulation Analysis Tools: Standard GROMACS tools used for simulation analysis included: gmx cluster, to cluster peptide structures within an empirically-defined RMSD cutoff (typically 1.4 Å) based on non-terminal backbone atoms within the Daura algorithm.[85]; gmx hbond, to measure the number of hydrogen bonds within a cutoff distance (donor–acceptor) of 3.5 Å and 30° angle (hydrogen-donor–acceptor); gmx gyrate, to obtain the radius of gyration (R_g); gmx density, to calculate atomic densities; gmx mindist, to measure the number of atoms within a given distance from the surface; gmx do_dssp, to deduce peptide secondary structures through the DSSP[86,87] algorithm. Molecular representations were generated by Visual Molecular Dynamics (VMD) 1.9.4.[88]

C. Results and Discussion

We hypothesized that conversion of tyrosine to Dopa would strengthen adhesion of mfp-3s peptides to mica surfaces. To test this hypothesis, we used a surface forces apparatus to measure adhesion to mica of peptides containing tyrosine (mfp-3s-pep-Tyr) and peptides with tyrosine residues converted to Dopa (mfp-3s-pep-Dopa). Figure 3.2A shows representative plots of force/radius F/R as a function of distance D between mica surfaces in salt solution (gray circles) and after deposition of mfp-3s-pep-Dopa (blue circles). Mfp-3s-pep-Dopa readily adsorbed into adhesive films on mica. In salt solution, the mica surfaces are slightly adhesive, with adhesion force 3.0 ± 0.3 mN/m, likely due to non-specific van der Waals interactions. After deposition of mfp-3s-pep-Dopa at approximate peptide concentration 0.1 μM, the adhesion force increased to $-F_{ad}/R$ = 11.0 ± 0.3 mN/m (E_{ad} = 1.8 mJ/m^2). Addition of more mfp-3s-pep-Dopa (to 0.2 μM) further increased the adhesion force to 17 ± 6 mN/m (2.7 mJ/m^2). The adhesion force was constant over consecutive measurements and was

independent of the separation velocity over the range of velocities tested here (Figure A5.1), indicating that adhesion resulted from short-ranged non-covalent interactions.

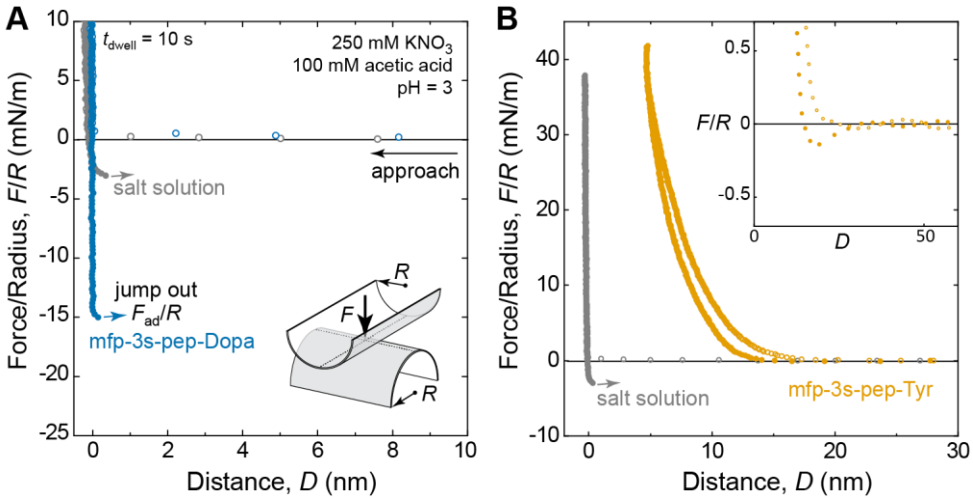

Figure 6.2. (A) Plot of force/radius F/R vs. mica separation distance D for bare mica surfaces in salt solution (gray circles), and for mica surfaces after deposition of mfp-3s-pep-Dopa (blue circles). (B) Force-distance plots for mica surfaces after deposition of mfp-3s-pep-Tyr (orange circles). Open circles correspond to approach and compression of the surfaces; closed circles correspond to separation.

The film thickness after deposition of mfp-3s-pep-Dopa was not significantly different from the thickness measured in salt solution, suggesting that monolayers of peptide adsorbed onto each mica surface. At the solution conditions used in this work, adsorbed potassium ions populate the negatively charged mica lattice. The diameter of a hydrated potassium ion is 6.6 Å.[1] The cross-sectional diameter of mfp-3s-pep-Dopa was estimated as 7 Å, the approximate diameter of a tyrosine amino acid.[89] Replacing hydrated potassium ions with a monolayer of peptide is expected to minimally change the film thickness, whereas a multilayer would increase the film thickness. Therefore, the increase in adhesion force without change in film thickness after deposition of peptides is consistent with adsorption of a monolayer on each surface. The further increase in adhesion force and unchanging film thickness upon injecting additional peptide suggests that the monolayer is incomplete and can accommodate additional peptides without forming a multilayer. With incomplete monolayers on each surface, adhesion forces likely result from bridging interactions, in which a single peptide binds to both mica surfaces.[42] The adhesion depended on the dwell time in contact and the time since incubation (Figure A5.2), consistent with change in the number or distribution of bridging interactions, discussed in greater detail in Appendix 5.

In contrast with mfp-3s-pep-Dopa, mfp-3s-pep-Tyr did not adsorb as adhesive monolayers on mica. Instead, deposition of mfp-3s-pep-Tyr yielded two different results. In some cases, no evidence of peptide adsorption was observed, with the adhesion force and film thickness remaining the same as the values measured in salt solution. In other cases, long-ranged repulsion and minimal adhesion were (Figure 3.2B). This behavior was attributed to association of the peptides in solution and subsequent adsorption of associated assemblies. Our results suggest that these assemblies deposit heterogeneously on the mica. Consequently,

contact between the surfaces either results in compression of one or more assemblies, or contact between bare mica surfaces. Peptide association was corroborated by dynamic light scattering measurements of the mfp-3s-pep-Tyr solution that revealed particles of diameter 200-300 nm (Figure A5.3). These findings are is consistent with a previous study[66] that reported coacervation of the same peptide in acidic aqueous solution, albeit at higher ionic strength than used here.

To explore the impact of hydroxylation of tyrosine to Dopa on peptide structure and adhesion, we performed replica-exchange molecular dynamics (REMD) simulations using the GROMOS force field. Single molecules of mfp-3s-pep-Tyr and mfp-3s-pep-Dopa were simulated in bulk water and in the presence of mica. Figure 3.3A-B (*left*) depicts representative structures of the three most dominant peptides conformations in bulk water. The probability of sampling a given conformation is shown under each cluster. Figure 3.3 (*right*) shows plots of the peptide radius of gyration (R_g) versus end-to-end distance (R_{ee}). The dominant conformations present β-sheets and interactions involving pairs of aromatic residues (Trp, Tyr and Dopa) or interactions between an aromatic residue and a charged residue (Arg, Lys and the N-terminal Gly). Small values of both R_g and R_{ee} correspond to more compact structures, while larger values of R_g and R_{ee} indicate extended structures. Large R_g and small R_{ee} correspond to an extended structure with a beta-hairpin that places the termini close to each other. Mfp-3s-pep-Tyr adopted both extended and compact structures in solution, whereas the mfp-3s-pep-Dopa adopted mostly extended states. Mfp-3s-pep-Dopa was also more solvent-exposed and formed additional hydrogen bonds with water compared with mfp-3s-pep-Tyr, consistent with the second hydroxyl group on each of the seven Dopa residues (Figure A6.1).

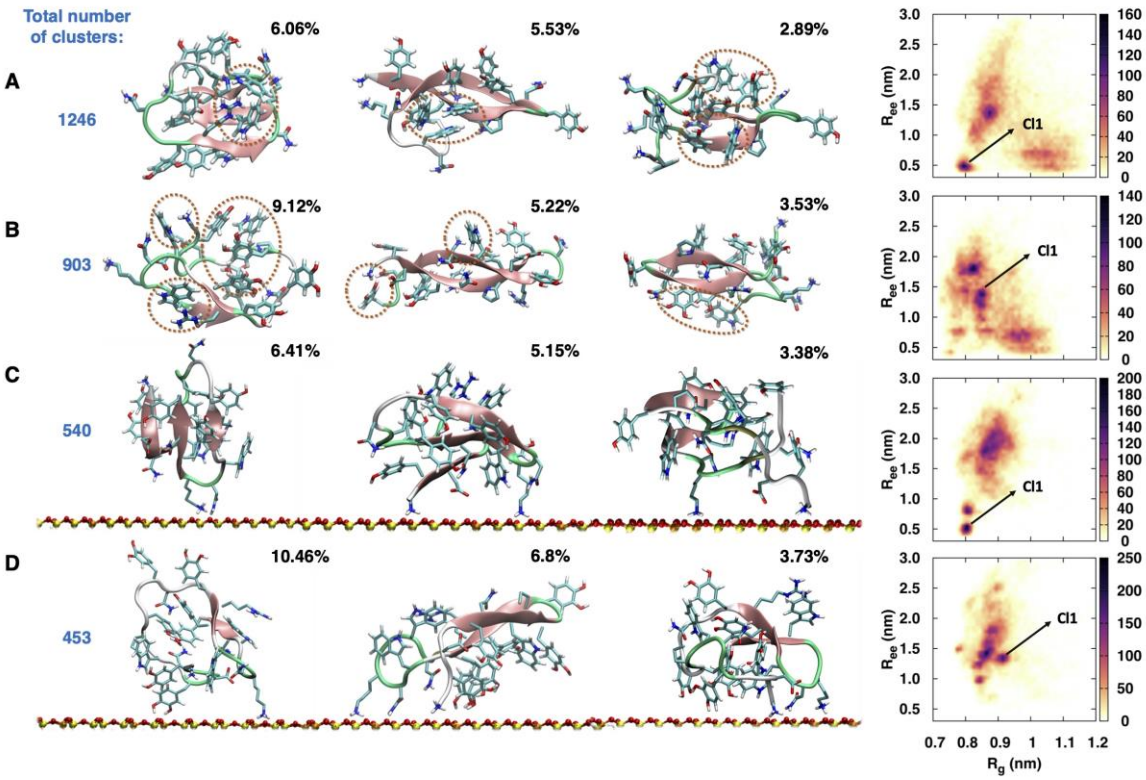

Figure 3.3. Top three clusters of likely conformations (*left*) and end-to-end distance R_{ee} vs radius of gyration R_g (*right*) for (A) mfp-3s-pep-Tyr and (B) mfp-3s-pep-Dopa in bulk water and (C) mfp-3s-pep-Tyr (D) mfp-3s-pep-Dopa in the presence of mica. The dashed ovals in the cartoon representations of the peptides indicate interactions between aromatic groups and/or charged groups. Arrows in the plots of R_{ee} vs. R_g indicate the most likely cluster.

In the presence of a mica surface, both peptides lost secondary structure. The three most likely conformations from GROMOS53a6 are shown in Figure 3.3C-D. The probability of adopting β-sheets decreased and the probability of adopting random coils increased (Figures A6.2 and A6.3) relative to the probabilities in bulk solution, commensurate with a decrease in water solvation (Figure A6.1). Adsorption to mica decreased the number of intramolecular hydrogen bonds in mfp-3s-pep-Tyr (Figure A6.4), consistent with the loss of β-sheets. In contrast, the number of intramolecular hydrogen bonds within mfp-3s-pep-Dopa was not significantly affected by adsorption. On mica, mfp-3s-pep-Tyr adopted more compact structures than in solution, while mfp-3s-pep-Dopa sampled structures with larger R_g and better spreading over the surface, as indicated by the radius of gyration in the *xy*-plane parallel to the interface, $R_g(z)$, which corresponds to the ability of the peptide to splay along the surface of mica (Figure 3.4A).

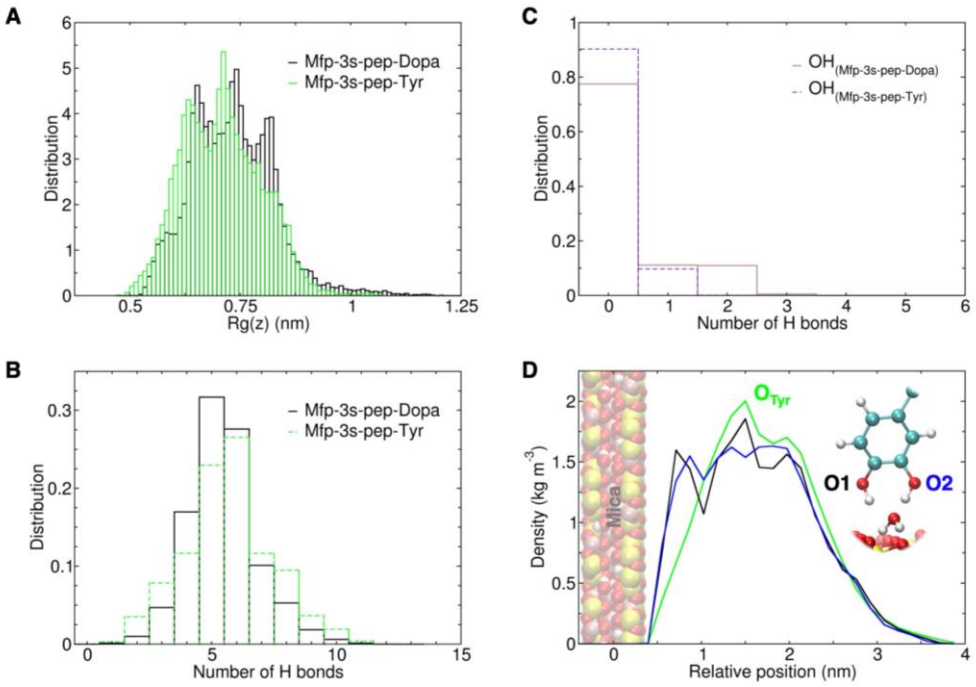

Figure 3.4. (A) Histogram of the radius of gyration about the z-axis for each peptide (B) Normalized histogram of the number of hydrogen bonds between each peptide and the mica surface. (C) Histogram of the number of hydrogen bonds between dopa and Tyr hydroxyls and mica. (D) Density distribution along the *z*-axis of the oxygen atoms from tyrosine and Dopa hydroxyls.

To quantify the contributions of each residue to peptide interactions with mica, we calculated the number of hydrogen bonds formed between each residue and mica (Figures A6.5 and A6.6). Interestingly, the positively charged groups (Lys, Arg, and the N-terminal Gly) formed most of the hydrogen bonds with mica. Lysine residues in each peptide formed an average of 2.4 hydrogen bonds with mica, indicating that lysine often binds to the surface with all three hydrogens on its pendant amine. The cationic N-terminal Gly of mfp-3s-pep-Tyr and mfp-3s-pep-Dopa formed 2.3 and 1.8 hydrogen bonds, respectively. Arg formed fewer hydrogen bonds with mica (0.2-0.4 avg). Uncharged residues including Dopa (0.3 avg) and Asn (0.5-0.7 avg) formed few hydrogen bonds with mica (Figure 3.4C and A6.5). However, 83% of the structures from the most sampled cluster of mfp-3s-pep-Dopa involved bidentate hydrogen bonding between the hydroxyls of Dopa and mica, (Figure 3.3D). After driving the peptide onto the surface to emulate the compression associated with SFA experiments, a single Dopa residue remained stably bound (Figure A6.7, Appendix 6). Nevertheless, Dopa localized at the mica surface much more than Tyr, as shown by the density of hydroxyl oxygens along the z-axis (normal to the mica surface) (Figure 3.4D), possibly corresponding to the formation of outersphere complexes between Dopa and bound water.[66] This result is also confirmed by the overall minimum distances between the hydroxyl oxygens of Dopa and the mica surface (Figure A6.8), and by the greater probability of finding two or more Dopa residues near mica compared with Tyr (Figure A6.9). We also observed correlations between the positions of Dopa and charged residues. The radial distribution function of NH_3^+ atoms around Dopa or Tyr aromatic rings in peptides exposed to a mica surface (Figure A6.10) shows that the density of NH_3^+ is higher within 4 Å of Dopa than

within the same distance of Tyr. Whether the proximity results from interactions between the residues or cooperative interactions with the mica surface remains to be determined.

Comparing our results to other studies of the adhesion of mussel-inspired peptides yields insights into the influence of Dopa content on adsorption and adhesion. A recent study[40] of peptides with similar Dopa content but greater lysine content than mfp-3s-pep-Dopa showed comparable adhesion to our SFA measurements of mfp-3s-pep-Dopa on mica. However, in that study, replacing Dopa by tyrosine or phenylalanine was shown to increase adhesion, in contrast with our results. The discrepancy can be explained by considering the relationship between adsorption and adhesion. Highly cationic peptides are favored to adsorb on mica. If a sparse monolayer adsorbs such that individual adhesive molecules can bridge both surfaces, or if a monolayer is deposited onto a single surface, then conversion of tyrosine to Dopa increases adhesion.[42,57] If a dense monolayer or multilayer adsorbs on both surfaces, then cohesion between the films will dictate the measured adhesion force, and conversion of tyrosine to Dopa decreases adhesion due to weakened cation-π interactions.[40] Our results demonstrate that the presence of Dopa enables mildly cationic, hydrophobic peptides to adsorb as monolayers, whereas peptides containing tyrosine associate in solution and adsorb in clusters. This observation is consistent with our simulations showing lower hydration and higher content of beta-sheets of mfp-3s-pep-Tyr than mfp-3s-pep-Dopa, both of which might favor association of multiple molecules. These results are also consistent with the association reported for mussel-inspired surface primer,[46] and with reports of the impact of molecular structure on association and adhesion of mussel-inspired materials.[57,63] Ultimately, the influence of Dopa on adhesion depends on the molecular context, including the density and thickness of the adsorbed adhesive and the balance between adhesion and cohesion. Our

results indicate that the propensity of an adhesive to aggregate is another key determinant of the impact of Dopa on adhesion.

The chemical character of the target surface is another important aspect of adhesion. We performed AMBER03* REMD simulations to compare the effects of hydrophilic and hydrophobic surfaces on peptide secondary structure. We first replicated the GROMOS53a6 REMD simulations by simulating the peptides in bulk water and on mica using the AMBER03* model (Figure A6.11). We observed qualitatively similar, but slightly more disordered monomer conformations compared with the GROMOS simulations. Hydrophilic surfaces including silica (Figure A6.12, *left*) and hydrophilic self-assembled monolayers (SAMs) (Figure A6.12, *right*) result in peptides that remain globular. In contrast, hydrophobic SAMs (Figure A6.12, *middle*) result in heavily splayed peptides on the surface. For each surface, there are only slight differences between the structures adopted by mfp-3s-pep-Tyr and mfp-3s-pep-Dopa. These results demonstrate that surface hydrophobicity strongly influences the conformation of bound peptides.

We also explored the effect of conversion of Tyr to Dopa on peptide adhesion to mica and additional inorganic and organic surfaces using umbrella sampling simulations. Our AMBER03* model shows that mfp-3s-pep-Tyr and mfp-3s-pep-Dopa bind with similar energy to mica (Figure A6.13, *top*) and hydrophilic SAMs (Figure A6.13, *third row*). In contrast, on silica (Figure A6.13, *second row*), mfp-3s-pep-Dopa is 50% more adhesive than mfp-3s-pep-Tyr. On hydrophobic SAMs, the adhesion previously reported for mfp-3s-pep-Dopa[61] is 250% larger than the adhesion of mfp-3s-pep-Tyr measured here (Figure A6.13, *third row*). Mfp-3s-pep-Dopa also binds to lipid (POPC) membranes (Figure A6.13, *fourth row*) with adhesion between the values measured for hydrophobic and hydrophilic SAMs.

These results indicate that the effect of hydroxylation of Tyr to Dopa on peptide adhesion depends on the chemical character of the surface. Interestingly, hydroxylation increases adhesion to silica, but not other hydrophilic surfaces (mica and hydrophilic SAMs), suggesting that the adhesion of polyphenolic peptides depends on factors beyond surface hydrophobicity such as charge density and counterion arrangement, density and organization of hydrogen bonding groups, and thermal mobility of surface groups.

Umbrella Sampling Simulations of Short, Palindromic Peptides: Effect of Hydroxylation and Position of Aromatic Groups on Adhesion. To evaluate the relationships between hydroxylation of aromatic groups, proximity of those groups to other residues, and adhesion to mica, we performed umbrella sampling simulations of short, palindromic peptides under identical conditions to the umbrella sampling simulations of mfp-3s peptides. We investigated the following peptides: P1 (XKGGGKX), P2 (XGKGKGX), and P3 (XWKGKWX), where X denotes an aromatic residue, either Phe (no hydroxyls), Tyr (one hydroxyl), or Dopa (two hydroxyls), nine peptides in total. Dopa and Lysine were identified as key amino-acids in our simulations of binding of mpf-3s peptides to mica, and glycine is a staple in mfp sequences that provides flexibility to the peptide chain. These peptides with minimal sequence complexity were designed to test the influences of hydroxylation and molecular context of binding groups on adhesion. P1 contained an aromatic residue adjacent to Lys, while P2 and P3 incorporated an amino acid spacer (Gly for P2, Trp for P3) between aromatic residues and lysine. Umbrella sampling simulations of each peptide (Figure 3.5) reveal that when Lys is adjacent to an aromatic group (P1), peptide adhesion to mica increases with increasing hydroxylation of aromatic groups, with P1-Dopa peptides exhibiting a more negative potential of mean force than P1-Tyr and P1-Phe. In peptides where Lys is separated from an aromatic

group by a Gly residue (P2), P2-Dopa and P2-Tyr yield equivalent adhesion and outperform P2-Phe. In peptides where Lys is separated from an aromatic group by a Trp residue (P3), we find that P3-Dopa adheres less strongly than P3-Tyr and P3-Phe. The results indicate that Tyr-containing peptides tend to outperform Phe-containing peptides, but that the adhesive performance of Dopa is influenced by proximity to charged and hydrophobic residues.

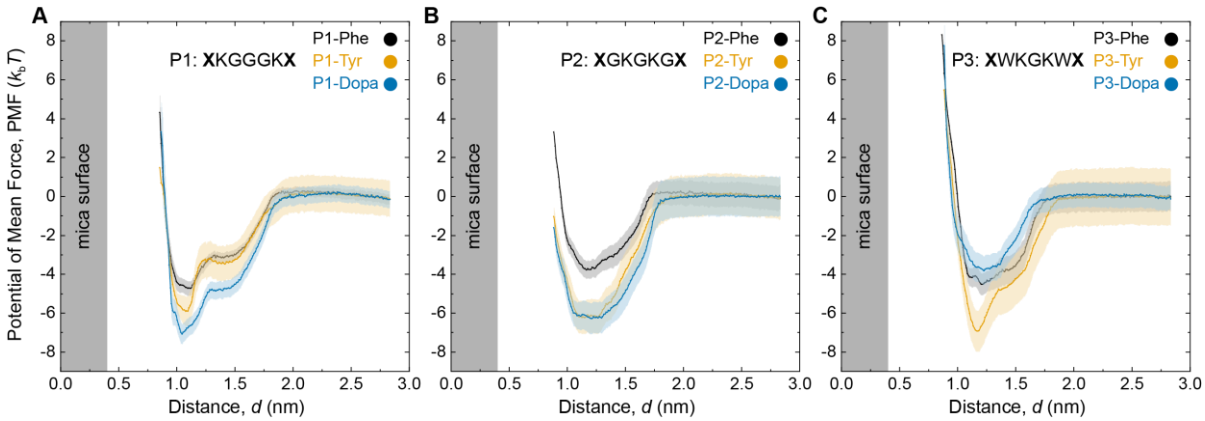

Figure 3.5. Plots of potential of mean force (PMF) vs. distance *d* from a mica surface calculated from umbrella sampling simulations of aromatic peptides. We investigated the following peptides: (A) P1, sequence XKGGGKX; (B) P2, sequence XGKGKGX; and (C) P3, sequence XWKGKWX. The letter X denotes an aromatic residue containing either no hydroxyls (Phe), one hydroxyl (Tyr), or two hydroxyls (Dopa).

D. Conclusions

We investigated three aspects of the molecular context of Dopa in mussel-inspired peptides: the tendency of the peptide to aggregate, the chemical character of the target surface, and the proximity of neighboring charged and aromatic groups. We demonstrated that sparsely charged, hydrophobic peptides containing Dopa form adhesive monolayers on mica, while peptides containing tyrosine associate in solution and adsorb in clusters. Atomistic molecular simulations revealed that positively charged residues drive adsorption onto mica through direct interactions with the surface. While we did not observe extensive hydrogen bonding between Dopa and mica, Dopa hydroxyls were more localized at the mica surface than Tyr hydroxyls. For surfaces other than mica, simulations show that hydrophobicity strongly influences peptide conformation, but that adhesion cannot be predicted from hydrophobicity alone. Simulations also showed that when the aromatic group is separated from Lys, peptides containing Dopa bind no more strongly to mica than peptides containing Tyr, and in some cases bind less strongly. Our results highlight ways in which the molecular context of Dopa

influences peptide association, adsorption, and adhesion. By exploring the roles of Dopa and other amino acids in peptide adhesion, this work clarifies the relationships between peptide structure, surface chemistry, and adhesive performance to ultimately enable rational design of mussel-inspired adhesives.

IV. The influence of charged and catecholic groups on adhesion and cohesion of pressure sensitive adhesives

A. Background

Design of wet adhesives is often inspired by natural materials, such as the adhesives produced by barnacles,[90] sandcastle worms,[91] and marine mussels.[2] Mussel adhesion has been especially widely studied, with many studies seeking to determine molecular mechanisms of adhesion.[8] An active area of investigation is cooperativity between catechols and cationic amines,[32,33,50] prompted by the prevalence of 3,4-dihydroxyphenylalanine (Dopa) and lysine in the most adhesive mussel proteins.[6,12] Recent studies investigated cooperativity of catecholic and charged binding groups in simplified model materials using a surface forces apparatus (SFA)[33,34,46] or atomic force microscope (AFM).[35,50] However, disagreement remains over whether catechols and cationic amine require intramolecular proximity to each other for cooperativity. Furthermore, the model systems use to investigate cooperative binding are far removed from polymeric pressure sensitive adhesives (PSAs) relevant to practical applications. To develop mussel-inspired adhesives for wet conditions, it is important to study and understand the cooperativity of catechols and cationic amines in practically relevant pressure sensitive adhesives.

Adhesion of PSAs often results from phenomena occurring over atomic to macroscopic length scales. As a result, recent studies have used a multi-scale approach to investigate mussel-inspired pressure sensitive adhesives. A study paired colloidal probe spectroscopy (CPS) with industry-standard adhesion static shear, 180° peel, and loop tack adhesion tests to distinguish between adhesive and cohesive effects in a catecholic PSA.[92] A more recent study

used single molecule force spectroscopy (SMFS), colloidal probe spectroscopy (CPS), and static shear and 180° peel tests to investigate cooperativity of catechols and cationic amines in another mussel-inspired PSA.[49] However, microscopic AFM adhesion measurements have several limitations. To measure adhesion of single polymer chains with an AFM requires the use of a good solvent. In the case of hydrophobic polymers, this requirement prohibits the use of water. It is also often difficult to accurately measure film thickness in an AFM, which complicates the interpretation of adhesion measurements in the case of heterogeneous films. Due to the need for large numbers of experiments, individual measurements are very sensitive to film heterogeneity which increases measurement variability and further complicates interpretation of the results. Furthermore, due to the relatively fast retraction velocities that preclude equilibrium measurements, and the uncertainty in contact geometry resulting from a relatively small contact area and unknown surface profiles, AFM experiments often do not directly yield thermodynamic quantities such as surface energy. As a result, it is often not straightforward to compare AFM results to measurements performed using other techniques.

Surface forces apparatus experiments avoid many of the limitations of AFM experiments. SFA experiments can be performed in water, even for hydrophobic polymers. Furthermore, the SFA allows direct measurement of film thickness which can help explain variations in measurements due to heterogeneous films. Finally, SFA measurements can be conducted at slow separation rates and with a controlled contact geometry, enabling measurement of thermodynamic quantities such as surface energy. As a result, SFA experiment can be directly compared with the foundational SFA studies of mussel adhesive proteins,[6,7,9,10,93,94] as well as studies of synthetic mussel-inspired adhesives performed with macroscopic techniques.[3,11] Therefore, SFA experiments are ideal for providing complementary information to

microscopic and macroscopic measurements for a better understanding of the mechanisms of adhesion.

Here, we use a surface forces apparatus to investigate the effect of intramolecular proximity of catechols and cationic amines on adhesion of mussel inspired adhesives. Measurements of adhesion and cohesion of PSA films in a good solvent match previously reported AFM measurements of the same polymers. Adhesion measurements of PSA films in water are compared to previously reported adhesion of mussel adhesive proteins and synthetic polymers. Our results reveal the influence of film composition and solvent-induced restructuring on adhesion, demonstrate the importance of hydrophobic interactions in PSA cohesion, and highlight the role of electrostatic interaction in binding to charged surfaces. By linking experiments performed at atomic and macroscopic length scales, our findings will yield a more complete understanding of the factors influencing adhesive performance and enable the development of mussel-inspired pressure sensitive adhesives for diverse applications.

B. Experimental Section

Surface Forces Apparatus (SFA) Surface Preparation and Force Measurement. Three polymers were synthesized according to a previously reported method,[49] with adjacent catechols and cationic amines (PSA-Lys-DA), catechols and cationic amines distributed randomly (PSA-DAc-ABA), and cationic amines without catechol (PSA-Lys-PEA), shown in Figure 4.1A. Freshly cleaved mica sheets (thickness 3-8 μm) were coated on one side with silver (thickness 50 nm) and glued, silver side down, to cylindrical glass disks (radius of curvature R = 2 cm). Forces measured between bare mica surface in a solution of 95% ethanol, 5% water, or pure water, are shown in Figure A7.1. Drop casting was used to deposit a

polymer film on either both mica surfaces (symmetric deposition) or one mica surface (asymmetric deposition). For symmetric deposition of polymers for experiments in 95% ethanol, polymers were deposited at 0.5 mg/ml, chosen because higher concentrations greatly increased the film thickness and separation force in ethanol solution, resulting in increased experimental error (Figure A7.2). To deposit asymmetric polymer films for experiments in 95% ethanol, polymers were deposited at 0.02 mg/ml, chosen by progressively decreasing the concentration until the resulting films were of nanometer thickness and jumped abruptly apart on separation (Figure A7.2). Asymmetric and symmetric films for experiments in water were deposited at 0.5 mg/ml. A schematic of the SFA configuration is shown in Figure 4.1B. Surface preparation is described in greater detail in the Appendix 7.

The surfaces were placed in a surface forces apparatus (SFA2000, SurForce LLC) in a crossed cylinder configuration. The contact region was wetted with a capillary meniscus (~50 uL) of either pure water or 95% ethanol, 5% waters between the surfaces. Evaporation of the meniscus was limited by a reservoir of the same solution in the sealed SFA chamber. The distance between the mica surfaces D was measured with white light multiple beam interferometry.[95] The deposition method involved removal of the mica surfaces from the SFA, which introduces an uncertainty to the distance measurements of ~1 nm.[96] One of the surfaces was suspended on a double cantilever spring (spring constant k = 1000–10,000 N/m). Deflections of the spring corresponded to the normal force F between the surfaces, which was normalized by the average radius of curvature R of the cylindrical surfaces. A motorized micrometer was used to drive the surfaces together and apart at constant zero-force velocity v = 10-80 nm/s. Figure 4.1C shows a representative plot of F/R vs. D measured during compression and separation of symmetric polymer films in 95% ethanol solution. Positive

forces correspond to compression; negative forces correspond to tension. The figure indicates the adhesion force divided by the radius of curvature of the surfaces F_{ad}/R, the corresponding adhesion distance D_{ad}, the separation work/radius W/R, and the maximum slope of the separation force $d(F/R)/dD$. The inset shows the film thickness at 10 mN/m and 100 mN/m of compression, D_{10} and D_{100}, respectively. For polymer films deposited symmetrically, D_{10} and D_{100} correspond to the combined thicknesses of the films on each surface. Since the measurements were conducted at finite separation velocities, integrating the separation forces over the entire separation likely overestimates the true separation work. A lower limit on the separation work W_{low} was obtained by integrating the separation force from the first negative force until D_{ad}. The JKR theory of contact mechanics[97] was used to calculated the adhesion energy $E_{ad} = F_{ad}/1.5\pi R$. Additional details of the SFA measurements are included in Appendix 7.

Colloidal Probe Spectroscopy (CPS). Colloidal probe spectroscopy experiments were performed using a JPK ForceRobot 300 Atomic Force Microscope (JPK Instruments AG, Berlin, Germany). AFM cantilevers of nominal spring constant 0.2 N/m (sQube, Bickenbach, Germany) were affixed with colloidal SiO_2 particles (diameter 3.5 µm). Polymer films were established on cleaved mica surfaces (Ted Pella, Inc, Redding, CA) by drop casting a solution of 0.5 mg/ml polymer in ethanol. Measurements were performed in 95% ethanol, 5% water. Experiments were conducted with a range of retraction velocities (100−2000 nm/s) and dwell times at maximum compression (0−8 s).

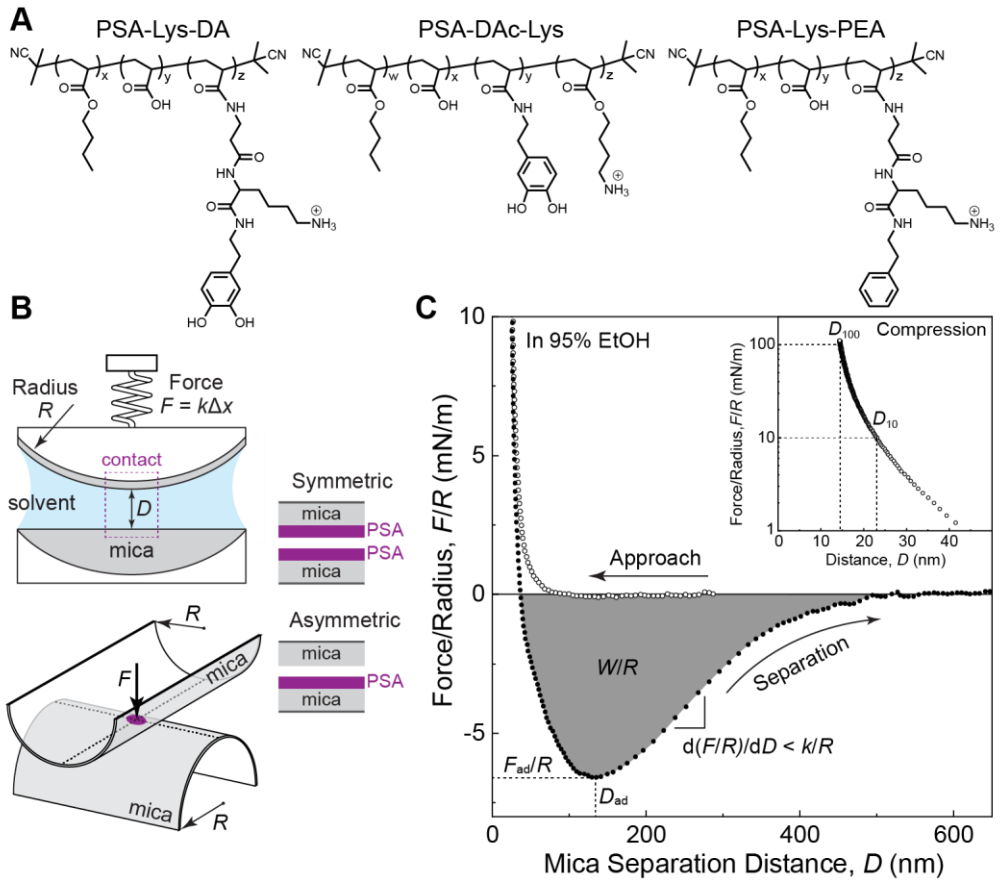

Figure 4.1. (A) The polymers investigated in this work. (B) Schematic of a Surface Forces Apparatus (SFA) showing the crossed cylinder geometry and polymer deposition modes. (C) Example plot of normal force/radius F/R vs. separation distance D for symmetric polymer films between mica surfaces in 95% ethanol. The plot shows the adhesion force divided by the radius of curvature of the surfaces F_{ad}/R, the corresponding adhesion distance D_{ad}, the separation work/radius W/R, and the maximum slope of the separation force $d(F/R)/dD$. The inset shows the film thickness at 10 mN/m and 100 mN/m of compression, D_{10} and D_{100}, respectively.

C. Results and Discussion

We first investigated cohesion between symmetric polymer films in a good solvent, 95% ethanol, 5% water. Figure 4.2A shows SFA measurements of force/radius F/R as a function of separation distance D between mica surfaces. The polymers deposited into nanometer-thick films on mica, with PSA-Lys-PEA consistently forming thinner films than the polymers containing catechols. The films of each polymer were equally compressible (Figure A7.3A), suggesting that the composition of the films was similar. Relatively long-range attractive forces were measured upon separation of the surfaces, and the adhesion forces were similar for each of the three polymers and were independent of the film thickness (Figure A7.4A). In contrast, the separation work did vary with the polymer type. Figure 4.2B shows the separation work/radius W/R as a function of the compressed film thickness D_{100} for each polymer type. The plot shows that polymers containing catechols (PSA-Lys-DA and PSA-DAc-ABA) yield larger separation works than the polymer without catechols (PSA-Lys-PEA). This finding is consistent with previously reported colloidal probe spectroscopy measurements of separation work of the same polymers.[49]

The difference in separation work between polymers with and without catechols can be understood by considering the film thickness and adhesion distance for each adhesion measurement. Figure 4.2B shows that as film thickness increases, so does separation work. We note that the lower limit of separation work shows a similar trend (Figure A7.3B). The adhesion distance D_{ad} also correlates with film thickness (Figure A7.4C). For a given adhesion force, increasing the range of interaction will increase the amount of energy dissipated, shown by the correlation between separation work and adhesion distance (Figure A7.4D). Therefore,

we propose that changes in film thickness contribute to the energy dissipation in ethanol solution by increasing the range of adhesive interactions.

The difference in film thickness between polymers with and without catechols is interesting, given that the deposition conditions are identical for each polymer. While all the polymers are soluble in ethanol, increased cohesive interactions involving catechols may within the films may limit dissolution of polymers into the capillary meniscus of solution between the surfaces, resulting in thicker films of catechol-containing polymers relative to polymers without catechols. Partial dissolution of the films in the capillary meniscus of ethanol solution is supported by measurements of films in water (described later), which show generally thicker films than in ethanol solution and no statistically significant difference between polymers with and without catechols (Table A7.1). Alternatively, interactions between catechols and the mica surface may enable an increased density or brush thickness).

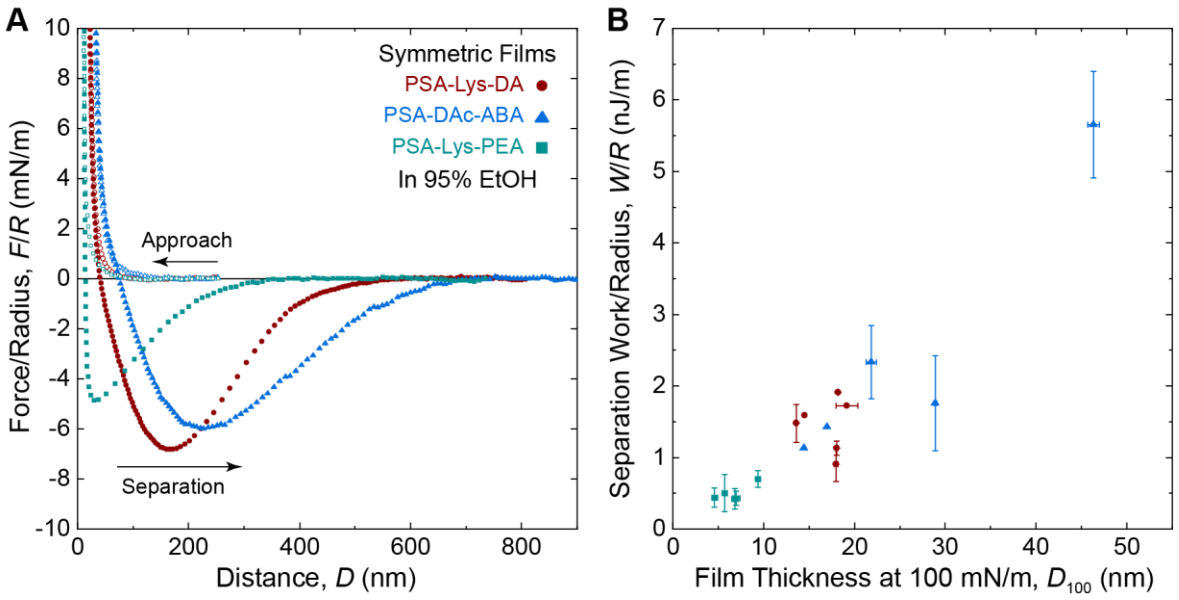

Figure 4.2. Measurements of symmetric polymer films in 95% ethanol. (A) Plot of force/radius F/R vs. distance D for each polymer. (B) Plot of separation work/radius W/R vs. films thickness at 100 mN/m compression D_{100}.

To investigate adhesive interactions between the polymers and mica, we measured the adhesion of asymmetric polymer films in 95% ethanol. Figure 4.3A shows force-distance plots for asymmetric films of each polymer type. The film thicknesses were low ($D_{100} \leq 8$ nm) but showed similar compressibility to the symmetric films (Figure A7.5) and longer ranged repulsion than bare mica surfaces (Figure A7.6), confirming the presence of polymers on the surface. The force-distance plots show that the surfaces jump abruptly from contact at adhesion force F_{ad}/R, where the slope of the measured force is approximately equal to the spring constant of the cantilever bearing one of the surfaces. The abrupt jump from contact suggests that adhesion results from short-ranged attractive interactions, likely a combination of polymer adhesion to mica and cohesion between adsorbed polymer monolayers. For the lowest film thickness, mica-mica interactions may contribute to the measured adhesion, although the van der Waals contribution for crossed cylinders decays with the square of the separation distance.[1] Assuming atomic contact occurs at 0.2 nm, a 1 nm separation corresponds to a 25-fold reduction in van der Waals force.

The adhesion forces measured for each polymer are plotted as a function of film thickness in Figure 4.3B. The adhesion of PSA-Lys-PEA was consistent, whereas the adhesion of polymers containing catechols showed large variability (Table A7.1). Previously reported single molecule force spectroscopy measurements of the same polymers demonstrated that polymers containing catechols formed stronger adhesive interactions with mica than polymers without catechols.[49] Colloidal probe spectroscopy from the same study showed large variability in separation work for polymers containing catechols, Comparing our SFA results after symmetric and asymmetric deposition to these AFM measurements suggests that the variability in adhesion force of asymmetric films in SFA and CPS likely results from changes

in the balance between adhesive and cohesive interactions. The highest adhesion forces measured for asymmetric films of polymers containing catechols likely correspond to bridging interactions where polymers bind to both mica surfaces. The density of adhesive interactions also likely influences the measured adhesion. Together, these SFA and AFM measurements demonstrate that film composition and failure mode, in addition to chemical composition, are key contributors to nano-scale adhesion.

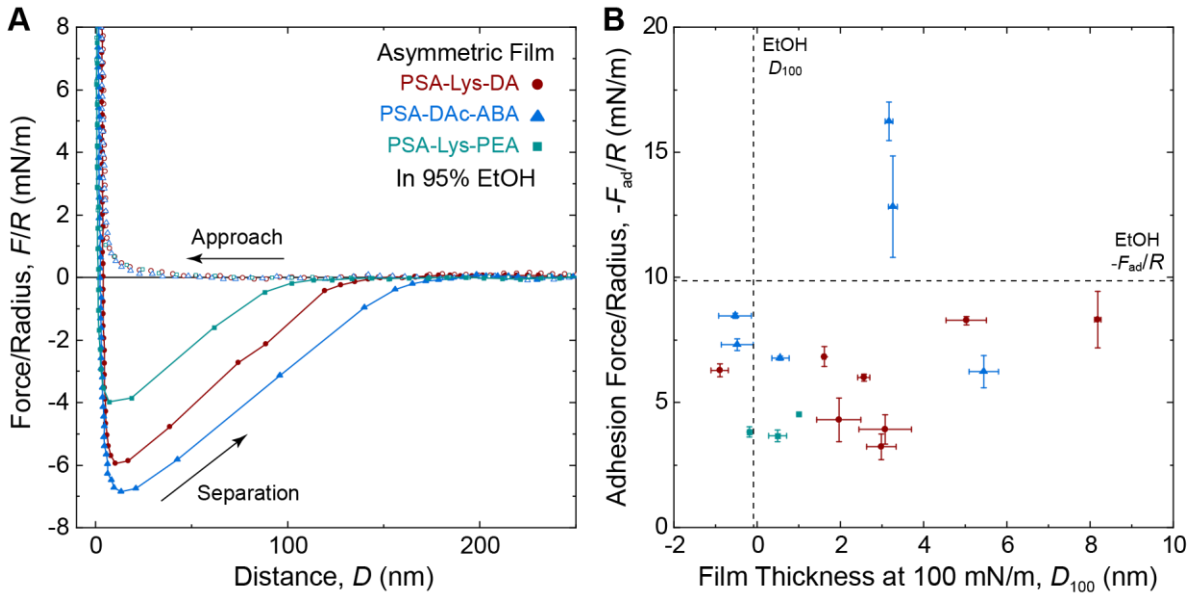

Figure 4.3. Measurements of asymmetric polymer films in 95% ethanol. (A) Plot of F/R vs. D. (B) Plot of $-F_{ad}/R$ vs. D_{100}. Dashed lines indicate the adhesion and film thickness measured for bare mica surfaces in ethanol solution.

To investigate the influence of catechols and cationic amines on adhesion in practical conditions, we measured the adhesion of polymer films in water. Figure 4.4A shows SFA adhesion measurements of films of symmetric and asymmetric films of each polymer type in water. As expected, asymmetric films (open circles in Figure 4.4A) were thinner than symmetric films (closed circles in Figure 4.4A). For both symmetric and asymmetric deposition, surfaces jumped abruptly from contact at adhesion force F_{ad}/R upon separation. Adhesion forces and film thicknesses were not statistically significantly different for each polymer type (Table A7.1). Instead, we observed correlations between film thickness, film composition, and adhesion force. Adhesion force increased with increasing film thickness (Figure 4.4B). Film compressibility varied and was inversely correlated with adhesion force (Figure 4.4C-D). Asymmetric films generally yielded weaker adhesion than symmetric films, but at the same film thickness and compressibility, asymmetric and symmetric films mediated similar adhesion, suggesting that material transfer occurs and that the measured forces correspond to cohesive failure, irrespective of the deposition method. The increased variability in thickness and compressibility of films in water relative to films in 95% ethanol may have resulted from rearrangement of the polymers in water due to surface tension, resulting in in films of heterogeneous composition. We proposed that film heterogeneity causes variations in adhesion force by influencing area of contact between the films and by introducing an energy penalty to compress asperities in the films.

Consistent with the interpretation of the influence of film heterogeneity on adhesion force, increasing the maximum compression increased the adhesion force (Figure A7.7). The increased load presumably prompted polymer rearrangement or flow to redistribute compressed asperities and increase the contact area. The behavior of the films after aging out

of contact further supports the interpretation of restructuring and increased heterogeneity of films in water. Polymer films exhibited changes in thickness and decreases in adhesion force after being left overnight in water (Figure A7.9). A portion of the decrease in adhesion of PSA-Lys-DA and PSA-DAc-ABA may result from catechol oxidation,[55] although catechol oxidation at pH 7 is expected to be slow.[98–100] However, PSA-Lys-PEA also showed a decrease in adhesion force, despite the lack of catechols, which further supports the interpretation of film restructuring. Finally, the dependence of film thickness and adhesion force on contact time (discussed later) is also consistent with film restructuring. These findings collectively support our interpretation that water induces polymer restructuring and film heterogeneity, which strongly influences the measured adhesion.

The magnitude of the adhesion mediated by symmetric and asymmetric films in water suggests possible molecular interactions responsible for adhesion. Adhesion measured in water was up to two orders of magnitude higher than in 95% ethanol, likely due to hydrophobic interactions and possibly hydrogen bonding or electrostatic interactions involving acrylic acid groups (pK_a = 4). Given the dramatic increase in adhesion, cation-π interactions appear much less influential than hydrophobic interactions since the strength of cation-π interactions is expected to be similar in ethanol and water.[101] To place the measured forces in the context of other experiments, the cohesion measured here in water is approximately two orders of magnitude larger than the cohesion of mussel proteins in water[3] and comparable to the cohesion reported for symmetric polystyrene films in water ($-F_{ad}/R$ = 400 ± 50 mN/m).[102] While polystyrene surfaces develop surface-bound bubbles in aqueous media,[102,103] clearly visible in SFA interference fringes, no bubbles were observed in our experiments, suggesting that our polymers are less hydrophobic than polystyrene, consistent

with the presence of hydrophilic amine and acrylic acid groups. Another key difference between our polymers and polystyrene is the ability to form adhesive contact with mica under water. Whereas asymmetric polystyrene films are not adhesive to mica,[103] asymmetric films of the polymers studied here yield the same adhesion force as symmetrically deposited films of the same thickness and compressibility. The fact that asymmetric films of the polymers studied here readily adhere to mica in water highlights the importance of positively charged groups for establishing adhesive contact with mica. Furthermore, the equivalent adhesive forces measured after asymmetric and symmetric deposition suggests that this electrostatic interaction on mica is sufficient to shift the failure plane from the polymer-mica interface to the polymer-polymer interface. Under these conditions (i.e., adhesion to a negatively charged surface in water), further increased in adhesive performance would be gained by increasing the cohesive strength of the polymers rather than their adhesion to mica.

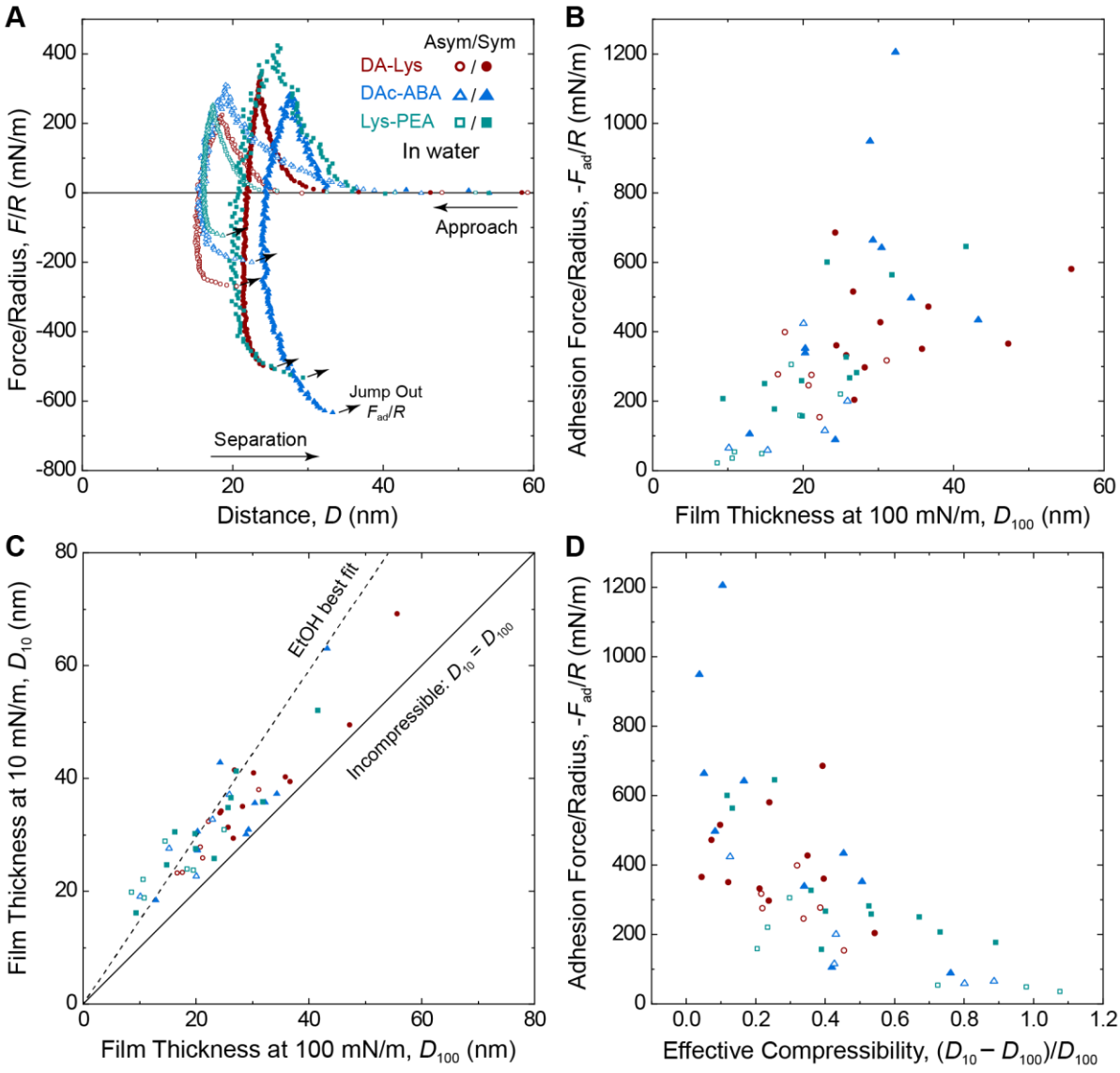

Figure 4.4. Measurements of symmetric and asymmetric polymer films in water. (A) Plots of F/R vs. D. (B) Plot of $-F_{ad}/R$ vs. D_{100}. (C) Plot of D_{10} vs. D_{100}. Dashed line indicates the trend of films in ethanol solution (Figure A7.3A). (D) Plot of $-F_{ad}/R$ vs. effective compressibility $(D_{10}-D_{100})/D_{100}$. Open circles correspond to asymmetric films; closed circles correspond to symmetric films.

Rate and time effects are known to influence polymer adhesion. We investigated the effects of contact time and retraction velocity on adhesion using surface forces apparatus and colloidal probe spectroscopy experiments. Figure 4.5A shows two force-distance plots measured with an SFA during consecutive adhesion cycles of symmetric films of PSA-Lys-DA in water. Red circles correspond to an adhesion cycle with negligible dwell time at maximum compression. Subsequently, the surfaces were compressed to a similar load and then allowed to relax under load for a dwell time of 60 minutes. After the dwell time, the film thinned by approximately 10 nm, and the adhesion force increased by over 300%. All polymers showed a 30-50% decrease in film thickness and a 100-110% increases in adhesion, with a general trend of increasing adhesion force with increasing film thickness (Figure A7.8). Figure 4.5B shows plots of normalized adhesion force and separation work as a function of dwell time at maximum compression measured with CPS in 95% ethanol. Both adhesion force and separation work increased with increasing dwell time, qualitatively consistent with SFA measurements.

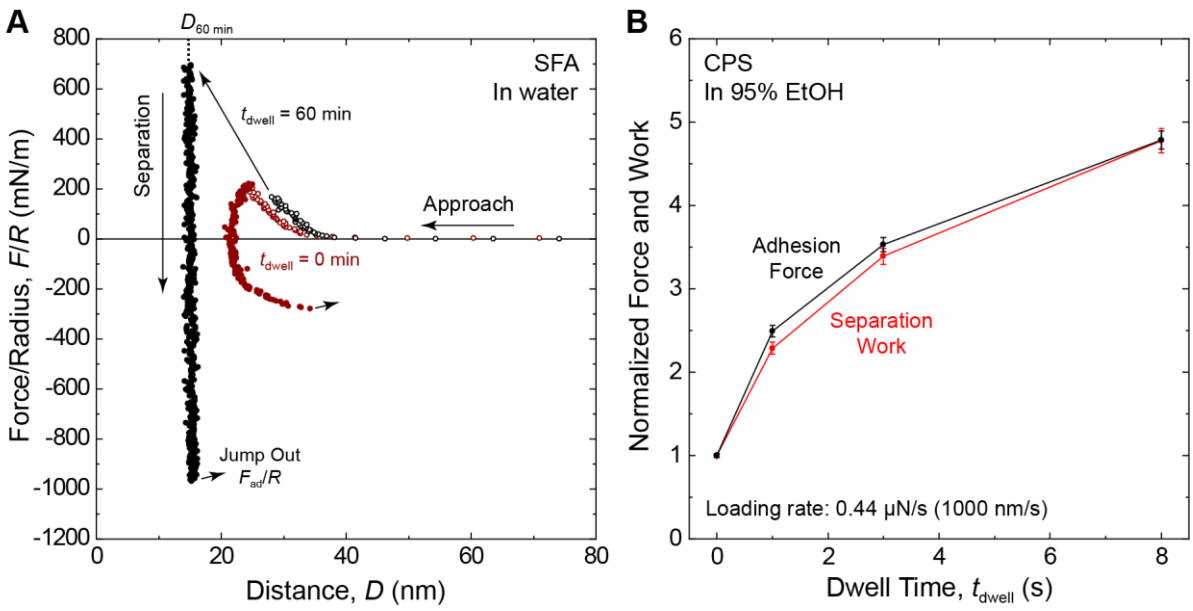

Figure 4.5. Effect of dwell time t_{dwell} on adhesion measured in SFA and CPS experiments. (A) Plot of F/R vs. D measured during sequential SFA adhesion measurements of symmetric films of PSA-Lys-DA in water. Red and black circles correspond to t_{dwell} = 0 and 60 min, respectively. Open circles correspond to compression of the surfaces; closed circles correspond separation. The increase in F/R after the dwell time likely results from thermal drift of the surfaces. (B) Plots of normalized adhesion force and separation work vs. t_{dwell} measured with colloidal probe spectroscopy. Force and work were normalized by the values measured for t_{dwell} = 0 min. Error bars in (B) show the standard error.

SFA and CPS were also used to measure the effect of separation rate on adhesion. Figure 4.6A shows a plot of normalized adhesion force vs. separation velocity for PSA-Lys-DA (red circles) and PSA-Lys-PEA). In the SFA, no trends in separation velocity were observed over the range of adhesion forces tested (10-80 nm/s), suggesting that the measured adhesion results from the cohesive energy of the polymer-polymer interface rather than energy dissipation. In contrast, adhesion force and separation work measured with CPS (Figure 4.6B) increased as separation velocity increased from 100 to 2000 nm/s, suggesting that energy dissipation influences adhesion at these velocities. While the difference in loading rates, contact geometry, and solvent between the SFA and CPS experiments preclude identification of the velocity at which dissipative effects become important, the results indicate that SFA and CPS measurements provide complementary information about thermodynamic and rate-dependent aspects of adhesion. Because an ideal adhesive would demonstrate both strong equilibrium cohesion and substantial energy dissipation, the combing SFA and CPS experiments is a promising strategy for understanding and optimizing new adhesive materials.

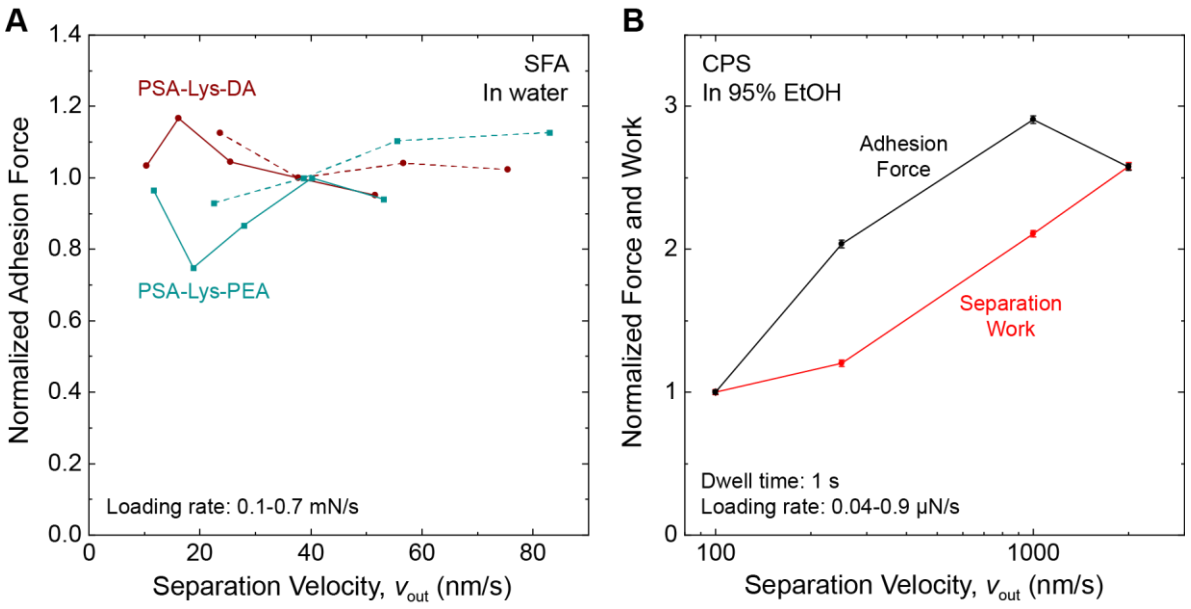

Figure 4.6. Effect of separation velocity v_{out} on adhesion measured in SFA and CPS experiments. (A) Plot of normalized adhesion force vs. v_{out} measured in an SFA. Force was normalized by the value measured at v_{out} = 38-40 nm/s. Dashed and solid lines indicate independent experiments. (B) Plots of normalized adhesion force and separation work vs. v_{out} measured using colloidal probe spectroscopy. Force and work were normalized by the values measured at v_{out} = 100 nm/s. Error bars in (B) show the standard error.

D. Conclusions

We have demonstrated that addition of catechols enhances energy dissipation and adhesion of polymer films in 95% ethanol, consistent with previously reported single-molecule and colloidal probe AFM. In water, the polymers mediate much larger adhesion forces, likely due to hydrophobic interactions between polymer films. The presence of catechols was not found to measurably influence the adhesion force in water. Instead, adhesion depended on the thickness and composition of the films. Asymmetric films established adhesive contact in water irrespective of the catechol content, demonstrating the importance of electrostatic interactions for adhesion to charged substrates. Surface forces apparatus and colloidal probe spectroscopy experiments yielded complementary information about rate and time effects on polymer adhesion. This work suggests that dense, homogeneous films that resist solvent-induced restructuring may provide superior adhesion, providing a target for the design of improved mussel-inspired adhesives.

V. Surface damage influences the cohesion of polystyrene films

A. Background

Possibly Surface energy is an important property governing the adhesion and cohesion of polymer materials. However, many methods to measure this quantity have limitations. Contact angles can be used to calculate surface energies indirectly, but these methods can be inaccurate and model-dependent[104] and cannot account for the effects of confinement. Macroscopic adhesion tests such as peel tests can require relatively large amounts of material, make identification of impurities/defects difficult, and can yield large, non-thermodynamic fracture energies,[104] e.g. due to crazing.[105] Therefore, controlled contact mechanics studies (e.g., using a surface force apparatus (SFA), JKR apparatus, or atomic force microscope (AFM)) are preferable alternatives for measuring the surface energy of solid polymer materials.

Contact mechanics studies of adhesive, elastically deformable surfaces usually employ the Johnson-Kendall-Roberts (JKR) theory.[1] The theory relates the force F_{ad} required to separate two adhering elastic spheres of the same material and radii R_1 and R_2 to the surface energy γ:

$$F_{ad} = -3\pi R\gamma \tag{5.1}$$

where $R = R_1R_2/(R_1 + R_2)$. The theory also relates the contact radius a to the normal force F:

$$a^3 = (3R/4E^*)(F + 6\pi R\gamma \pm (12\pi R\gamma F + (6\pi R\gamma)^2)^{1/2}) \tag{5.2}$$

where the contact modulus E^* is related to the elastic moduli (E_1 and E_2) and Poisson's ratios (ν_1 and ν_2) of the contacting materials by $1/E^* = (1 - \nu_1^2)/E_1 + (1 - \nu_2^2)/E_2$. For layered materials, an effective contact modulus E^*_{eff} is used. Thus, two ways to calculate γ are by

measuring F_{ad} and applying Equation 5.1 or by measuring a as a function of F and fitting Equation 5.2 with γ as a fitting parameter.

The JKR theory has been extensively used to calculate the surface energy of polymers in contact mechanics studies of thin polymer films on elastic substrates.[106,107] Although solid polymers are typically rigid and can have nonlinear elasticity,[108] both of which make JKR measurements of bulk polymer materials difficult, thin polymer films on elastic substrates generally satisfy the assumptions of the JKR theory. Specifically, many contact mechanics studies have involved thin films of polystyrene (PS).[102,104,106,109–114] However, the adhesion measured between polymer films often exceeds the value predicted from thermodynamics, and Equation 5.2 often predicts a during compression of the surfaces (increasing F and a), but not during separation (decreasing F and a). When such deviations from the JKR theory occur, called contact or adhesion hysteresis, the surface energy γ in Equations 5.1 and 5.2 is replaced with effective surface energy γ_{eff}.

Contact hysteresis is often attributed to energy dissipation due to viscoelasticity of the substrates underlying the polymer films and/or polymer diffusion across the interface, also known as interdiffusion.[115] Interdiffusion can increase F_{ad} and γ_{eff} by increasing the real area of contact and therefore the number of bonds across the interface.[108] Since the JKR theory assumes contact between infinitely smooth surfaces, if the real area of contact is greater than the nominal area of contact, the measured F_{ad} will be larger than the value of F_{ad} predicted by Equation 5.1. Interdiffusion occurs readily for contacting polymer melts[115] or grafted brushes into a melt[116] or network,[117] but the extent to which interdiffusion can occur for polymers at temperatures below the glass transition temperature ($T < T_g$) is unclear. Self-diffusion of glassy polymers has been thought unmeasurably slow.[118] However, it has been shown that the

T_g of PS near a solid-vapor interface can be lower than the bulk T_g,[119,120] which corresponds to an increase in molecular mobility at the surface.[121] Simulations confirm the enhanced mobility of polymer chains at a free interface and correlate this mobility to an interfacial region of decreased polymer density.[122] Therefore, an interface between two such regions, e.g. between self-mated PS films, is expected to be fundamentally different from bulk PS. Polymer chains at the interface between self-mated films may be more mobile than chains in the bulk and therefore better able to interdiffuse. Furthermore, limited interdiffusion between self-mated films (here called interdigitation) and penetration by as few as 1-2 monomer units of polymer chains into the opposite film is sufficient to increase adhesion.[109] Such interdigitation corresponds to penetration distances (<5 Å) that are difficult to directly measure—neutron scattering is often used to measure interdiffusion but small interfacial widths can be difficult to distinguish from interfacial roughness.[117] Nevertheless, interdigitation has been proposed to contribute to adhesion and contact hysteresis of glassy PS.[109,110,114,123,124]

Contact mechanics of polymer films can also be influenced by surface damage, including polymer chains pulled out of the film, cohesive failure within the film, or film detachment from the underlying substrate. Previous studies have described damage of films of low-MW PS (<3 kDa) in air[110–114] and films of much higher MW PS (1000 kDa) in water.[102] However, the studies did not explore the impact of damage on the contact mechanics of the films, including adhesion and contact radius.

Here, we use a surface forces apparatus (SFA) to simultaneously measure normal force and contact radius during cycles of compression, separation, and jump from contact (here collectively called adhesion cycles) of self-mated films of low-MW PS (MW = 2.33 kDa) and high-MW PS (MW = 280 kDa). We show that damage to the low-MW PS films occurs as

early as the first adhesion cycle. This damage is correlated to changes in the measured forces and contact radii. In particular, the adhesion force can increase by up to 100% over repeated adhesion cycles. In contrast, films of high-MW PS (MW = 280 kDa) remain undamaged over >100 adhesion cycles, yielding consistent forces and contact radii. To explain our results, we propose that entanglements in the high-MW PS films enable the films to resist damage, and that the low-MW PS films are susceptible to damage due to their inability to form entanglements.

B. Experimental Section

Normal forces between self-mated PS films deposited on mica were measured using a surface forces apparatus (SFA), described in detail elsewhere.[125] Briefly, molecularly smooth mica sheets of thickness 3-5 μm were cleaved and then coated on one side with a reflective silver layer of thickness 50 nm via thermal evaporation. Mica surfaces were prepared using established methods to avoid contamination.[126] The silver-coated mica was then glued (EPON 1004F, Miller-Stephenson Chemical; or NOA81, Norland Products) onto semi-cylindrical fused silica disks (radius of curvature 2 cm) with the mica surface exposed. For each experiment, two such surfaces were prepared. Films of PS of the same MW were then deposited on each mica surface. Two molecular weights of PS were used: low-MW PS (MW = 2.33 kDa, T_g = 69 °C)[111] and high-MW PS (MW = 280 kDa, T_g = 106 °C)[111] (Sigma Aldrich). Solid PS samples were dissolved at 5 wt% in toluene and spin-coated onto the mica surfaces. The surfaces were then dried in active vacuum for >12 h at 22 °C.

White light multiple beam interferometry was used to measure the distance between the surfaces. Because the refractive index of PS (1.5)[127] is close to the refractive index of mica (1.6)[128] over the wavelength range used for the analysis (~500-600 nm), the combined mica/PS

thickness was calculated from the interference fringes by assuming a single refractive index equal to the refractive index of mica and assuming uniform PS films of equal thickness. The mica thickness, measured from contact between bare mica surfaces, was subtracted from the mica/PS thickness to yield the PS film thickness (low-MW PS: 300-400 nm, high-MW PS: 750-800 nm). The interference fringes also yielded the average radius of curvature R of the contact region, described further in Appendix 8. Experiments were conducted at 22 ± 1 °C, well below the bulk T_g of the PS samples. We note that these film thicknesses are well above the film thickness below which the bulk T_g of polystyrene has been observed to decrease (~100 nm).[129]

The surfaces were arranged in a crossed-cylinder configuration, geometrically equivalent to contact between a spherical surface of radius R and a flat surface, and therefore described by the JKR theory. The crossed cylinder configuration is preferable to sphere-on-flat and flat-on-flat configurations for several reasons: i) mica sheets can be glued onto a cylinder without wrinkling or creasing (unlike mica on a spherical surface); ii) crossed cylinders yield a single circular contact, enabling easy alignment of the surfaces (unlike flat-on-flat); iii) proper translation of one surface results in contact between previously uncontacted regions on each surface (unlike sphere-on-flat and flat-on-flat).

To measure the normal force F between the surfaces, one of the surfaces was suspended on a double cantilever spring (k = 30-40 kN/m). Deflections of the spring were converted to force with Hooke's law. For the force-distance profiles shown here, the separation distance corresponds to the distance between the contacting PS films. Adhesion cycles (approach, jump into contact, compression, separation, and jump from contact) were performed using a motorized micrometer to move one of the surfaces at constant velocity (6-17 nm/s) and

corresponding constant compression and separation rate (0.2-0.5 mN/s) to an average maximum compression F = 15-50 mN. The adhesion force F_{ad} was the force required to separate the surfaces from contact. The value of R changed over the course of an experiment (Figure A8.1), likely due to viscoelastic deformations of the glue layer beneath the mica. Equation 5.1 gives F_{ad} proportional to R, and since both F_{ad} and R were directly measured for each adhesion cycle, γ_{eff} calculated with Equation 5.1 was independent of the change in R.

A MATLAB script was written to extract the radius of the contact area a from the interference fringes. A two-parameter least squares regression was used to fit Equation 5.2 to plots of a vs. F by varying γ_{eff} and E^*_{eff} of the layered surfaces. R was measured for each adhesion cycle as described above and was therefore not a fitting parameter. Fits were performed over three force ranges: F = 0-10, 0-20, and 0-30 mN. Negative (tensile) forces were excluded from the fitting ranges for separation to match the fitting ranges for compression.

The JKR theory is considered valid for symmetric surfaces when a dimensionless number called the Tabor parameter $\mu = (4R\gamma^2/E^{*2}z_0^3)^{1/3}$ exceeds 5, where z_0 is the equilibrium separation of the surfaces.[130] Another model describing the contact mechanics of adhesive materials, the Derjaguin-Muller-Toporov (DMT) model,[68] becomes valid as the Tabor parameter approaches zero. Taking z_0 = 0.3 nm (atomic contact) and representatively values from our experiments E^*_{eff} = 20 GPa, R = 2 cm, and γ = 40 mJ/m^2 yields μ = 20, indicating that the JKR theory is applicable for our experimental system. We note that the use of the JKR theory to describe SFA measurements of polymer films has extensive precedent in the literature, but that in general the JKR theory cannot be assumed to be valid, since E^*_{eff} and γ

can vary widely with the choice of surfaces. Therefore, the Tabor parameter should be calculated for each experimental system to determine whether the JKR theory is applicable.

Another dimensionless number, the adhesion parameter $\alpha = (4\gamma R^2(1 - \nu^2)/Eh^3)^{1/2}$ corresponds to deviation from the JKR theory due to the use of layered materials in the SFA[131] rather than homogeneous and isotropic materials. Here, E, ν, and h are the Young's modulus, Poisson's ratio, and thickness, respectively, of the mica. Taking γ = 40 mJ/m^2, R = 2 cm, E = 70 GPa,[132] ν = 0.25,[133] and h = 4 μm yields α = 4, indicating that Equation 5.1 will underpredict γ by 10-20 %.[131] We assume that the polystyrene film determines the surface energy but does not otherwise impact the contact mechanics of the layered system because it is thin relative to the mica and glue layers, a common assumption in studies of polymer films on deformable substrates.[106] Quantifying any additional influence of the polymer film on the calculation and interpretation of α is beyond the scope of this work. For the present study, the values of the Tabor parameter and the adhesion parameter suggest that the JKR theory is appropriate for our experimental system.

C. Results and Discussion

The measured adhesion force F_{ad} and effective surface energy γ_{eff} varied over repeated adhesion cycles of films of low-MW PS. Figure 5.1 shows γ_{eff} of the low-MW PS films calculated from F_{ad} with Equation 5.1 and plotted as a function of adhesion cycle number. The results of four independent experiments are shown, each with a different pair of mica surfaces. Experiments involved sequential adhesion cycles at the same contact location (closed circles). Waiting time between adhesion cycles was minimized (t_{relax} < 60 s). Subsequently, the surfaces were held out of contact (t_{relax} > 8 h). After this relaxation period, sequential adhesion cycles were again conducted at the same contact location (open circles). γ_{eff} generally

increased over repeated adhesion cycles by up to 100%. After the relaxation period, γ_{eff} returned to approximately the initial value, and then increased on subsequent adhesion cycles. An example of the reversible change in γ_{eff} for a single experiment is shown in Figure A8.2.

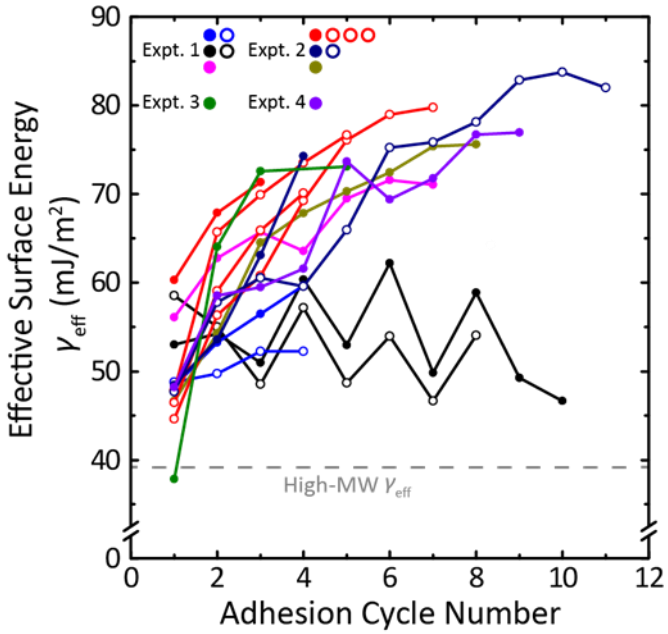

Figure 5.1. Plots of effective surface energy γ_{eff} vs. adhesion cycle number for self-mated low-MW PS films. γ_{eff} measured for high-MW PS films is shown for reference (dashed gray line).

We hypothesize that the change in γ_{eff} measured for low-MW PS films results from surface damage of the films. Upon jump from adhesive contact, discontinuities appeared in the interference fringes that gradually faded over the course of minutes with the surfaces out of contact (Figure A8.3). We attribute these discontinuities to damage of the films. Consistent with this interpretation, measured forces and contact radii changed after the first adhesion cycle. Figure 5.2A shows plots of normal force divided by the radius of curvature F/R vs. surface separation distance D for self-mated low-MW PS films. Black circles show an adhesion cycle in which neither film had been previously contacted at that location. As the surface are compressed (open circles), F increase to >800 mN/m while D decreases by <1 nm. In contrast, red circles show a subsequent adhesion cycle in which D decreases by ~2 nm as F increases to >800 mN/m, an increase in the range of repulsion. The value of D at F = 800 mN/m also increases by ~3 nm from the first to the second adhesion cycle. Since D = 0 corresponds to contact between a specific location on each PS film, changing the contact location results in nonzero values of D due to variations in film thickness. For a fixed contact location, changes in D indicate changes in film thickness. Here, the range of repulsion and film thickness increase from the first to the second adhesion cycle, consistent with damage occurring during the first cycle. The range of repulsion and compressed film thickness returned to the initial values after the surfaces were held out of contact (t_{relax} > 8 h) (Figure A8.4). Damage may heal in a process similar to craze healing,[134] which can be enhanced by an elevated concentration of chain ends at a fractured interface due to chain scission.[135]

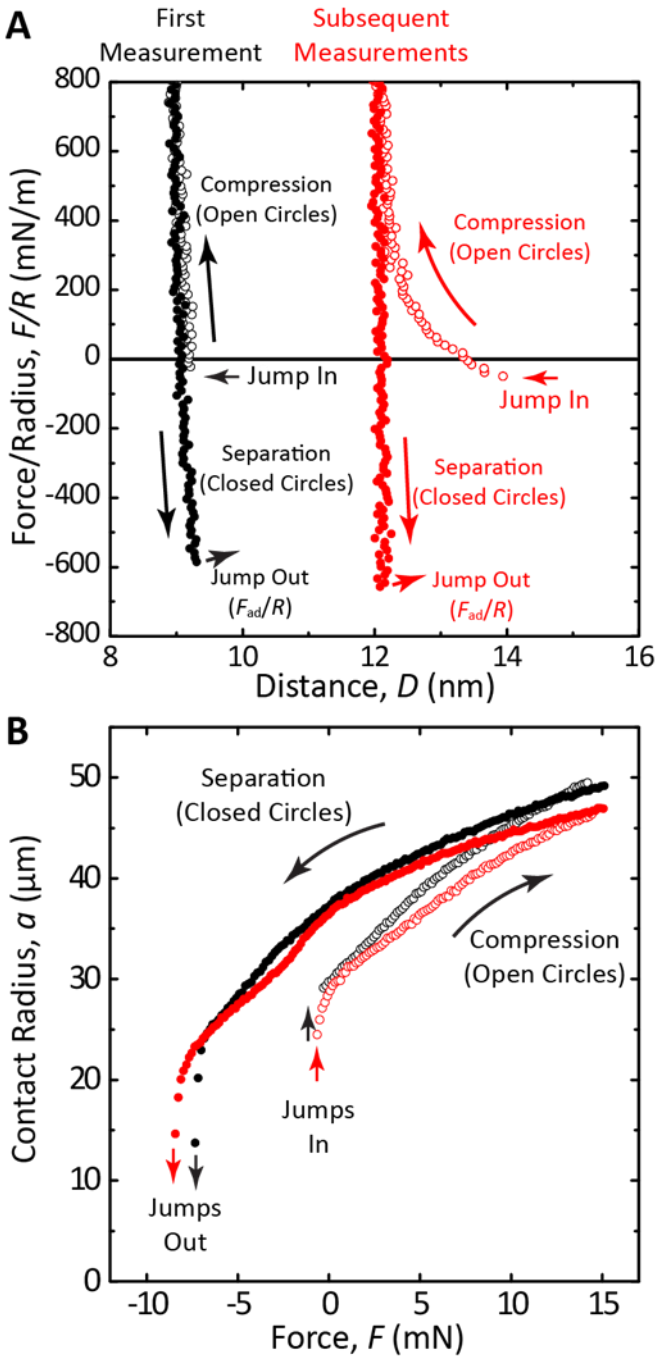

Figure 5.2. (A) Plots of normal force divided by the radius of curvature of the surfaces F/R vs. surface separation distance D for self-mated low-MW PS films. (B) Corresponding plots of contact radius a vs. normal force F between the surfaces.

Measured contact radii further suggest that damage occurs during the first adhesion cycle. Figure 5.2B shows plots of contact radius a vs. normal force F between the surfaces for the same adhesion cycles shown in Figure 5.2A. Values of a measured in the first adhesion cycle (black circles) were larger than values of a measured in subsequent adhesion cycles (red circles) during both compression (open circles) and separation for F > -5 mN (closed circles). The decrease in a after the first adhesion cycle is consistent with damage occurring during the cycle. Damaged films may require larger compressive forces than undamaged films to reach the same nominal contact area due to the need to compress surface asperities on the damaged films.

Interestingly, the damage was also correlated with increasing F_{ad} and γ_{eff} (Figure 5.1), which we propose results from an increase in the real contact area between the films. A previous study showed that surface roughness can increase adhesion between polymer surfaces by increasing the real contact area.[136] In our experiments, damage increases the surface roughness and may similarly increase the real contact area. Damage may also increase the percentage of chain ends at the interface due to chain scission,[135] which can promote interdigitation of the films and thereby increase the real contact area and adhesion.[110] It has also recently been shown that plastic deformation can increase polymer mobility, resulting in increased interdigitation and adhesion between glassy polymer films.[137] As a result, surface damage to low-MW PS films may result in the seemingly contradictory effects of increasing the adhesion force while also increasing the range of repulsion and decreasing the nominal contact area.

Increased waiting time at maximum compression (t_{wait}) resulted in irreversible damage to the low-MW PS films. For t_{wait} = 60 s, stick-slip detachment was observed (Figure A8.5),

consistent with previous studies of PS adhesion to mica.[114] Longer waiting times (t_{wait} = 10, 30, and 60 min) resulted in substantially more damage to the films, including cohesive failure within the films and material transfer between films (Figure A8.6). The damage dramatically altered the interference fringes and precluded further accurate measurements. Such catastrophic damage did not heal after the surfaces were held out of contact, and therefore no further adhesion cycles were performed at such irreversibly damaged contact locations.

Damage to the low-MW PS films also occurred at the edge of the contact region during adhesion cycles. Figure 5.3 shows plots of a vs. F for sequential adhesion cycles of low-MW PS films. Black circles show an adhesion cycle in which neither film had been previously contacted at that location. Open circles correspond to compression of the surfaces; closed circles correspond to separation. Blue circles show a vs. F for a subsequent adhesion cycle in which the surfaces were compressed to a larger maximum force than in the first adhesion cycle. For F = 15-20 mN during the second compression, a was approximately constant, suggesting that the advancing contact edge was pinned. Pinning during the second compression occurred at the contact radius corresponding to maximum compression during the first adhesion cycle (a = 48 μm at F = 15 mN). Therefore, damage occurring at the contact edge during the first adhesion cycle may have pinned the advancing contact edge during the second adhesion cycle due to the need to compress asperities before further increase in contact area. Evidence of edge damage sometimes appeared in the interference fringes (Figure A8.7) for sufficiently large asperities (1-2 nm). Evidence of edge damage disappeared after the surfaces were held out of contact (t_{relax} > 8 h).

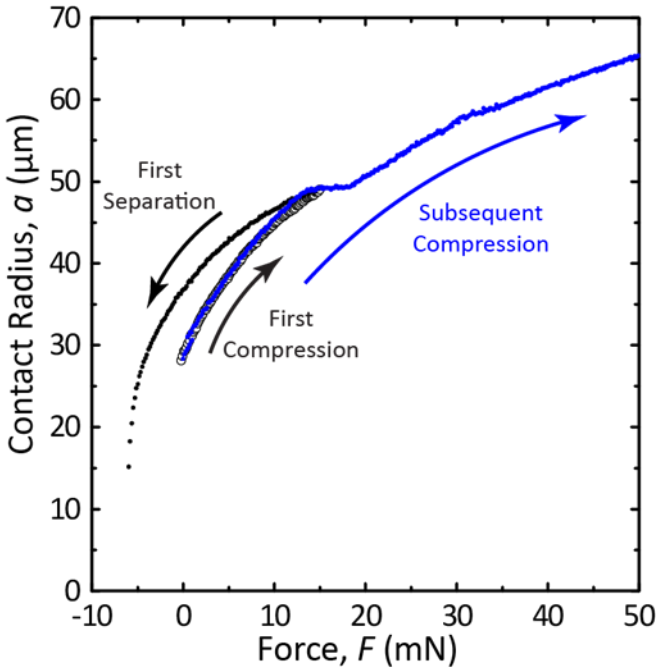

Figure 5.3. Plots of contact radius *a* vs. normal force *F* for self-mated low-MW PS films.

Edge damage may result from enhanced interdigitation of polymers at the contact edge. During the transition from compression to separation of the surfaces in an adhesion cycle, backlash of the motorized micrometer typically resulted in a wait time of ~20 s during which the surfaces were stationary. This wait time may have enabled increased amounts of interdigitation to occur between the films. Interdigitation due to enhanced polymer chain mobility at the polymer-vapor interface has previously been proposed[124] to occur for PS at temperatures as low as 50 °C below the bulk T_g and could therefore be expected to occur for the low-MW PS in this work ($T_g - T = 47$ °C), especially since the low-MW PS has a relatively large concentration of chain ends at the interface, which are known to enhance interdigitation.[110] While interdigitation would seemingly occur throughout the entire contact area during an adhesion cycle, compressive stress can increase viscosity[138] and relaxation time(s) of polystyrene.[139–141] The JKR theory gives the following stress distribution across the contact:

$$P = (2E^*a/\pi R)(1 - r^2/a^2)^{1/2} - ((4E^*\gamma/\pi a)/(1 - r^2/a^2))^{1/2} \quad (5.3)$$

where r is the radial distance from the center of contact, plotted in Figure A8.8. Equation 5.3 shows that the maximum compressive stress occurs at the center of the contact area, and that a transition from compressive to tensile stress occurs at the edge of the contact. As a result, interdigitation may be enhanced at the edge of the contact relative to the interior of the contact, where compressive stress may reduce molecular mobility and limit interdigitation. Therefore, enhanced interdigitation at the contact edge during the wait time at maximum compression discussed above may result in damage upon separation of the surfaces.

In contrast with the low-MW PS films, high-MW PS films resisted damage during adhesion cycles and yielded consistent forces and contact radii. Figure 5.4A shows a

representative force-distance plot for an adhesion cycle involving self-mated high-MW PS films. Open circles correspond to approach and compression of the surfaces; closed circles correspond to separation and jump from contact. Figure 5.4B shows a plot of a vs. F for the same adhesion cycle shown in Figure 5.4A. Open circles correspond to compression and closed circles correspond to separation. Equation 5.2 was fit to the plots of a vs. F for compression (blue line) and separation (red line).

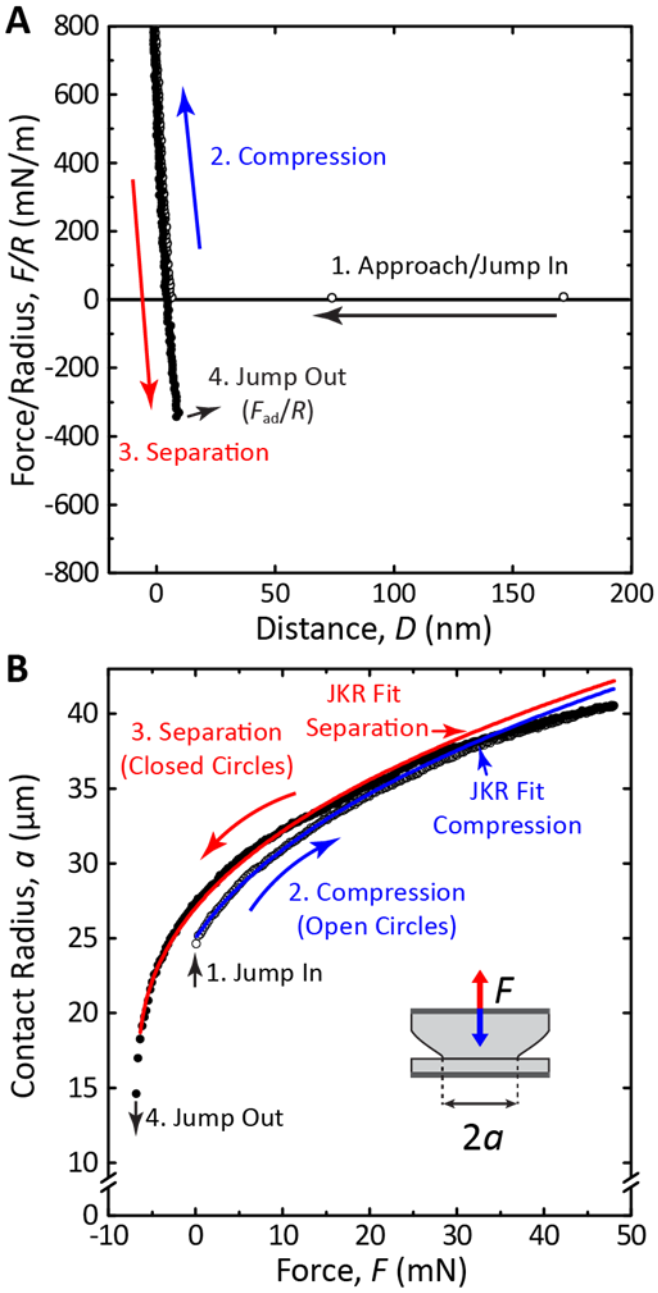

Figure 5.4. (A) Plots of normal force divided by the radius of curvature of the surfaces (F/R) vs. surface separation distance (D) for self-mated high-MW PS films. (B) Corresponding plots of contact radius (a) vs. normal force (F). Blue and red lines show fits using Equation 5.2 for compression and separation of the surfaces, respectively.

Effective surface energies and contact moduli were approximately constant over repeated adhesion cycles (Figure A8.9), and were consistent with previous measurements of PS surface energy.[104,106,142] Figure 5.5 shows effective surface energies of the high-MW PS films calculated by fitting Equation 5.2 to plots of a vs. F for compression ($\gamma_{\text{eff, advancing}}$) and separation ($\gamma_{\text{eff, receding}}$) over the force ranges F = 0-10, 0-20, and 0-30 mN. γ_{eff} calculated from F_{ad} with Equation 5.1 is shown for comparison. Hysteresis was observed: $\gamma_{\text{eff, advancing}}$ was lower than $\gamma_{\text{eff, receding}}$ for all fitting ranges. We attribute the hysteresis to viscoelastic energy dissipation during deformation of the glue layer. Complimentary experiments of contact between bare mica surfaces showed dramatic hysteresis (Figure A8.10), consistent with previous SFA studies.[131,143] The surface energy of mica is higher than the surface energy of PS, resulting in greater deformation of the surfaces, thus magnifying the effects of viscoelastic energy dissipation. Unlike for the low-MW PS, interdigitation is not expected to occur for the high-MW PS ($T_{\text{g}} - T$ = 84 °C). Therefore, the dramatic hysteresis measured for contact between bare mica surfaces suggests viscoelastic energy dissipation as the principal contributor to the hysteresis of the high-MW PS films.

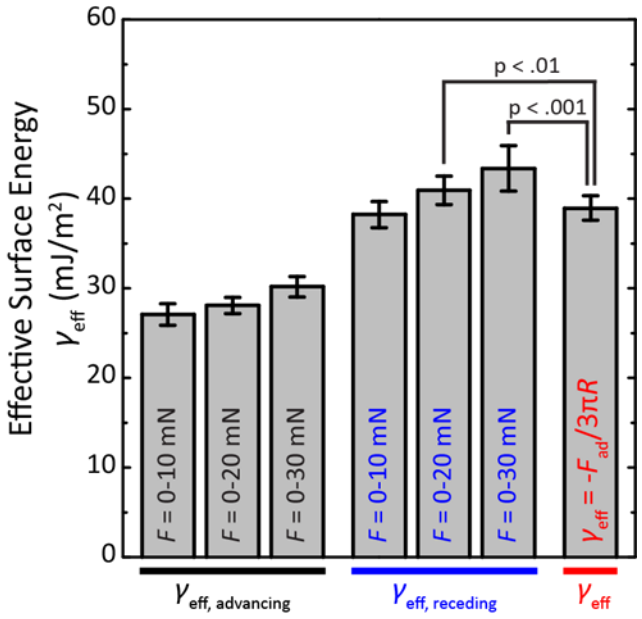

Figure 5.5. Effective surface energies from fitting Equation 5.2 for compression ($\gamma_{eff, advancing}$) and separation ($\gamma_{eff, receding}$) of high-MW PS films. γ_{eff} calculated from F_{ad} with Equation 5.1 is shown for comparison.

The values of γ_{eff} and E^*_{eff} calculated with Equation 5.2 depended on the fitting range. The fit over F = 0-10 mN yielded $\gamma_{eff,\ receding}$ in good agreement with γ_{eff} from Equation 5.1. Fits over larger force ranges (F = 0-20 and F = 0-30 mN) yielded $\gamma_{eff,\ receding}$ greater than γ_{eff} from Equation 5.1. The fit over F = 0-10 mN yielded a better prediction of a at tensile forces (F < 0) than the fits over F = 0-20 mN and F = 0-30 mN, but a worse prediction at the largest compressive forces (Figure A8.11). All fits overpredicted a for F < 0, consistent with a previous study.[142] The value of E^*_{eff} also depended on the fitting range (Figure A8.12), with an approximately 20% difference between the minimum ($E^*_{eff,\ advancing}$ for F = 0-10 mN) and maximum ($E^*_{eff,\ receding}$ for F = 0-30 mN) values. The value of E^*_{eff} increased with increasing maximum force included in the fitting range (i.e., from F = 0-10 mN to F = 0-30 mN), consistent with an increasing influence of the stiff underlying silica disks at increased indentation depths.[143] Calculations of γ_{eff} and E^*_{eff} with Equation 5.2 were likely also influenced by the hysteresis discussed above.

The high-MW PS films resisted damage, and Equations 5.1 and 5.2 yielded consistent values of γ_{eff} and E^*_{eff}, even after >100 consecutive adhesion cycles. We propose that the difference in susceptibility to damage between low-MW and high-MW PS films can be explained by entanglement of the polymer chains in the high-MW PS films. Entanglements are defined as topological restrictions to polymer chain mobility caused by the inability of polymer chains to pass through one another without breaking.[144] Entangled polymer networks are characterized by the entanglement length (the average length of a macromolecule segment between neighboring entanglements) and by the corresponding entanglement molecular weight, M_e.[145] For polystyrene, M_e = 16.6 kDa.[127] Here, low-MW PS (MW = 2.33 kDa) is well below M_e and thus cannot form entanglements. In contrast, high-MW PS (MW = 280

kDa) is well above M_e and is therefore expected to be entangled. We propose that the lack of entanglement in films of low-MW PS makes the films susceptible to damage, and that entanglements in the high-MW PS films may strengthen film cohesion and prevent damage. Elevated adhesion forces resulting from interdigitation of low-MW PS as discussed above may also contribute to damage of the low-MW films.

D. Conclusions

We investigated the contact mechanics of self-mated glassy polystyrene films using a surface forces apparatus. Films of low-MW PS were susceptible to surface damage over repeated adhesion cycles, resulting in an increased effective surface energy and changes in measured contact radii. The effects of damage were reversed after the surfaces were held out of contact. In contrast, films of high-MW PS films yielded consistent surface energies over repeated adhesion cycles. Viscoelastic energy dissipation was likely responsible for hysteresis of the high-MW PS films. We propose that susceptibility to damage of low-MW PS results from the inability of the polymer chains to form entanglements, and that entanglements in the high-MW PS films prevent surface damage. The results suggest that films of polymers of molecular weight below M_e will in general be more susceptible to damage than films of polymers of molecular weight above M_e. A deeper understanding of the relationship between polymer entanglement and surface damage will require further contact mechanics studies of polymers of molecular weight at and around M_e.

VI. Fluid flow influences the contact mechanics of confined polymer gels

Adapted from Degen, G. D. *et al*. Soft Matter, 2020, 16, 8096-8100 by permission of The Royal Society of Chemistry.

A. Background

Possibly Hydrated biopolymer films coat surfaces throughout the human body and include the surface layers of articular cartilage (thickness 4-8 μm)[146–148] and the mucosal layers lining the endothelium (1-5 μm),[149] ocular surface (1-5 μm),[150] airways (7-70 μm),[151] and intestines (20-150 μm).[152] Because these materials can be difficult to study directly, synthetic hydrogels with matching water content and stiffness are often used as model systems. Hydrogels are also used for medical implants[153] and drug delivery.[154,155] Natural and synthetic hydrated networks often exhibit poroelasticity, where elasticity and fluid flow govern mechanical properties. For a poroelastic film compressed between impermeable surfaces, the effect of fluid flow is amplified when the width of the contact region is much larger than the film thickness.[156] Such confinement is particularly likely for thin films. Therefore, to better understand and mimic biological surfaces, it is important to study the poroelasticity of highly confined gel films.

Although the mechanical properties of hydrogels have been widely investigated,[157] most studies of hydrogel poroelasticity report relatively low levels of confinement. These studies typically involve a sphere of radius R compressing a gel film of thickness h to a depth d and approximate contact radius $\sqrt{2Rd}$. Confinement in this geometry is described by the dimensionless number[158] $\alpha = \sqrt{Rd}/h$, proportional to the ratio of contact width to film thickness. Poroelasticity has been observed in hydrogels with low confinement ($\alpha << 1$),[159–

[162] and moderate confinement ($\alpha \approx 1$),[158,163] but few studies of highly confined ($\alpha >> 1$) hydrogels have been reported.[164–166]

The surface forces apparatus (SFA) is often used to study highly confined films.[167] While early SFA experiments were limited to nanoscale films, developments in instrumentation and analysis[96,125,168,169] have enabled studies of microscale films of poroelastic biological materials. For example, poroelasticity was shown to influence the mechanical properties of sections of corneal tissue[170] (thickness 150-300 μm). Films of fibronectin[171] (10-20 μm) and cartilage[172] (8-12 μm) have also been studied, but the experimental designs minimized poroelastic effects. Despite these examples of SFA studies of poroelastic materials, microscale films of synthetic hydrogels have not previously been studied in an SFA. Here, we investigated the contact mechanics of highly confined hydrogel films using a surface forces apparatus. We demonstrate that fluid flow through the hydrogel polymer network dictates the apparent stiffness of the gels and model our results with a theory of poroelasticity.

B. Experimental Section

In each experiment, a swollen crosslinked polyacrylamide film (7.5 wt% PAAm, 0.3 wt% bisacrylamide) was established on a cylindrical silver-coated glass surface (Figure 6.1A, Figure A9.1). In the SFA, the film was compressed against a bare silver surface in a crossed cylinder geometry (Figure 6.1B), equivalent to a sphere compressing a flat gel. The film thickness h, compression depth d and velocity $\mathrm{d}(d)/\mathrm{d}t$, and normal force F were measured. The cylinder radii (R = 2 cm) were much larger than the film thickness (h = 1-70 μm), yielding a highly confined contact region (α = 10-40), with α calculated from d at maximum compression. A schematic of the SFA is shown in Figure A9.2. Details of film preparation, distance/force measurements, and crossed cylinder geometry are included Appendix 9.

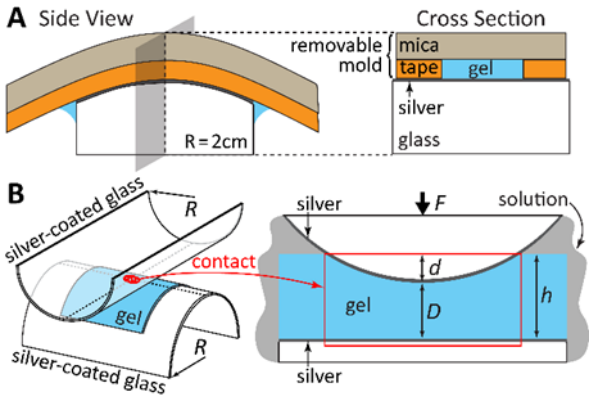

Figure 6.1 (A) Casting a hydrogel film on a cylindrical silver-coated glass surface. (B) Crossed cylinder configuration and schematic of the contact region for a gel film of thickness *h* under applied force *F*, resulting in surface separation *D* and compression depth *d*.

C. Results and Discussion

The gels were modeled as thin poroelastic films[164] where the normal force F needed to compress a film to a depth d is

$$F = \frac{\pi R d^2}{h}\left(E + \frac{\eta R}{2k}\frac{\mathrm{d}(d)}{\mathrm{d}t}\right) \tag{6.1}$$

Here, E and k are the elastic modulus and permeability of the gel, η is the dynamic viscosity of the fluid, R is the radius of each cylindrical surface, and $\mathrm{d}(d)/\mathrm{d}t$ is the compression velocity. Compression forces were also approximated by the Winkler model,[97] adapted to include the influence of fluid flow:

$$F = \frac{\pi R d^2}{h} E_{\mathrm{eff}} = \frac{\pi R d^2}{h}(E + E_{\mathrm{flow}}) \tag{6.2}$$

where the effective modulus E_{eff} is the sum of the elastic modulus E and the average contribution of fluid flow E_{flow}. At equilibrium, $\mathrm{d}(d)/\mathrm{d}t = 0$, $E_{\mathrm{flow}} = 0$, and both equations give $F = \pi R E d^2/h$. Viscoelasticity was neglected because confinement makes the timescales of poroelasticity much longer than the timescales of viscoelasticity.[158]

The apparent stiffness of the hydrogel films depended on the compression velocity. Figure 6.2A shows plots of normal force F vs. compression depth d for a hydrogel film (h = 11 μm, α = 10) compressed at different initial velocities $\mathrm{d}(d)/\mathrm{d}t|_{d=0}$ = 11, 28, and 61 nm/s. As velocity increased, larger forces were needed to reach a given compression depth and the pressure at maximum compression increased from P_{avg} = 2 to 7 kPa. Velocity-dependent stiffness was also observed for thicker films (Figure A11.1).

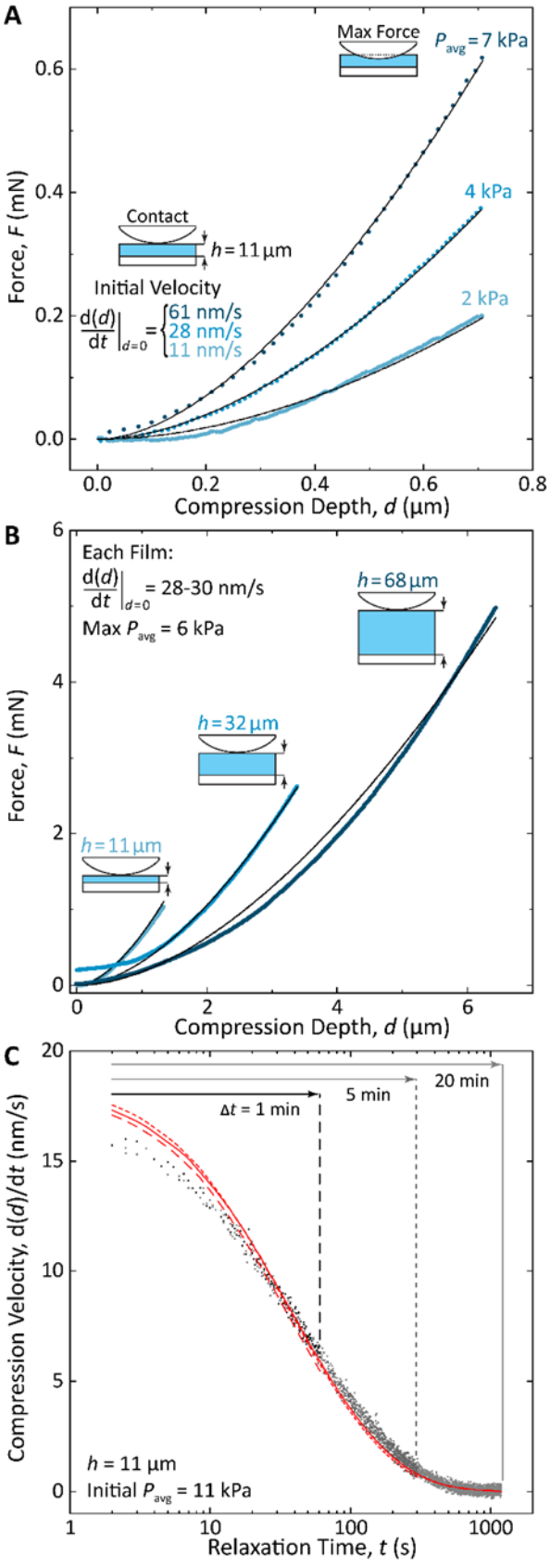
A
Max Force
P_{avg} = 7 kPa
4 kPa
2 kPa
Contact
h = 11 µm
Initial Velocity
d(d)/dt |d=0 = {61 nm/s, 28 nm/s, 11 nm/s
Force, F (mN)
Compression Depth, d (µm)
B
Each Film:
d(d)/dt |d=0 = 28-30 nm/s
Max P_{avg} = 6 kPa
h = 68 µm
h = 32 µm
h = 11 µm
Force, F (mN)
Compression Depth, d (µm)
C
Δt = 1 min
5 min
20 min
h = 11 µm
Initial P_{avg} = 11 kPa
Compression Velocity, d(d)/dt (nm/s)
Relaxation Time, t (s)

Figure 6.2 (A) Normal force F vs. compression depth d for a hydrogel film compressed at different initial velocities $\mathrm{d}(d)/\mathrm{d}t|_{d=0}$. (B) F vs. d for compressions of films of different thicknesses. Curves in (A) and (B) were calculated using Equation 6.1. (C) Compression velocity $\mathrm{d}(d)/\mathrm{d}t$ vs. relaxation time t for sequential relaxations (Δt = 1, 5, and 20 min). Dashed and solid red curves show fits of Equation 6.1 for permeability k.

The apparent stiffness also depended on the film thickness. Figure 6.2B shows plots of F vs. d for three films of different thicknesses (h = 11, 32, and 68 μm), each compressed at the same initial compression velocity 28-30 nm/s to pressure P_{avg} = 6 kPa. As thickness increased, confinement decreased from α = 14 to 5 and less force was needed to reach a given compression depth. We note that the repulsion at d = 0 for the 32 μm film may have resulted from roughness due to swelling (see Appendix 9).

Equation 6.1 accounted for the variations in apparent stiffness of the gels. To determine the elastic modulus E and permeability k for the equation, relaxation experiments were conducted. A hydrogel film (h = 11 μm) was compressed to initial force F_0 and compression depth d_0, at which point the motor driving the cantilever spring suspending one surface was stopped, denoted time t = 0. For $0 < t < \Delta t$, compression depth increased, and force decreased as $F = F_0 - K(d - d_0)$, where K is the cantilever spring constant. Figure 6.2C shows plots of compression velocity $\mathrm{d}(d)/\mathrm{d}t$ vs. relaxation time t for three consecutive relaxation periods (Δt = 1, 5, and 20 min). During each period, compression velocity decreased. The surfaces eventually became nearly stationary, $\mathrm{d}(d)/\mathrm{d}t \approx 0$, at compression depth d_∞ and force $F_\infty = F_0 - K(d_\infty - d_0)$. Equations 6.1 and 6.2 then reduce to $E = hF_\infty/\pi R d_\infty^2$, giving E = 14.9 ± 0.7 kPa. The uncertainty corresponds to variations in d_∞ with time, likely due to thermal drift (Figure A11.2). This value of E is consistent with previous studies of polyacrylamide hydrogels of the same polymer and crosslinker concentrations. A colloidal probe compression study[173] found E = 9 kPa; a bulk compression study[174] suggested $E \approx$ 22 kPa, calculated from the reported plane strain modulus $E^* = E/(1 - \nu^2)$, assuming Poisson's ratio ν = 0.5.

The relaxation experiments also yielded the permeability k of the gels. Fits for k of Equation 6.1 to the three relaxations shown in Figure 6.2C were performed. The fits are shown

as dashed and solid red curves in Figure 6.2C and yielded k = 1.28 ± 0.01 nm^2, where the uncertainty corresponds to the standard deviation. Fits using the lower and upper bounds of E (14.2 and 15.6 kPa, respectively) also gave k varying by ± 0.01 nm^2. The fitted value of permeability is consistent with reported values[157] and a theoretical approximation ($k \approx 2$ nm^2, Appendix 10).

The elastic modulus and permeability from the relaxation experiments were used to calculate hydrogel compression forces with Equation 6.1 (Appendix 11). To validate the model, calculated forces were compared to the data shown in Figure 6.2A-B. The film thickness used to calculate each compression was determined with a one-parameter fit of Equation 6.1 to the measured forces. Calculated forces are shown as black curves in Figure 6.2A-B and match the measured forces. This agreement supports the accuracy of E and k and justifies the use of the poroelastic model. Discrepancies between predicted and measured forces may result from surface roughness or, particularly for the thicker films, failure of the thin film assumption used to derive Equation 6.1 (Appendix 11).

As shown above, the film thickness, elastic modulus, and permeability contribute to the apparent stiffness of highly confined hydrogel films. These parameters are related to the water content of the gel. To explore the influence of hydration on hydrogel poroelasticity, ethanol solutions were used to dehydrate a gel film. The film was initially immersed in a capillary meniscus of pure water which was exchanged with solutions of increasing ethanol fraction x_{EtOH}. Because ethanol is a poor solvent for polyacrylamide,[175] increased x_{EtOH} corresponded to decreased hydration of the gel. Figure 6.3A shows compression forces measured at each ethanol fraction. As x_{EtOH} increased, more force was needed to reach a given compression depth. This increase in apparent stiffness is consistent with previously reported stiffening of

hydrogels in ethanol.[159] For $x_{EtOH} < 1$, repeated compressions showed no hysteresis, while for $x_{EtOH} = 1$, the film thinned and stiffened over repeated compressions (Figure A11.3). The data for $x_{EtOH} = 1$ in Figure 6.3A correspond to the last compression of the film.

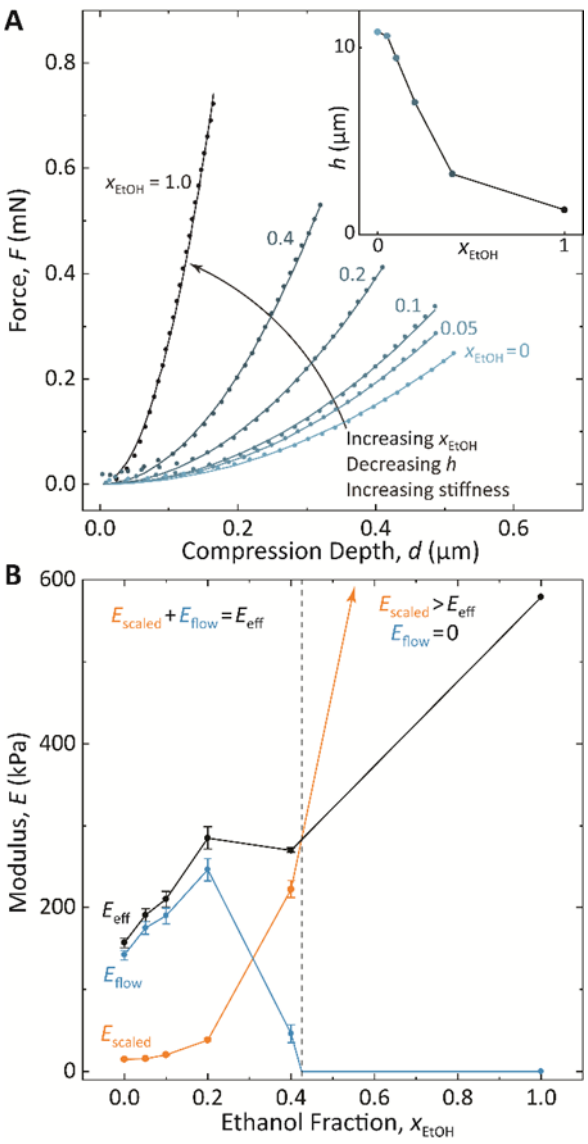

Figure 6.3 (A) F vs. d for a gel film in a solution of increasing ethanol fraction x_{EtOH}. Curves show fits of Equation 6.2. Inset: Film thickness h vs. x_{EtOH}. (B) Effective modulus E_{eff} (black circles), scaled elastic modulus E_{scaled} (orange circles), and contribution of fluid flow E_{flow} (blue circles) vs. x_{EtOH}. Dotted line shows the ethanol fraction at which E_{scaled} exceeds E_{eff}. Error bars correspond to the standard deviation for E_{eff}, the scaled uncertainty in the measured elastic modulus in water for E_{scaled}, and the square root of the sum of squared errors of E_{eff} and E_{scaled} for E_{flow}.

The increase in apparent stiffness of the film with increasing ethanol fraction was partially attributed to a change in film thickness. The forces shown in Figure 6.3A were fit with Equation 6.2 for h and E_{eff}. The fits appear as curves in Figure 6.3A; the inset shows the fitted h vs. x_{EtOH}. As x_{EtOH} increased, h decreased, consistent with a previous report of deswelling of polyacrylamide hydrogels in ethanol solutions.[176] When compressing a soft film on a rigid substrate, more force is needed to reach a given compression depth for a thin film than a thick film, shown by h in the denominator of Equations 6.1 and 6.2. Therefore, the decrease in film thickness with increasing ethanol fraction was expected to increase the apparent stiffness of the gel.

However, the increase in apparent stiffness with increasing ethanol fraction cannot be entirely attributed to the decrease in film thickness. Figure 6.3B shows the effective modulus E_{eff} from the fits (black circles). As x_{EtOH} increased, E_{eff} increased. If the decrease in h entirely accounted for the stiffening, then E_{eff} would be independent of x_{EtOH}. Since E_{eff} increased with x_{EtOH}, changes in film properties likely contributed to the increase in apparent stiffness.

Polymer scaling theory accounts for the increase in effective modulus. Scaling theory[177] relates the elastic modulus of a swollen crosslinked gel in a good solvent to the polymer concentration c as $E \propto c^{2.25}$. For a gel film of thickness h_0 and polymer concentration c_0 collapsing to thickness h and concentration c, conservation of mass requires that $c_0h_0 = ch$. This expression assumes that the gel shrinks in only one dimension due to the surface preparation, justified by the uniform profile after swelling (Figure A9.1) and the agreement between swelling ratios calculated for thin films and macroscopic gels (Figure A11.4). The scaled elastic modulus at each ethanol fraction can thus be calculated as $E_{scaled} = E_0(h_0/h)^{2.25}$ (Figure 6.3B, orange circles), where h_0 (11 μm) and E_0 (15 kPa) are the thickness and elastic

modulus of the gel in pure water ($x_{EtOH} = 0$) and h is the film thickness at each ethanol fraction. Because h monotonically decreased with increasing x_{EtOH}, E_{scaled} increased. For $x_{EtOH} = 1$, the scaled elastic modulus exceeded the effective modulus ($E_{scaled} = E_{eff}$). This result is not physically meaningful because neither E nor E_{flow} may exceed E_{eff} in Equation 6.2. The inaccuracy likely occurs because the scaling relationship assumes a good solvent, but ethanol is a poor solvent for polyacrylamide.[175] Therefore, the relationship is expected to fail at high ethanol concentrations. Linear interpolation gives $E_{scaled} > E_{eff}$ for $x_{EtOH} > 0.42$ (Figure 6.3B, right of dotted line), suggesting that for $x_{EtOH} > 0.42$, the scaling relationship fails and the apparent stiffness results entirely from elasticity ($E = E_{eff}$).

The values of E_{scaled} and E_{eff} were used to calculate the average contribution of fluid flow to the effective modulus. Taking $E = E_{scaled}$ in Equation 6.2 gives $E_{flow} = E_{eff} - E_{scaled}$ for $x_{EtOH} < 0.42$. For $x_{EtOH} > 0.42$, $E_{flow} = 0$ because $E = E_{eff}$ as discussed above. The value of E_{flow} at each ethanol fraction is shown in Figure 6.3B (blue circles). The non-monotonic dependence of E_{flow} on x_{EtOH} likely results from a combination of three factors: i) scaling theory[177] predicts that permeability of a swollen gel decreases with increasing polymer concentration as $k \propto c^{-1.5}$; decreased permeability increases E_{flow}. ii) The viscosity of an ethanol/water solution changes non-monotonically with ethanol fraction (Figure A11.5); increased viscosity increases E_{flow}. iii) The changes in elastic modulus, permeability, and solution viscosity influence the compression velocity $d(d)/dt$; increased velocity increases E_{flow}. Calculation of E_{flow} is further complicated by the uncertainty in E as the gel collapses and the assumption of a good solvent used to derive the scaling relationship is increasingly violated.

Comparing E_{scaled} to E_{flow} reveals the relative contributions of elasticity and fluid flow to the apparent stiffness. Linear interpolation suggests that for $x_{EtOH} < 0.3$, fluid flow provides a

greater contribution to E_{eff} than elasticity ($E_{flow} > E_{scaled}$), while for $x_{EtOH} > 0.3$, elasticity contributes more than fluid flow ($E_{scaled} > E_{flow}$). As discussed above, for $x_{EtOH} > 0.42$, E_{scaled} is not physically meaningful, and instead $E = E_{eff}$ and $E_{flow} = 0$. However, it is likely that polymer scaling fails somewhat before $x_{EtOH} = 0.42$, possibly near $x_{EtOH} = 0.3$ where E_{scaled} exceeds E_{flow}. Nevertheless, the results indicate that fluid flow is predominantly responsible for the apparent stiffness of the hydrated gels. We suggest that fluid flow may similarly influence the mechanical properties of thin gel layers in the body, especially since the strain rates applied here (10^{-4}-10^{-2} s^{-1}) are low compared to the strain rates relevant to articular cartilage[178] (10^{-5}-10^{3} s^{-1}) and tissues in the heart and lungs[179] (10^{-1}-10^{1}). Relatively large strain rates likely also occur in the corneal epithelium during eye rubbing.[180] These biological strain rates are expected to further amplify the effect of fluid flow on the mechanical properties of confined poroelastic films.

D. Conclusions

In summary, we used a surface forces apparatus to study the contact mechanics of highly confined polyacrylamide films. The elastic modulus and permeability were measured and used to calculate compression forces for different film thicknesses and compression velocities. Polymer scaling theory explained film stiffening with decreasing hydration and showed that fluid flow dictates the contact mechanics of highly confined hydrated gels. We anticipate that our work will enable future studies of thin hydrogel films for improved medical implants and drug delivery systems.

VII. Appendices

Appendix 1. Synthesis and Characterization of Siderophore Analogs

Synthesis and characterization of siderophore analogs was performed by Robert Lewis and Parker Stow.

Materials: 2,3-dihydroxybenzoic acid (2,3-DHBA), N-Ethyl-N′-(3-dimethylaminopropyl)carbodiimide hydrochloride (EDC-HCl), hydroxybenzotriazole (HOBT), and tris(2-aminoethyl)amine (TREN) were purchased from Sigma Aldrich. THF, acetic acid, triethylamine (NEt3), glycine, N-hydroxysuccinimide (NHS), and potassium hydroxide were purchased from Fisher. Glycine trimer (H-Gly-Gly-Gly-OH) was purchased from Chem Impex International. Benzyl bromide and N,N'-dicyclohexylcarbodiimide were purchased from Alfa Aesar. H-Lys(Z)-OH was purchased from Bachem. Palladium on carbon (10 wt %) was purchased from Acros. All commercially obtained reagents were used as received. Unless stated otherwise, reactions were performed at room temperature (rt, approximately 23 ˚C). Thin-layer chromatography (TLC) was conducted with E. Merck silica gel 60 F254 pre-coated plates, (0.25 mm) and visualized by exposure to UV light (254 nm) or stained with potassium permanganate. Flash column chromatography was performed using normal phase silica gel (60 Å, 230-240 mesh, Geduran®). Synthesis of Siderophore analogs

Synthesis and Characterization: Siderophore analogs Tren(GGK-Cat)$_3$, Tren(GKG-Cat)$_3$, Tren(KGG-Cat)$_3$, Tren(GGG-Cat)$_3$, Tren(GGK-Benz)$_3$, and Tren(KGGG-Cat)$_3$ were synthesized according to previously published methods with minor variations.[33,181–184] O,O'-dibenzyl-2,3-dihydroxybenzoic acid (Bn-2,3-DHBA) was synthesized from known procedure.[26] An example synthesis of Tren(GGK-Cat)$_3$ can be seen in Figure A1.1. Tren(GGGGGGK-Cat)$_3$ was synthesized using a modified procedure outlined in Figure A1.2, owing to the insolubility of the intermediate Bn-2,3-DHB-Gly-Gly-Gly-Gly-Gly-Gly-OH in solvents commonly used for DCC/NHS coupling. The general procedures for the syntheses and purifications are outlined below.

Step a, Synthesis of O,O'-dibenzyl-2,3-dihydroxybenzoic acid: To a mixture of 2,3-dihydroxybenzoic acid (1 equiv.) and powdered KOH (13 equiv.) was added DMSO (0.3 M). Benzyl bromide (5 equiv.) was added, and the reaction mixture was stirred for 4 h. Aqueous work-up and extraction with EtOAc yielded a crude product that was purified by recrystallization from CH_2Cl_2/hexanes or flash chromatography with EtOAc/hexanes.

Step b, NHS ester activation: In a flame-dried flask under argon, the carboxylic acid (1 equiv.) and N-hydroxysuccinimide (NHS, 1.1 equiv.) were dissolved with sonication in anhydrous THF. The contents of this flask were added via syringe to a second flame-dried flask, containing N,N'-dicyclohexylcarbodiimide (DCC, 1.1 equiv.) dissolved in anhydrous THF. The reaction was stirred overnight at room temperature. The following day, the reaction was concentrated in vacuo then resuspended in ethyl acetate. The suspension was filtered to remove the insoluble N,N'-dicyclohexylurea byproduct. The filtrate was then concentrated in

vacuo to give a crude, white to yellowish white product. This product was used in subsequent coupling reactions without further purification.

Steps c and d, coupling reaction: Crude NHS-activated product (1 equiv.) was dissolved with sonication in THF. This solution was added via syringe to a second flask containing the desired amino acid (e.g. glycine or H-Lys(Z)-OH, 1.1 equiv.) and triethylamine (4 equiv.) dissolved in 40% water in THF. The reaction was stirred overnight at room temperature. The following day, THF was removed in vacuo and the resulting aqueous solution was acidified with 1 M HCl then extracted three times with ethyl acetate. The combined organic layers were dried over $MgSO_4$ and concentrated to obtain crude product. The product was purified by recrystallization from 2-propanol/hexanes or H_2O/ethanol to obtain white crystals.

Step e, attachment to Tren core: In a flame-dried flask under argon, the NHS-activated arms (3.3 equiv.) was dissolved with sonication in anhydrous THF. This solution was added via syringe to a second flame-dried flask containing tris(2-aminoethyl)amine (TREN, 1 equiv.) and triethylamine (6 equiv.) dissolved in anhydrous THF. The reaction was stirred overnight at room temperature. The following day, the reaction was concentrated in vacuo to give the protected siderophore analogs as crude crystals. This product was used in subsequent deprotection reactions without further purification.

Step f, global deprotection: In a triple washed flask (conc. HCl-H_2O-MeOH), the protected siderophore analog (1 equiv.) was dissolved in 25% water in THF with 3% acetic acid. The flask was then alternatively purged and flushed with N_2 five times before palladium on carbon (10 wt %, 0.25 equiv.) was added. The reaction was then alternatively purged and flushed with H_2 five times. The reaction was stirred at room temperature for three hours under H_2. Once complete, the reaction was filtered through a grade 5 Whatman filter to remove the palladium on carbon. The filtrate was concentrated in vacuo to give a white to yellowish-white powder. Product was purified via reverse phase HPLC.

Purification: Siderophore analogs were purified via RP-HPLC using either a preparative C4 column (22 mm i.d. x 250 mm, Vydac) or a preparative C18 column (20 mm i.d. x 250, YMC-Actus-ODS-A). Compounds were eluted with a linear gradient of 10% methanol (with 0.05% TFA) in H2O (nanopure with 0.05% TFA) to 30% methanol in H2O over 38 minutes. The column was exchanged back to 10% methanol over 12 minutes. The eluent was monitored at 215 nm and each prominent peak was manually collected and analyzed by ESI-MS until the desired siderophore analog was identified. The desired fractions were concentrated in vacuo then lyophilized to obtain a product. Products were stored under argon at -20 ˚C.

Characterization: ^{1}H NMR spectra were recorded on a Varian Unity Inova 600 MHz spectrometer and are reported relative to deuterated solvent signals. Data for ^{1}H NMR spectra are reported as follows: chemical shift (δ ppm), multiplicity, coupling constant (Hz) and integration. ^{13}C NMR spectra were recorded on a Varian Inova 500 MHz spectrometer. Data for ^{13}C NMR spectra are reported in terms of chemical shift (δ ppm). ^{1}H-^{13}C HMBC NMR spectra were recorded on a Varian Unity Inova 600 MHz spectrometer. ESI-MS was performed on a Xevo G2-XS TOF mass spectrometer, part of a shared facilities of the UCSB MRSEC (NSF DMR 1702056).

A total of 7 siderophore analogs were synthesized. Tren(GGK-Cat)$_3$ (Figure A1.3), Tren(GKG-Cat)$_3$ (Figure A1.4), and Tren(KGG-Cat)$_3$ (Figure A1.5) retain the same molecular weight and ratio of catechol to lysine but vary the spacing between the two groups by zero, one, or two glycine residues. Tren(GGK-Benz)$_3$ (Figure A1.6) retains the lysine residue but lacks the hydroxyl groups of catechol responsible for strong adhesion. Tren(GGG-Cat)$_3$ (Figure A1.7) retains the catechol moiety but lacks cationic lysine residues. Tren(KGGG-Cat)$_3$ (Figure A1.8) and Tren(KGGGGGG-Cat)$_3$ (Figure A1.9) retain the same ratio of catechol to lysine, but have a higher molecular weight and greater spacing between the catechol and lysine residues.

Siderophore analogs were purified by RP-HPLC as discussed above. Purified siderophore analogs were checked for purity via RP-HPLC (Figures A1.10 and A1.11) and ESI-MS (Figures A1.12-A1.18) prior to characterization via NMR. An asymmetric homologue of Tren(GGK-Benz)$_3$, Tren(GGK-Benz)$_2$(GK-Benz), co-elutes with the desired compound under all attempted RP-HPLC conditions and can be seen in the ESI-MS (Figure A1.15).

Synthesis and purification of Tren(GGK-Cat)$_3$: The synthesis of Tren(GGK-Cat)$_3$ is shown in Figure A1.1 and it follows the general procedure outlined above without any variation. Tren(GGK-Cat)$_3$ was purified using RP-HPLC using the general procedure outlined above without any variations. The final product after lyophilization was a hygroscopic white powder, which was stored under argon at -20 ˚C.
Tren(GGK-Cat)$_3$: white powder; ^{1}H, ^{13}C, 2D NMR data; ESI-MS m/z 1281.72 $[M + H]^+$.

Synthesis and purification of Tren(GKG-Cat)$_3$: The synthesis of Tren(GKG-Cat)$_3$ follows the general procedure outlined above without any variation. Tren(GKG-Cat)$_3$ was purified using RP-HPLC using the general procedure outlined above without any variations. The final product after lyophilization was a hygroscopic white powder, which was stored under argon at -20 ˚C.
Tren(GKG-Cat)$_3$: white powder; ^{1}H, ^{13}C, 2D NMR data; ESI-MS m/z 1281.58 $[M + H]^+$.

Synthesis and purification of Tren(KGG-Cat)$_3$: The synthesis of Tren(KGG-Cat)$_3$ follows the general procedure outlined above with minor variation. The arm prior to attachment, Bn-2,3-DHBA-Gly-Gly-Lys-OH, proved difficult to recrystallize. As such, it was used without further purification. Tren(KGG-Cat)$_3$ was purified using RP-HPLC using the general procedure outlined above without any variations. The final product after lyophilization was a hygroscopic white powder, which was stored under argon at -20 ˚C.
Tren(KGG-Cat)$_3$: white powder; ^{1}H, ^{13}C, 2D NMR data; ESI-MS m/z 1281.61 $[M + H]^+$.

Synthesis and purification of Tren(GGK-Benz)$_3$: The synthesis of Tren(GGK-Benz)$_3$ follows the same procedure as the synthesis of Tren(GGK-Cat)$_3$ with the exception of using benzoic acid in place of 2,3-DHBA, which obviates step a and allows the synthesis to begin directly with step b (Figure A1.1). Additionally, the intermediates to this compound proved difficult to purify by recrystallization and were therefore used without further purification. After collecting the appropriate peak from the general RP-HPLC purification method, Tren(GGK-Benz)$_3$ was further purified via RP-HPLC using a preparative C4 column (22 mm i.d. x 250 mm, Vydac). Compounds were eluted with a linear gradient of 10% methanol (with 0.05% TFA) in H_2O (nanopure with 0.05% TFA) to 30% methanol in H_2O over 45 minutes.

The column was exchanged back to 10% methanol over 10 minutes. The final product after lyophilization was a hygroscopic white powder, which was stored under argon at -20 ˚C.
Tren(GGK-Benz)$_3$: white powder; ^{1}H, ^{13}C, 2D NMR data; ESI-MS m/z 1186.73 $[M + H]^+$.

Synthesis and Purification of Tren(GGG-Cat)$_3$: The synthesis of Tren(GGG-Cat)$_3$ follows the same general procedure outlined above outline above, except that a glycine trimer (H-Gly-Gly-Gly-OH) was used to couple with NHS-activated Bn-2,3-DHBA. The arm prior to attachment, Bn-2,3-DHBA-Gly-Gly-Gly-OH, proved difficult to recrystallize. As such, it was used without further purification. Tren(GGG-Cat)$_3$ was purified using RP-HPLC using a preparative C4 column (22 mm i.d. x 250 mm, Vydac). Compounds were eluted with a linear gradient of 10% methanol (with 0.05% TFA) in H_2O (nanopure with 0.05% TFA) to 37% methanol in H_2O over 17 minutes. The column was flushed with 100% methanol for 10 minutes, then exchanged back to 10% methanol over 10 minutes. The final product after lyophilization was a hygroscopic white powder, which was stored under argon at -20 ˚C.
Tren(GGG-Cat)$_3$: white powder; ^{1}H, ^{13}C, 2D NMR data; ESI-MS m/z 1068.35 $[M + H]^+$.

Synthesis and purification of Tren(KGGG-Cat)$_3$: The synthesis of Tren(KGGG-Cat)$_3$ follows the same general procedure outlined above for the lower molecular weight siderophore analogs, except that a glycine trimer (H-Gly-Gly-Gly-OH) was used to couple to NHS activated Bn-2,3-DHBA. Additionally, the workup for various intermediates departed from the general strategy owing to their poor solubility in ethyl acetate. Following coupling of Bn-2,3-DHB-Osu with H-Gly-Gly-Gly-OH, THF was removed and the crude aqueous reaction mixture was acidified to pH 2 at which point a white precipitate formed. The resulting precipitate was isolated by filtration, rinsed with ethyl acetate, and dried to yield Bn-2,3-DHB-Gly-Gly-Gly-OH as a white powder. Similarly, Bn-2,3-DHB-Gly-Gly-Gly-Lys(Z)-OH was isolated by precipitating the product out of a 2:1:1 mixture of 0.1 M HCl, ethyl acetate, and hexanes. Tren(KGGG-Cat)$_3$ was purified using RP-HPLC using a preparative C18 column (20 mm i.d. x 250 mm, Ymc-Actus-ODS-A). Compounds were eluted with a linear gradient of 20% methanol (with 0.05% TFA) in H2O (nanopure with 0.05% TFA) to 40% methanol over 25 minutes. The column was exchanged back to 20% methanol over 11 minutes. The final product after lyophilization was a hygroscopic white powder, which was stored under argon at -20 ˚C.
Tren(KGGG-Cat)$_3$: white powder; ^{1}H, ^{13}C; ESI-MS m/z 1452.6257 $[M + H]^+$.

Synthesis and purification of Tren(KGGGGGG-Cat)$_3$: The synthesis of Tren(KGGGGGG-Cat)$_3$ was accomplished using a modified procedure described in Figure A1.2 and discussed in detail below. Intermediate compound Bn-2,3-DHB-Gly-Gly-Gly-Gly-Gly-Gly-OH displayed poor solubility in common solvents compatible with DCC/NHS coupling. To reduce the number of steps that could be complicated by the poor solubility of intermediates, the Tren core was first coupled to Boc-Lys(Z)-OH to yield Tren(Boc-Lys(Z))$_3$ and the Boc protecting groups were subsequently deprotected. 3 equivalents of Bn-2,3-DHB-Gly-Gly-Gly-Gly-Gly-Gly-OH was coupled to Tren(Lys(Z))$_3$ using standard EDC/HOBT coupling conditions. The trimeric protected intermediate was globally deprotected following the conditions described for the other siderophore analogs. Tren(KGGGGGG-Cat)$_3$ was purified using RP-HPLC using a preparative C18 column (20 mm i.d. x 250 mm, Ymc-Actus-ODS-A). Compounds were eluted with a linear gradient of 20% methanol (with 0.05% TFA)

in H2O (nanopure with 0.05% TFA) to 40% methanol over 25 minutes. The column was exchanged back to 20% methanol over 11 minutes. The final product after lyophilization was a hygroscopic white powder, which was stored under argon at -20 ˚C.
Tren(KGGGGGG-Cat)$_3$: white powder; ^{1}H, ^{13}C; ESI-MS m/z 983.4402 $[M + 2H]^{2+}$.

Step a, coupling of H-Gly-Gly-Gly-OH to NHS-activated esters. H-Gly-Gly-Gly-OH was dissolved in 60% THF (aq) with 3.5 equivalents of TEA. Purified NHS-activated ester was added as a solid in four equal parts over the course of an hour. Coupling of Bn-2,3-DHB-Osu to H-Gly-Gly-Gly-OH was allowed to proceed at room temperature for 6 hours and the coupling of Bn-2,3-DHB-Gly-Gly-Gly-OH to H-Gly-Gly-Gly-OH was allowed to proceed at room temperature for 2 hours at which point all starting material was deemed to be gone by TLC. Bn-2,3-DHB-Gly-Gly-Gly-OH and Bn-2,3-DHB-Gly-Gly-Gly-Gly-Gly-Gly-OH were isolated following removal of THF and acidification of the aqueous reaction mixture to pH <2. The resulting white precipitate was filtered off in either case, rinsed thoroughly with ethyl acetate, and dried overnight in a vacuum desiccator to yield a white powder deemed pure by ^{1}H NMR.

Step b, DCC/NHS activation of Bn-2,3-DHB-Gly-Gly-Gly-OH: Bn-2,3-DHB-Gly-Gly-Gly-OH was activated following the method described previously for the other siderophore analogue intermediates, however anhydrous DMF was used in place of THF. The reaction was allowed to proceed overnight at room temperature. The following day, the dicyclohexylurea byproduct was removed by filtration and DMF was removed in vacuo. The crude product was precipitated from a 1:1 mixture of ethyl acetate and water. The resulting white precipitate was filtered off and rinsed with hot 2-propanol to remove traces of DCU byproduct. Bn-2,3-DHB-Gly-Gly-Gly-Osu was dried overnight in a vacuum desiccator to yield a white, solid deemed pure by ^{1}H NMR.

Step c, coupling of Boc-Lys(Z)-OH to Tren: Boc-Lys(Z)-OH was activated in anhydrous THF following standard DCC/NHS conditions described previously for other intermediates. The carboxylic acid was allowed to activate overnight at room temperature. The following day the DCU byproduct was filtered off and the filtrate was directly added to a flask containing 1 eq. Tren and 3.5 eq TEA in 80% THF (aq.) The reaction mixture was stirred at room temperature for an additional 8 h. Following removal of THF, the crude reaction mixture was acidified with 1 M HCL and then extracted three times with ethyl acetate. The combined organic fractions were dried over $MgSO_4$ and concentrated to yield a crude product. This crude product was subsequently purified by flash chromatography on a silica column using 3% MeOH in DCM as the mobile phase. The pure fractions were combined and concentrated to yield a white crystalline solid.

Step d, deprotection of Boc-amines: Boc protecting groups were removed under acidic conditions using 15% TFA in DCM. Tren(Boc-Lys(Z))$_3$ was stirred for 1.5 h at room temperature after which point volatiles were removed by evaporation to yield a yellow oily-solid. The crude product was used directly in the next coupling step without any further purification.

Step e, EDC/HOBT coupling of Gly arms to Tren(Lys(Z))$_3$: 3.0 equivalents of Bn-2,3-DHB-Gly-Gly-Gly-Gly-Gly-Gly-OH was suspended in dry DMF under anhydrous

conditions. 3.3 equivalents of EDC-HCl, 3 equivalents of HOBT, 6 equivalents of TEA, and 1 equivalent of Tren(Lys(Z))$_3$ were added dropwise as a concentrated solution in anhydrous DMF. The reaction mixture was stirred at room temperature for 8 h and over the course of the reaction a thick white precipitate formed in solution. The crude reaction mixture was poured directly into an equivalent volume of ice-cold water and the white precipitate was filtered off. The crude solid was rinsed with a small volume of ice-cold DMF and copious amounts of methanol to yield the trimeric protected intermediate as a white solid.

Step f, global deprotection: In a triple washed flask (conc. HCl-H_2O-MeOH), the protected siderophore analog (1 equiv.) was dissolved in 25% water in THF with 3% acetic acid. The flask was then alternatively purged and flushed with N_2 five times before palladium on carbon (10 wt %, 0.25 equiv.) was added. The reaction was then alternatively purged and flushed with H_2 five times. The reaction was stirred at room temperature for three hours under H_2. Once complete, the reaction was filtered through a grade 5 Whatman filter to remove the palladium on carbon. The filtrate was concentrated in vacuo to give a white to yellowish-white powder. Product was purified via reverse phase HPLC.

Characterization of Siderophore Analogs

Mass Spectrometry: Siderophore analogs structures were characterized with ESI-MS (Figures A1.12-A1.18). Due to the presence of 5 possible cationic amine groups, masses corresponding to $[M + H]^+$, $[M + 2H]^{2+}$, $[M + 3H]^{3+}$, and $[M + 4H]^{4+}$ were observed for most compounds, with the exception of Tren(GGG-Cat)$_3$ as this compound lacks cationic lysine residues (Figure A1.16).

NMR: ^{1}H, ^{13}C, and ^{1}H-^{13}C HMBC NMR confirmed the desired molecular structures of each siderophore analog, with the exception of Tren(KGGG-Cat)$_3$ and Tren(KGGGGGG-Cat)$_3$ which were characterized solely by ^{1}H and ^{13}C NMR due to the presence of many overlapping glycine peaks. ^{1}H and ^{13}C results are summarized in Tables A1.1-A1.3. ^{1}H NMR results for Tren(GGK-Cat)$_3$ show peaks characteristic of the 2,3-DHBA moiety at δH 6.70 (t, J = 7.9 Hz, 1H), 6.94 (d, J = 7.7 Hz, 1H), and 7.40 (d, J = 7.7 Hz, 1H). There are two sets of diastereotopic protons centered at δH 1.78 (m, 2H) and 1.37 (m, 2H), labeled 9 and 10 in Figure A1.19, which reside near the chiral α-carbon of the lysine residue. The protons on carbon 11, seen at δH 1.54 (m, 2H), also appear to be diasterotopic in the ^{1}H-^{13}C HMBC spectrum, though the coupling constant appears to be small enough that the peaks are not resolved in the ^{1}H NMR spectra. The methine α-carbon give a signal at δH 4.52 (m, 1H). The remaining protons of the lysine residue were seen at δH 2.77 (m, 2H). While water obscured the protons of the Tren scaffold in other analogs, the protons can be seen in the spectrum of Tren(GGK-Cat)$_3$ at δH 3.21 (s, 1H) and 3.40 (s, 1H), though they appear as singlets rather than well-defined multiplets. Assignments of the glycine residue protons was aided by ^{1}H-^{13}C HMBC (Figure A1.20) and were seen at δH 3.73 (m, 2H) and 3.79 (m, 2H). Protons attached to catechol oxygens (δH 11.91, 9.38) and amide nitrogens (δH 8.18, 8.36, 7.71, and 8.79) were assigned through correlation with carbonyl carbons and other adjacent groups in the ^{1}H-^{13}C HMBC spectrum.

In the ^{13}C NMR results for Tren(GGK-Cat)$_3$, the carbonyl group of the 2,3-DHBA moiety and the lysine group can be seen at δC 168.86 and 171.75, respectively. The carbonyl groups of the two glycine residues were resolved with the use of ^{1}H-^{13}C HMBC and are seen at δC

169.38 and 169.23. DMSO obscures the methylene carbons of the Tren scaffold in the ^{13}C Spectra. The methylene carbons of the lysine residue are observed at δC 31.07, 22.48, 26.62, and 38.65, and the methine lysine carbon at δC 52.79. The two methylene carbons of the glycine spacers were resolved by ^{1}H-^{13}C HMBC and are seen at δC 41.94 and 42.10.

The ^{1}H and ^{13}C NMR spectra for Tren(GKG-Cat)$_3$ and Tren(KGG-Cat)$_3$ closely resemble that of Tren(GGK-Cat)$_3$. The characteristic ^{1}H NMR peaks for the 2,3-DHBA and the diastereotopic peaks of the lysine residue are present in all spectra. Key differences between the siderophore analogs are seen in the different correlations in the ^{1}H-^{13}C HMBC spectra. Correlation between the α-carbon of the lysine residue and adjacent groups confirms the sequence of the arm in each siderophore analog. The ^{1}H spectra of Tren(GGK-Benz)$_3$ (Figure A1.25A, Table A1.2) shows the characteristic splitting pattern and integration of a singly substituted phenyl group and retains the peaks corresponding to a lysine residue. Tren(GGG-Cat)$_3$ is easily identified due to the absence of all signals associated with the lysine residue present in the other siderophore analogs.

The ^{1}H and ^{13}C NMR spectra for Tren(KGGG-Cat)$_3$ and Tren(KGGGGGG-Cat)$_3$ closely resemble Tren(KGG-Cat)$_3$. The characteristic ^{1}H NMR peaks for the 2,3-DHBA and the diastereotopic peaks of the lysine residue are present in all spectra. The ^{1}H NMR integrates cleanly to reflect the increase in glycine residues in Tren(KGGG-Cat)$_3$ and Tren(KGGGGGG-Cat)$_3$. ^{1}H-^{13}C HMBC was not able to fully resolve the internal glycine residues in Tren(KGGG-Cat)$_3$ and Tren(KGGGGGG-Cat)$_3$ and assignments were hence made in reference to those of Tren(KGGG-Cat)$_3$ and Tren(GGG-Cat)$_3$.

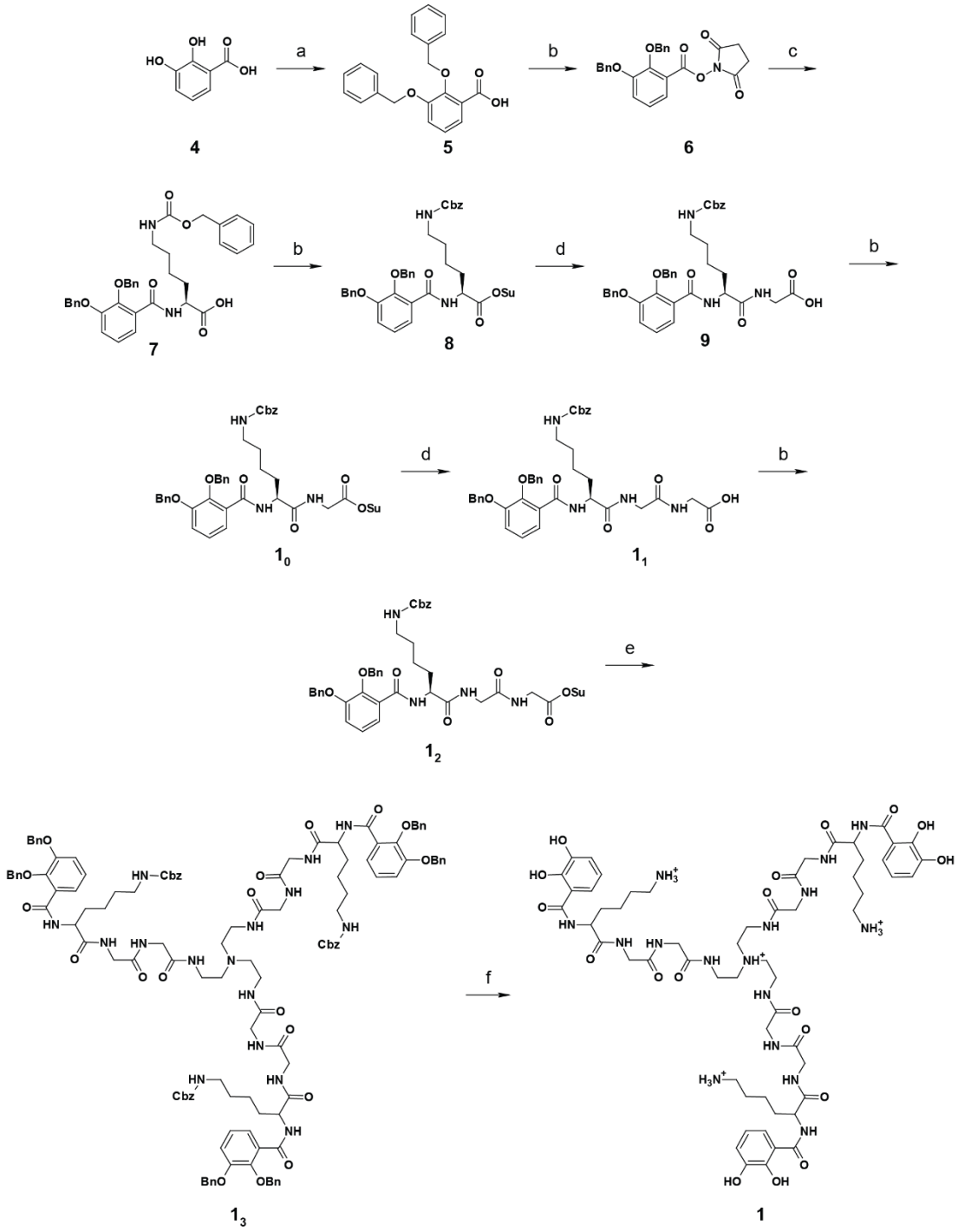

Figure A1.1. Representative synthetic scheme. Synthesis for Tren(GGK-Cat)$_3$ following the general procedure of all siderophore analogs. Reaction conditions: (a) KOH, DMSO, benzyl bromide, 4 h. (b) NHS, DCC, anhydrous THF under argon, overnight. (c) THF, H_2O, Et_3N, H-Lys(Z)-OH, overnight. (d) THF, H_2O, Et_3N, glycine, overnight. (e) Et_3N, Tren, anhydrous THF under argon, overnight. (f) THF, H_2O, 3% AcOH, Pd/C, 3 h.

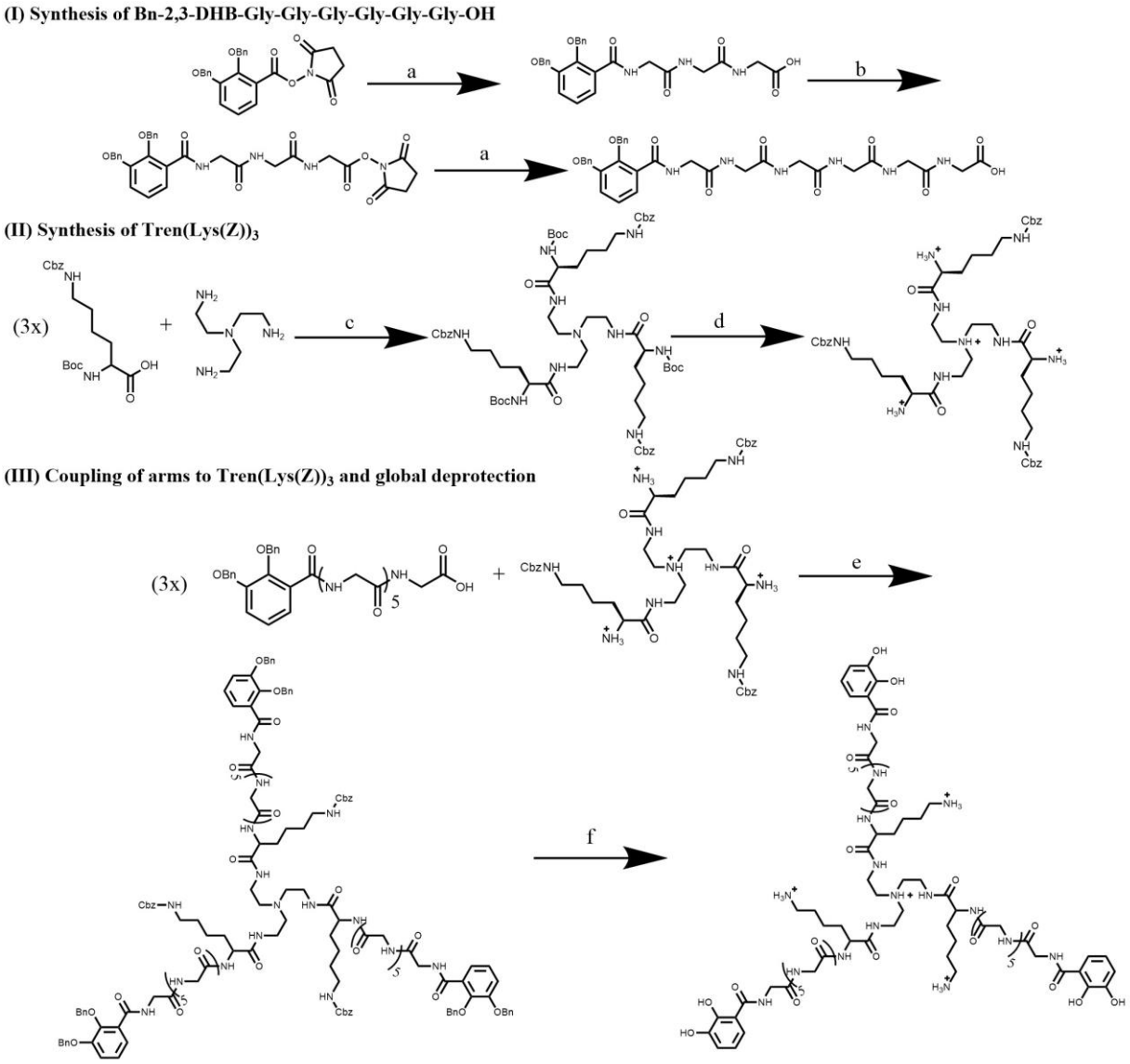

Figure A1.2. Synthetic scheme for Tren(KGGGGGG-Cat)$_3$. Reaction conditions: a)THF, H_2O, Et_3N, H-Gly-Gly-Gly-OH, 6 h. b) DCC, NHS, anhydrous DMF under argon, overnight. c) Phase 1: Boc-Lys(Z)-OH, DCC, NHS, anhydrous THF under argon, overnight. Phase 2: THF, H_2O, Et_3N, tris(2-aminoethyl)amine. (d) 15% TFA in DCM, 1.5 h, RT. (e) 1 eq. tren(Lys(Z))$_3$, 3 eq. Bn-2,3-DHB-GGGGGG-OH, 3.3 eq. EDC-HCl, 3 eq. TEA, DMF, RT, overnight. (f) THF, H_2O, 3% AcOH, 10% Pd/C, 3 h.

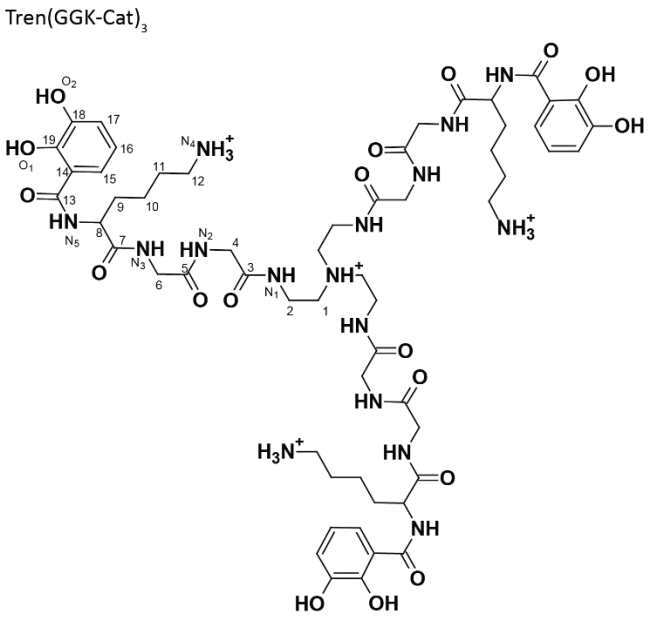

Figure A1.3. Structure of Tren(GGK-Cat)$_3$. Numbered carbons correspond to NMR data in Table A1.1.

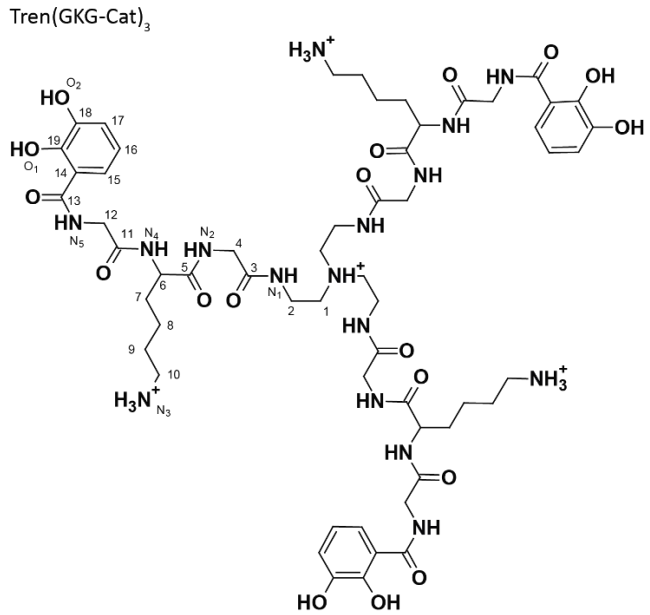

Figure A1.4. Structure of Tren(GKG-Cat)$_3$. Numbered carbons correspond to NMR data in Table A1.1.

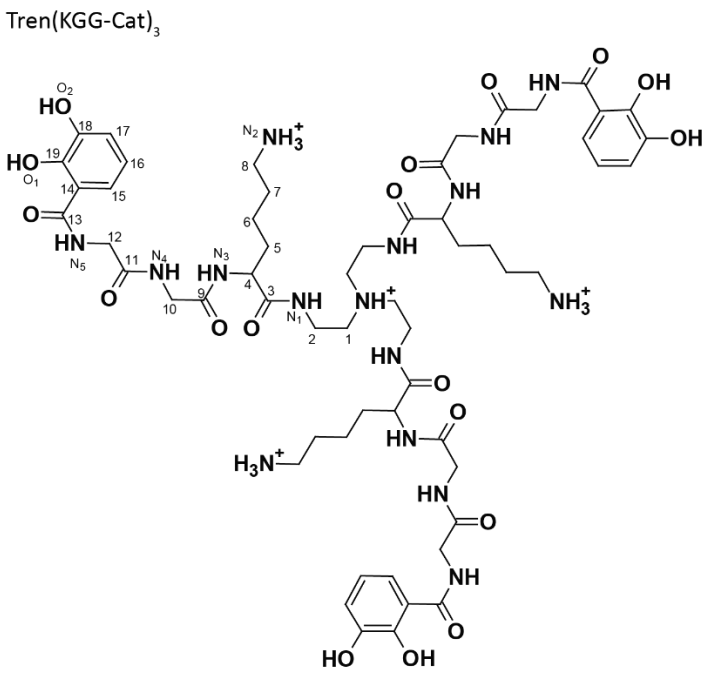

Figure A1.5. Structure of Tren(KGG-Cat)$_3$. Numbered carbons correspond to NMR data in Table A1.1.

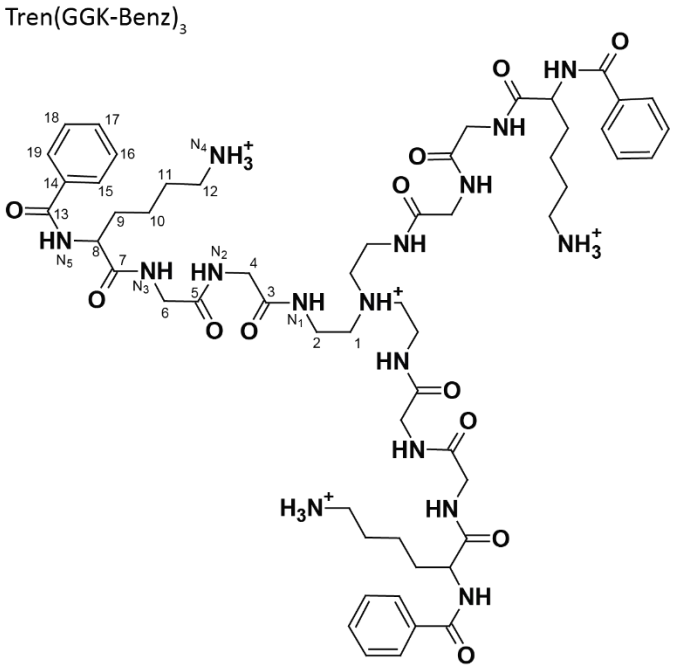

Figure A1.6. Structure of Tren(GGK-Benz)$_3$. Numbered carbons correspond to NMR data in Table A1.2.

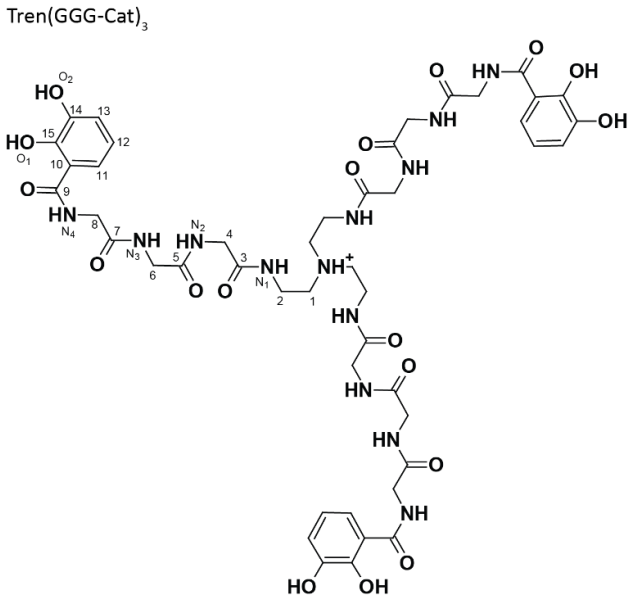

Figure A1.7. Structure of Tren(GGG-Cat)$_3$. Numbered carbons correspond to NMR data in Table A1.2.

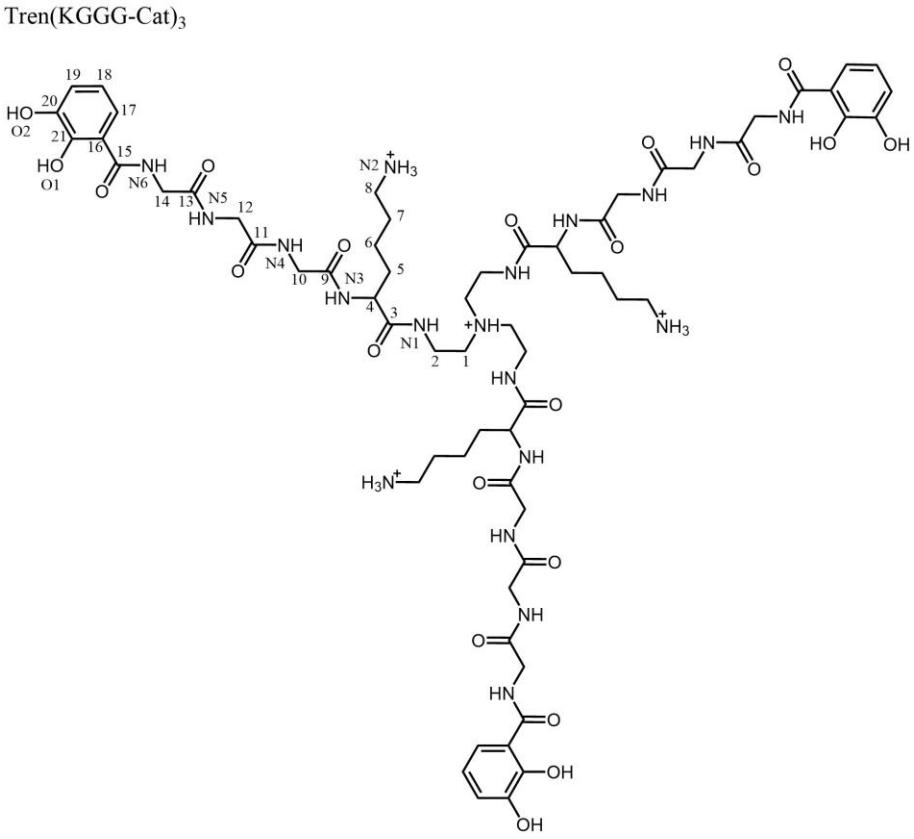

Figure A1.8. Structure of Tren(KGGG-Cat)$_3$. Numbered carbons correspond to NMR data in Table A1.3.

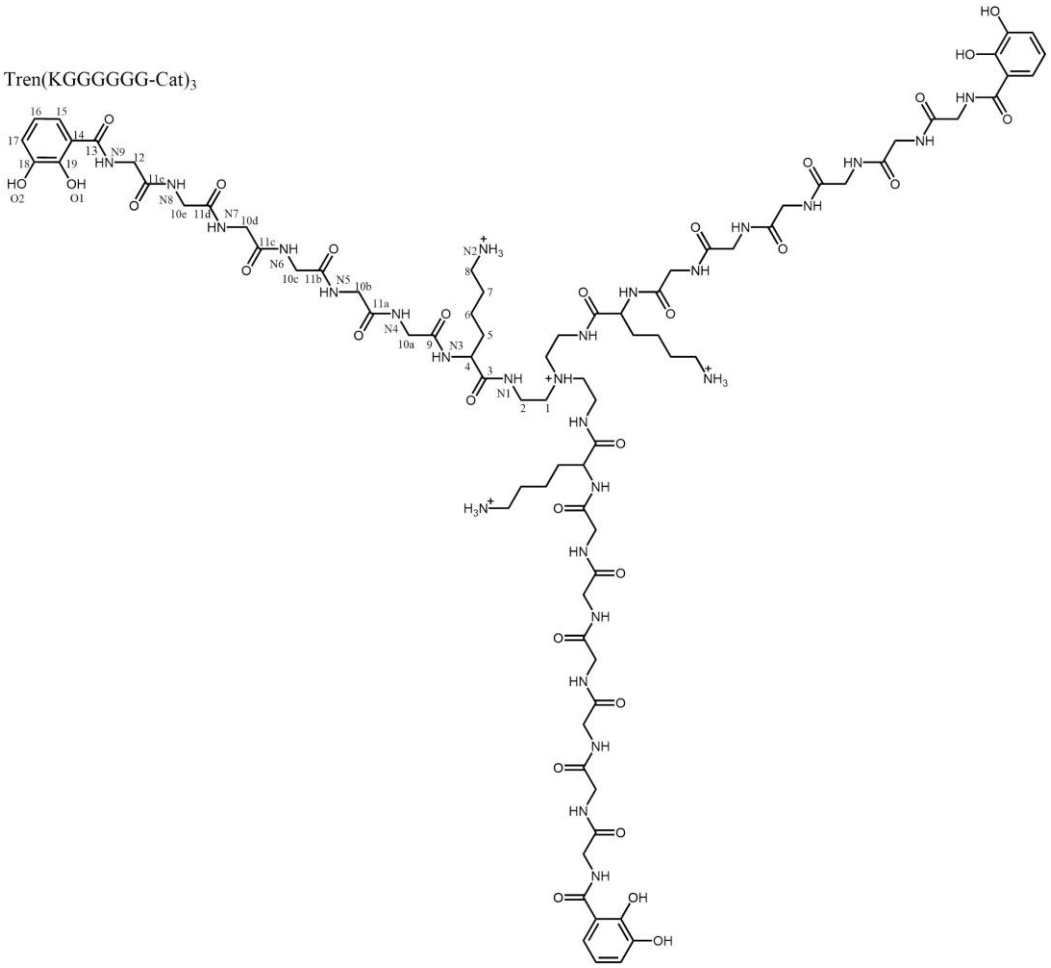

Figure A1.9. Structure of Tren(KGGGGGG-Cat)$_3$. Numbered carbons correspond to NMR data in Table A1.3.

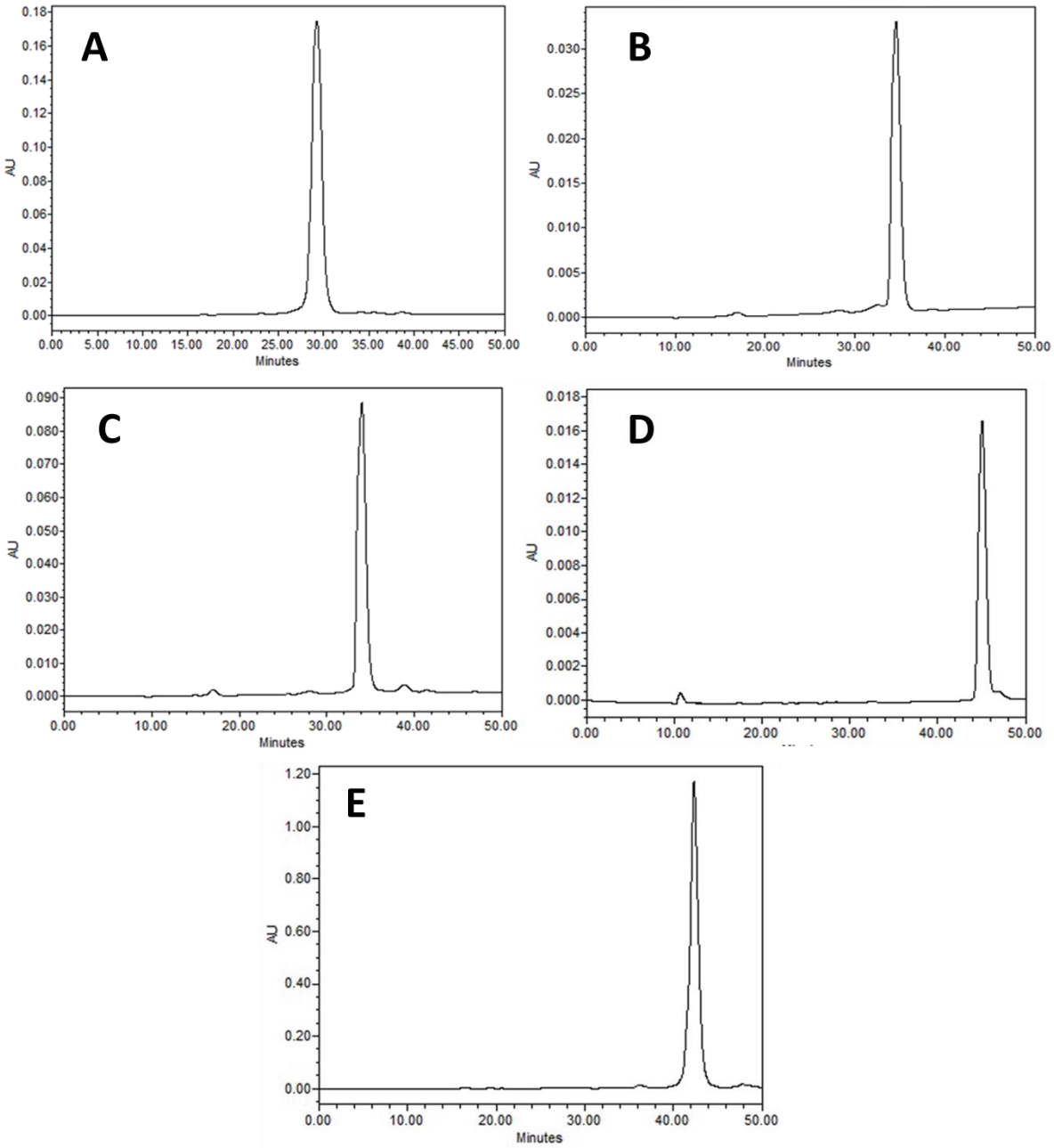

Figure A1.10. Reverse Phase HPLC traces of purified siderophore analogs. RP-HPLC was carried out on a C4 preparative column (22 mm i.d. x 250 mm, Vydac). Compounds were eluted with a linear gradient of 10% methanol (with 0.05% trifluoroacetic acid (TFA)) in H_2O (nanopure with 0.05% TFA) to 30% methanol in H_2O over 38 min. The column was exchanged back to 10% methanol over 12 minutes. The samples were detected at 215. (A) Tren(GGK-Cat)$_3$. (B) Tren(GKG-Cat)$_3$. (C) Tren(KGG-Cat)$_3$. (D) Tren(GGK-Benz)$_3$. (E) Tren(GGG-Cat)$_3$.

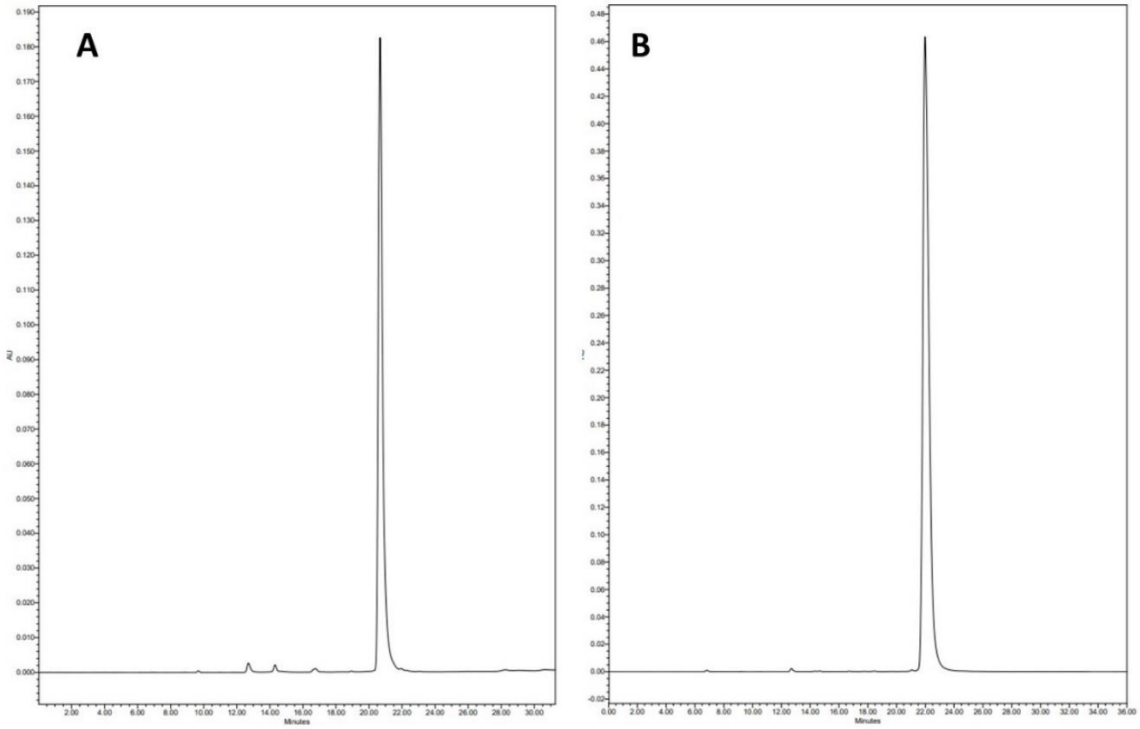

Figure A1.11: Reverse Phase HPLC traces of higher MW purified siderophore analogs Tren(KGGG-Cat)$_3$ and Tren(KGGGGGG-Cat)$_3$. RP-HPLC was carried out on a C18 preparative column (20 mm i.d. x 250 mm, YMC-Actus-ODS-A). Compounds were eluted with a linear gradient of 20% methanol (with 0.05% trifluoroacetic acid (TFA)) in H_2O (nanopure with 0.05% TFA) to 40% methanol in H_2O over 25 minutes. The column was exchanged back to 20% methanol over 11 minutes. The samples were detected at 215 nm and 310 nm (shown). (A) Tren(KGGG-Cat)$_3$. (B) Tren(KGGGGGG-Cat)$_3$.

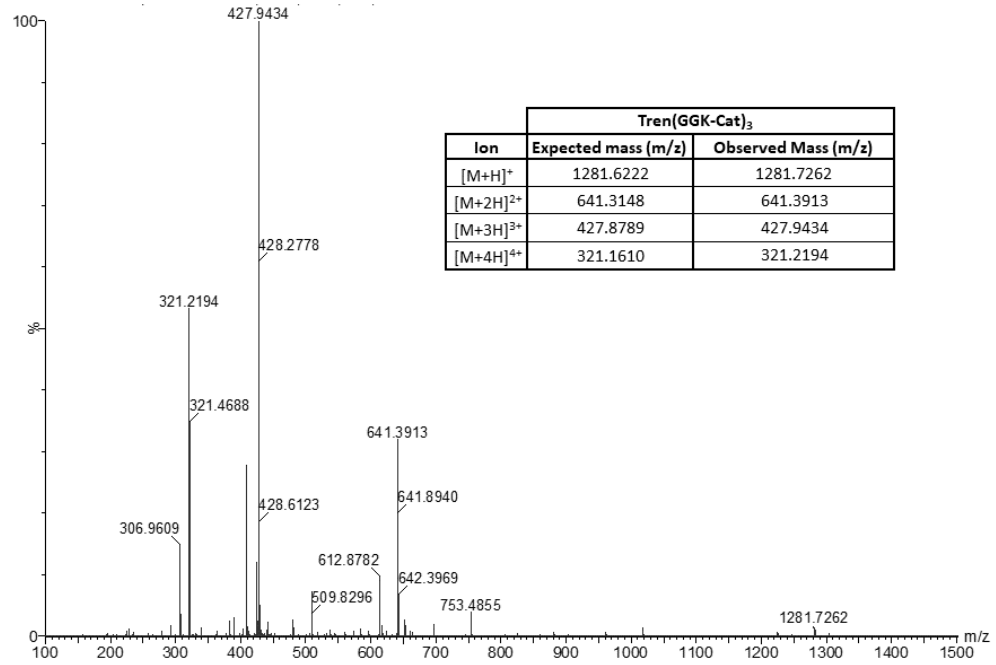

	Tren(GGK-Cat)$_3$	
Ion	Expected mass (m/z)	Observed Mass (m/z)
$[M+H]^+$	1281.6222	1281.7262
$[M+2H]^{2+}$	641.3148	641.3913
$[M+3H]^{3+}$	427.8789	427.9434
$[M+4H]^{4+}$	321.1610	321.2194

Figure A1.12. ESI-MS of Tren(GGK-Cat)$_3$.

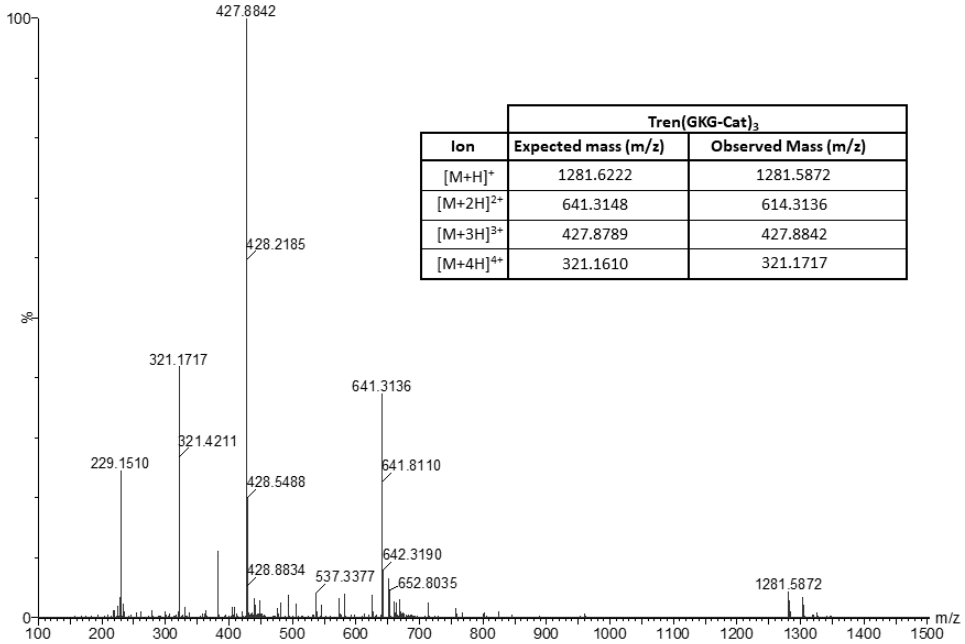

	Tren(GKG-Cat)$_3$	
Ion	Expected mass (m/z)	Observed Mass (m/z)
$[M+H]^+$	1281.6222	1281.5872
$[M+2H]^{2+}$	641.3148	614.3136
$[M+3H]^{3+}$	427.8789	427.8842
$[M+4H]^{4+}$	321.1610	321.1717

Figure A1.13. ESI-MS of Tren(GKG-Cat)$_3$.

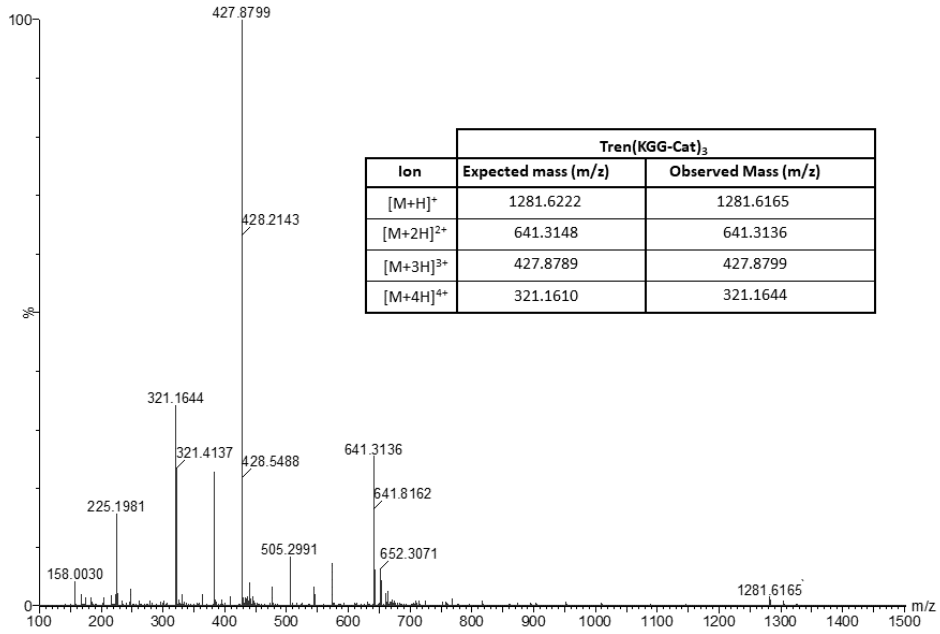

	Tren(KGG-Cat)$_3$	
Ion	Expected mass (m/z)	Observed Mass (m/z)
$[M+H]^+$	1281.6222	1281.6165
$[M+2H]^{2+}$	641.3148	641.3136
$[M+3H]^{3+}$	427.8789	427.8799
$[M+4H]^{4+}$	321.1610	321.1644

Figure A1.14. ESI-MS of Tren(KGG-Cat)$_3$.

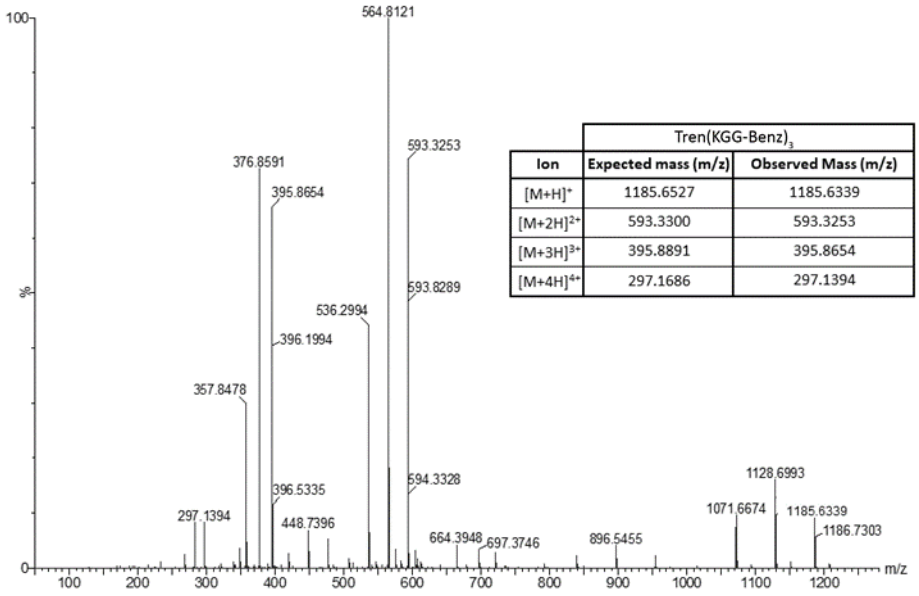

	Tren(KGG-Benz)$_3$	
Ion	Expected mass (m/z)	Observed Mass (m/z)
$[M+H]^+$	1185.6527	1185.6339
$[M+2H]^{2+}$	593.3300	593.3253
$[M+3H]^{3+}$	395.8891	395.8654
$[M+4H]^{4+}$	297.1686	297.1394

Figure A1.15. ESI-MS of Tren(GGK-Benz)$_3$.

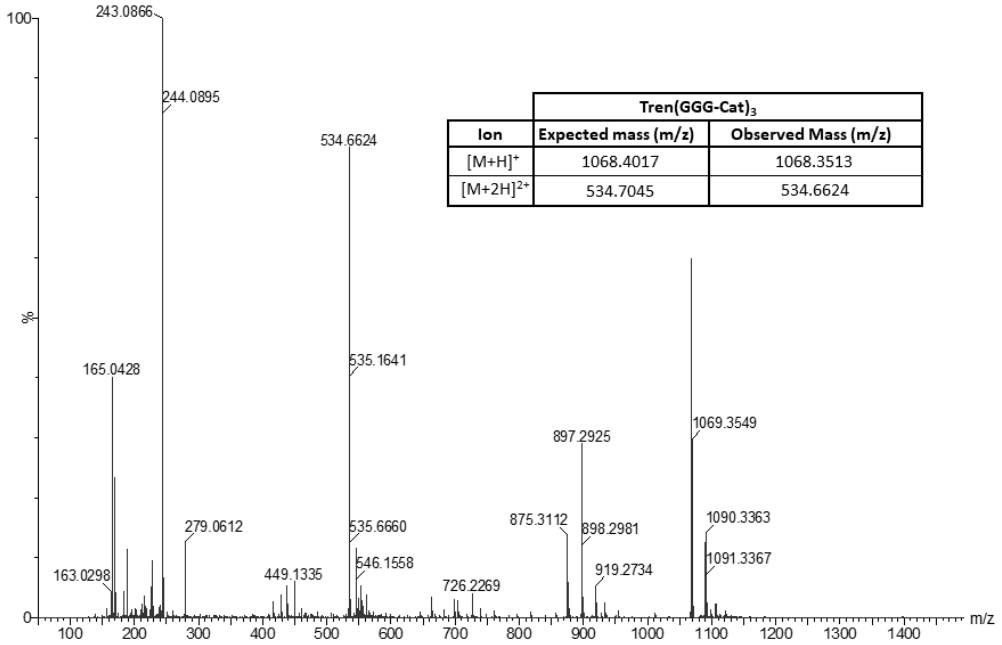

	Tren(GGG-Cat)$_3$	
Ion	Expected mass (m/z)	Observed Mass (m/z)
$[M+H]^+$	1068.4017	1068.3513
$[M+2H]^{2+}$	534.7045	534.6624

Figure A1.16. ESI-MS of Tren(GGG-Cat)$_3$.

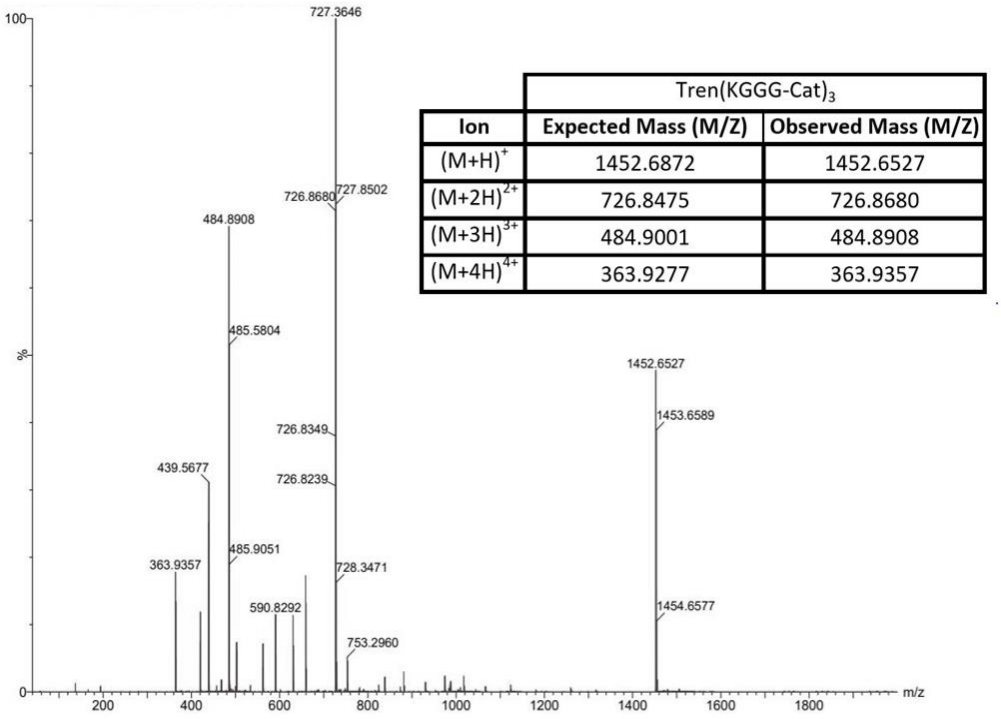

	Tren(KGGG-Cat)$_3$	
Ion	Expected Mass (M/Z)	Observed Mass (M/Z)
$(M+H)^+$	1452.6872	1452.6527
$(M+2H)^{2+}$	726.8475	726.8680
$(M+3H)^{3+}$	484.9001	484.8908
$(M+4H)^{4+}$	363.9277	363.9357

Figure A1.17: ESI-MS of Tren(KGGG-Cat)$_3$.

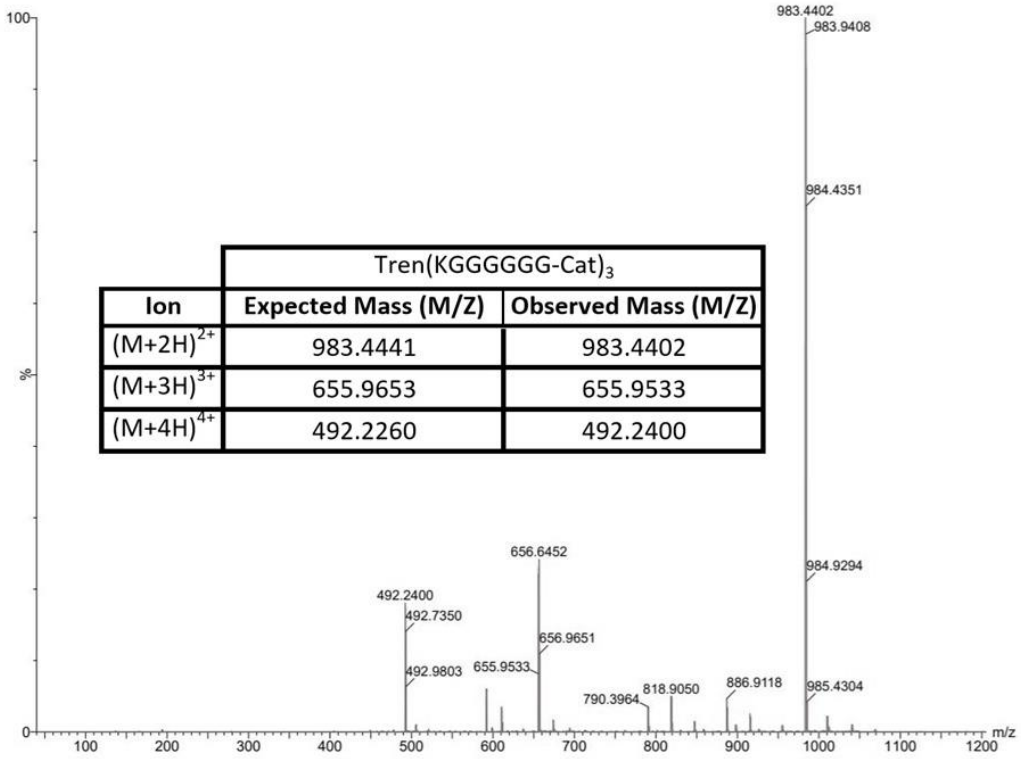

	Tren(KGGGGGG-Cat)$_3$	
Ion	**Expected Mass (M/Z)**	**Observed Mass (M/Z)**
$(M+2H)^{2+}$	983.4441	983.4402
$(M+3H)^{3+}$	655.9653	655.9533
$(M+4H)^{4+}$	492.2260	492.2400

Figure A1.18: ESI-MS of Tren(KGGGGGG-Cat)$_3$.

	Tren(KGG-Cat)$_3$		Tren(GKG-Cat)$_3$		Tren(GGK-Cat)$_3$	
Position	**δ_C (ppm)**	**δ_H (ppm)**	**δ_C (ppm)**	**δ_H (ppm)**	**δ_C (ppm)**	**δ_H (ppm)**
1	Obscured by DMSO	Obscured by water	Obscured by DMSO	3.19 (s, 2H)	Obscured by DMSO	3.21 (s, 2H)
2	Obscured by DMSO	Obscured by water	Obscured by DMSO	3.39 (s, 2H)	Obscured by DMSO	3.40 (s, 2H)
3	172.06	-	169.59	-	169.38	-
4	52.56	4.17 (td, J = 8.5, 4.7 Hz, 1H)	42.22	3.72 (m, 2H)	41.94	3.73 (m, 2H)
5	30.92	1.68 (m, 1H)	171.91	-	169.23	-
6	22.34	1.28 (ddt, J = 34.6, 17.7, 8.1 Hz, 2H)	52.50	4.28 (td, J = 8.5, 5.0 Hz, 1H)	42.10	3.79 (m, 2H)
7	26.58	1.49 (m, 3H) (H7 and H5' overlap)	31.22	1.71 (m, 1H)	171.75	-
8	38.69	2.73 (m, 2H)	22.23	1.33 (m, 2H)	52.79	4.52 (m, 1H)
9	168.94	-	26.63	1.52 (m, 3H) (H9 and H7' overlap)	31.07	1.78 (m, 2H)
10	42.07	3.93 (d, J = 5.7 Hz, 2H)	38.74	2.75 (m, 2H)	22.48	1.37 (m, 2H)
11	168.58	-	168.82		26.62	1.54 (m, 2H)
12	42.4	3.77 (d, J = 5.7 Hz, 2H)	42.00	3.97 (d, J = 5.6 Hz, 2H)	38.65	2.77 (m, 2H)
13	169.62	-	169.30	-	168.86	-
14	115.36	-	115.60	-	115.73	-
15	118.02	7.29 (d, J = 8.0 Hz, 1H)	118.22	7.30 (d, J = 7.7 Hz, 1H)	118.38	7.40 (d, J = 7.7 Hz, 1H)
16	117.81	6.69 (t, J = 7.9 Hz, 1H)	117.87	6.70 (t, J = 7.9 Hz, 1H)	118.11	6.70 (t, J = 7.9 Hz, 1H)
17	118.84	6.93 (d, J = 7.7 Hz, 1H)	118.86	6.94 (d, J = 7.7 Hz, 1H)	118.8	6.94 (d, J = 7.7 Hz, 1H)
18	146.12	-	146.15	-	146.02	-
19	148.97	-	148.86	-	148.61	-
N1	-	-	-	-	-	-
N2	-	7.69 (s, 3H)	-	9.01 (t, J = 5.8 Hz, 1H)	-	8.18 (t, J = 6.1 Hz, 2H)
N3	-	-	-	7.75 (m, 3H)	-	8.36 (t, J = 5.9 Hz, 1H)
N4	-	8.28 (t, J = 5.5 Hz, 1H)	-	8.26 (d, J = 7.8 Hz, 2H)	-	7.71 (m, 3H)
N5	-	9.07 (t, J = 5.6 Hz, 1H)	-	-	-	8.79 (d, J = 7.5 Hz, 1H)
O1	-	12.11 (s, 1H)	-	12.07 (s, 1H)	-	11.91 (s, 1H)
O2	-	9.31 (s, 1H)	-	9.36 (s, 1H)	-	9.38 (s, 1H)

Table A1.1. NMR data for Tren(KGG-Cat)$_3$, Tren(GKG-Cat)$_3$, and Tren(GGK-Cat)$_3$. ^{1}H NMR was obtained on a Varian Unity Inova 600 MHz spectrometer and ^{13}C on a Varian Unity Inova 500 MHz spectrometer. NMR data was taken in deuterated DMSO. See Figures A1.19-A1.24 for NMR spectra.

	Tren(KGG-Benz)$_3$		Tren(GGG-Cat)$_3$	
Position	**δ_C (ppm)**	**δ_H (ppm)**	**δ_C (ppm)**	**δ_H (ppm)**
1	Obscured by DMSO	3.19 (s, 2H)	Obscured by DMSO	3.24 (s, 2H)
2	Obscured by DMSO	3.38 (s, 2H)	Obscured by DMSO	Obscured by H_2O
3	168.51	-	169.39	-
4	42.01	3.73 (m, 2H)	42.15	3.79 (d, J = 5.6 Hz, 2H)
5	169.23	-	169.09	-
6	42.12	3.77 (d, *J* = 5.8 Hz, 1H)	42.10	3.73 (d, J = 5.8 Hz, 2H)
7	172.31	-	170.30	-
8	53.43	4.43 (m, 1H)	42.35	3.96 (d, J = 5.6 Hz, 2H)
9	30.71	1.76 (m, 2H)	169.56	-
10	22.69	1.38 (m, 2H)	115.34	-
11	26.67	1.55 (m, 2H)	118.11	7.31 (dd, J = 8.3, 1.5 Hz, 1H)
12	38.72	2.77 (m, 2H)	117.79	6.70 (t, J = 7.9 Hz, 1H)
13	166.91	-	118.86	6.93 (dd, J = 7.7, 1.5 Hz, 1H)
14	133.9	-	146.12	-
15	128.19	7.90 (d, *J* = 6.9 Hz, 2H)	149.07	-
16	127.56	7.47 (t, *J* = 7.6 Hz, 2H)	-	-
17	131.44	7.55 (t, *J* = 7.4 Hz, 1H)	-	-
N1	-	-	-	-
N2	-	8.18 (m, 1H)	-	8.21 (t, J = 5.8 Hz, 1H)
N3	-	8.28 (m, 1H)	-	8.32 (t, J = 5.7 Hz, 1H)
N4	-	7.73 (br, 3H)	-	9.05 (t, J = 5.8 Hz, 1H)
N5	-	8.56 (d, *J* = 7.6 Hz, 1H)	-	-
O1	-	-	-	12.18 (s, 1H)
O2	-	-	-	9.27 (s, 1H)

Table A1.2. NMR data for Tren(GGK-Benz)$_3$ and Tren(GGG-Cat)$_3$. ^{1}H NMR was obtained on a Varian Unity Inova 600 MHz spectrometer and ^{13}C on a Varian Unity Inova 500 MHz

spectrometer. NMR data was taken in deuterated DMSO. See Figures A1.25-A1.28 for NMR spectra

	Tren(KGGG-CAT)$_3$			Tren(KGGGGGG-CAT)$_3$	
Position	$\delta_C(ppm)$	$\delta_H(ppm)$	Position	$\delta_C(ppm)$	$\delta_H(ppm)$
1	-	3.21 (S, 2H)	1	-	3.23 (s, 2H)
2	-	3.42 (S, 2H)	2	-	3.44 (s, 2H)
3	172.34	-	3	172.37	-
4	52.56	4.16 (m, 1H)	4	52.59	4.16 (td, J = 8.3, 4.5 Hz, 1 H)
5	30.83	1.68 (m, 1H)	5	30.78	1.70 (m, 1H)
6	22.36	1.28 (m, 2H)	6	22.37	1.28 (m, 2 H)
7	26.59	1.50 (m, 3H) H7 and H5' overlap	7	26.58	1.53 (m, 3H) H7 and H5' overlap
8	38.69	2.75 (m ,2H)	8	38.71	2.76 (m, 2H)
9	169.10	-	9	169.18	-
10	42.09	3.77 (d, J = 5.5 Hz, 2H) H10 and H12 overlap	10 a - e	42.15	3.77 (m, 10 H)
11	169.46	-	11 a - e	169.10, 169. 39, 169.52, 169. 54	-
12	42.18	3.77 (d, J = 5.5 Hz, 2H) H10 and H12 overlap	12	42.37	3.96 (d, J = 5.7 Hz, 2 H)
13	169.18	-	13	169.61	-
14	42.39	3.96 (d, J = 5.70 Hz, 1H)	14	115.39	-
15	169.56	-	15	117.83	7.31 (d, J = 8.3 Hz, 1 H)
16	115.43	-	16	118.14	6.70 (t, J = 8.0 Hz, 1 H)
17	117.85	7.31 (d, J = 8.09 Hz, 1 H)	17	118.9	6.94 (d, J = 7.7 Hz, 1 H)
18	118.14	6.71 (t, J = 8.09 Hz, 1 H)	18	146.17	-
19	118.88	6.94 (d, J = 7.90 Hz, 1 H	19	149.13	-
20	146.16		-	-	-
21	149.05	-	-	-	-
N1	-	8.21 (s, 2H) N1 and N4 overlap	N1	-	-
N2	-	7.77 (br, 3H)	N2	-	7.75 (br, 3H)
N3	-	8.09 (d, J = 7.05 Hz, 1 H)	N3	-	8.07 (d, J = 7.7 Hz, 1 H)
N4	-	8.18 (t, J = 5.7 Hz, 2H) N1 and N4 overlap	N4 - N7	-	8.20 (m, 5 H) N4 - N7 overlap with N1
N5	-	8.36 (t, J = 5.9 Hz, 1 H)	N8	-	8.32 (t, J = 5.9 Hz, 1 H)
N6	-	9.06 (t, J = 6.0 Hz, 1 H)	N9	-	9.06 (t, J = 5.8 Hz, 1 H)
O1	-	12.15 (s, 1H)	O1	-	12.20 (s, 1 H)
O2	-	9.33 (s, 1H)	O2	-	9.26 (br, < 1 H)

Table A1.3. NMR data for Tren(KGGG-Cat)$_3$ and Tren(KGGGGGG-Cat)$_3$. ^{1}H NMR was obtained on a Varian Unity Inova 600 MHz spectrometer and ^{13}C on a Varian Unity Inova 500 MHz spectrometer. NMR data was taken in deuterated DMSO. See Figures A1.29 and A1.30 for NMR spectra

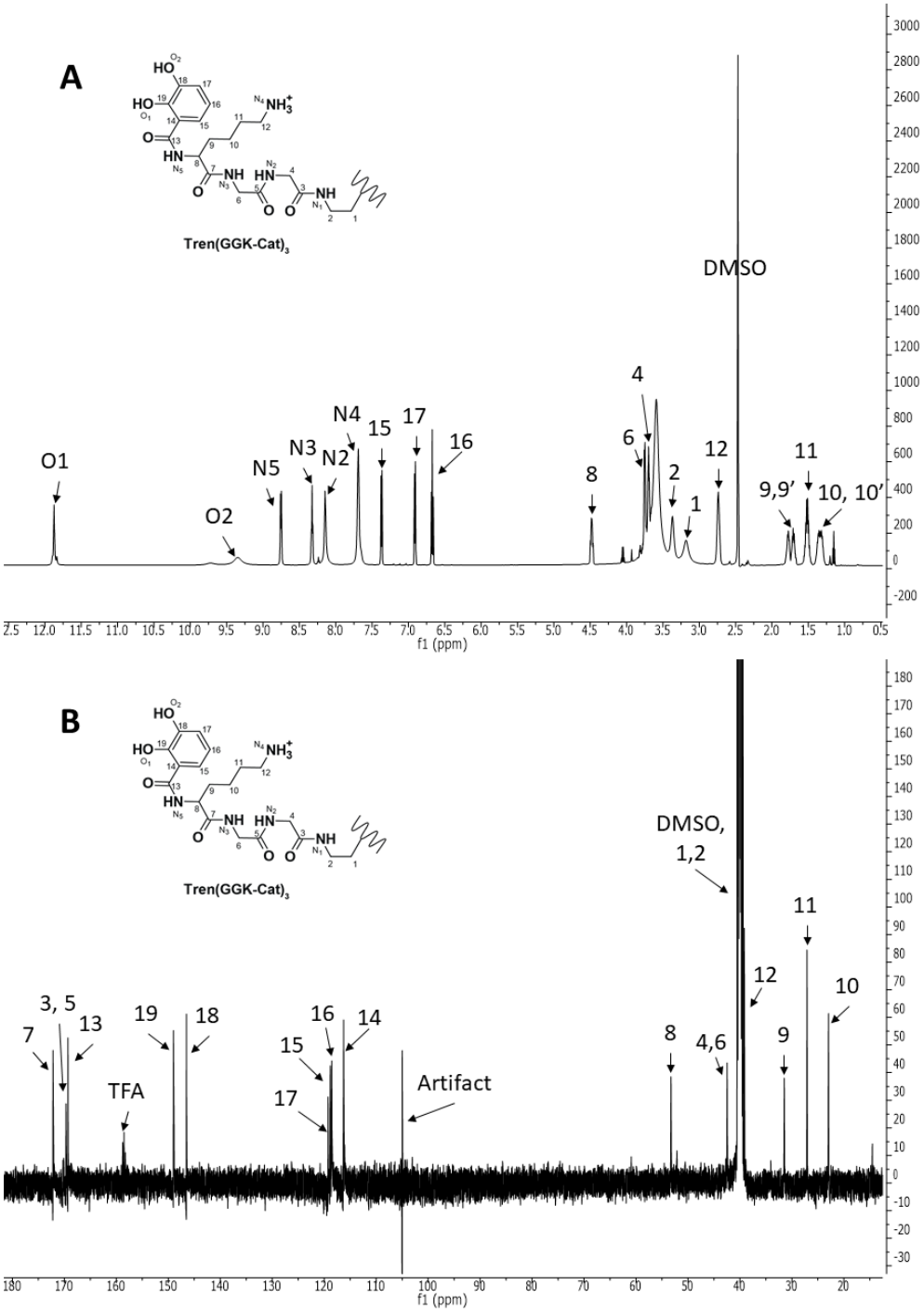

Figure A1.19. NMR data for Tren(GGK-Cat)$_3$. (A)^{1}H NMR data for Tren(GGK-Cat)$_3$. NMR (600 MHz) in DMSO. (B) ^{13}C NMR data for Tren(GGK-Cat)$_3$. NMR (500 MHz) in DMSO. Trifluoroacetic acid (TFA) originates from RP-HPLC purification. Assignments were confirmed with HMBC, Figure A1.20. The artifact present in the ^{13}C NMR is from a damaged receiver.

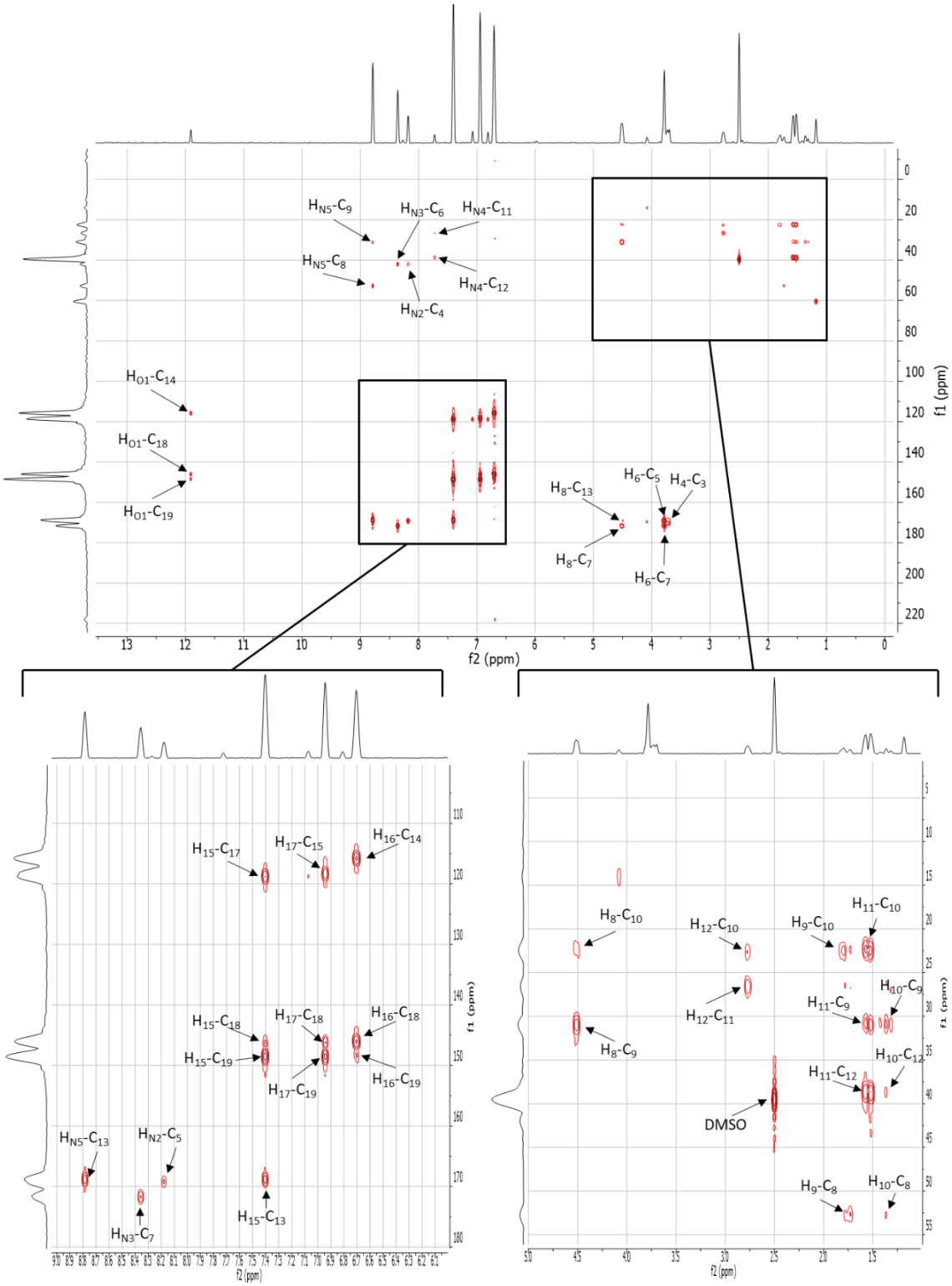

Figure A1.20. ^{1}H-^{13}C HMBC NMR for Tren(GGK-Cat)$_3$. NMR (600 MHz) in DMSO. Enlarged regions of the ^{1}H-^{13}C HMBC NMR spectrum are in the bottom panels. The spectrum is annotated with the correlations between specific hydrogens and carbons.

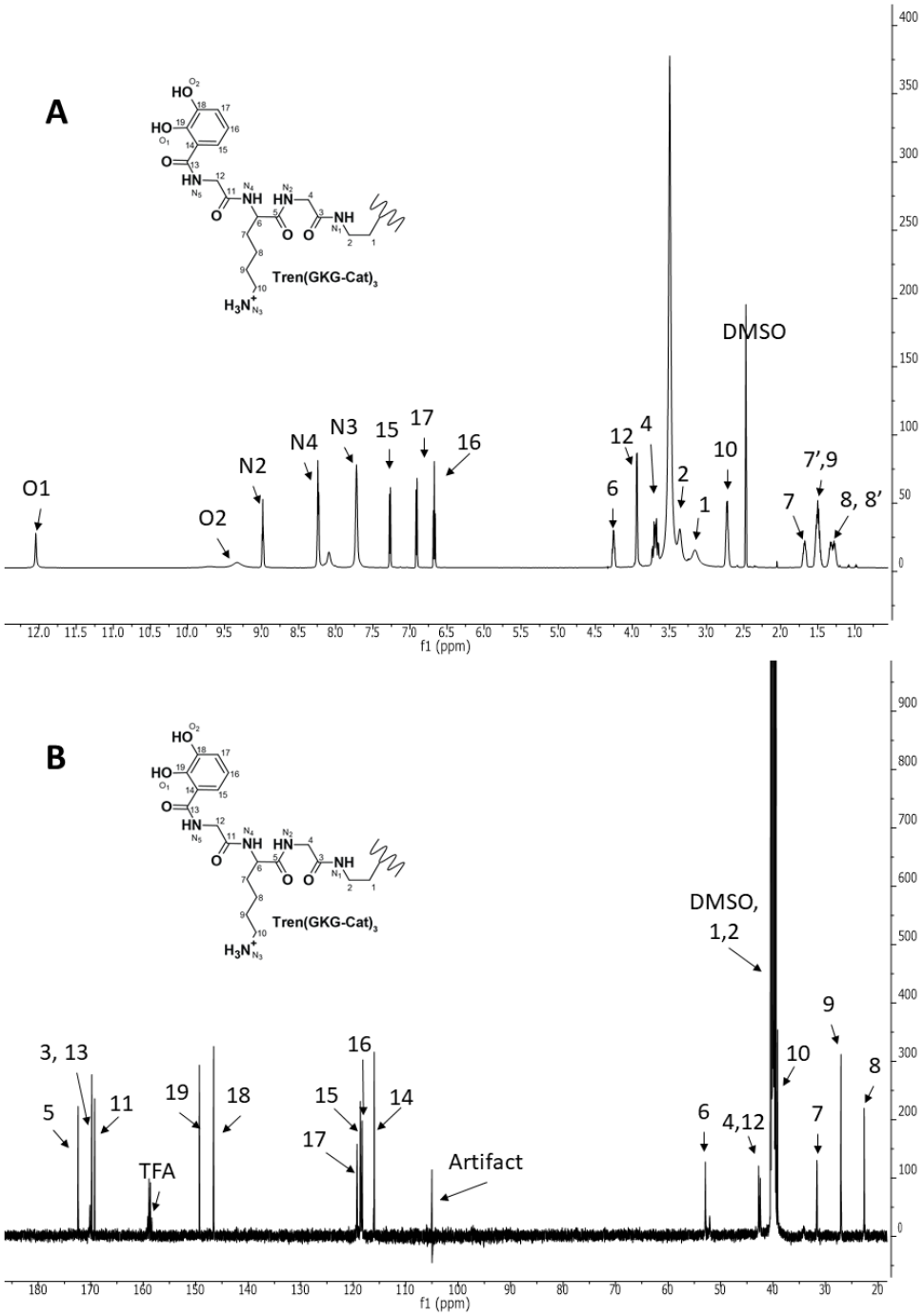

Figure A1.21. NMR data for Tren(GKG-Cat)$_3$. (A)^{1}H NMR data for Tren(GKG-Cat)$_3$. NMR (600 MHz) in DMSO. (B) ^{13}C NMR data for Tren(GKG-Cat)$_3$. NMR (500 MHz) in DMSO. Trifluoroacetic acid (TFA) originates from RP-HPLC purification. Assignments were confirmed with HMBC, Figure A1.22. The artifact present in the ^{13}C NMR is from a damaged receiver.

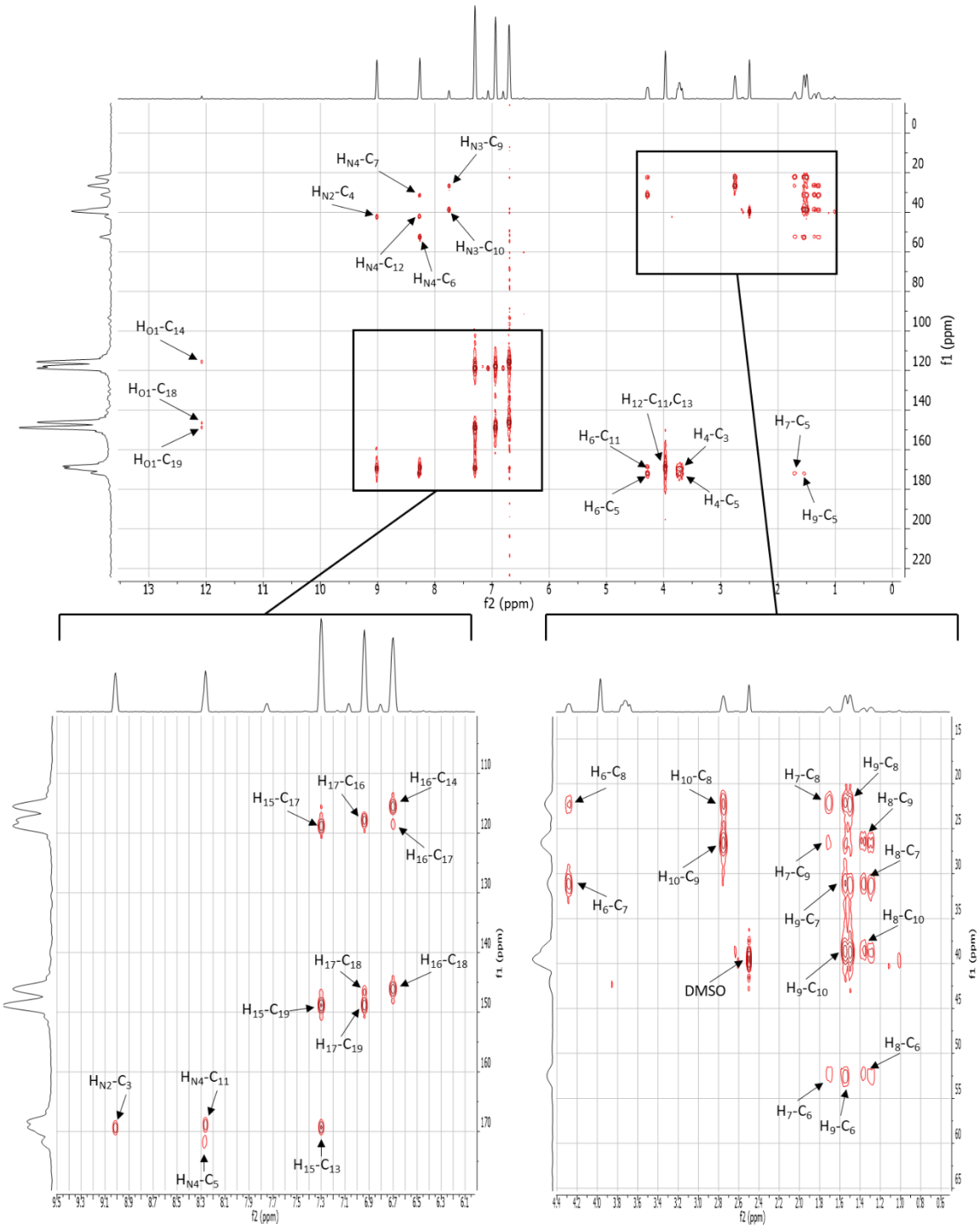

Figure A1.22. ^{1}H-^{13}C HMBC NMR for Tren(GKG-Cat)$_3$. NMR (600 MHz) in DMSO. Enlarged regions of the ^{1}H-^{13}C HMBC NMR spectrum are in the bottom panels. The spectrum is annotated with the correlations between specific hydrogens and carbons.

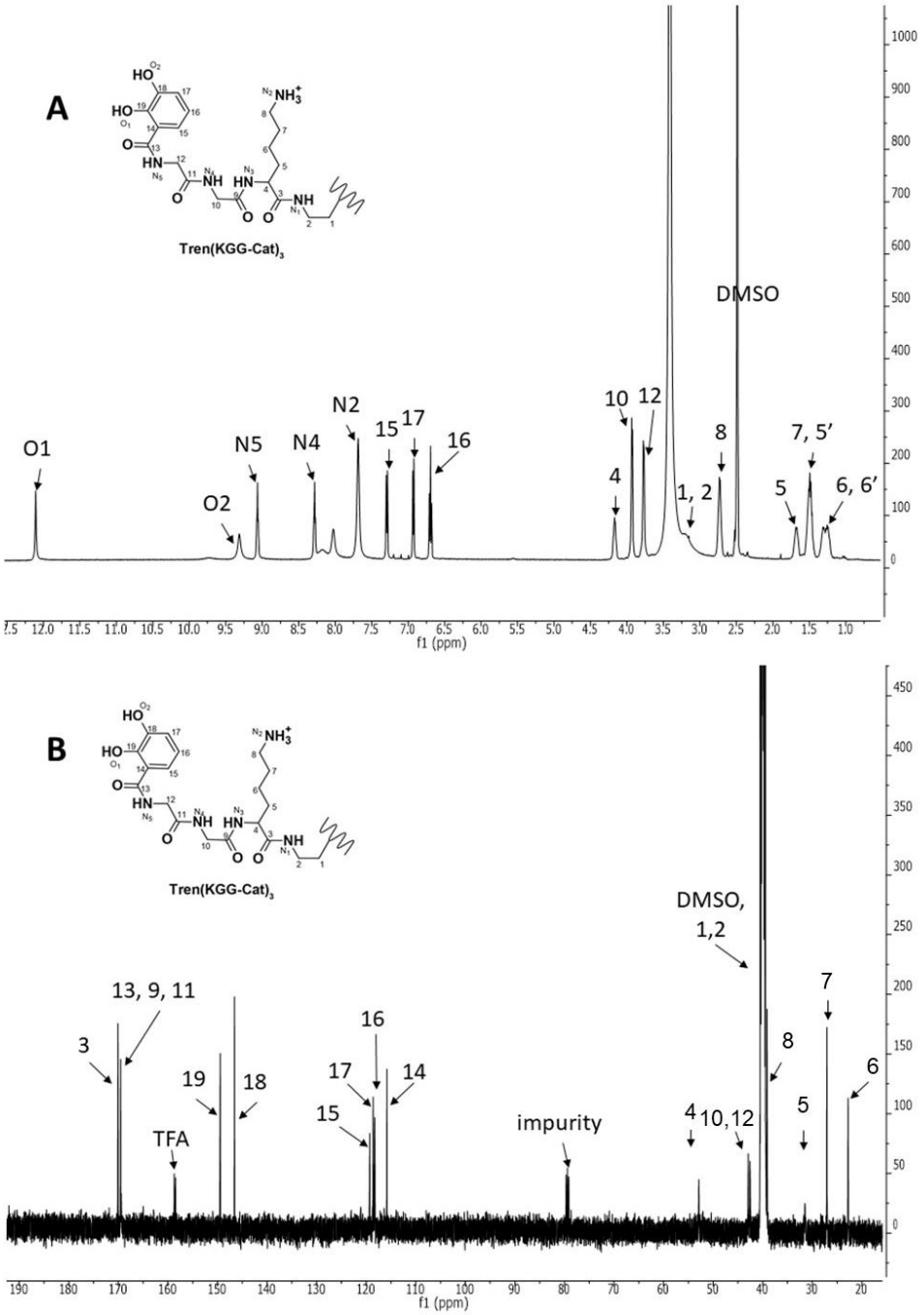

Figure A1.23. NMR data for Tren(KGG-Cat)$_3$. (A)^{1}H NMR data for Tren(KGG-Cat)$_3$. NMR (600 MHz) in DMSO. (B) ^{13}C NMR data for Tren(KGG-Cat)$_3$. NMR (500 MHz) in DMSO. Trifluoroacetic acid (TFA) originates from RP-HPLC purification. Assignments were confirmed with HMBC, Figure A1.24.

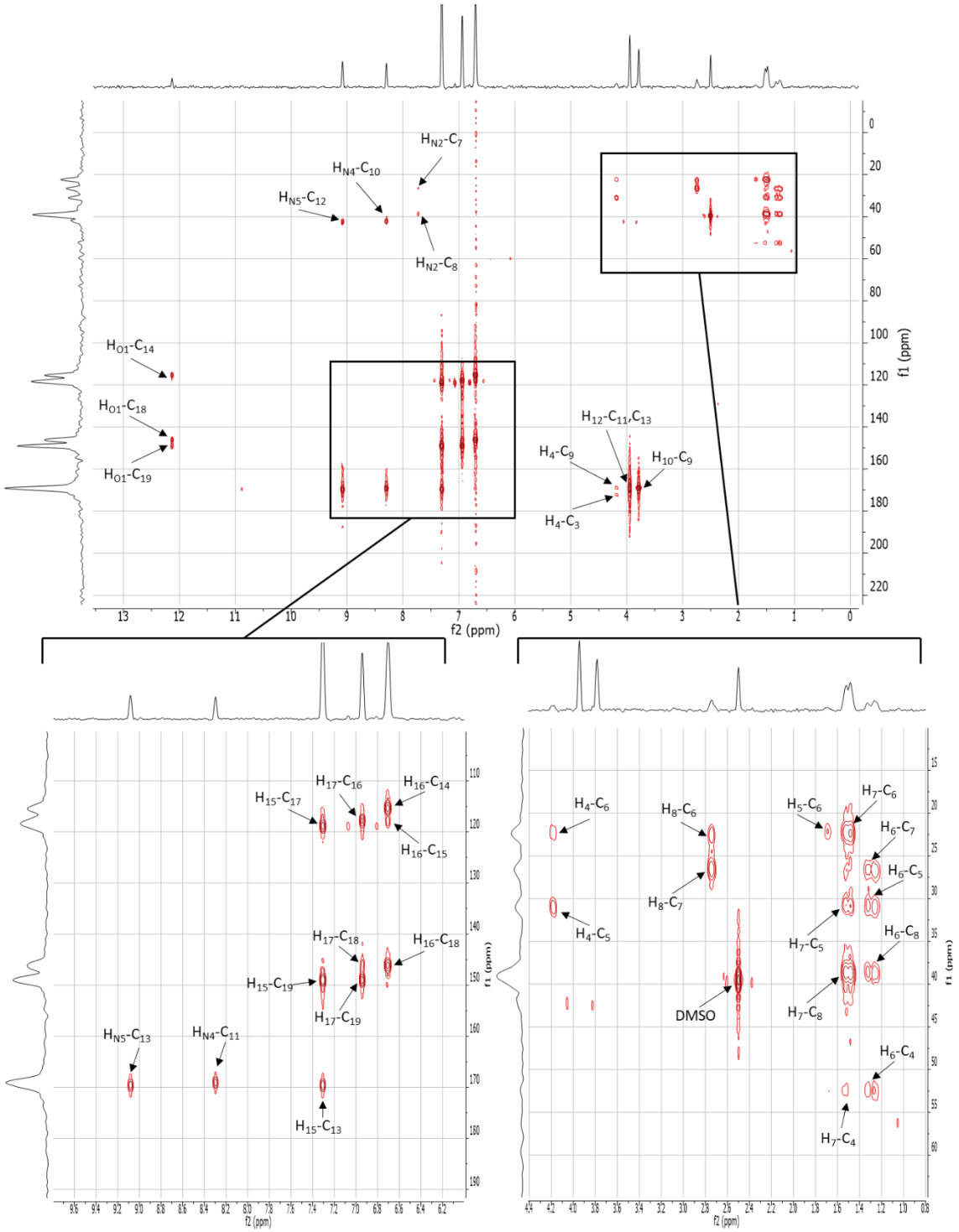

Figure A1.24. ^{1}H-^{13}C HMBC NMR for Tren(KGG-Cat)$_3$. NMR (600 MHz) in DMSO. Enlarged regions of the ^{1}H-^{13}C HMBC NMR spectrum are in the bottom panels. The spectrum is annotated with the correlations between specific hydrogens and carbons.

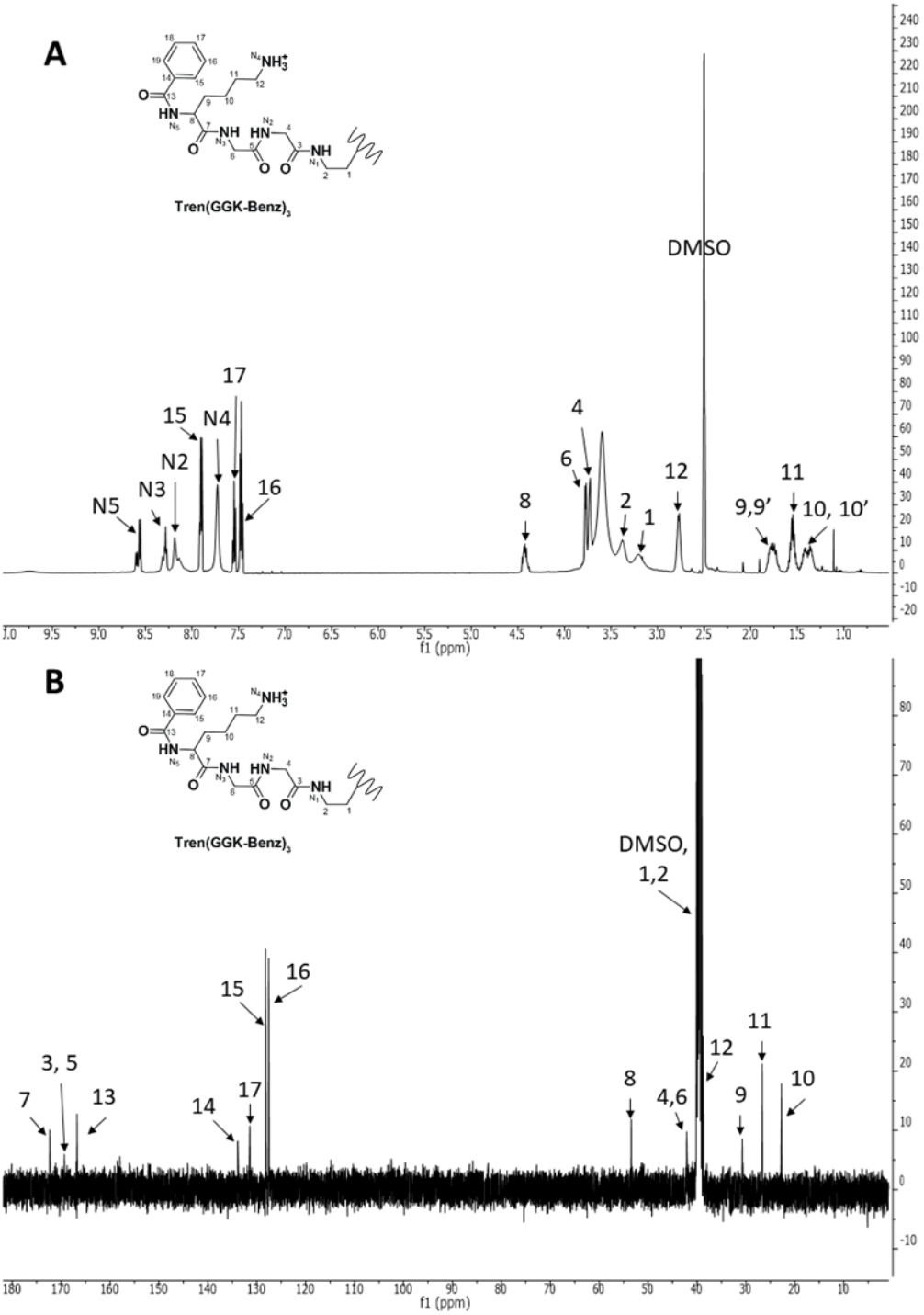

Figure A1.25. NMR data for Tren(GGK-Benz)$_3$. (A)^{1}H NMR data for Tren(GGK-Benz)$_3$. NMR (600 MHz) in DMSO. (B) ^{13}C NMR data for Tren(GGK-Benz)$_3$. NMR (500 MHz) in DMSO. Assignments were confirmed with HMBC, Figure A1.26.

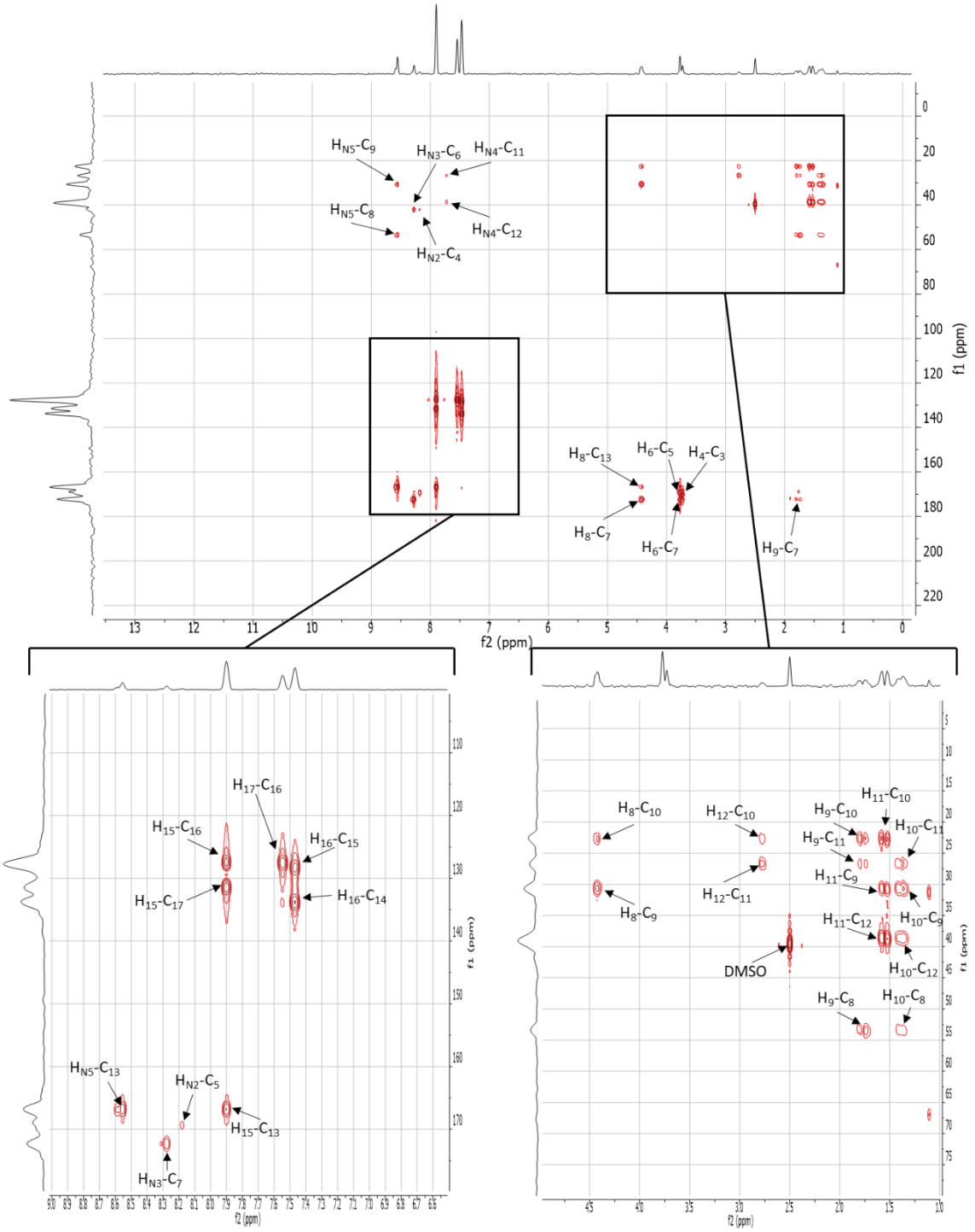

Figure A1.26. ^{1}H-^{13}C HMBC NMR for Tren(GGK-Benz)$_3$. NMR (600 MHz) in DMSO. Enlarged regions of the ^{1}H-^{13}C HMBC NMR spectrum are in the bottom panels. The spectrum is annotated with the correlations between specific hydrogens and carbons.

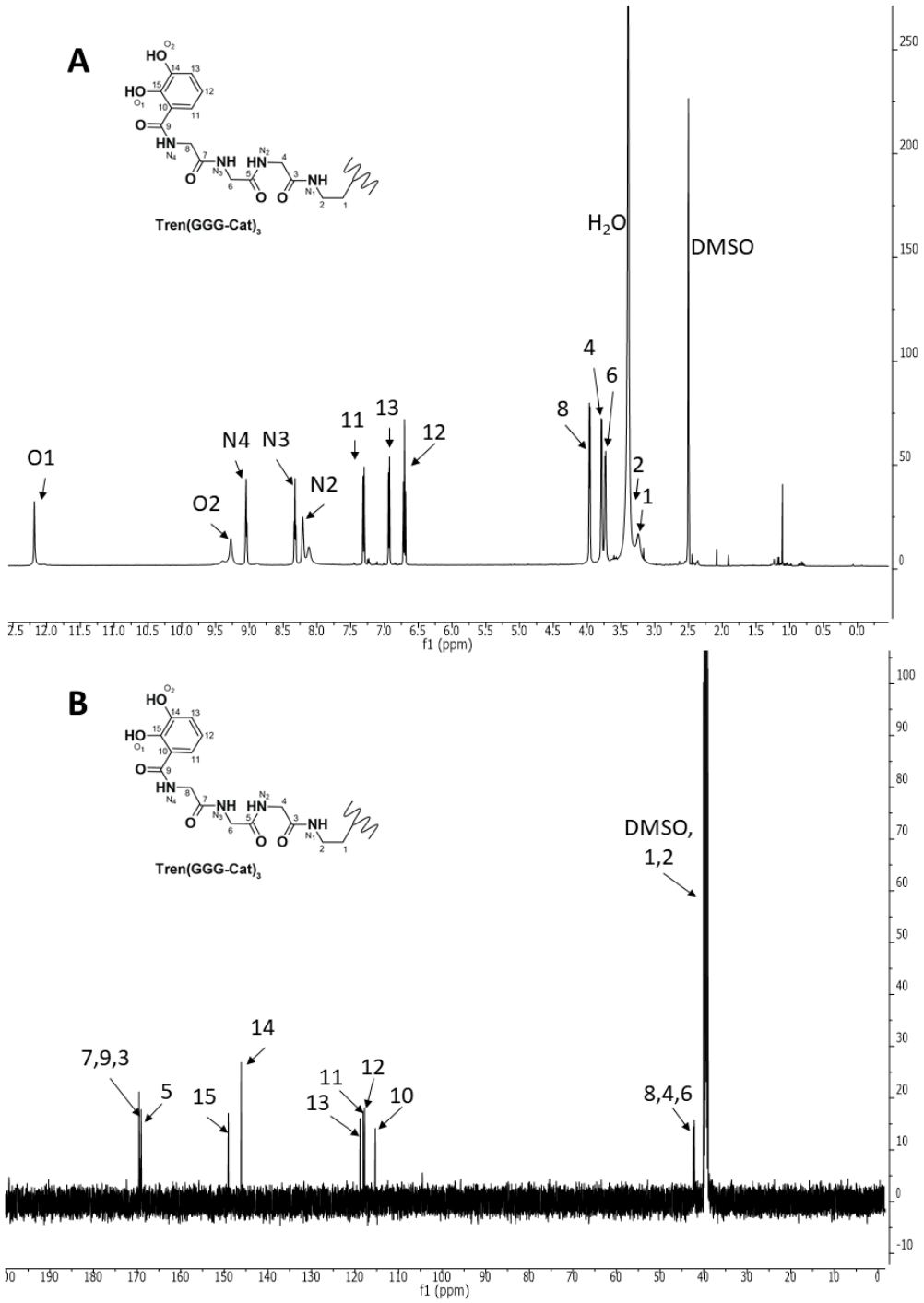

Figure A1.27. NMR data for Tren(GGG-Cat)$_3$. (A)^{1}H NMR data for Tren(GGG-Cat)$_3$. NMR (600 MHz) in DMSO. (B) ^{13}C NMR data for Tren(GGG-Cat)$_3$. NMR (500 MHz) in DMSO. Assignments were confirmed with HMBC, Figure A1.28.

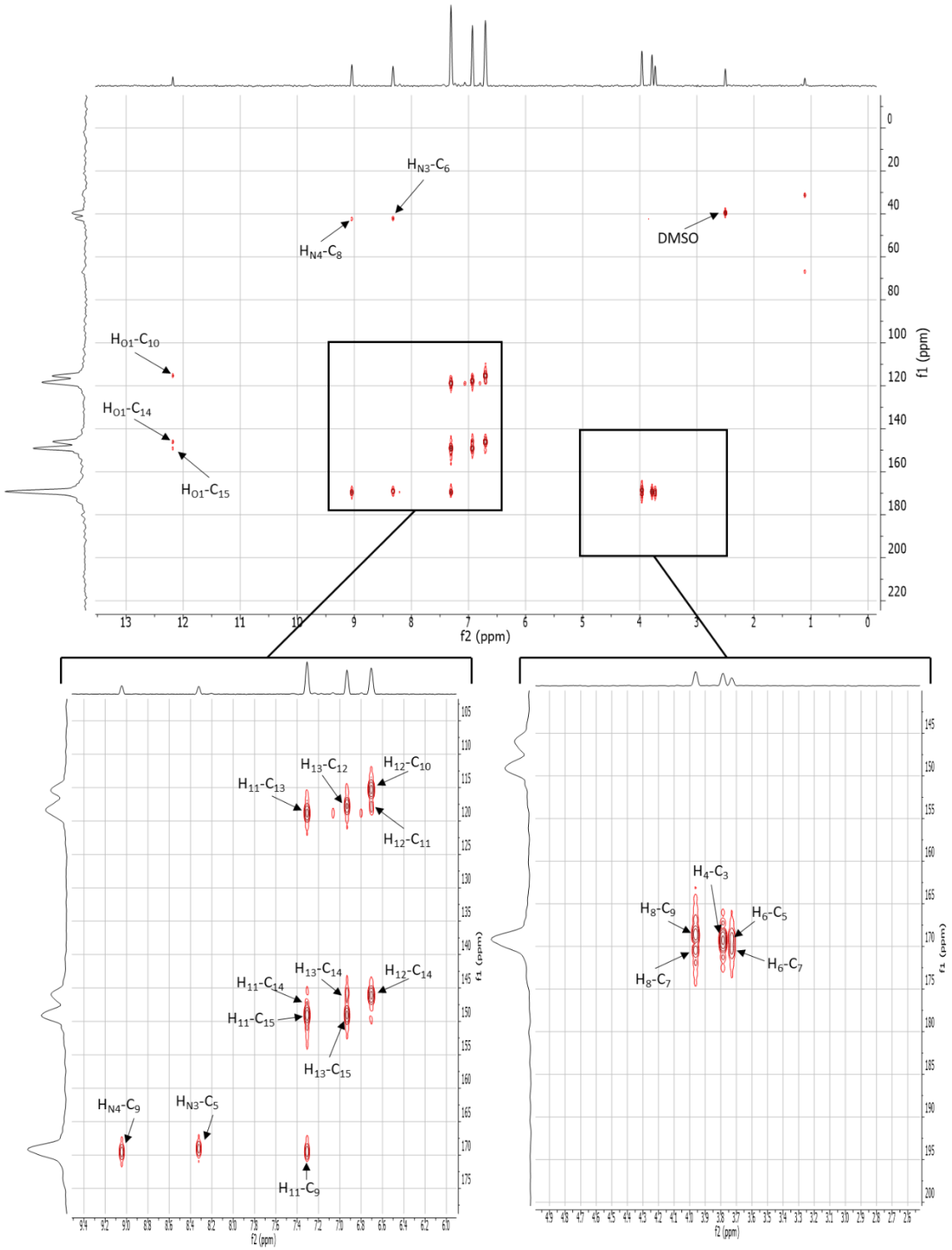

Figure A1.28. ^{1}H-^{13}C HMBC NMR for Tren(GGG-Cat)$_3$. NMR (600 MHz) in DMSO. Enlarged regions of the ^{1}H-^{13}C HMBC NMR spectrum are in the bottom panels. The spectrum is annotated with the correlations between specific hydrogens and carbons.

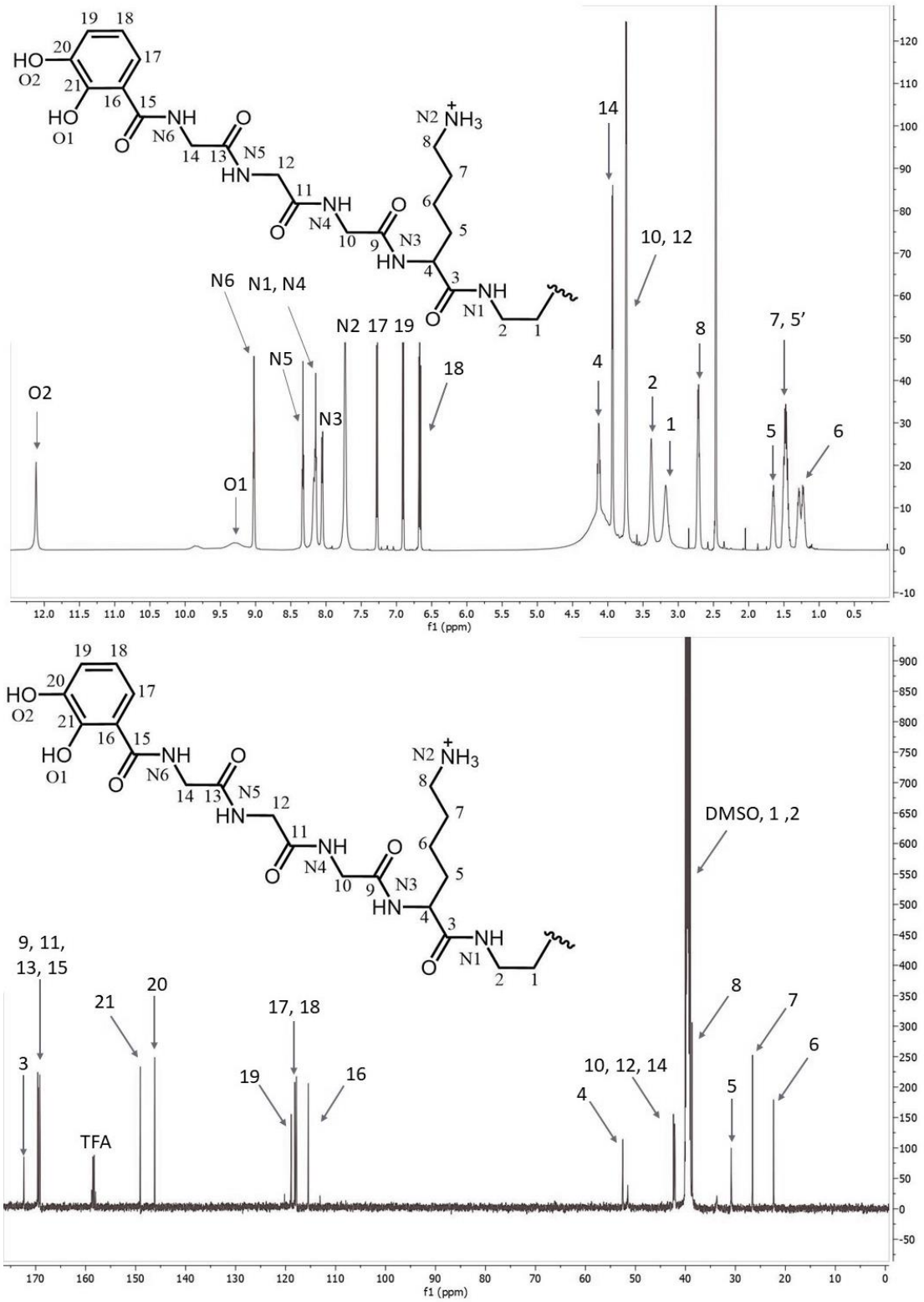

Figure A1.29. NMR data for Tren(KGGG-Cat)$_3$. (A)^{1}H NMR data for Tren(KGGG-Cat)$_3$. NMR (600 MHz) in DMSO. (B) ^{13}C NMR data for Tren(KGGG-Cat)$_3$. NMR (500 MHz) in DMSO. Trifluoroacetic acid (TFA) originates from RP-HPLC purification. Assignments were made in reference to Tren(KGG-Cat)$_3$

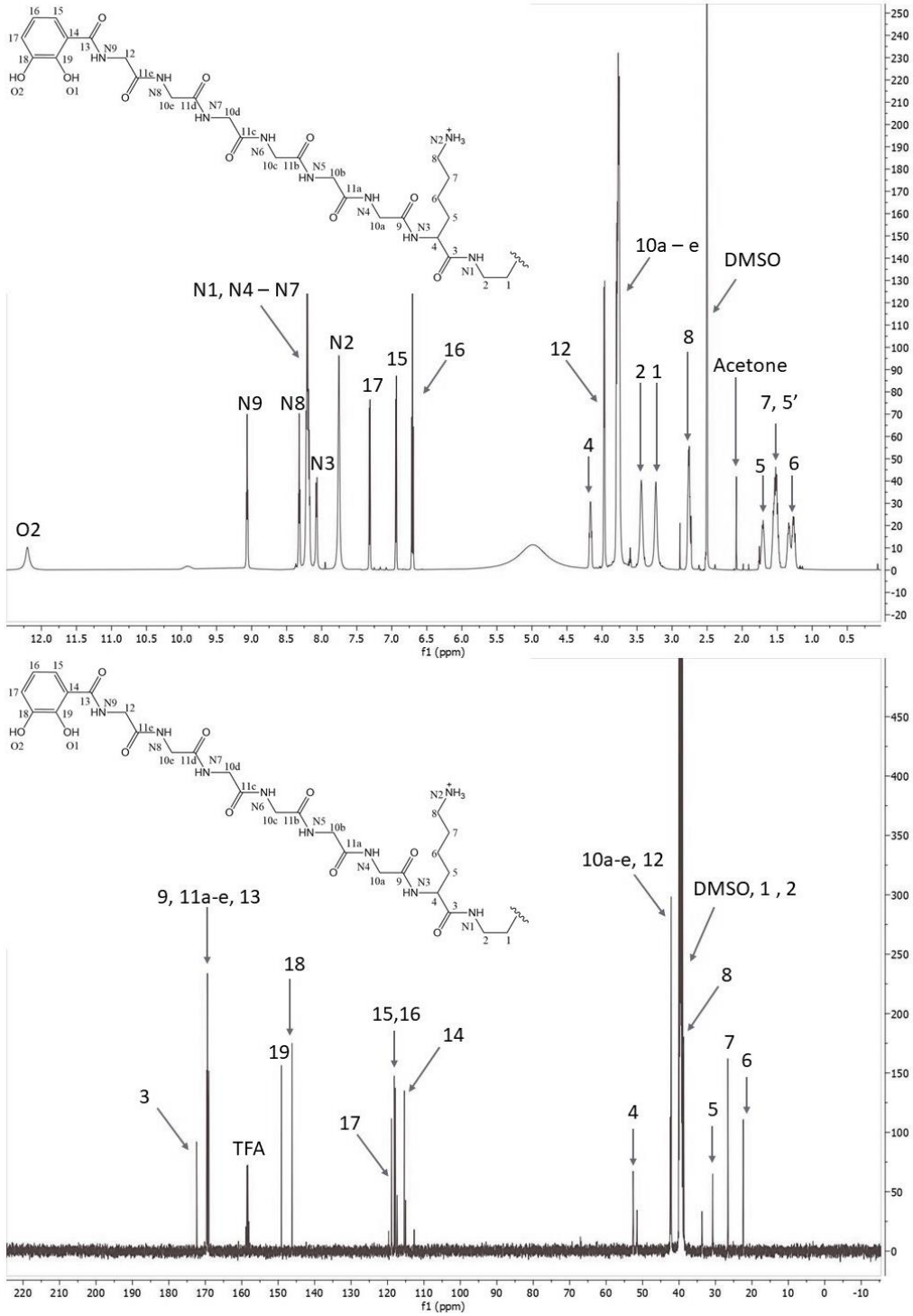

Figure A1.30. NMR data for Tren(KGGGGGG-Cat)$_3$. (A)^{1}H NMR data for Tren(KGGGGGG-Cat)$_3$. NMR (600 MHz) in DMSO. (B) ^{13}C NMR data for Tren(KGGGGGG-Cat)$_3$. NMR (500 MHz) in DMSO. Trifluoroacetic acid (TFA) originates from RP-HPLC purification. Assignments were made in reference to Tren(KGG-Cat)$_3$

Appendix 2. Supporting SFA Information—Chapter 2

Full details of SFA components and operation are included elsewhere.[125] The SFA substrates used in this work consisted of mica sheets, approximately 3-5 μm thick, prepared using established methods[126] to preserve the molecular smoothness (~2 Å rms[185]) of the mica, confirmed in Figure A3.1. The mica sheets were coated with a 50 nm reflective silver layer via thermal evaporation. The silver-coated mica was glued onto semi-cylindrical fused silica disks using either a UV curing adhesive (Norland OA 81) or uncured epoxy resin (EPON 1004), with the silvered side of the mica facing the disk and the mica side exposed. The disks were then mounted in a crossed cylinder geometry, locally equivalent to a sphere on flat configuration at the contact point between the surfaces. White light multiple beam interferometry was used to measure the absolute distance between the mica surfaces and area of contact. One of the surfaces was suspended on a double cantilever spring (spring constant k = 500-1200 N/m). By displacing one of the surfaces by known increments with a motor or piezoelectric actuator and measuring the distance between the surfaces with interferometry, deflections of the spring (Δx) were measured and used to calculate the normal force (F) between the surfaces via Hooke's law ($F = k\Delta x$). For adhesive surfaces, the distance that the surfaces jumped apart upon separation (Δx_{jump}) was therefore related to the pull-off force (F_{ad}) by $F_{ad} = k\Delta x_{jump}$.

Siderophore analogs were deposited onto the mica surfaces from solution as described in the main text. Although the 2,3-DHBA functionalities are much more resistant to oxidation than Dopa, the catechol found in marine mussel proteins,[33] they may still slowly oxidize in solutions at neutral pH. Since the goal of this work is to understand the mechanism of catechol cation synergy, we chose a solution in which 2,3-DHBA does not oxidize but that mimics physiological ionic strength. This solution is not expected to change the molecular interactions responsible for adhesion, as even a neutral solution is well below the pKa of lysine and so the pendant amines will be positively charged in neutral or acidic solutions. The impact of pH on interactions between 2,3-DHBA and mica is less clear, but based on previous studies of siderophore analog adhesion,[33,34] an acidic pH is not expected to drastically interfere with the ability of the catechol to donate hydrogen bonds. To determine the optimal concentration of siderophore analogs to maximize adhesion, the deposition concentration was varied, resulting in different film densities and different pull-off forces (shown in Figure 3 in the main text). The dependence of pull-off force on concentration of siderophore analogs in solution during symmetric deposition is shown in Figure A2.1. Symmetric deposition with solutions of concentration greater than 300 μM results in reduced pull-off forces due to a transition from a single monolayer between the surfaces (adhesive failure) to two monolayers, one on each surface (cohesive failure), described in the main text. To maximize adhesion force, a single dense monolayer between the surfaces is necessary. To achieve this monolayer via symmetric deposition, it is necessary to deposit sparse monolayers onto both surfaces using a solution of lower siderophore analog concentration. These sparse monolayers, when combined during compression of the surfaces, form a complete monolayer, as illustrated in the main text, Figure 6B (vi). Figure A2.1 suggests that the optimal siderophore analog concentration to maximize adhesion with symmetric deposition is 200-300 μM. To deposit a dense monolayer of siderophore analogs on a single surface via asymmetric deposition (and thereby maximize adhesion), 50 μL of 400 μM siderophore analog solution was sufficient. Higher concentrations

could be used to deposit a monolayer via asymmetric deposition, but this would result in unnecessary use of materials.

After deposition of siderophore analogs, adhesion measurements consisting of cycles of compression and separation were performed, described in the main text. The pull-off forces mediated by monolayers of siderophore analogs were independent of the retraction velocity of the surfaces for the separation velocities used in this work, suggesting that such small molecules are unable to dissipate enough energy during separation of the surfaces to influence the measured pull-off force. Figure A2.32 compares a dynamic compression and separation cycle in which the surfaces were moved at 5 nm/s to a compression and retraction cycle in which the surfaces were allowed to relax for 10 seconds after each change in separation on approach. After the surfaces jumped into adhesive contact, the surfaces were compressed further to a maximum compression consistent with the dynamic compression, and then dynamically loaded to a force about 80 percent of the pull-off force needed to separate the surfaces. At that point, the surfaces were again allowed to relax 10 seconds after each change in separation until the surfaces jumped from adhesive contact. The pull-off forces measured in these static and dynamic experiments were the same within error, justifying the use of the JKR theory to relate the pull-off force measured in the dynamic compression and retraction cycles to interfacial energy for the relatively slow separation velocities used in this work (<10 nm/s). Larger separation velocities are expected to result in contact hysteresis and elevated pull-off forces due to viscoelasticity of the glue layer beneath the mica surfaces. As such, the separation velocity was kept below 10 nm/s.

The SFA is designed to minimize mechanical drift, but both mechanical and thermal drift do occur, particularly for long contact times (t_{wait} = 60 min). This drift occasionally changed the compressive force during the wait time during our experiments, but because the pull-off force was not sensitive to the maximum applied load, the drift did not appear to influence the measured pull-off force. We note that the insensitivity of the measured pull-off force to the applied load is consistent with the JKR theory, which predicts that the pull-off force is independent of the maximum applied load. To prevent evaporation of the liquid meniscus, 2-3 ml of water was placed in the bottom of the SFA chamber, which was then sealed, thus saturating the interior of the chamber with water vapor.

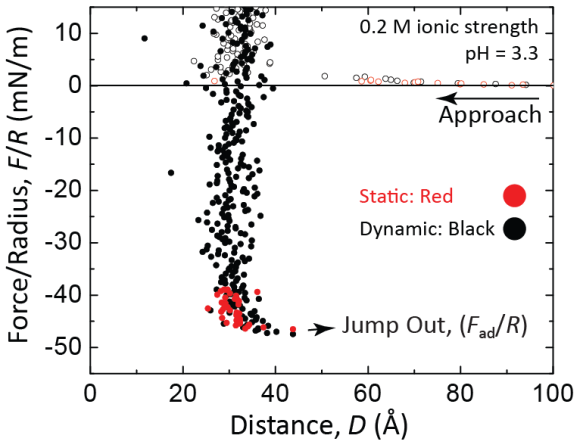

Figure A2.1. Comparison of static and dynamic force measurements of Tren(GKG-Cat)$_3$. Static measurements were made by waiting 10 seconds between each measurement of surface separation. Dynamic measurements were performed by moving one of the surfaces at a constant velocity of 5 nm/s.

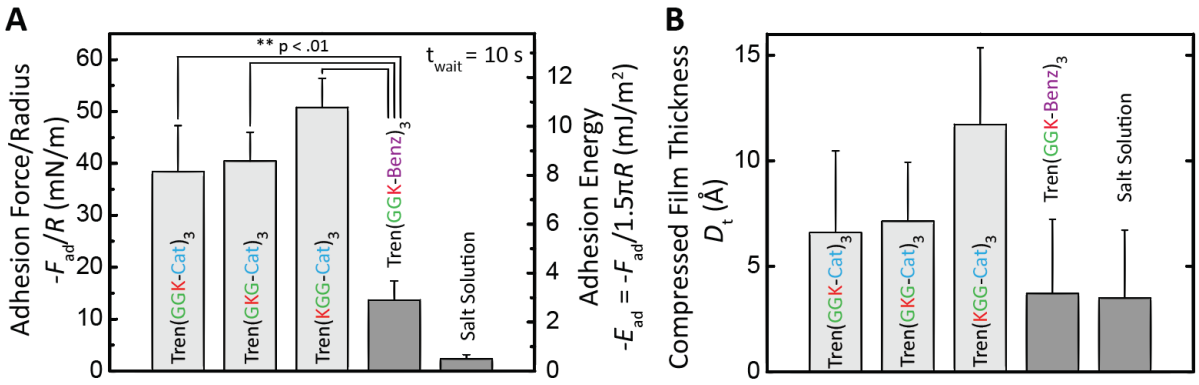

Figure A2.2. (A) Adhesion force ($-F_{ad}/R$) and energy (E_{ad}) and (B) compressed film thickness (D_t) of monolayers of siderophore analogs. F_{ad}/R was converted to E_{ad} using the JKR theory of contact mechanics[1] ($E_{ad} = F_{ad}/1.5\pi R$). Error bars correspond to the standard deviation of four independent experiments. Significance determined via one-way ANOVA with post-hoc Tukey HSD test, $\alpha = .01$.

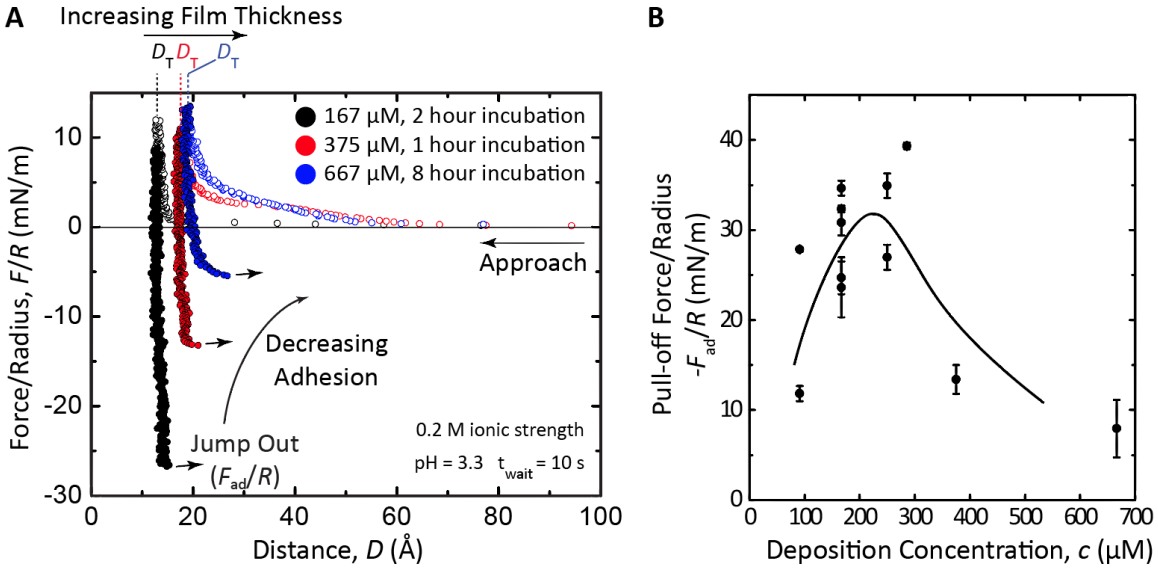

Figure A2.3. Impact of incubation concentration on adhesion. (A) Plots of force normalized by the radius of curvature of the surfaces vs. surface separation distance for compressed films of Tren(GGK-Cat)$_3$ after symmetric deposition at 167 µM (black circles), 375 µM (red circles), and 667 µM (blue circles). Open circles correspond to approach and compression of the surfaces, closed circles correspond to separation and jump from contact. (B) Plot of pull-off force vs. deposition concentration for symmetric depositions of Tren(GGK-Cat)$_3$, Tren(GKG-Cat)$_3$, and Tren(KGG-Cat)$_3$. Line is included to guide the eye.

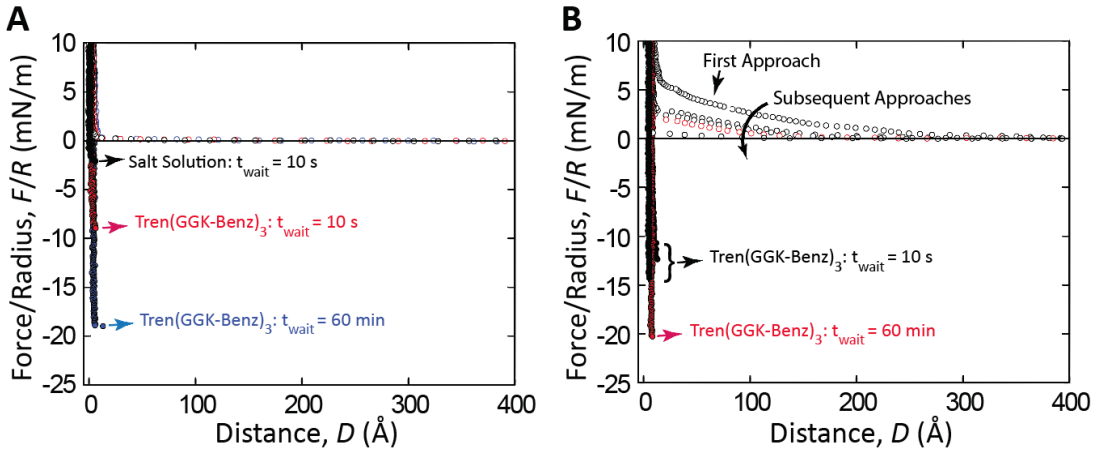

Figure A2.4. Plots of force normalized by the radius of curvature of the surfaces (F/R) vs. surface separation distance (D) for a film of Tren(GGK-Benz)$_3$. Open circles correspond to approach and compression of the surfaces, closed circles correspond to separation and jump from contact. (A) Pull-off forces measured after 10 s (red circles) and 60 min (blue circles) waiting at maximum compression. Pull-off force measured in salt solution (black circles) is shown for comparison. (B) Decreasing onset of interaction upon sequential compression and retraction cycles, attributed to rearrangement of adsorbed aggregates.

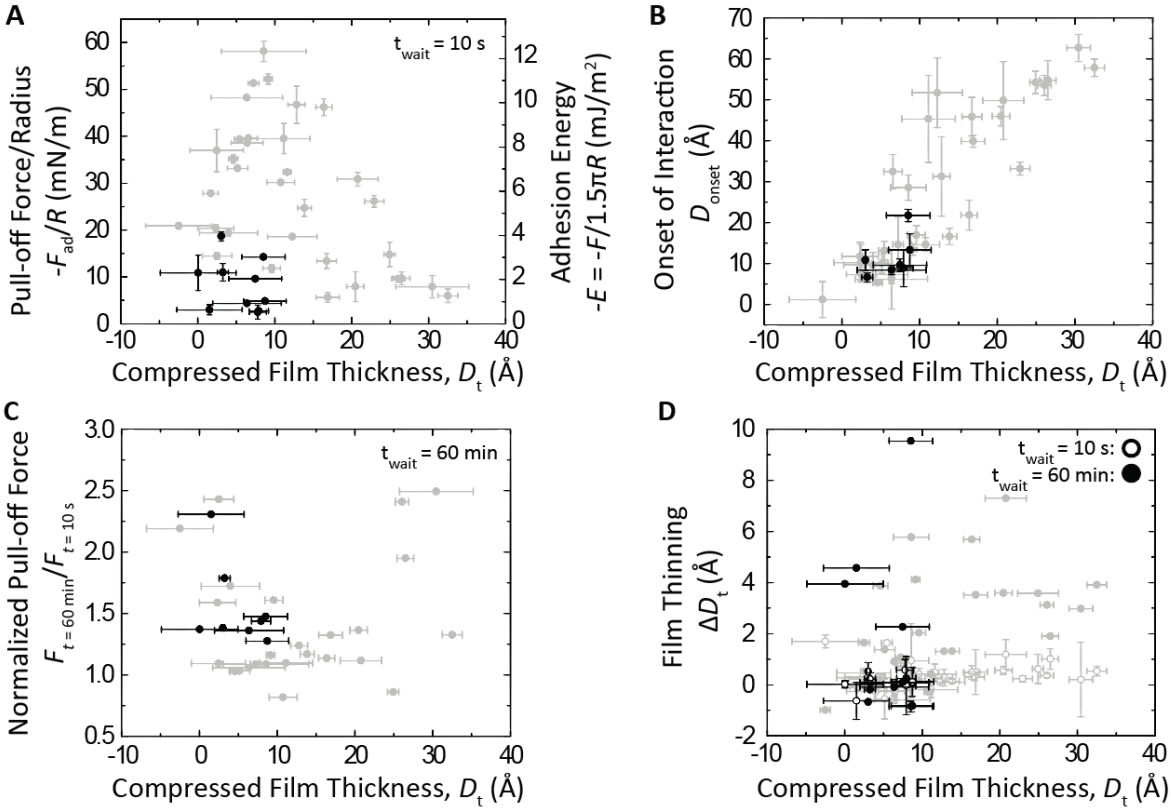

Figure A2.5. Properties of films of Tren(GGK-Benz)$_3$. (A) Pull-off force ($-F_{ad}/R$) and energy (E_{ad}) vs. compressed film thickness (D_t). (B) Onset of interaction (D_{onset}) vs. D_t. (C) Normalized pull-off force ($F_{t = 60\ min}/F_{t = 10\ s}$) vs. D_t. (D) Change in film thickness (ΔD_t) after waiting 10 seconds (open circles) and 60 minutes (closed circles) at maximum compression

vs. D_t measured before the waiting time. Error bars correspond to the standard deviation, with additional error in D_t introduced from measuring D_t relative to the surface separation in salt solution. Results for films of Tren(GGK-Cat)$_3$, Tren(GKG-Cat)$_3$, and Tren(KGG-Cat)$_3$ are shown in gray, reproduced from Figures 2.3, 2.4, and 2.5 in the main text.

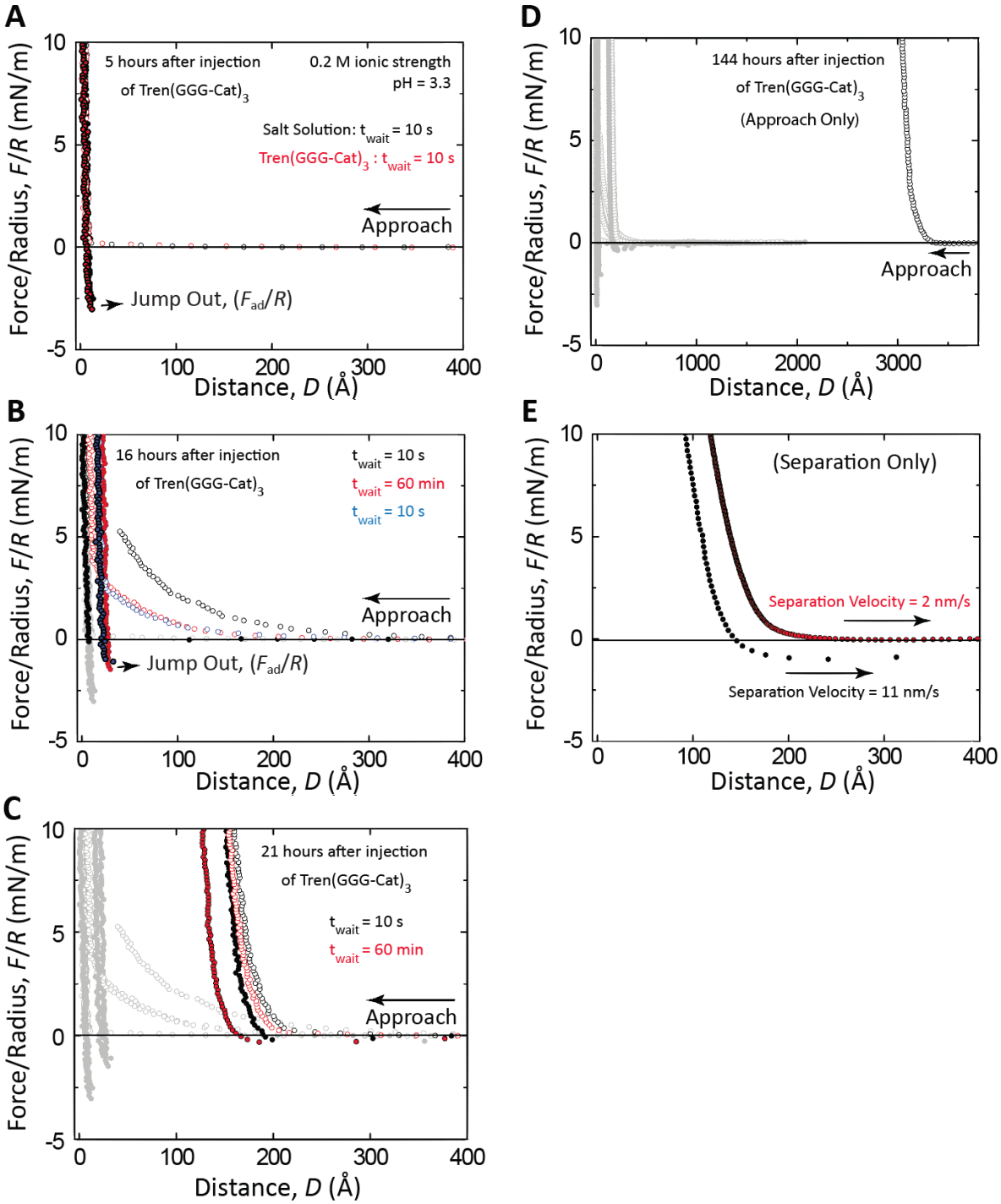

Figure A2.6. Plots of force normalized by the radius of curvature of the surfaces (F/R) vs. surface separation distance (D) for a compressed film of Tren(GGG-Cat)$_3$. Open circles correspond to approach and compression of the surfaces; closed circles correspond to

separation and jump from contact. (A) Forces remain unchanged 5 h after injection of siderophore analogs, suggesting that no adsorption has occurred. (B) 16 hours after injection, the onset of interaction (D_{onset}) increases to 400 Å (black circles) and decreases on subsequent force measurements (red and blue circles) suggesting molecular rearrangement. (C) 21 h after injection, the onset of interaction and compressed film thickness (D_t) further increase. The film thinned after t_{wait} = 60 min, again suggesting molecular rearrangement. (D) 144 h after injection, D_t increases to hundreds of nanometers. (E) Low pull-off forces (<2 mN/m) are attributed to viscous dissipation.

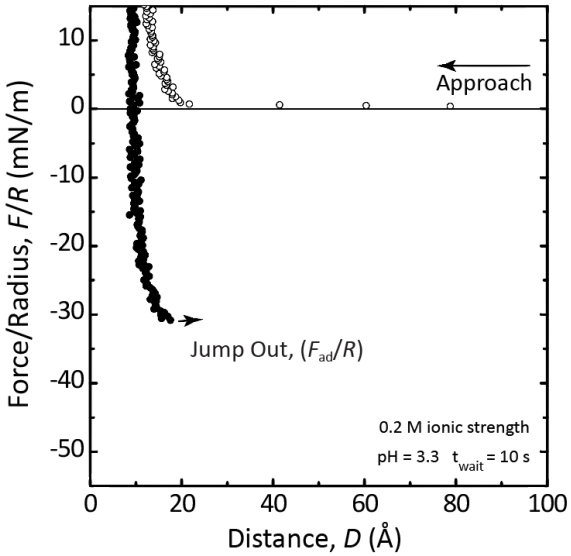

Figure A2.7. Plot of force normalized by the radius of curvature of the surfaces vs. surface separation distance for a compressed film of Tren(KGGG-Cat)$_3$.

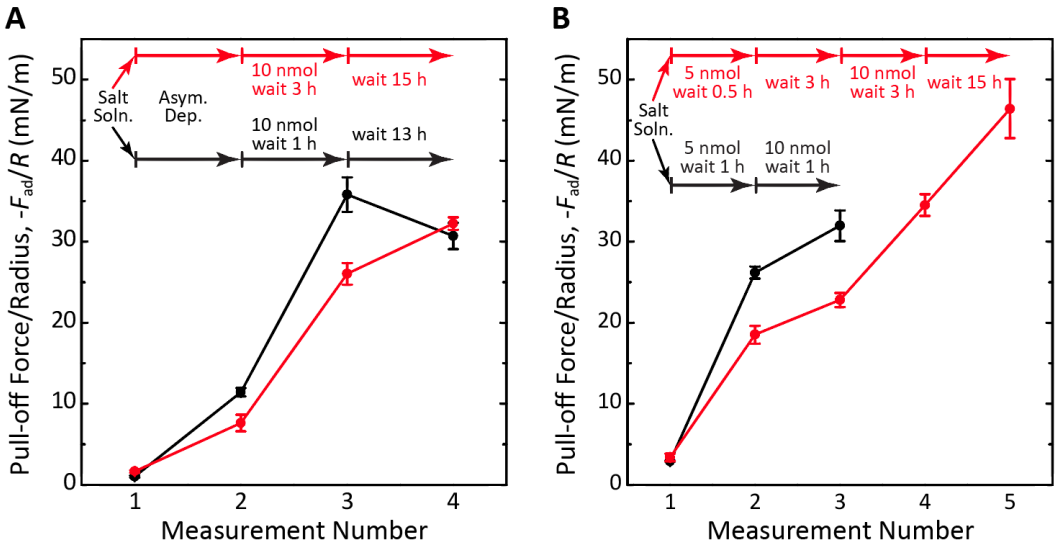

Figure A2.8. Plots of pull-off force for Tren(KGGG-Cat)$_3$. (A) Pull-off force after asymmetric deposition at 300 µM as described in the main text followed by subsequent symmetric depositions and waiting times as indicated. (B) Pull-off force after sequential symmetric depositions and waiting times as indicated. t_{wait} = 10 s for all measurements.

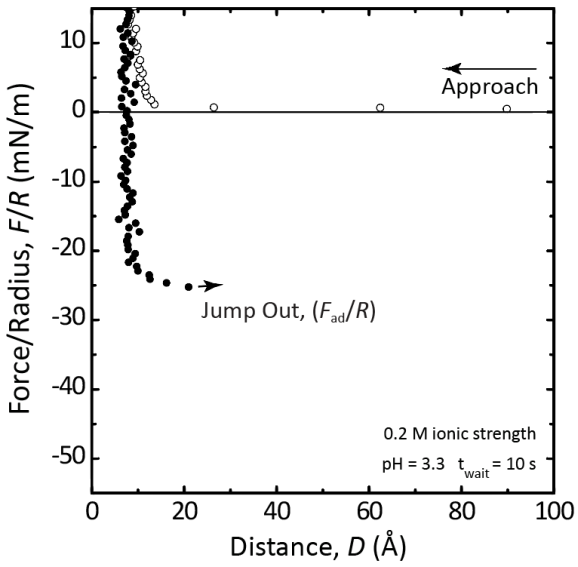

Figure A2.9. Plot of force normalized by the radius of curvature of the surfaces vs. surface separation distance for a compressed film of Tren(KGGGGGG-Cat)$_3$.

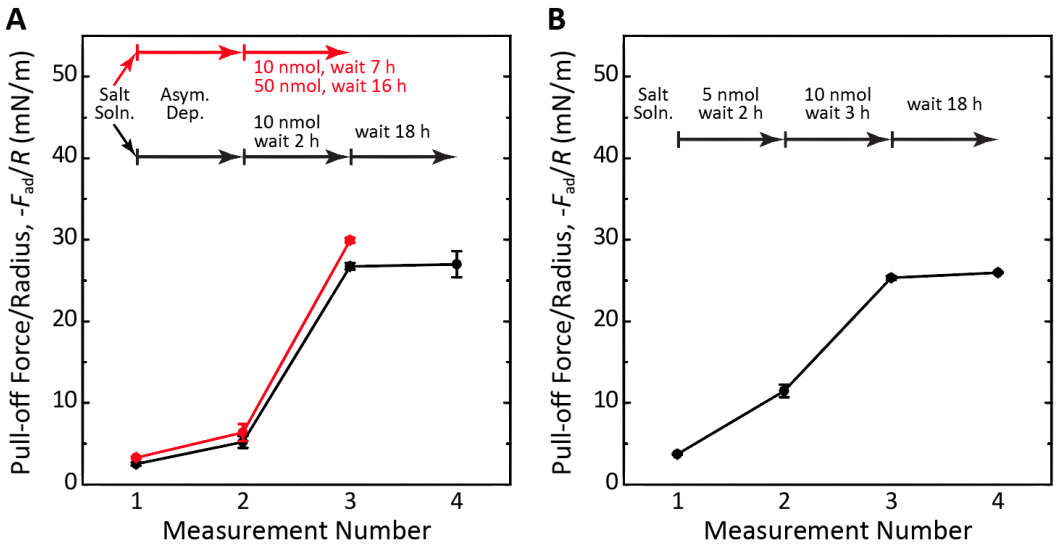

Figure A2.10. Plots of pull-off force for Tren(KGGGGGG-Cat)$_3$. (A) Pull-off force after asymmetric deposition at 300 μM as described in the main text followed by subsequent symmetric depositions and waiting times as indicated. (B) Pull-off force after sequential symmetric depositions and waiting times as indicated. t_{wait} = 10 s for all measurements.

Appendix 3. Supporting AFM Information—Chapter 2

AFM measurements were performed by Eric Valois.

Measurements were taken using BioLever Mini Probes purchased from Asylum Research (f = 130 kHz, k = 0.25 N/m). Prior to imaging, the cantilever was tuned with the thermal tune method. 20 µm X 20 µm images were collected at a scan rate of 0.7 Hz. To prepare surfaces for AFM imaging, 10 µL of salt solution (150 mM KNO_3, 50 mM acetic acid, pH 3.3) with dissolved siderophore analogs was injected onto a freshly cleaved muscovite mica surface. The mica surface was initially molecularly smooth (Figure A3.1). The surface was incubated in a saturated water vapor environment to avoid evaporation. After incubation, the surface was rinsed with three 100 µL injections of salt solution. 50 µL of salt solution was then injected onto the mica prior to imaging. All height profiles are plotted with relative heights (*h*) on the y axis.

Figure A3.2 shows a transition from sparse adsorption after a 1-hour incubation of 4 µM Tren(GGK-Cat)$_3$ to dense adsorption and a relatively smooth film after a 1-hour incubation of 400 µM Tren(GGK-Cat)$_3$. A 24-hour incubation of 400 µM Tren(GGK-Cat)$_3$ resulted in a heterogeneous film with a mixture of smooth regions and large aggregates. Figure A3.3 shows the adsorption of large aggregates after 24- and 48-hour incubations of Tren(GGG-Cat)$_3$. The film after the 48-hour incubation appears much more heterogeneous than the film after the 24-hour incubation, with the largest features (>100nm) not shown in the line height profile. This increasing heterogeneity suggests that adsorbed Tren(GGG-Cat)$_3$ may further aggregate on the surface after adsorption.

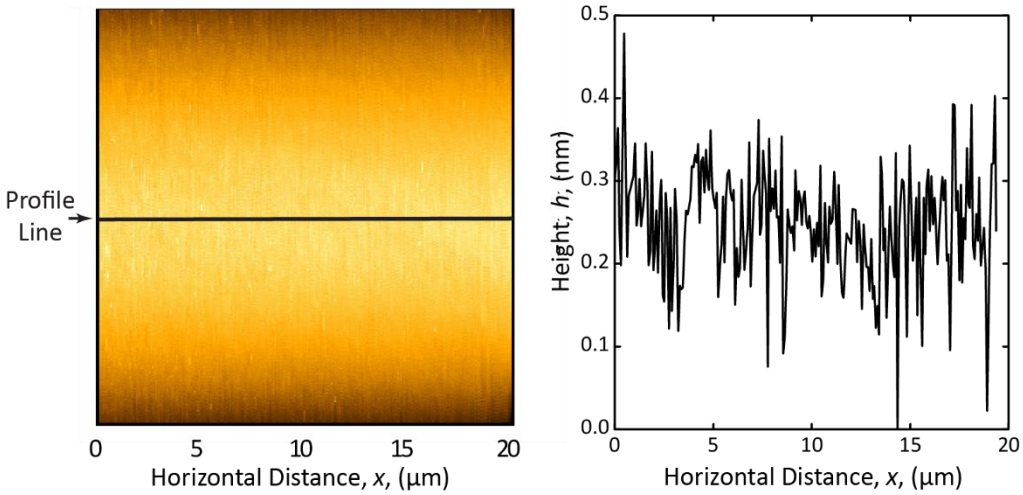

Figure A3.1. AFM image and line height profile of muscovite mica in salt solution.

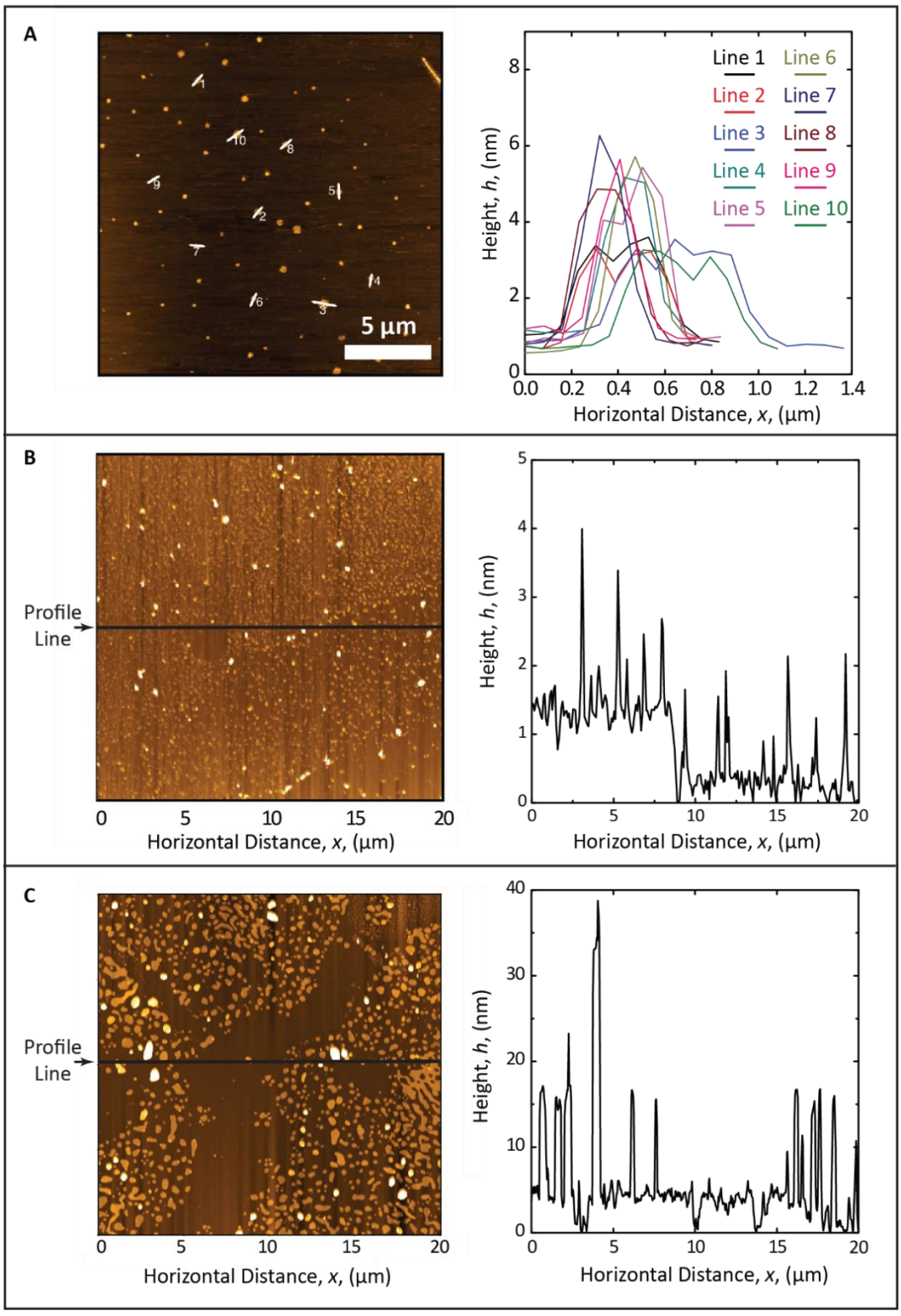

Figure A3.2. AFM image and line height profiles of muscovite mica in salt solution after a (A) 1-hour incubation of 4 µM Tren(GGK-Cat)$_3$ solution, (B) 1-hour incubation of 400 µM Tren(GGK-Cat)$_3$ solution, and (C) 24-hour incubation of 400 µM Tren(GGK-Cat)$_3$ solution.

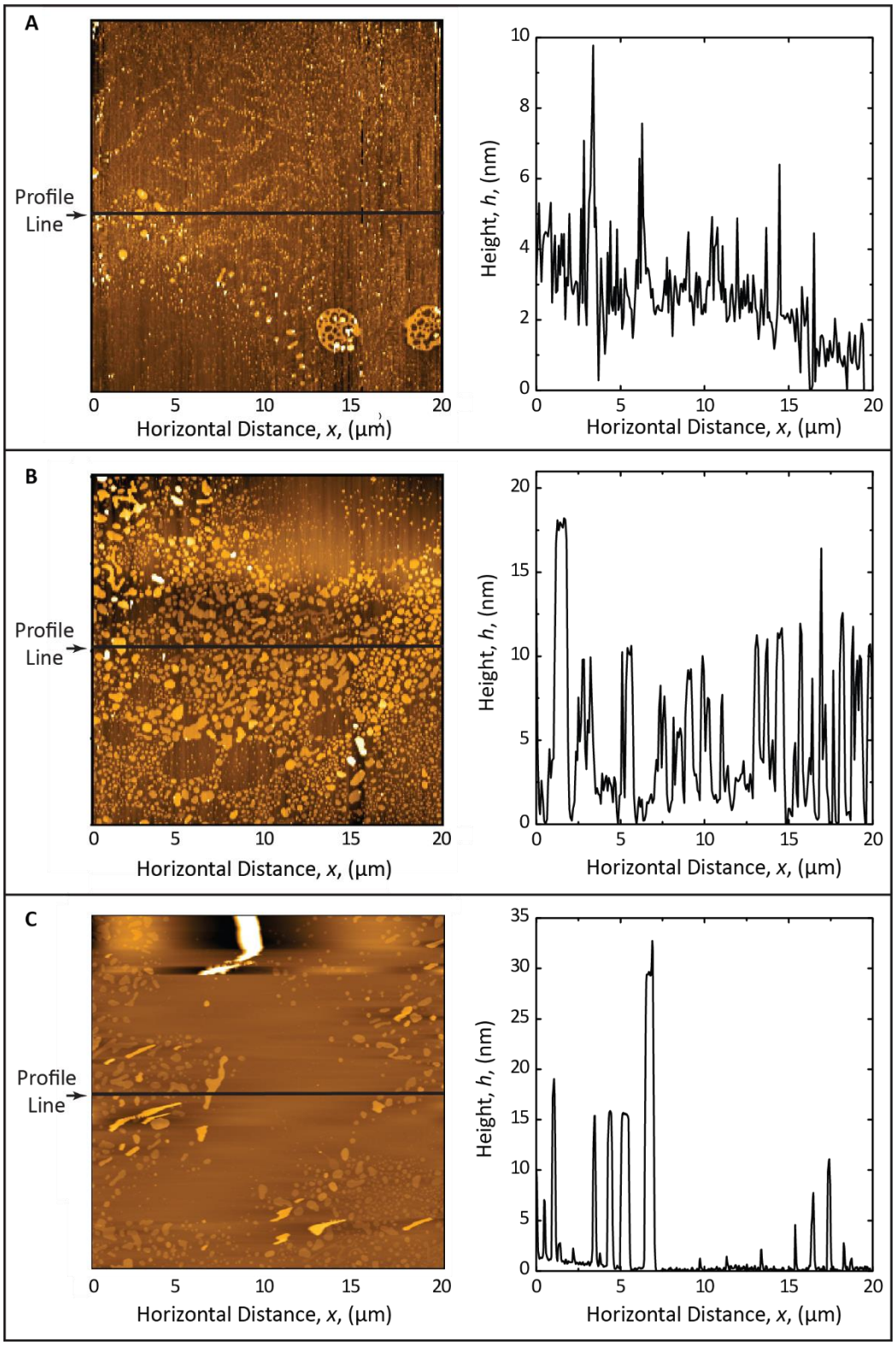

Figure A3.3. AFM image and line height profiles of muscovite mica in salt solution after a (A) 1-hour incubation of 400 µM Tren(GGG-Cat)$_3$ solution, (B) 24-hour incubation of 400 µM Tren(GGG-Cat)$_3$ solution, and (C) 48-hour incubation of 400 µM Tren(GGG-Cat)$_3$ solution.

Appendix 4. Qualitative Siderophore Analog Adsorption Model

Due to the regular spacing of negative charges on the basal plane of mica, cations adsorb at regular locations on the lattice. In aqueous electrolyte solutions, there is a competition between cations for the negatively charged binding sites. With multiple charged species able to adsorb to the mica surface, the fraction of surface covered by each species is determined by the solvent, the charge of cations, and the bare and hydrated radii of the cations, all of which influence the bond distance, bond energy, bond lifetime, and the residence time of cations and small molecules on the surface. Bond lifetimes can vary widely even in systems with the same surface binding energy. For example, adsorbed K^+ is replaced by H^+ in about a minute in water at pH 5.6,[186] yet cationic surfactants remain adsorbed even after substantial rinsing in water.[187] Also, surfactants can take seconds to initially adsorb to substrates, hours to fully adsorb, and days to equilibrate.[188]

We assume that a molecule bound to a substrate detaches due to thermally induced molecular vibrations normal to the substrate (one degree of freedom). This assumption gives a first approximation for the forces acting to detach a molecule adsorbed at a solid-liquid interface in the absence of shear stress from bulk fluid motion, reasoning that has precedent for estimating bond lifetimes.[1] Equating the kinetic energy ($\frac{1}{2} mv^2$) to the thermal energy ($\frac{1}{2} k_B T$ for one degree of freedom) of the molecule, we have $\frac{1}{2} mv^2 = \frac{1}{2} k_B T$ and therefore $v = (k_B T/m)^{\frac{1}{2}}$, where k_B and T are the Boltzmann constant and the temperature, respectively. For a bond length l, the time to traverse one vibration cycle (t_0) is approximately $t_0 = l/v = l/(k_B T/m)^{\frac{1}{2}}$. Following the theory describing bond lifetime developed by George Bell,[43] the average time a molecule with binding energy E will remain bound in the absence of external applied force is $t_0 \exp(E/k_B T) = l \exp(E/k_B T)/(k_B T/m)^{\frac{1}{2}}$. For N types of molecules in solution competing for surface binding sites, where the i^{th} molecule has concentration c_i and average binding time t_i, the fractional surface coverage (f_i) can be calculated: $f_i = t_i c_i / (\Sigma_i t_i c_i)$.

The molecular weight of Tren(GGK-Cat)$_3$, Tren(GKG-Cat)$_3$, and Tren(KGG-Cat)$_3$ is 1285 Da, with a single molecule having mass $m = 2*10^{-24}$ kg. The binding energy of a single coulomb interaction is unclear due to the complex dielectric environment at the mica interface: the dielectric constant of mica[189] (~9) is different from the dielectric constant of water[190] (~80), and the dielectric constant of water at the interface with mica is known to differ from the dielectric constant of bulk water.[191] Calculating the bond length—the distance between the centers of charge—is also difficult due to the varying hydration states of the charged groups, the diffuse charge on the mica lattice, and uncertainty in the height above the mica lattice at which cations adsorb. Nevertheless, assuming that the dielectric constant is equal to the dielectric constant of bulk water, and calculating the distance between the center of the cation and the oxygens in the mica basal plane lattice (~3 Å) using the lattice spacing[192] and an average height of cations adsorbed at the mica surface determined by experiments[193,194] and simulations,[195] Coulomb's law yields a binding energy $E = 2.3\ k_B T = 5.6$ kJ/mol for a potassium ion or the cationic amine of a lysine residue. This calculated value for a single coulombic bond can be taken as a lower limit on the binding energy because it is lower than the electrostatic binding energy of a single charge-charge interaction given by experiments[196] ($E = 4.1\ k_B T = 10$ kJ/mol) and simulations[195] ($E = 12.3\ k_B T = 30.2$ kJ/mol). Using the calculated value for the binding energy of a single charge-charge interaction, the binding energy of a siderophore analog due to electrostatic interactions is $E = 3*2.3\ k_B T = 6.9\ k_B T =$ 16.8 kJ/mol because each siderophore analog has three pendant cationic amines that can bind

to the substrate. For the purposes of this calculation, we assume that the positive charge on the Tren scaffold does not bind to mica due to steric hindrance. To predict the binding energy in our adsorption model, we also exclude other interactions between the siderophore analogs and mica, such as hydrogen bonds involving the catechol functionalities or the peptide backbones of each arm of the siderophore analogs, electrostatic interactions involving the Tren core, and non-specific van der Waals interactions. This exclusion is justified by the experimental results: Tren(GGG-Cat)$_3$ adsorbed via a different mechanism than siderophore analogs with pendant cationic amines (slow adsorption of multilayers rather than rapid adsorption of monolayers), suggesting that catechols do not drive rapid adsorption of siderophore analogs into monolayers on the mica.

At the solution conditions used to deposit siderophore analogs onto mica in this work, 150 mM potassium ions and 0.4 mM siderophore analogs, our model predicts that siderophore analogs with binding energy $E = 6.9\ k_B T$ have a lifetime on the mica surface about 500 times longer than the lifetime of a potassium cation and to occupy 60 percent of the available negatively charged binding sites. Using the coulombic binding energies for a single charge-charge interaction given by the experiments and simulations referenced above, the siderophore analogs are predicted to occupy at least 98 percent of the available binding sites. While it is unlikely that the cationic amines of the siderophore analogs would occupy every binding site on the mica lattice due to the constrained conformation of siderophore analogs that this would require, accounting for a reduced number of maximum possible binding sites does not change the conclusion of the qualitative model: our model predicts that siderophore analogs can adsorb to mica solely via electrostatic interactions between the three pendant cationic amines and the mica surface. This prediction is consistent with the ready adsorption of polycations to mica[197] which are often used to anchor other functionalities to mica, e.g., antibiofouling polymers.[23,198]

Appendix 5. Supporting SFA Information—Chapter 3

Full detail of SFA operation are included elsewhere.[125] For each experiment, two mica sheets (thickness 2-10 μm) were coated with a 50 nm silver layer via thermal evaporation. Each sheet was glued, silver side down, to a cylindrical glass disk with either UV curing glue (Norland OA 81) or an epoxy resin (EPON 1004). Peptides were dissolved at 0.1 mg/ml (0.3 mM) in a salt solution (250 mM KNO_3, 100 mM acetic acid, pH 3). This ionic strength is intermediate between physiological and marine conditions, and the low pH limits Dopa oxidation. To deposit peptides on the surfaces, the surfaces were separated and 30-50 μL peptide solution was injected into a capillary meniscus between the surfaces. The surfaces were incubated in peptide solution for at least 20 min before making force measurements.

To calculate the adhesion energy E_{ad}, the Derjaguin-Muller-Toporov (DMT) theory[68] was used, which gives $E_{\mathrm{ad}} = -F_{\mathrm{ad}}/2\pi R$. This theory was selected over the Johnson-Kendall-Roberts (JKR) theory[97] on the basis of the Tabor Parameter,[130] $\mu = (4R\gamma^2/E^{*2}z_0^3)^{1/3}$, where R is the radius of curvature of the surfaces, γ is the interfacial energy, E^* is the composite modulus of the surfaces, and z_0 is the equilibrium separation distance of the surfaces. Taking E^* = 20 GPa as an approximate modulus of the layered SFA surface[199] and z_0 = 0.3 nm (atomic contact) gives $\mu < 5$. Therefore, the JKR theory is invalid, and we selected the DMT theory to approximate the surface energy, although we note that more complicated treatments of the transition from DMT to JKR are possible.

The adhesion mediated by mfp-3s-pep-Dopa depended on the time in contact and the time since incubation. Figure A5.2A shows force-distance plots for films of mfp-3s-pep-Dopa with different dwell times at maximum compression. After 60 min at maximum compression (t_{dwell} = 60 min), adhesion force increased relative to the adhesion force measured for t_{dwell} = 10 s. We attributed the increase in adhesion force to rearrangement of surface binding groups and an increase in the number of bridging interactions. Rearrangement may increase bridging interactions by increasing the total number of peptide-surface bonds or by balancing the bonds that a single peptide forms with both between surfaces. The increase in adhesion force persists on subsequent adhesion measurements, suggesting irreversible rearrangement of surface binding groups. Further changes in mfp-3s-pep-Dopa adhesion occurred over days. Leaving the surfaces out of contact for 1-2 days resulted in a decrease in the measured adhesion force but no change in film thickness (Figure A5.2B). After the adhesion force decreased, increasing dwell time (t_{dwell} = 60 min) partially restored the adhesion. The decrease in adhesion force may result from rearrangement of adsorbed peptides on each surface, which might increase the number of Dopa residues binding to the surface, thereby making these groups unavailable to bind to the opposite surface upon contact and reducing bridging interactions. Alternatively, auto-oxidation of Dopa residues to dopaquinone would also be expected to decrease adhesion,[54–56] although Dopa oxidation at pH 3 is not expected.

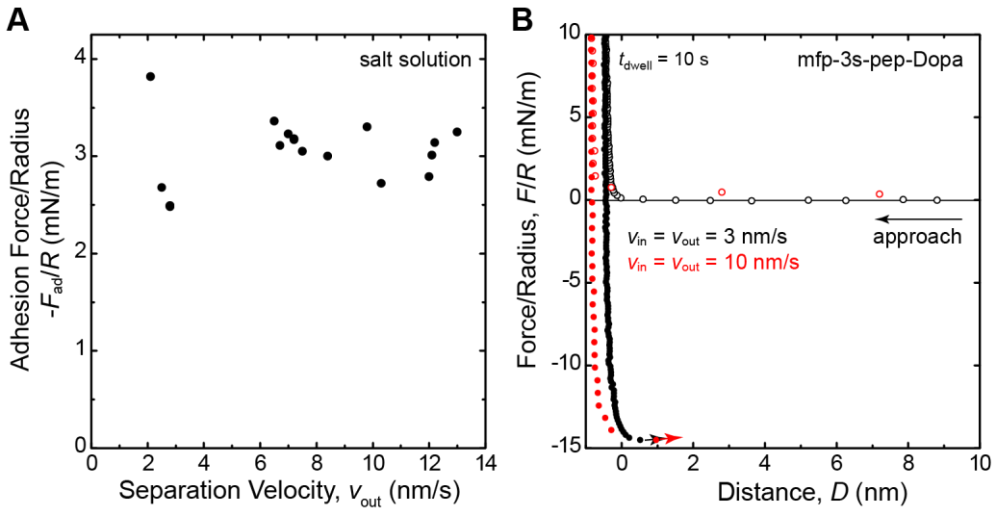

Figure A5.1. Effect of velocity on measured forces. (A) Plot of adhesion force/radius $-F_{ad}/R$ vs. surface separation velocity v_{out} for mica surfaces in salt solution. Adhesion force was independent of retraction velocity, showing that hydrodynamic forces had a negligible contribution on adhesion for the separation velocities used in this work. (B) Plot of force/radius F/R vs. surface separation distance D between mica surfaces for different compression and separation velocities v_{in} and v_{out} after deposition of mfp-3s-pep-Dopa.

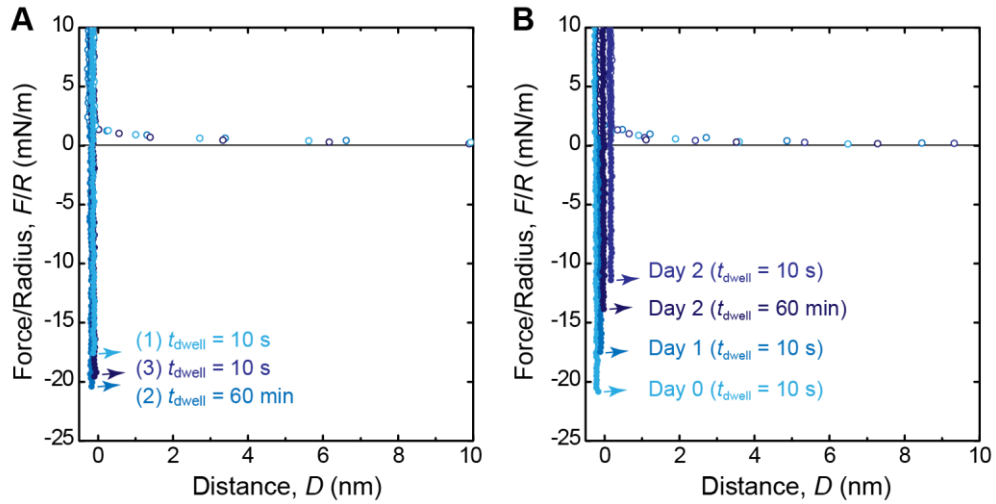

Figure A5.2. (A) Plot of force/radius F/R vs. surface separation distance D for films of mfp-3s-pep-Dopa during 3 consecutive adhesion cycles with the following dwell times at maximum compression: t_{dwell} = 10 s, t_{dwell} = 60 min, t_{dwell} = 10 s. (B) Plot of F/R vs. D for films of mfp-3s-pep-Dopa measured over three days.

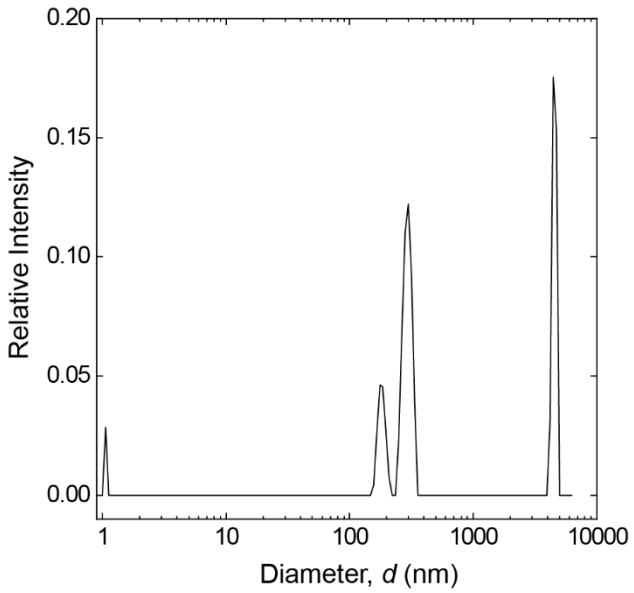

Figure A5.3. Plot of relative intensity vs. particle diameter *d* measured with dynamic light scattering. The peak at 4-5 μm can be attributed to contaminant particles. The peaks at 200-400 nm suggest that the peptide is aggregating in solution.

Appendix 6. Simulation Details—Chapter 3

Simulations were performed by Keila Cunha and Zachary Levine.

To evaluate if biasing the peptides toward the surface could induce a greater number of hydrogen bonds with the surface, we performed simulations pulling the center of mass of each peptide structure (obtained from the most sampled cluster) toward the mica surface. This simulation configuration was intended to emulate the compression of the peptides between mica surfaces that occurred in the SFA experiments, although we note that in an SFA experiment, peptides are compressed between two mica surfaces. We used a simulation box more than 50% larger in volume than in the REMD simulations to decrease the ionic strength of the system and varied the pulling rates (0.01, 0.001, and 0.0001 nm/ps) and simulation times (50, 70, 80, and 100 ns). We evaluated the impact of these parameters on the number of Dopa residues bound to the surface via bidentate interactions. However, we did not observe more than two bidentate bound Dopa residues during the pulling simulations, regardless of the pulling rate and simulation time. The structures obtained after 70 ns of simulations using the slowest pulling rate 0.0001 nm/ps had 2 Dopa residues forming bidentate hydrogen bonds with mica, thus, these simulations were chosen as the initial frames for the next simulations. The stability of the compressed peptides was accessed by 200 ns of simulations using an NVT ensemble. After about 75 ns of simulation of the mfp-3s-pep-Dopa, only one Dopa residue remained bound, and predominantly formed a single hydrogen bond with the mica surface. This hydrogen bond persisted throughout the simulation, indicating a strong and stable interaction (Figure A6.7). No hydrogen bonds between Tyr residues and mica persisted during analogous simulations of mfp-3s-pep-Tyr.

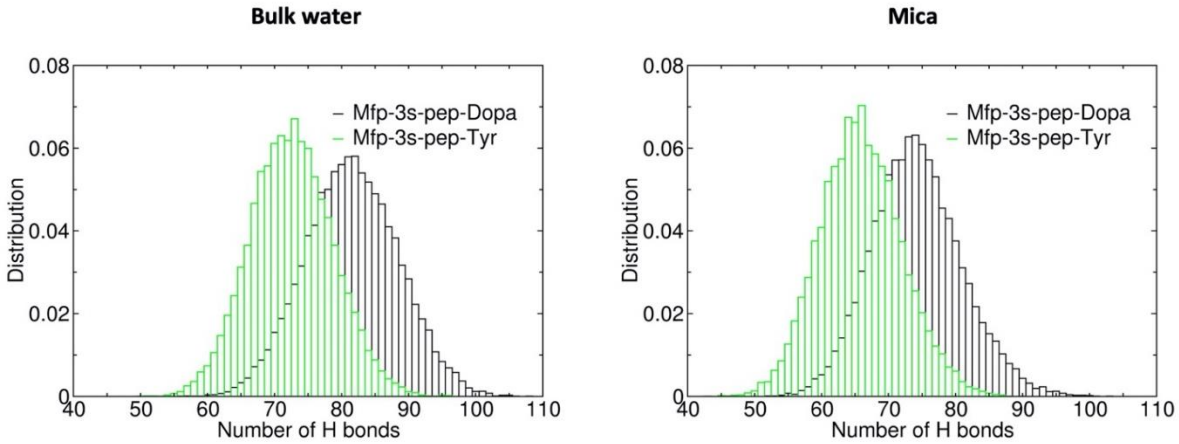

Figure A6.1. Normalized histogram of the number of hydrogen bonds between the peptides and water molecules for: peptides in bulk water (left) and peptides exposed to a mica surface (right). Analyses were done for every 20 ps of the last 300 ns of simulation.

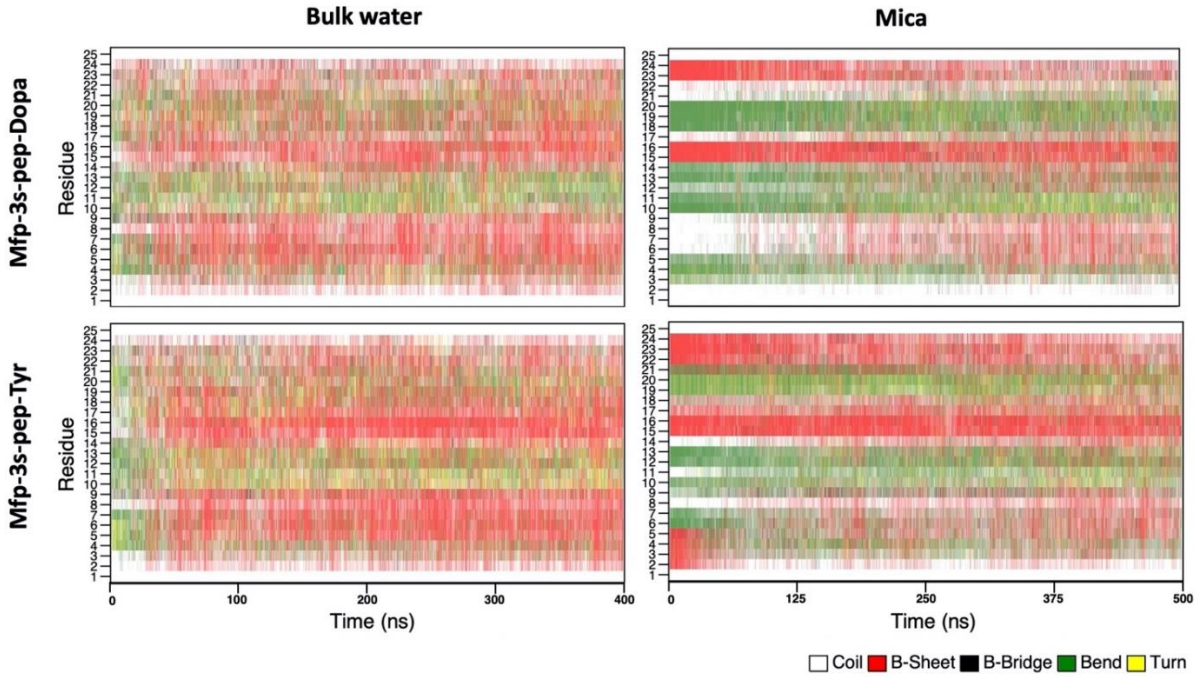

Figure A6.2. Secondary structure content adopted by each residue of the peptides in a bulk water and in the presence of mica surface. Analyses were done for every 20 ps of simulation.

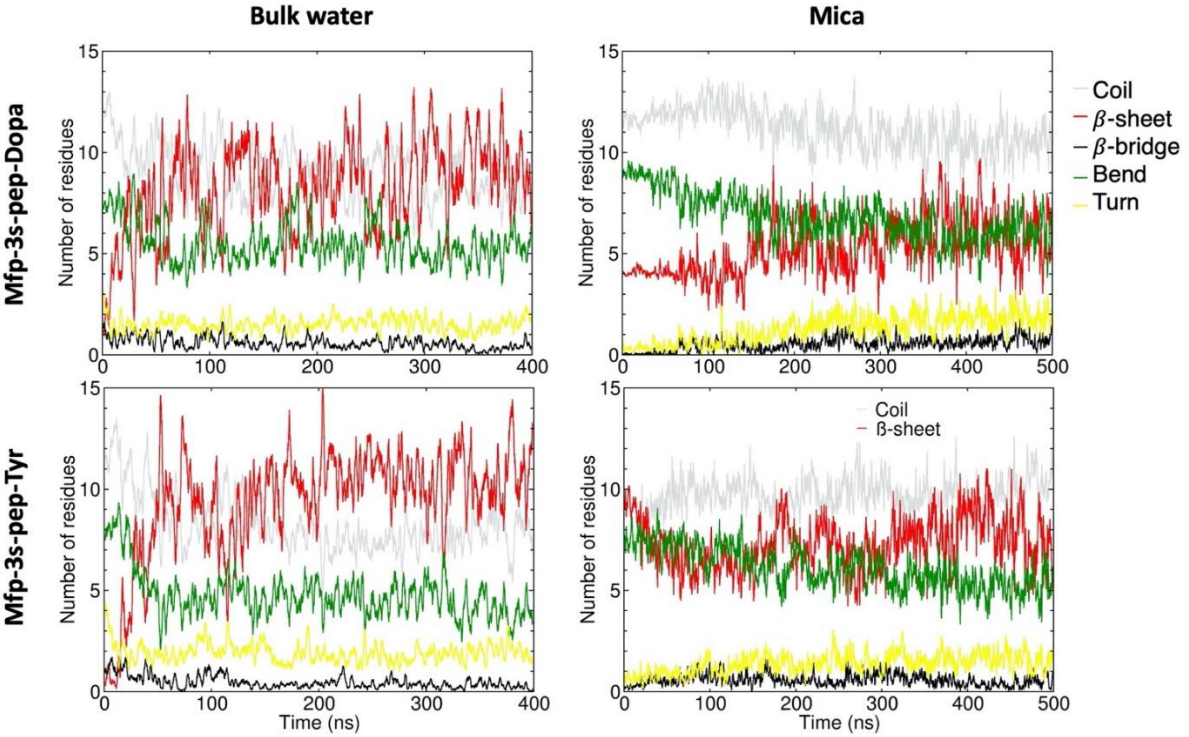

Figure A6.3. Average number of residues adopting a secondary structure along the simulation time. Analyses were done for every 20 ps of simulation and the average calculated by every 100 points.

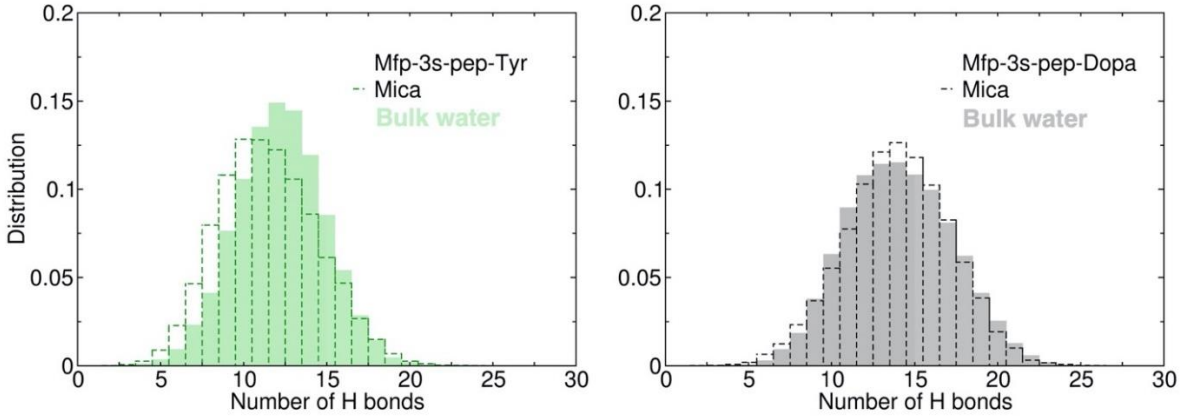

Figure A6.4. Normalized histogram of total number of intramolecular hydrogen bonds for peptides in bulk water (solid lines) and exposed to a mica surface (dash lines) for mfp-3s-pep-Tyr (left) and mfp-3s-pep-Dopa (right). Analyses were done for every 20 ps of the last 300 ns of simulation.

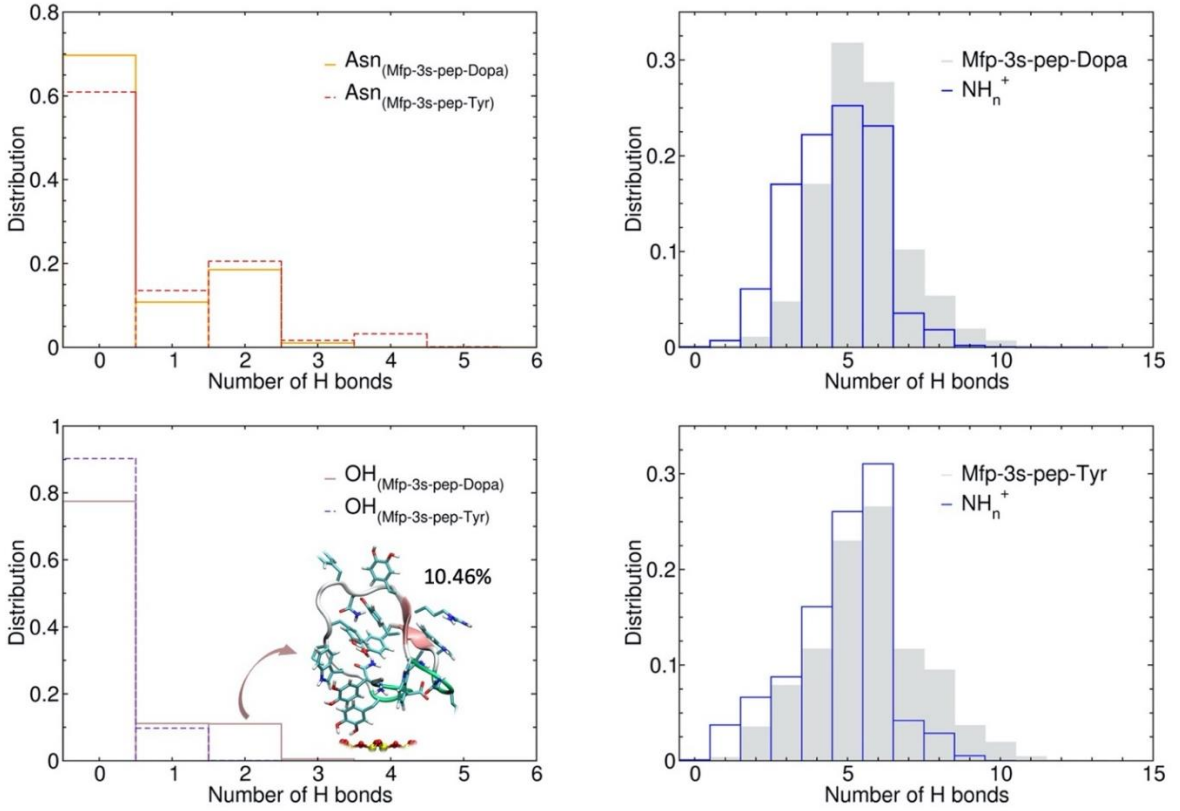

Figure A6.5. Normalized histograms of the number of hydrogen bonds between: the mica surface and the asparagine residues (top left); the mica surface and the hydroxyls from Dopa or Tyr residues (bottom left). On the right: Histograms of the total number of hydrogen bonds between the surface and each peptide (solid gray); and between the surface and the positively charged amines from each peptide (open blue bars). Analyses were done for every 20 ps of the last 300 ns of simulation.

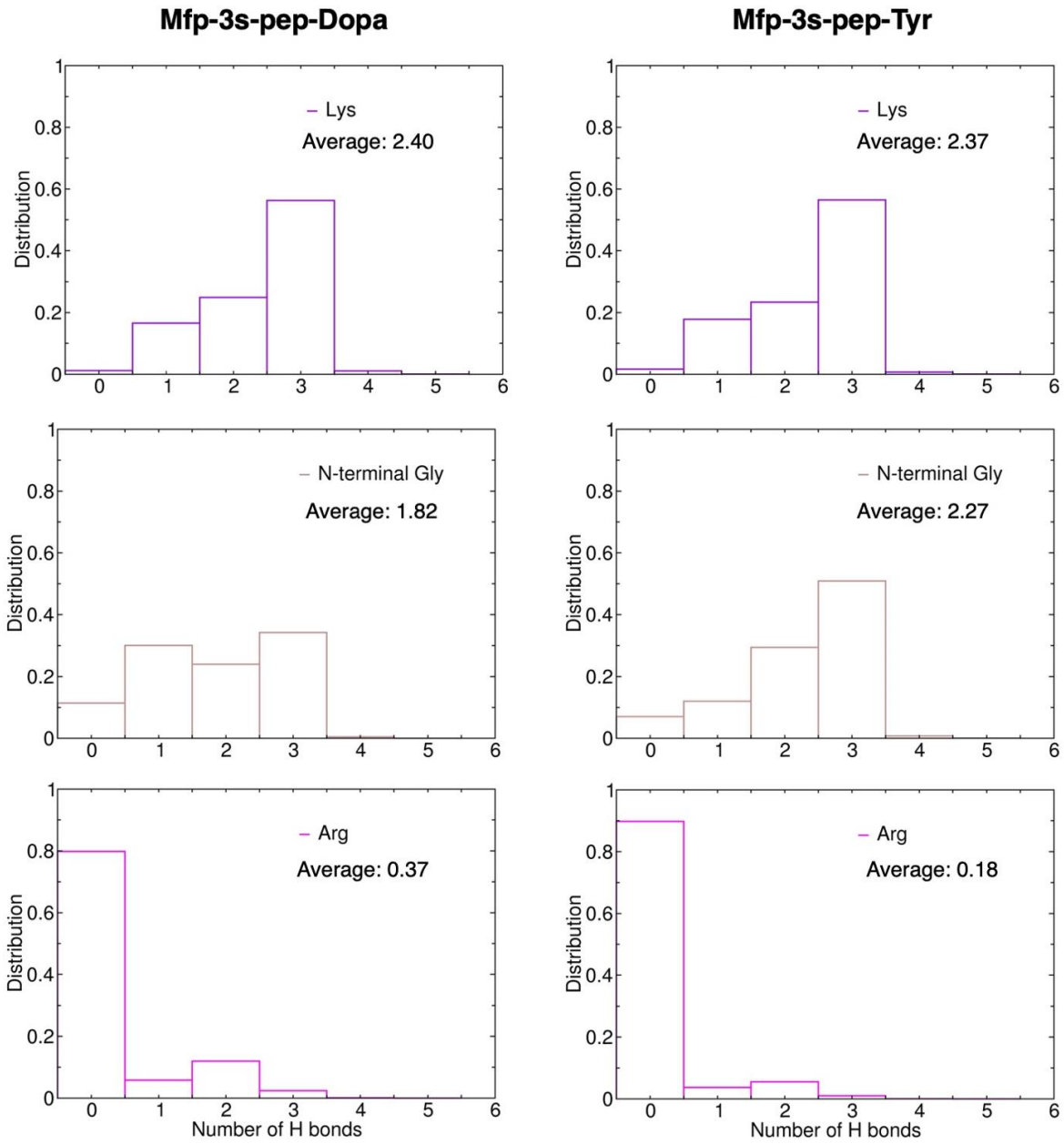

Figure A6.6. Normalized histogram of the number of hydrogen bonds between the mica surface and each positively charged sidechain for: mfp-3s-pep-Dopa (left) and mfp-3s-pep-Tyr (right). Analyses were done for every 20 ps of the last 300 ns of simulation.

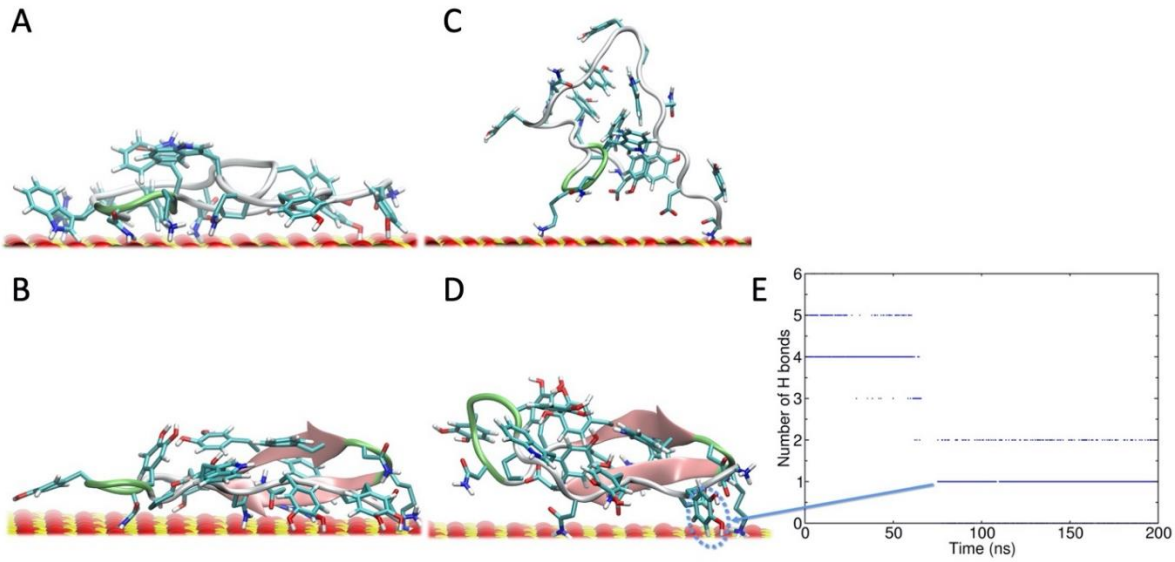

Figure A6.7. Snapshots of (A) mfp-3s-pep-Tyr and (B) mfp-3s-pep-Dopa after 70 ns of simulation pulling the center of mass of the peptides towards a mica surface at a rate of 0.0001 nm/ps. From the final structures obtained in the pulling simulations, we performed 200 ns of NVT simulation. The final snapshots obtained are represented for (C) mfp-3s-pep-Tyr and (D) mfp-3s-pep-Dopa. (E) Time evaluation of the number of hydrogen bonds between mica and the hydroxyls of Dopa. This analysis was done for the 200 ns of the NVT simulation.

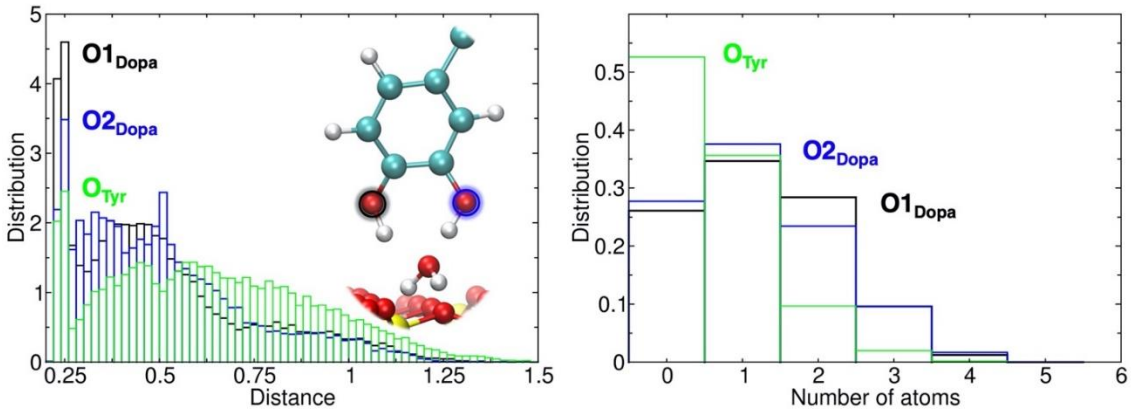

Figure A6.8. Normalized histogram of the minimum distance between the mica surface and the oxygens from the Dopa or Tyr hydroxyls (left). On the right: normalized histogram of number of contacts between mica and the Dopa or Tyr oxygens, considering a distance up to 3Å. Analyses were done for every 20 ps of the last 300 ns of simulation.

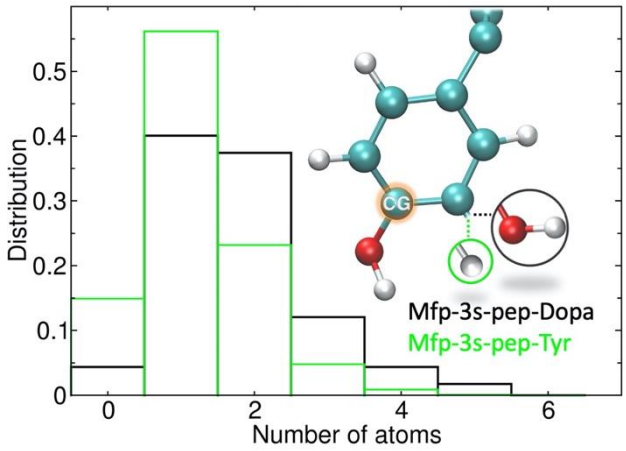

Figure A6.9. Normalized histogram of number of Dopa or Tyr residues in proximity to the surface. For these analyses we counted the number of CG atoms (shown in the cartoon representation) near the mica surface, considering cutoff distance of 5 Å. Analyses were done for every 20 ps of the last 300 ns of simulation.

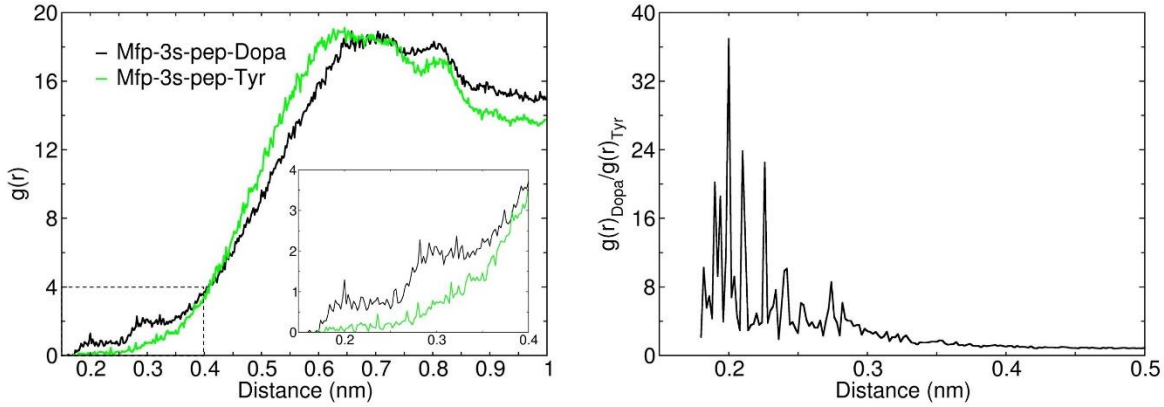

Figure A6.10. Radial distribution function between the Dopa or Tyr sidechains and the NH_3^+ groups from the Lys and the N-terminal Gly for peptides exposed to a mica surface. The second panel shows the radial distribution function for Dopa divided by the radial distribution function for tyrosine. The plots show that it is significantly more likely to find Dopa within 3 Å of a positively charged group than to find tyrosine. Analyses were done for every 20 ps of the last 300 ns of simulation.

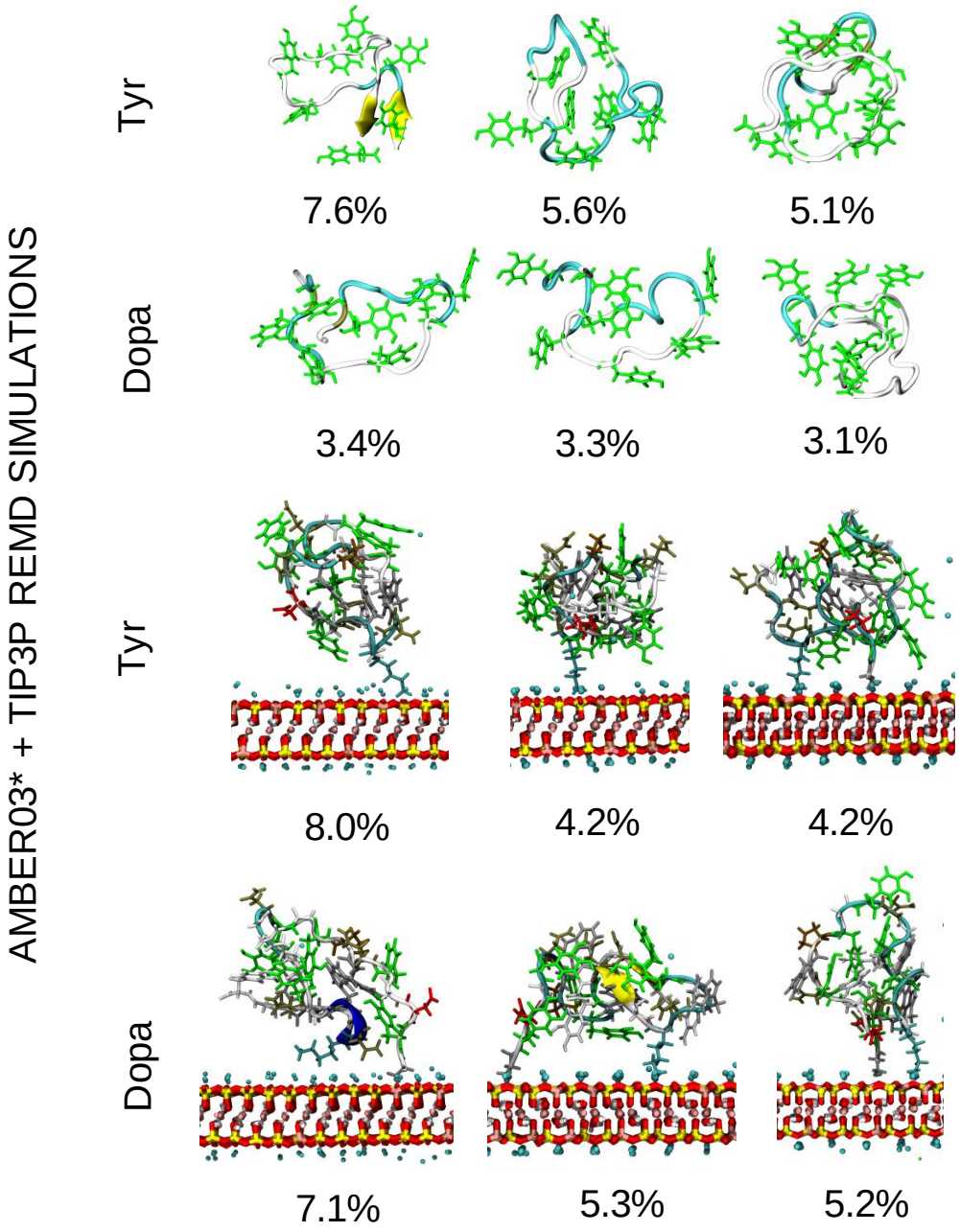

Figure A6.11. Representative peptide conformations from duplicated REMD simulations using the AMBER03* + TIP3P force field show qualitatively similar eigenstates to REMD simulations under the GROMOS53a6 force field. However, bulk conformations tend to remain more disordered compared to GROMOS conformations, which can favor sampling transient b-strands. Green residues correspond to either Tyr or Dopa, while red and cyan residues correspond to negatively- or positively-charged amino acids, respectively.

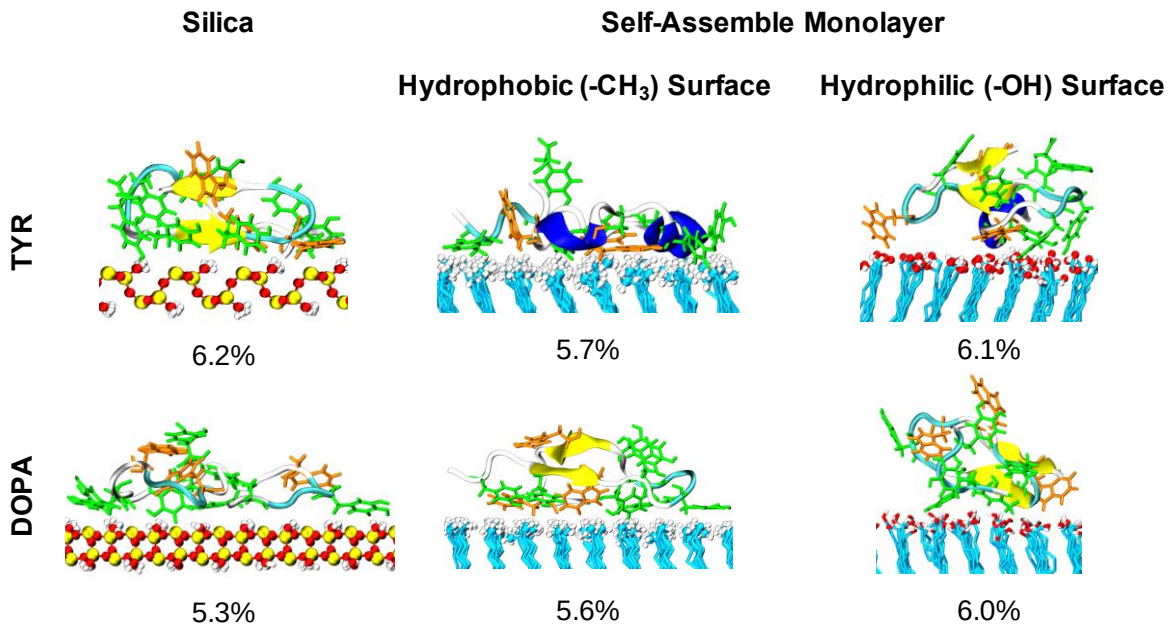

Figure A6.12. The most dominant peptide eigenstates from AMBER03* REMD simulations on the surface of related inorganic (silica) and organic (SAM) surfaces reveal that surface chemistry plays a central role in dictating the secondary structures of adsorbed peptides. While Dopa-containing peptides differ slightly in structure from Tyr-containing peptides, the choice of surface appears to be key in determining how peptides adhere. On hydrophilic silica (l*eft*) or SAM (*right*) surfaces, peptides remain largely globular, as we observe in solution. (Dopa-containing peptides on silica do, however, show more extended structures versus Tyr-containing peptides.) However, peptides are heavily splayed on the surface of hydrophobic SAMs. While this was observed previously for Dopa-containing peptides on SAMs,[61] the current study shows similar conformations for mfp-3s-pep-Tyr as well, thereby supporting the hypothesis that surface chemistry is key in dictating the conformations of mussel-inspired peptides. Conformations of Dopa-containing peptides on SAM surfaces were adapted from our prior study[61] and are printed here with permission. Copyright 2016 National Academy of Sciences.

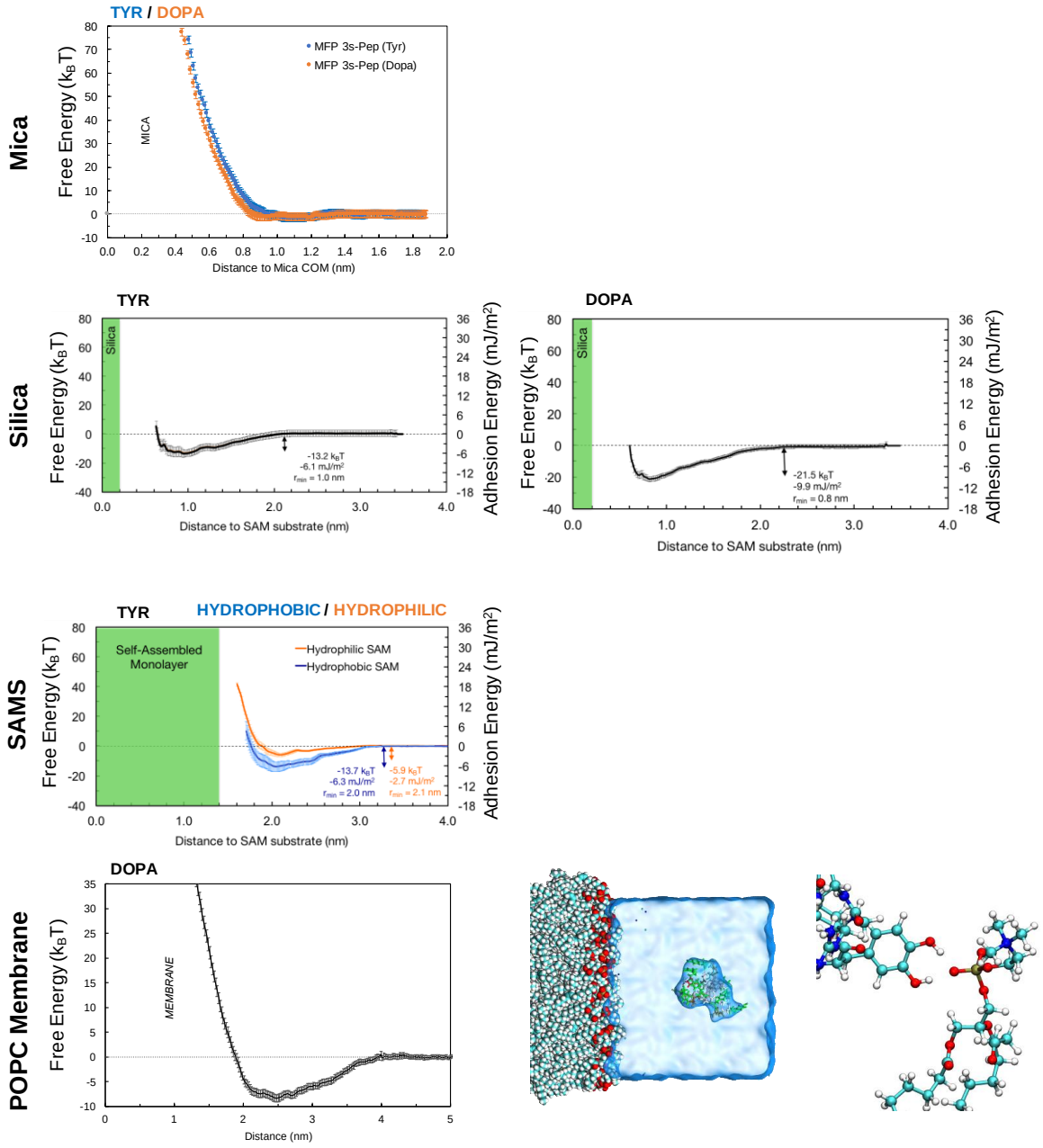

Figure A6.13. Potentials of mean force derived from AMBER03* umbrella sampling simulations reveal that while peptide adhesion to mica is relatively weak in simulations (*top*), the presence of Dopa versus tyrosine has a marked effect on adhesion to multiple organic and inorganic surfaces. On inorganic silica (*second row*), Dopa-containing peptides are 50% more adhesive than Tyr-containing peptides. On hydrophilic organic self-assembled monolayers (SAMs) (*third row*), mfp-3s-pep-Tyr shows the same adhesion as was previously reported for mfp-3s-pep-Dopa,[61] whereas on hydrophobic SAMs, the previously reported adhesion of mfp-3s-pep-Dopa[61] exceeds the adhesion of mfp-3s-pep-Tyr measured here by 250%. Interestingly, mfp-3s-pep-Dopa can also bind to lipid (POPC) membranes (*fourth row*) with adhesion between the values reported for hydrophobic and hydrophilic SAMs.[61] Adhesion to the lipid membrane appears due, in part, to coordinated hydrogen bonding of Dopa hydroxyls to phosphates.

Appendix 7. SFA Supporting Information—Chapter 4

Surface Preparation

Optical grade ruby muscovite mica (S & J Trading, Inc.) was cleaved to thickness 3-8 μm. Thermal evaporation was used to deposit a layer of silver of thickness 50 nm on one side of the mica. The silver-coated mica was then glued, mica side up, on a cylindrical glass disks with an epoxy resin (EPON 1004F, Miller-Stephenson). Established procedures[126] were followed to avoid particle contamination of the surfaces. A polymer film was established on the mica surface via drop casting. Each polymer was dissolved in 95% (v/v) ethanol in deionized water, here called ethanol solution. The mica surfaces were removed from the SFA, and 20 μL of the polymer solution was deposited onto either one of the two mica surfaces (asymmetric deposition) or both mica surfaces (symmetric deposition). Symmetric deposition was conducted with a polymer concentration of 0.5 mg/ml. Asymmetric deposition was conducted at polymer concentrations ranging from 10-0.02 mg/ml. The deposited solution was left to evaporate for at least 15 min. The surfaces were then rinsed with 2 mL ethanol solution and then placed in a surface forces apparatus (SFA) in crossed cylinder orientation. Approximately 50 μL of ethanol solution was injected between the surfaces. A portion of the injected solution remained trapped in a capillary meniscus between the surfaces. Due to the relatively low surface tension of the ethanol solution, the exact volume of solution remaining between the cylindrical surfaces was not known but was estimated to be 10-20 μL. Several mL of ethanol solution was placed in the bottom of the SFA chamber. The SFA chamber was sealed, allowing the vapor in the chamber to equilibrate with the liquid ethanol solution. Throughout the course of the experiments, the liquid between the surfaces did not appear to evaporate.

Measurement of Surface Separation Distance

The distance between the mica surfaces was measured as follows. Optical interference between the silver layer on each mica surface creates fringes of equal chromatic order. When the mica surfaces contact each other directly, the nth order fringe has wavelength λ_n. When the surfaces are separated to a distance D, the wavelength of the nth order fringe shifts to λ_D. D can be calculated from λ_D as follows:

$$\tan\left(\frac{2\pi\mu_{etOH}D}{\lambda_D}\right) = \frac{2\bar{\mu}\sin\left(\pi\left(1-\frac{\lambda_n}{\lambda_D}\right)\left(1-\frac{\mu_{n-1}\lambda_n}{\mu_n\lambda_{n-1}}\right)^{-1}\right)}{(1+\bar{\mu}^2)\cos\left(\pi\left(1-\frac{\lambda_n}{\lambda_D}\right)\left(1-\frac{\mu_{n-1}\lambda_n}{\mu_n\lambda_{n-1}}\right)^{-1}\right)\pm(\bar{\mu}^2-1)} \quad \text{(A7.1)}$$

with + and – corresponding to odd and even n, respectively. Here, μ_{etOH} is the refractive index of the ethanol solution between the mica surfaces, calculated at λ_D. λ_n and λ_{n-1} are the wavelengths of the fringes of order n and n-1, respectively, measured with the surfaces in contact in air. μ_n and μ_{n-1} are the refractive indices of the mica at wavelengths λ_n and λ_{n-1}, respectively. $\bar{\mu} = \mu_D/\mu_{etOH}$ where μ_D is the refractive index of mica measured at λ_D. To account for the birefringence of mica, the mica refractive index is reported as the average of the β and γ components of the mica refractive index. The refractive indices of mica, ethanol, and water depend on the wavelength, and are calculated with the Cauchy dispersion formula,

$$\mu = A + B\,\lambda^{-2} + C\,\lambda^{-4} \quad \text{(A7.2)}$$

where constants A, C, and C are taken from the literature for ruby muscovite mica,[200] ethanol,[201] and water.[202] The dispersive refractive index of pure ethanol was used as an estimate for the refractive index of the ethanol solution, since the refractive index of pure

ethanol is within 0.2% of the refractive index of 95% ethanol in water.[203] For mica, only the leading two terms of the Cauchy formula were used. Since mica is a natural product, the refractive index is expected to vary, but the shape of the dispersion curve is similar.[128] As the surfaces are separated, the nth order interference fringe eventually moves out of the field of view of the video camera. At this time, the fringe of order $n + 1$ can be used to calculate the surface separation distance, where λ_D in Equation A7.1 is the wavelength of the $n + 1$ fringe at separation distance D, and λ_n, λ_{n-1}, μ_n, and μ_{n-1}, are replaced by λ_{n+1}, λ_n, μ_{n+1}, and μ_n. The value of λ_{n+1} can be calculated from the following equation:

$$\lambda_m = \frac{\mu_m}{\mu_n} \frac{\lambda_n}{1-(n-m)(1-\frac{\mu_{n-1}\lambda_n}{\mu_n\lambda_{n-1}})} \tag{A7.3}$$

where m is an arbitrary fringe order. Since μ_m is calculated from λ_m, an approximate value of λ_m can be first calculated by neglecting dispersion:

$$\lambda_m = \frac{\lambda_n}{1-(n-m)(1-\frac{\lambda_n}{\lambda_{n-1}})} \tag{A7.4}$$

This approximate value of λ_m can then be used to calculate μ_m via Equation A7.2, which can then be used to calculate λ_m in Equation A7.3.

Force Measurement

Full details of SFA operation are described by Israelachvili et al.[125] During adhesion cycles, the approach and separation velocities were measured with the surfaces out of contact, where the separation distance varies linearly with time. Extrapolating this velocity yields an expected surface separation distance, D_0. As the surfaces contact each other, the measured separation distance D differs from D_0, indicating deflection of the spring, $\Delta x = D - D_0$. The normal force F between the surfaces was calculated from the deflection via Hooke's law, $F = k\Delta x$. Measured forces were normalized by the average radius of curvature R of the cylindrical surfaces, the geometric mean of the radii of curvature of each cylinder.

The largest tensile force measured during separation of the surfaces was denoted the adhesion force, F_{ad}/R. To calculate the adhesion energy E_{ad}, the Johnson-Kendall-Roberts (JKR) theory[97] was used. This theory was selected on the basis of the Tabor Parameter,[130] $\mu = (4R\gamma^2/E^{*2}z_0^3)^{1/3}$, where R is the average radius of curvature of the surfaces, γ is the interfacial energy, E^* is the composite modulus of the surfaces, and z_0 is the equilibrium separation distance of the surfaces. Taking $E^* = 20$ GPa as an approximate modulus of the layered SFA surface[199] and $z_0 = 0.2$ nm (atomic contact) gives $\mu > 5$ for adhesion measured in water. The adhesion measured in 95% ethanol yielded $\mu < 5$, but for simplicity, and given the estimations of E^* and z_0, we use the JKR theory to approximate E_{ad} for asymmetric polymer films in ethanol solution as well. We did not calculate the adhesion energy for symmetric polymer films in ethanol because the long-range interactions violate the JKR assumption of short-range interactions.

The JKR theory gives the work of adhesion

$$W = -\frac{2F_{ad}}{3\pi R} \tag{A7.5}$$

the contact radius at zero load

$$a_0 = \left(\frac{9\pi R^2 W}{2E^*}\right)^{1/3} \tag{A7.6}$$

and the total energy at zero load

$$E_0 = -0.6\pi {a_0}^2 W = \left(\frac{72}{125}\frac{{F_{ad}}^5}{RE^{*2}}\right)^{1/3} \tag{A7.7}$$

where the contact modulus E^* is estimated as 20 GPa for the layered mica-glue-glass surfaces[199] and R = 2 cm is the radius of curvature of the glass disks. Comparing E_0 to the effective separation work shows the extent to which cohesive dissipation increases the efficacy of these polymeric adhesives.

To estimate the elastic modulus E of the films, consider an isotropic linear elastic film compressed between crossed cylinders, where the axis of the upper cylinder is aligned with the x_1-axis, the axis of the lower cylinder is aligned with the x_2-axis, and direction normal to the plane of the film at the contact point is aligned with the x_3-axis. The film thickness is the mica separation distance at zero force D_0 and the radius of each cylinder is R. We assume that $D_0 << R$. At mechanical equilibrium, the strain in the film is

$$\varepsilon_{ij} = \frac{1}{2}\left(\frac{\partial u_i}{\partial x_j} + \frac{\partial u_j}{\partial x_i}\right) = \frac{1+\nu}{E}\sigma_{ij} - \frac{\nu}{E}\sigma_{kk}\delta_{ij} \tag{A7.8}$$

where x_i is the location of a point within the film, u_i is the displacement of that point, E is the elastic modulus, ν is the Poisson's ratio, and δ is the Kronecker delta. The films were described as a Winkler foundation,[97] where lateral stress in the film is ignored ($\sigma_{11} = \sigma_{22} = 0$), and the contact is assumed to be frictionless. These assumptions yield the following expression for stress in the film

$$\sigma_{33} = P = E\frac{\partial u_3}{\partial x_3} \tag{A7.9}$$

The normal strain in the film can be written as

$$\frac{\partial u_3}{\partial x_3} = \frac{D_0 - D}{D_0} \tag{A7.10}$$

where D_0 is the film thickness at zero force and D is the compressed film thickness. The pressure can therefore be written as

$$P = \frac{E}{D_0}(D_0 - D) = E(1 - D/D_0) \tag{A7.11}$$

This expression gives the pressure at F = 10 mN/m

$$P_{10} = E(1 - D_{10}/D_0) \tag{A7.12}$$

and the pressure at F = 100 mN/m

$$P_{100} = E(1 - D_{100}/D_0) \tag{A7.13}$$

Dividing P_{10} by P_{100} gives

$$\frac{P_{10}}{P_{100}} = \frac{D_0 - D_{10}}{D_0 - D_{100}} \tag{A7.14}$$

which can be rearranged as:

$$D_0 = \frac{P_{100}D_{10} - P_{10}D_{100}}{P_{100} - P_{10}} \tag{A7.15}$$

dividing by D_{100} and inverting gives

$$\frac{D_{100}}{D_0} = \frac{P_{100} - P_{10}}{P_{100}(D_{10}/D_{100}) - P_{10}} \tag{A7.16}$$

To calculate E, the expression for P_{100} can be rearranged as

$$E = \frac{P_{100}}{1 - D_{100}/D_0} \tag{A7.17}$$

Replacing D_{100}/D_0 with the expression above yields

$$E = P_{100}\left(1 - \frac{P_{100} - P_{10}}{P_{100}(D_{10}/D_{100}) - P_{10}}\right)^{-1} \tag{A7.18}$$

This expression can be simplified as

$$E = \frac{D_{10}P_{100} - P_{10}D_{100}}{D_{10} - D_{100}} = \frac{P_{100}(D_{10}/D_{100}) - P_{10}}{(D_{10}/D_{100}) - 1} \tag{A7.19}$$

Taking the slope of the data shown in Figure A7.3A yields D_{10}/D_{100} = 1.48. The Hertz theory of contact mechanics was used to calculate the pressure at the center of the contact area:

$$P = \left(\frac{6E^{*2}}{\pi^3 R}\frac{F}{R}\right)^{1/3} \quad \text{(A7.20)}$$

This expression was used to approximate the pressures for F/R = 10 and 100 mN/m, P_{10} and P_{100}, respectively. Having calculated D_{10}/D_{100}, P_{10}, and P_{100}, Equation A7.19 yields E = 23 MPa. We note that this value likely underestimates the true value of the modulus due to polymer chain restructuring and plastic deformation of the films.

Control SFA Experiments: Bare Mica in Ethanol Solution and Water

Adhesion measurements of bare mica surfaces in ethanol solution yielded moderate adhesion force/radius ($-F_{ad}/R$ = 9.7 ± 0.6 mN/m) and negligible separation between the surfaces (D_{100} = -0.1 ± 1 nm) in the first hour after addition of ethanol solution (Figure A7.1). This adhesion is lower than the previously reported adhesion between mica surfaces in pure ethanol ($-F_{ad}/R$ > 40 mN/m)[204] and deionized water ($-F_{ad}/R$ = 20–40 mN/m).[205–207] 4 h after addition of ethanol solution, the adhesion decreased to 8.2 ± 0.5 mN/m, and after 24 h decreased further to 6.5 ± 0.4 mN/m. These decreases in adhesion were likely due to dissolution of the epoxy resin and contamination of the mica surfaces.[204] Based on these results, measurements of the polymer films were conducted in the first several hours after addition of ethanol solution. Over this period, no changes in the measured forces or film thicknesses were observed, suggesting that surface contamination due to glue dissolution did not impact the results. Adhesion measurements of bare mica surfaces in water yielded adhesion force $-F_{ad}/R$ = 69 ± 8 mN/m and film thickness 7 ± 6 nm. The adhesion measured between mica surfaces exceeds previously reported adhesion in water, possibly due to acidification of the capillary meniscus, which would be expected to yield more hydronium ions populating the mica surfaces rather than potassium ions and reduced hydration repulsion.

Solvent	Deposition Mode (Concentration)	Polymer Type	Film Thickness D_{100} (nm)	Adhesion Force $-F_{ad}/R$ (mN/m)	Adhesion Energy $E_{ad} = -F_{ad}/1.5\pi R$ (mJ/m^2)
95% EtOH 5% Water	Bare Mica	-	-0.1 ± 1	9.7 ± 0.6	2.1 ± 0.1
	Symmetric (0.5 mg/ml)	DA-Lys	17 ± 2	6.0 ± 1.5	-
		DAc-ABA	26 ± 13	7 ± 5	-
		Lys-PEA	6.7 ± 1.7	4.4 ± 1.0	-
	Asymmetric (0.02 mg/ml)	DA-Lys	3 ± 3	5.9 ± 1.9	1.3 ± 0.4
		DAc-ABA	1.3 ± 2.7	9 ± 4	2.0 ± 0.8
		Lys-PEA	0.4 ± 0.6	4.0 ± 0.5	0.9 ± 0.1
Water	Bare Mica	-	7 ± 6	69 ± 8	15 ± 2
	Symmetric (0.5 mg/ml)	DA-Lys	33 ± 10	420 ± 140	90 ± 30
		DAc-ABA	28 ± 9	520 ± 350	110 ± 70
		Lys-PEA	23 ± 9	340 ± 180	70 ± 40
	Asymmetric (0.5 mg/ml)	DA-Lys	22 ± 5	280 ± 80	60 ± 20
		DAc-ABA	19 ± 6	170 ± 150	40 ± 30
		Lys-PEA	15 ± 6	120 ± 110	30 ± 20

Table A7.1. Film thickness at 100 mN/m of compression D_{100}, adhesion force/radius $-F_{ad}/R$, and adhesion energy E_{ad} calculated from the JKR theory.

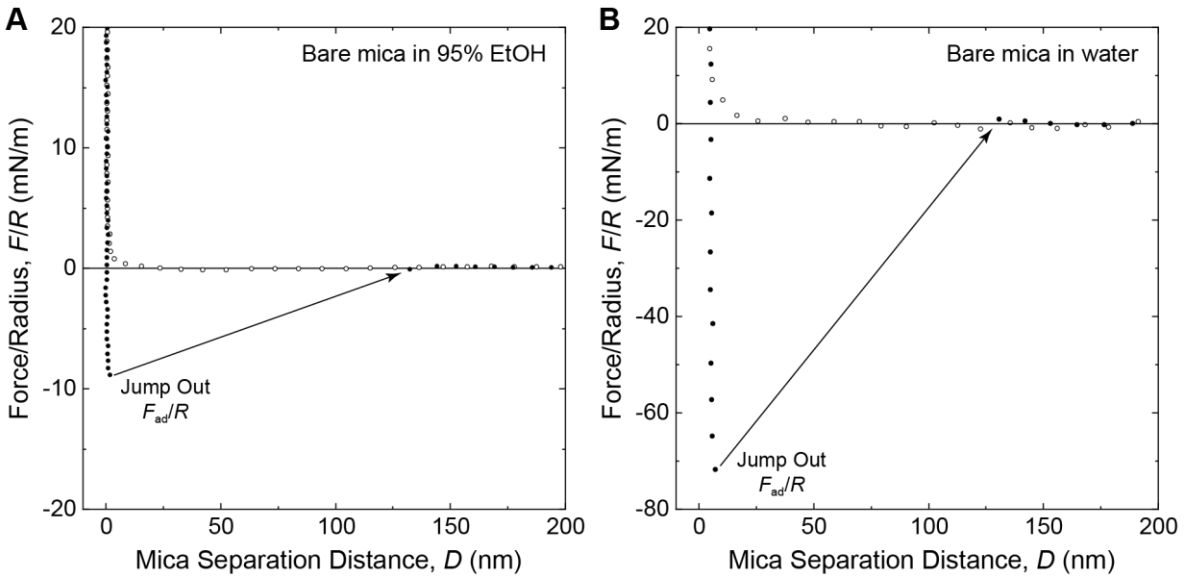

Figure A7.1. (A) Plot of force/radius F/R vs. separation distance D between bare mica surfaces in ethanol solution (95% ethanol, 5% water). (B) Plot of F/R vs. D between bare mica surfaces in water.

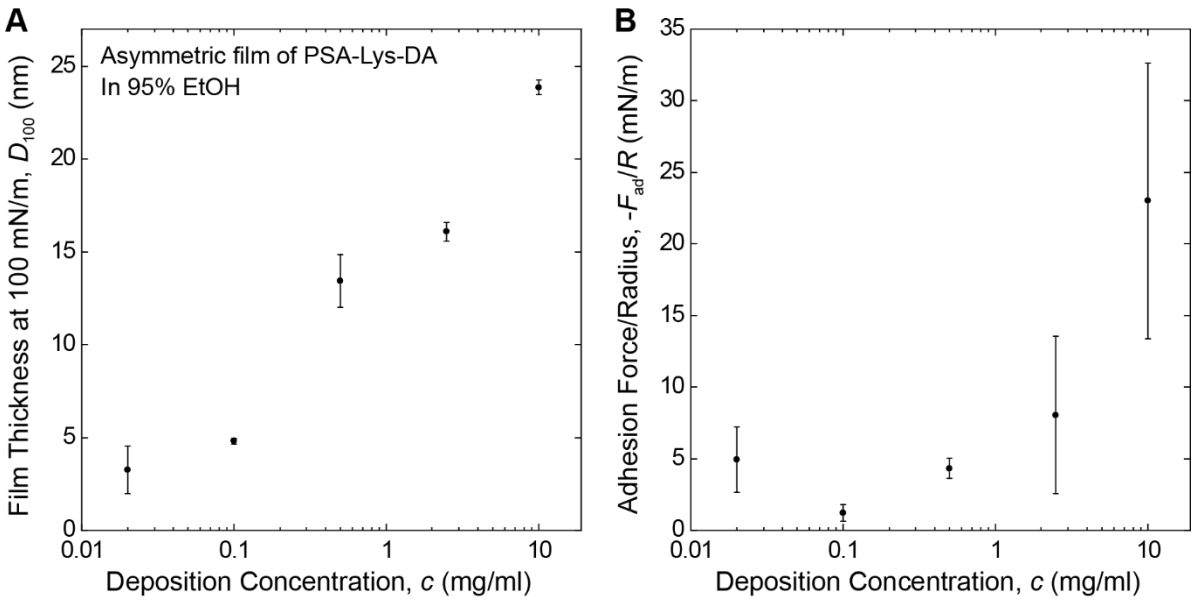

Figure A7.2. Measurements of asymmetric films of PSA-Lys-DA deposited at different polymer concentrations c. Measurements were performed in 95% ethanol solution. (A) Film thickness at 100 mN/m compression D_{100} vs. c. (B) Adhesion force/radius $-F_{ad}/R$ vs. c.

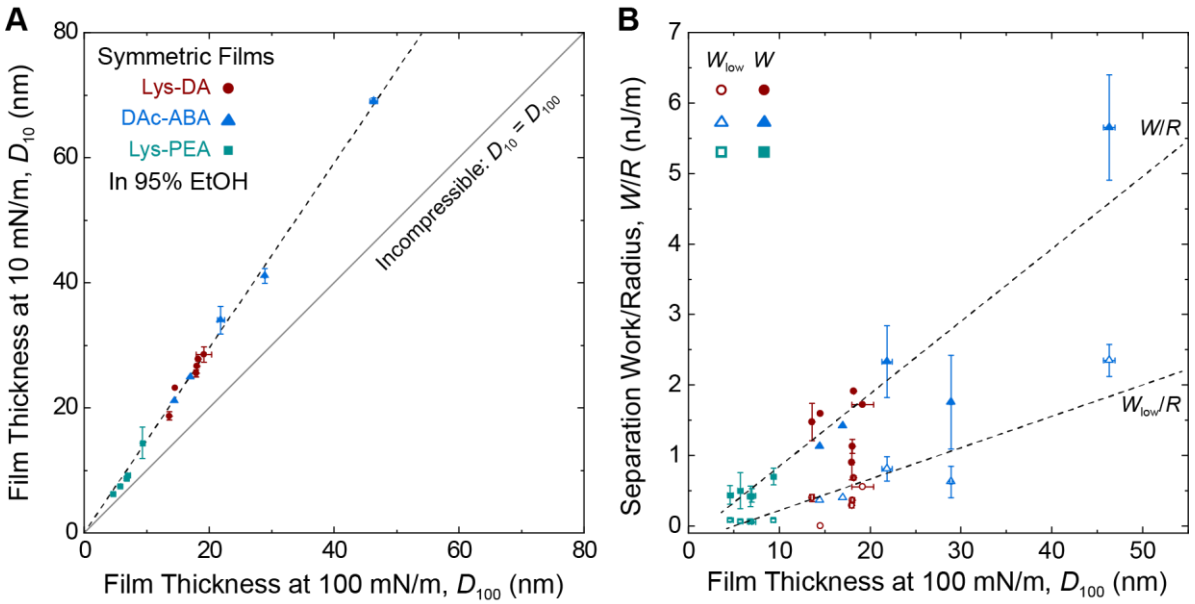

Figure A7.3. Measurements of symmetric polymer films in 95% ethanol solution. (A) Plot of film thickness at 10 mN/m compression D_{10} vs. film thickness at 100 mN/m compression D_{100}. Solid line indicates incompressible films, where $D_{10} = D_{100}$. Dashed line is included to guide the eye. (B) Plot of separation work/radius W/R vs. D_{100}. Closed circles show the separation work shown in Figure 2B in the main text. Open circles show the lower limit of the separation work W_{low}, calculated by integrating the separation force from the separation distance where $F = 0$ to the adhesion distance D_{ad}. Dashed lines are included to guide the eye.

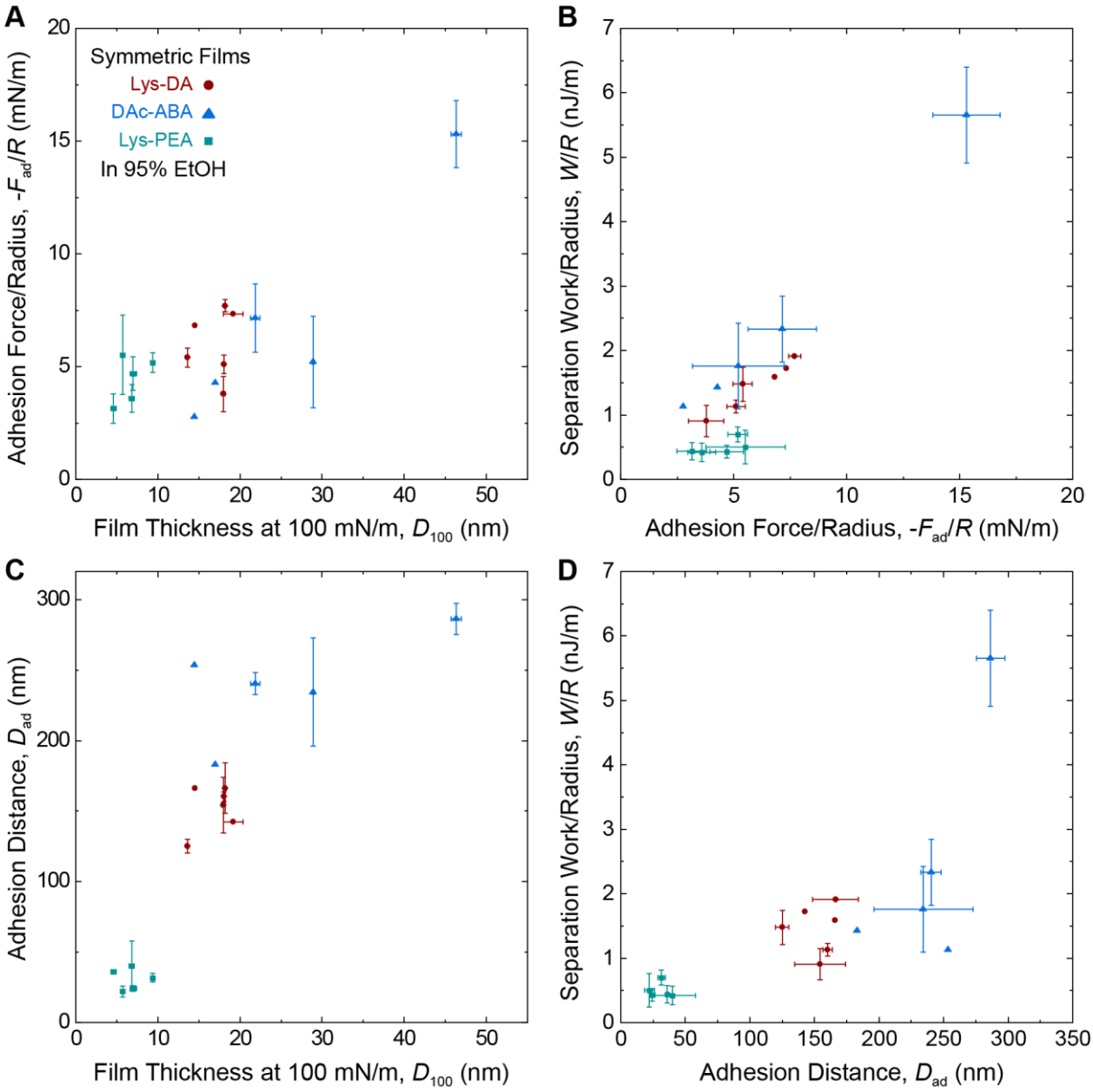

Figure A7.4. Measurements of symmetric polymer films in 95% ethanol solution. (A) Plot of adhesion force/radius -F_{ad}/R vs. D_{100}. (B) Plot of separation work/radius W/R. (C) Plot of adhesion distance D_{ad} vs. D_{100}. (D) Plot of W/R vs. D_{ad}. We note the adhesion distances were less than the calculated contour lengths for each polymer (PSA-Lys-DA = 552 nm, PSA-DAc-ABA = 470 nm, PSA-Lys-PEA = 373 nm).

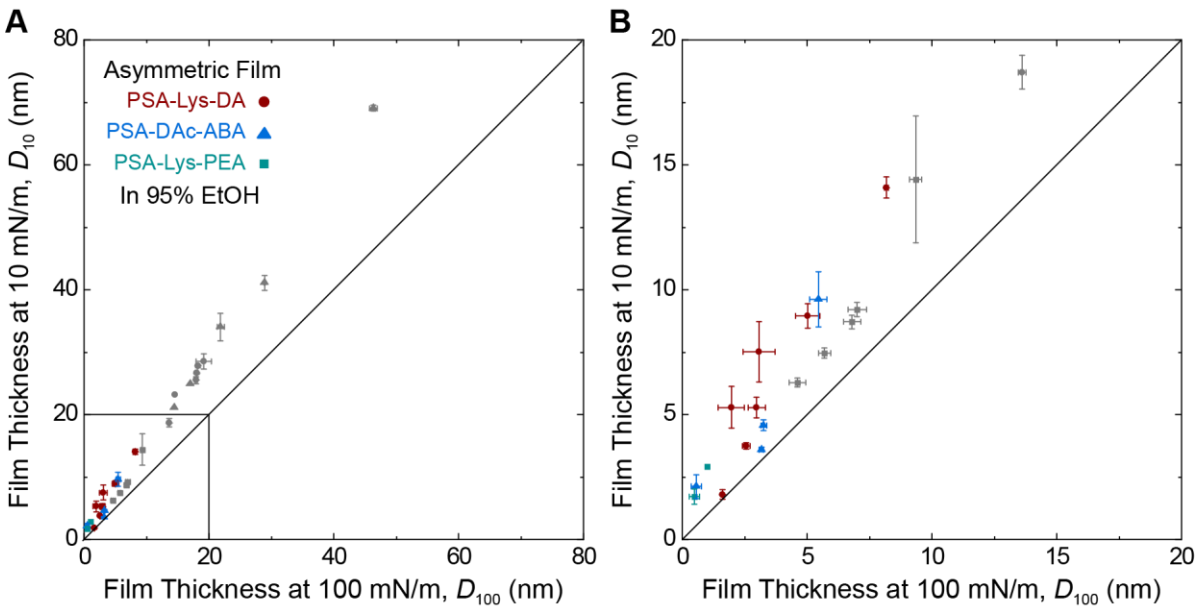

Figure A7.5. Measurements of asymmetric PSA films in ethanol solution. (A) Plot of D_{10} vs. D_{100} for asymmetric polymer films in 95% ethanol, 5% water. (B) Enlarged plot of the boxed region in (A). Gray symbols correspond to values measured for symmetric films (Figure A7.3A).

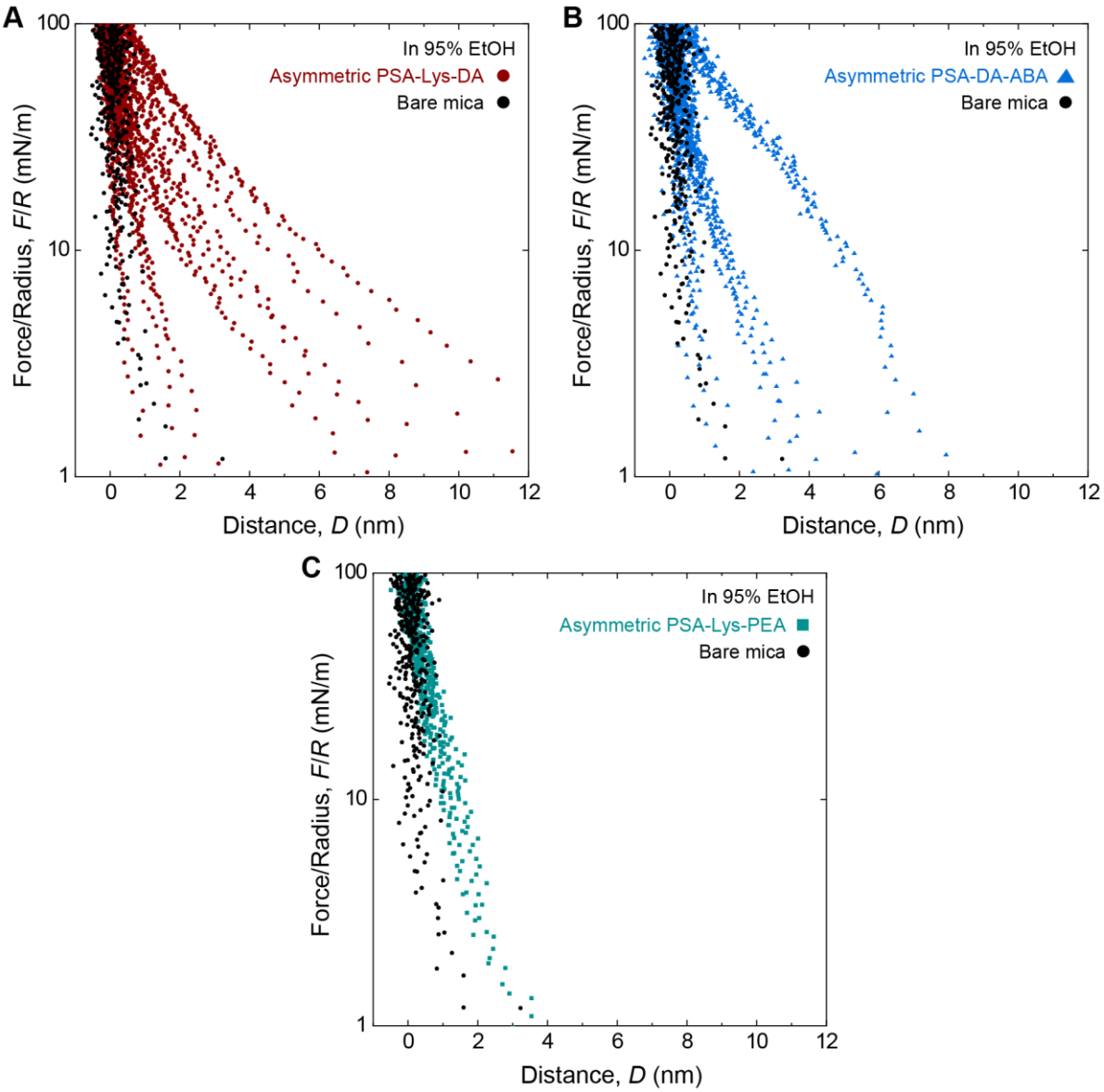

Figure A7.6. Plots of *F*/*R* vs. *D* measured during compression of asymmetric films of (A) PSA-Lys-DA, (B) PSA-DAc-ABA, and (C) PSA-Lys-PEA. Each plot includes forces measured during multiple independent experiments. Black circles show forces measured between bare mica surfaces during two independent experiments. The plots indicate the presence of polymer films, likely of varying thickness or average density, as shown by the varying range of the repulsive interactions.

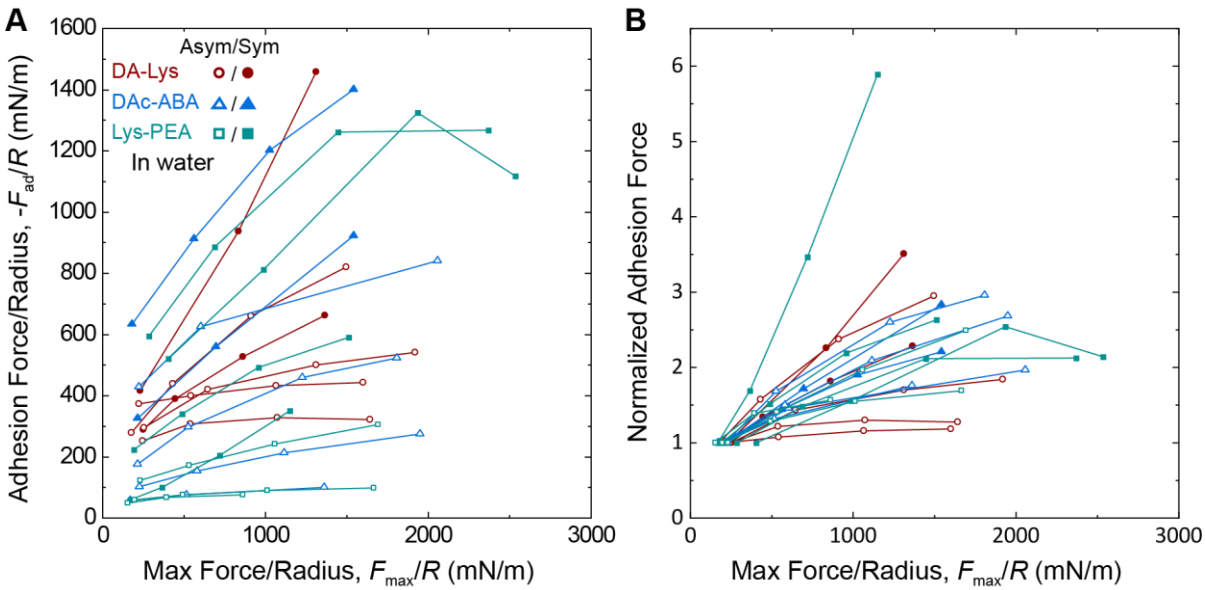

Figure A7.7. Effect of compression on adhesion force. (A) Plot of $-F_{ad}/R$ vs. the maximum compressive force/radius before separation F_{max}/R. Open circles correspond to asymmetric polymer films; closed circles correspond to symmetric films. All measurements were performed in water. (B) Normalized adhesion force vs. F_{max}/R. Adhesion force was normalized by the adhesion force measured after approximately 200 mN/m compression. All polymers show an increase in adhesion with increased compression, a typical characteristic of pressure sensitive adhesives.

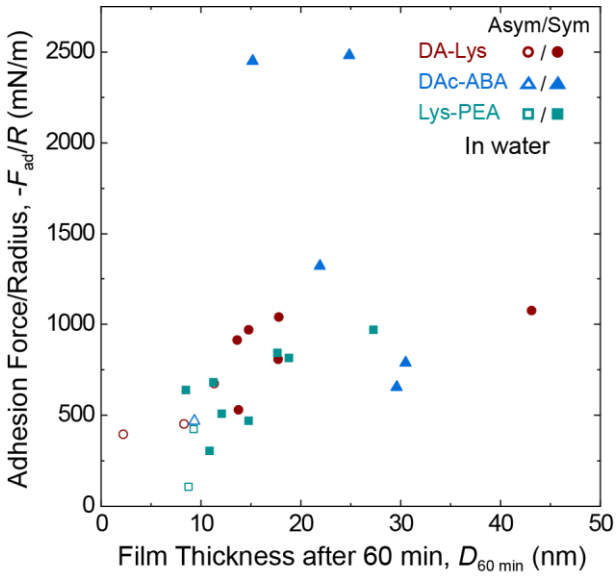

Figure A7.8. Plot of $-F_{ad}/R$ after 60 min dwell time for each polymer. Open circles correspond to asymmetric films; closed circles correspond to symmetric films. Each circle corresponds to a unique contact location between the mica surfaces, with at most two contacts per pair of mica surfaces. All measurements were performed in water. After the 60 minute dwell time, the relative decreases in film thickness were 0.5 ± 0.2, 0.3 ± 0.2, and 0.4 ± 0.1, and the relative increases in adhesion force were 1.1 ± 0.6, 1.0 ± 0.4, and 1.0 ± 0.6, for PSA-Lys-DA, PSA-DAc-ABA, and PSA-Lys-PEA, respectively.

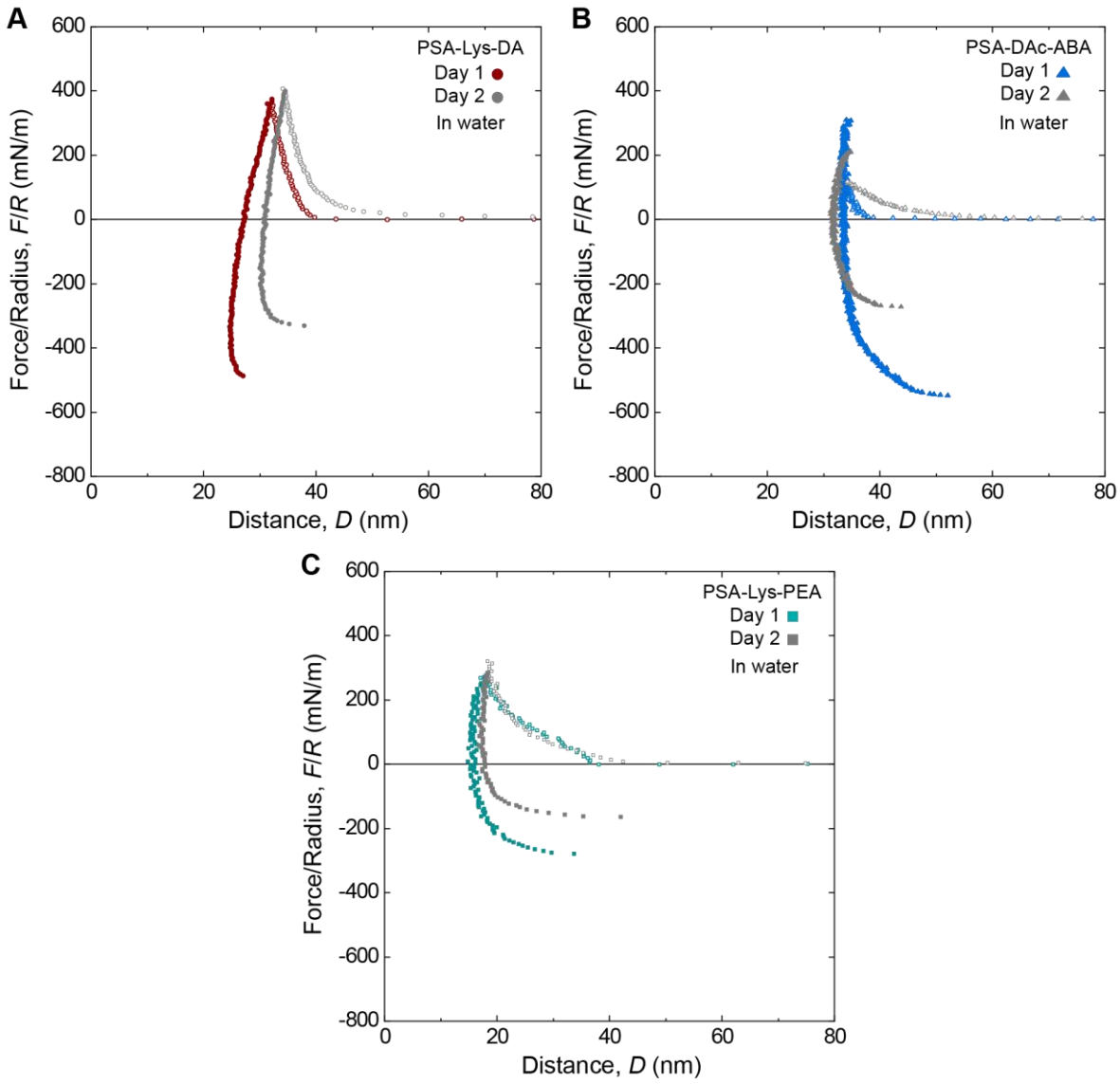

Figure 7.9. Plots of F/R vs. D for symmetric films of (A) PSA-Lys-DA, (B) PSA-DAc-ABA, and (C) PSA-Lys-PEA. Data labeled Day 1 were collected within approximately 4 h of deposition of the films. Data labeled Day 2 were collected 12-24 h after deposition of the films. Measurements conducted on the second day generally yielded a decrease in adhesion and an increase in D_{10} and D_{100}.

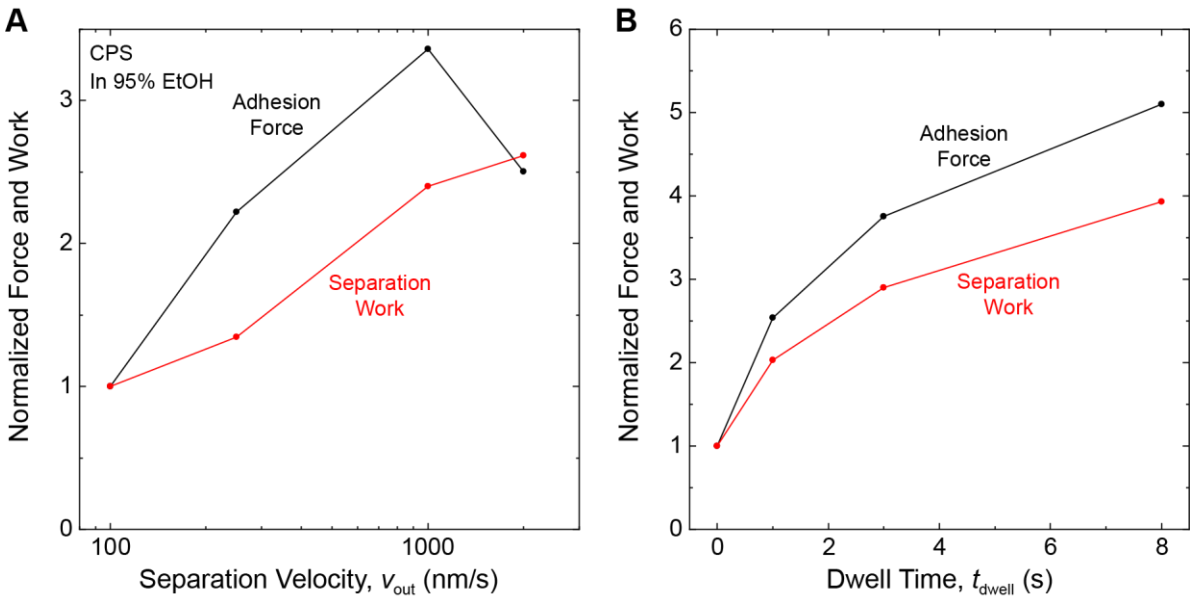

Figure A7.10. (A) Plots of median normalized adhesion (black) and separation work (red) vs. separation velocity v_{out}. (B) Plots of median normalized adhesion force and separation work vs. dwell time t_{dwell}.

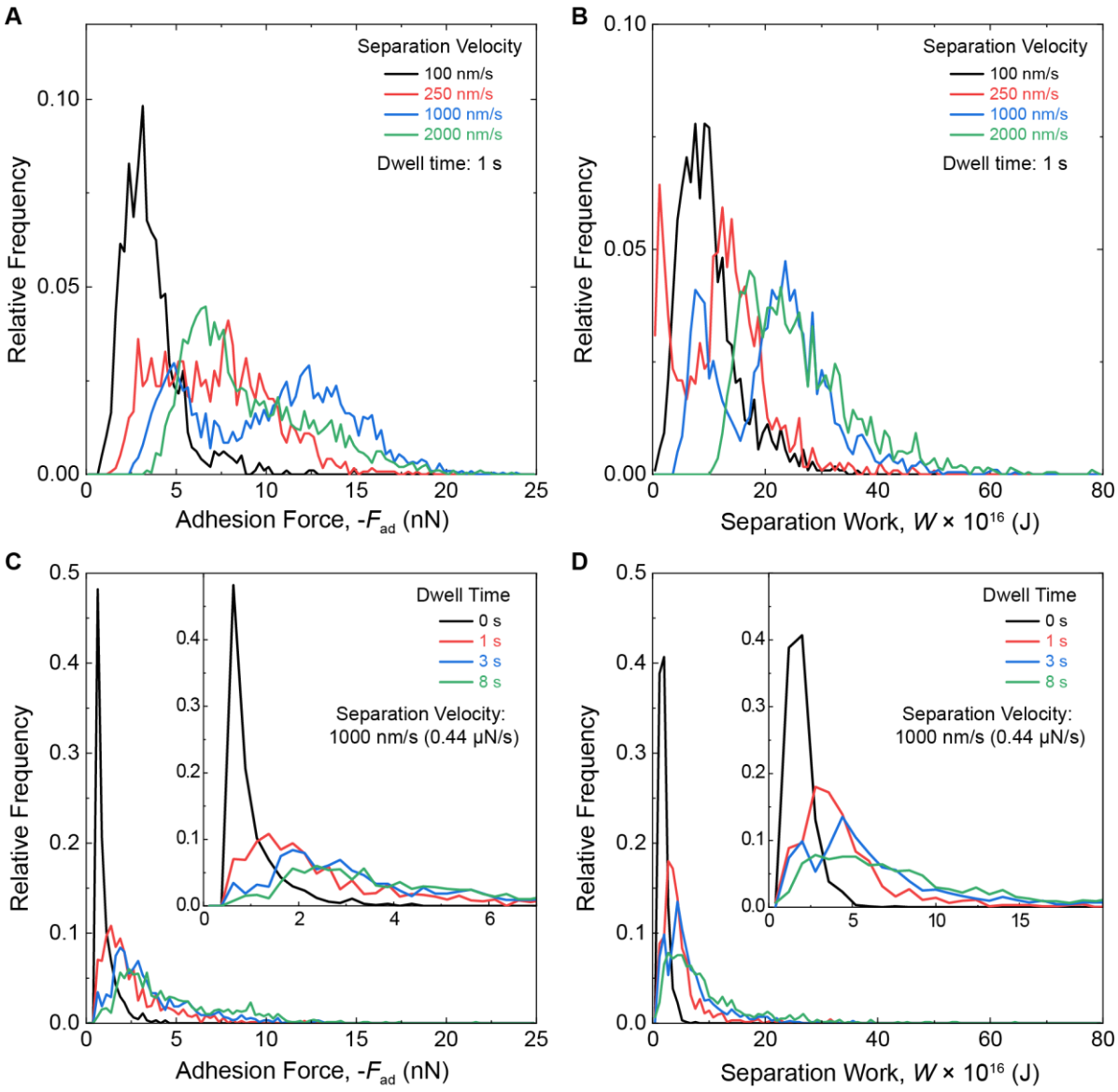

Figure A7.11. Plots of relative frequency of adhesion forces and separation works for different retraction velocities (A-B) and dwell times (C-D).

Appendix 8. Radius of Curvature Calculation and Supporting Figures

The crossed-cylinder geometry used in this work is equivalent to a sphere of radius R contacting a flat surface. Therefore, the interference fringes, which give the separation distance between the surfaces along a cross section of the contact region, can be used to calculated R when the surfaces are out of contact. To measure the radii of curvature of the cylindrical surfaces, two images of the interference fringes corresponding to orthogonal profiles of the surface separation distance across the contact region were taken with the surfaces out of contact. For a spherical cap of height t and base width $2r$ on a sphere of radius R, the Pythagorean theorem gives the following:

$$(R - t)^2 + r^2 = R^2 \tag{A8.1}$$

Assuming that t is much smaller than R yields:

$$2Rt = r^2 \tag{A8.2}$$

From the interference fringes, a value of t and corresponding value of r can be chosen such that t is tens to hundreds of nanometers, much smaller than R which is typically close to 2 cm, making the above approximation valid. The value of R can thus be calculated for orthogonal profiles of the surface separation distance across the contact region. A geometric mean of the two values of R yields the equivalent radius of curvature of the contact region, which accounts for possible differences in the radius of each cylindrical surface and misalignment of the crossed cylindrical surfaces, both of which result in an elliptical contact area.

After repeated adhesion cycles, a larger effective radius of curvature is measured. It should be noted that Equation A8.2 assumes that the surfaces are cylindrical. As the surfaces deform, they are likely not perfect cylinders. However, we use Equation A8.2 to calculate an effective value of R as an approximation of the contact geometry. This increase in the radius of curvature is attributed to deformations in the underlying glue layer beneath the mica substrates rather than deformations of the PS films. For the effective radius of curvature to increase by 10% (for example as seen in the black circles in Figure A8.1A below), the value of t for a given r in Equation A8.2 would have to decrease by approximately 10%. Taking typical values of r, t, and R of 50 μm, 60 nm, and 2 cm, respectively, the value of t would need to decrease by approximately 6 nm to increase R by 10%. If this decrease in t were due to deformation of the PS film, then the combined thickness of the two films measured upon contact of the films in the SFA would be expected to decrease by 6 nm. However, the film thickness generally changed by <1 nm over repeated adhesion cycles. For example, for the experiment corresponding to the black circles in Figure A8.1A, the measured film thickness decreased by approximately 0.5 nm over 10 adhesion cycles. Since this decrease in film thickness is an order of magnitude lower than the decrease in thickness necessary to account for the change in the measured radius of curvature, an increase in the measured radius of curvature due to deformations in the PS films is unlikely.

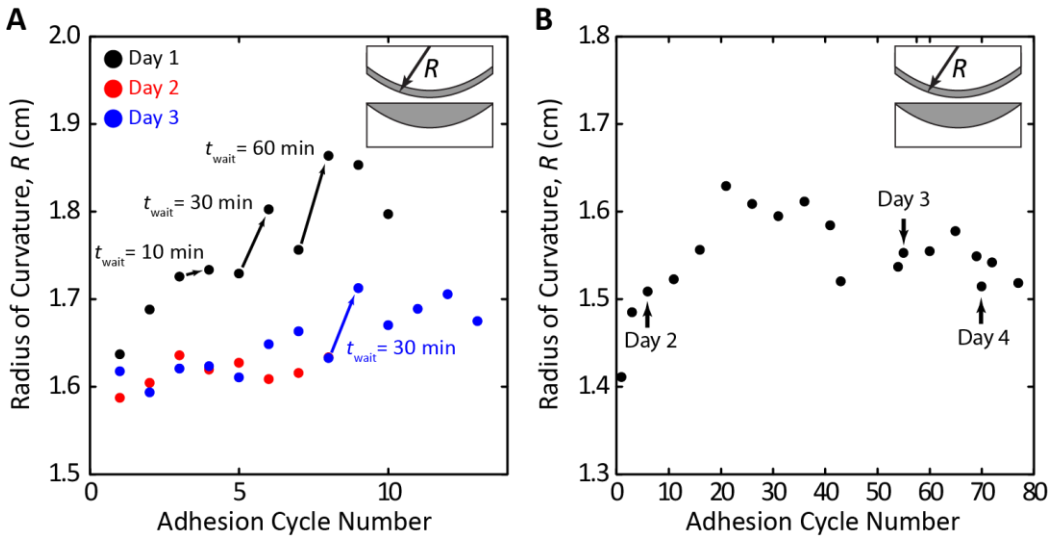

Figure A8.1. Approach-retraction cycles deform the surfaces and change the average radius of curvature. (A) Waiting at maximum compression (here 10, 30, or 60 min) results in increases in average radius of curvature. The average radius then decreases on subsequent measurements and decreases further after >12 h with the surfaces out of contact (Day 1 to Day 2). (B) Successive compression-retraction cycles without waiting at maximum compression also change the average radius. Time spent out of contact (12-24 h) does not return the average radius to the initial value. The partial reversibility of changes in contact radius is likely due to viscoelasticity of the glue layer beneath the mica surfaces. Radii were measured from the interference fringes as described above.

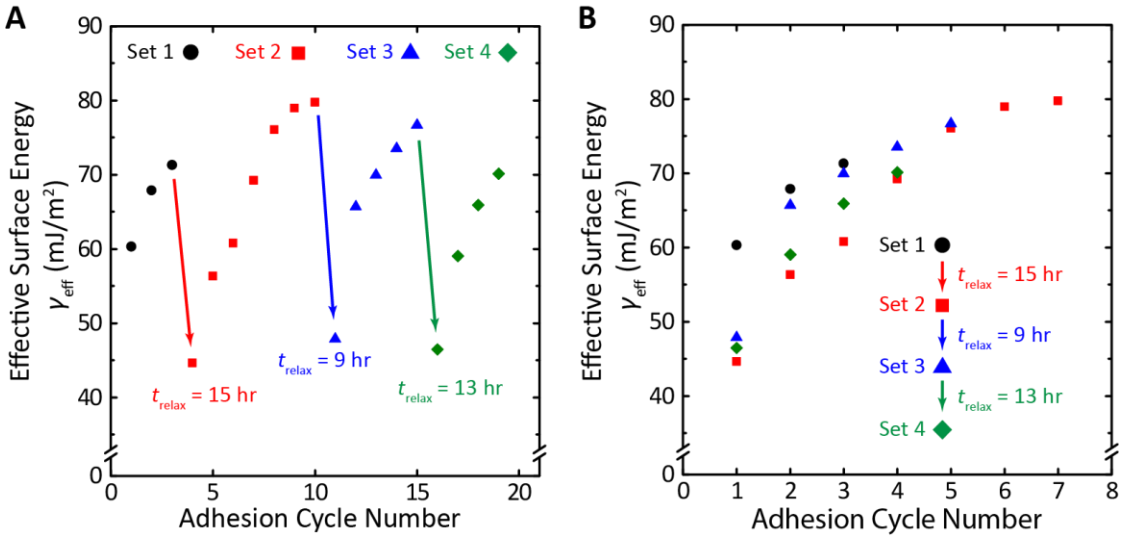

Figure A8.2. Effective surface energy of films of low-MW PS increases over consecutive adhesion cycles and decreases after surfaces relax out of contact. (Data reproduced from the red circles in Figure 5.1 in the main text). (A) The effective surface energy of low-MW PS films is plotted for subsequent force measurements (waiting time <1 min between cycles) (B) The same data, replotted to show that the increases in effective surface energy over repeated loading/unloading cycles follow a similar pattern after relaxation.

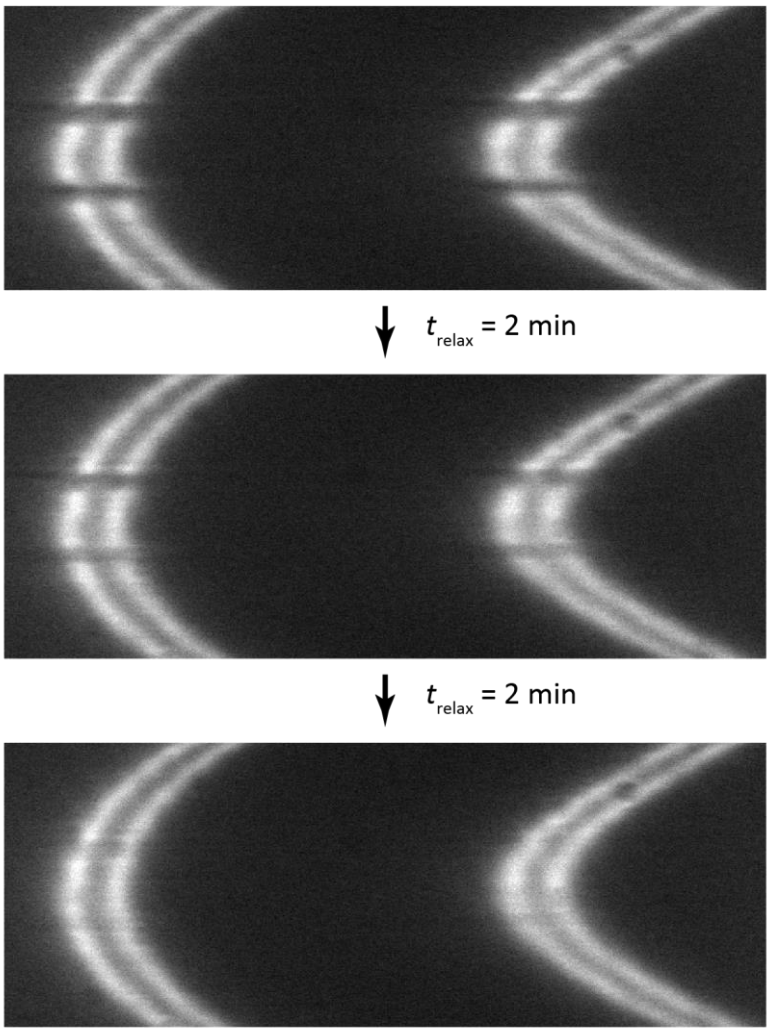

Figure A8.3. Discontinuities in the SFA interference fringes corresponding to center surface damage fade over the course of minutes after separation of the surfaces.

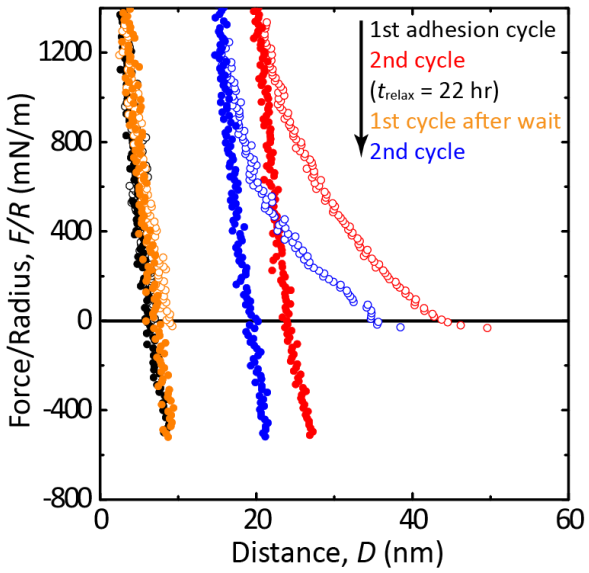

Figure A8.4. Repulsion due to moderate center damage disappears after time out of contact and reappears on subsequent adhesion cycles.

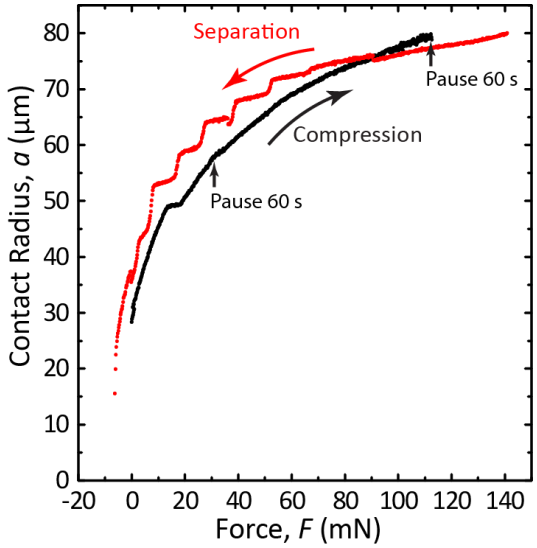

Figure A8.5. Moderate waiting times (t_{wait} = 60 s) at maximum compression promote stick-slip detachment of self-mated low-MW PS films. The temporary plateau in contact radius at approximately 15 mN is due to damage from prior adhesion cycles, discussed in Figure 5.3 in the main text.

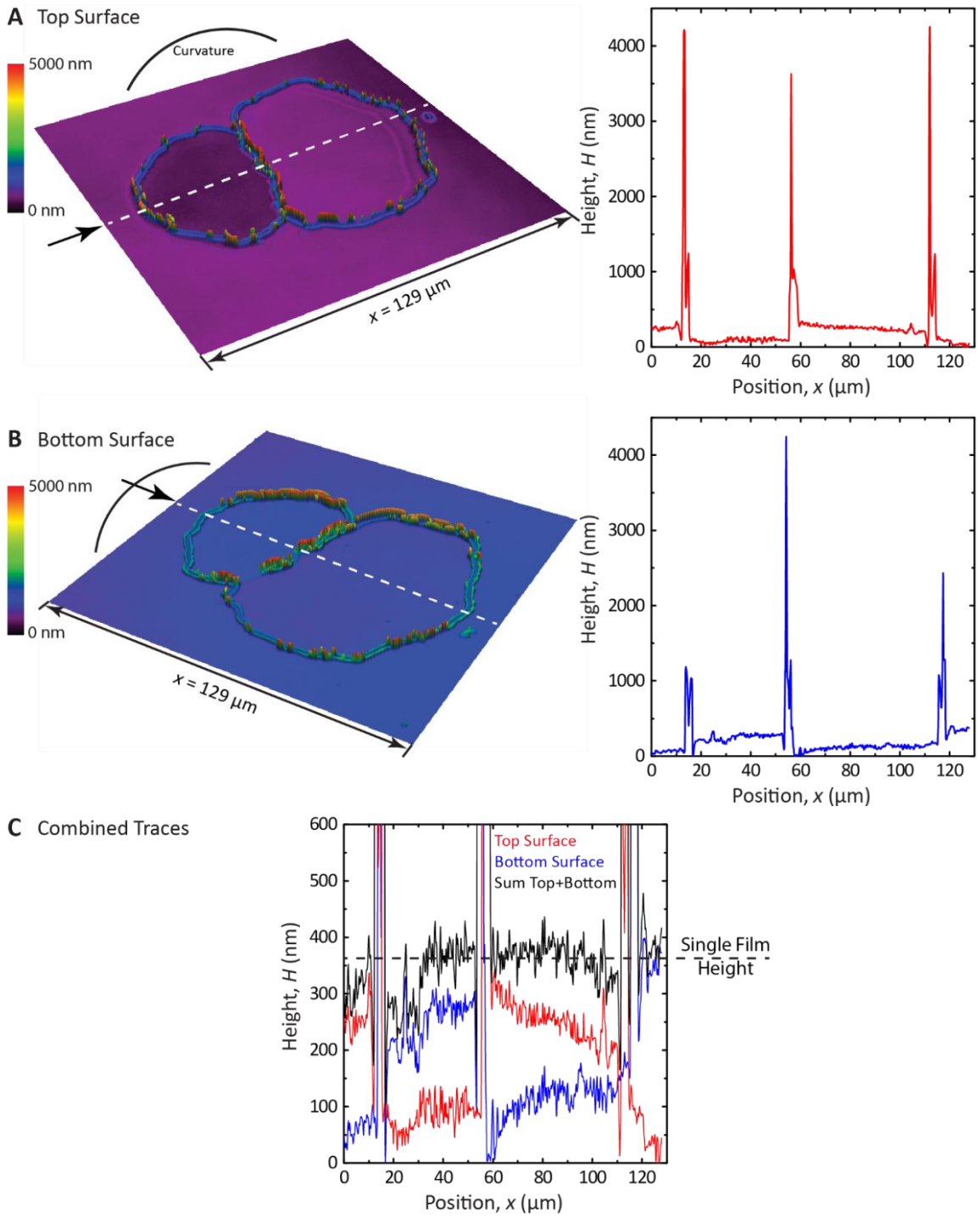

Figure A8.6. Confocal microscopy images show damage to the low-MW PS films. Top and bottom surfaces for the same contact point are shown in (A) and (B), respectively, with corresponding height traces. Height traces are replotted in (C) and show that complete film transfer does not occur, which would appear as a top or bottom surface height of 350 nm. Instead, cohesive failure within the film and subsequent partial film transfer occurs. This film transfer process also likely results in the formation of the 1-4 µm structures seen in (A) and (B).

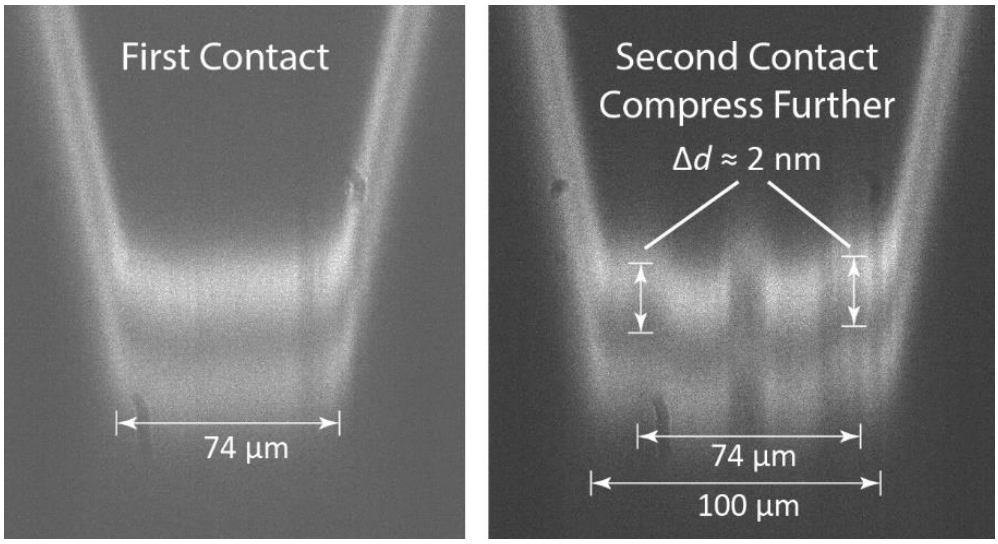

Figure A8.7. Damage at the contact edge is visible in the interference fringes during subsequent adhesion cycles upon further compression.

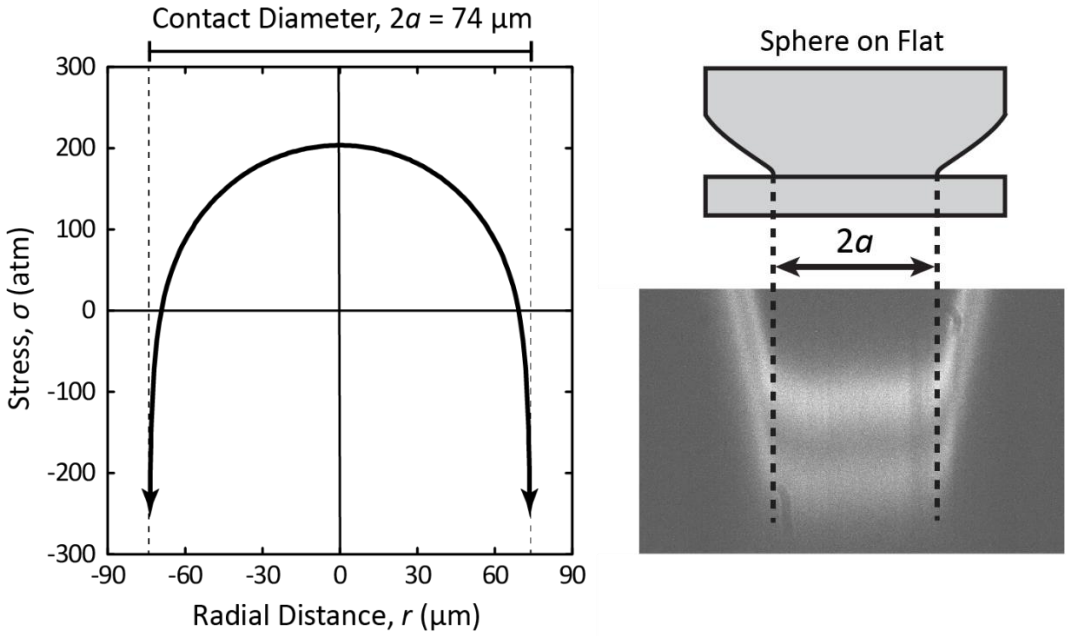

Figure A8.8. The stress distribution across the contact area given by Equation 5.3 in the main text. The maximum compressive stress occurs at the center of the contact, with tensile stress diverging to negative infinity at the contact edge.

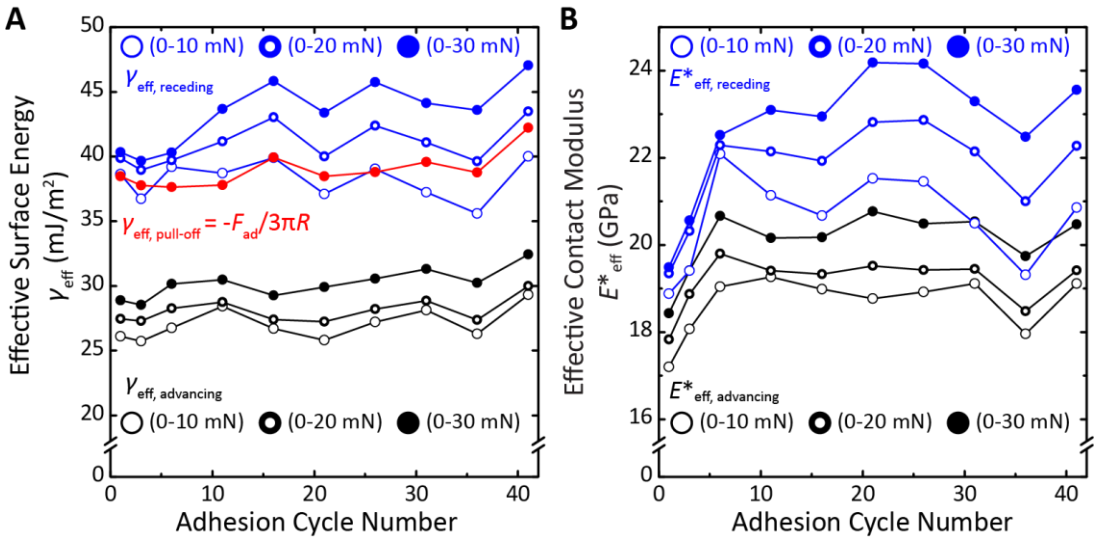

Figure A8.9. (A) Effective surface energies and (B) effective combined moduli remain constant over repeated adhesion cycles of films of high-MW PS. Surface energies and combined moduli were calculated by fitting Equation 5.2 in the main text to plots of contact radius vs. normal force for compression and separation, and effective surface energy was also calculated from the adhesion force with Equation 5.1.

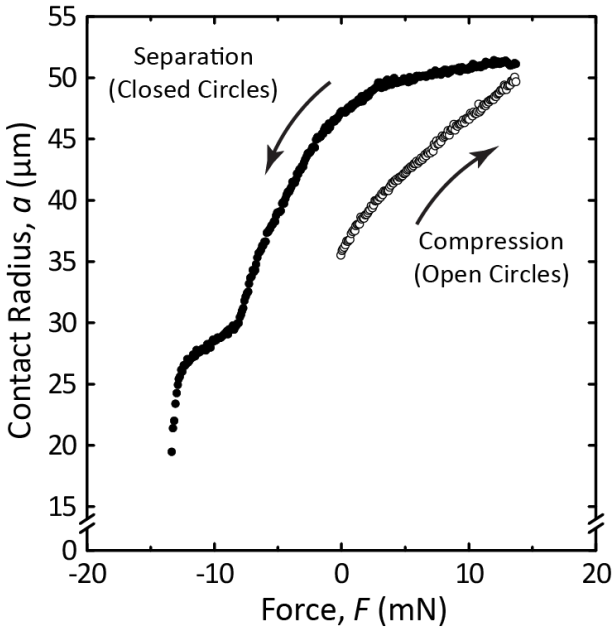

Figure A8.10. Representative plot of contact radius (a) vs. applied load (F) for mica surfaces contacting in dry nitrogen. The data could not be fit with the JKR theory to yield reasonable values of γ and E^*_{eff}, consistent with previous studies of mica-mica contact in an inert gas.[143]

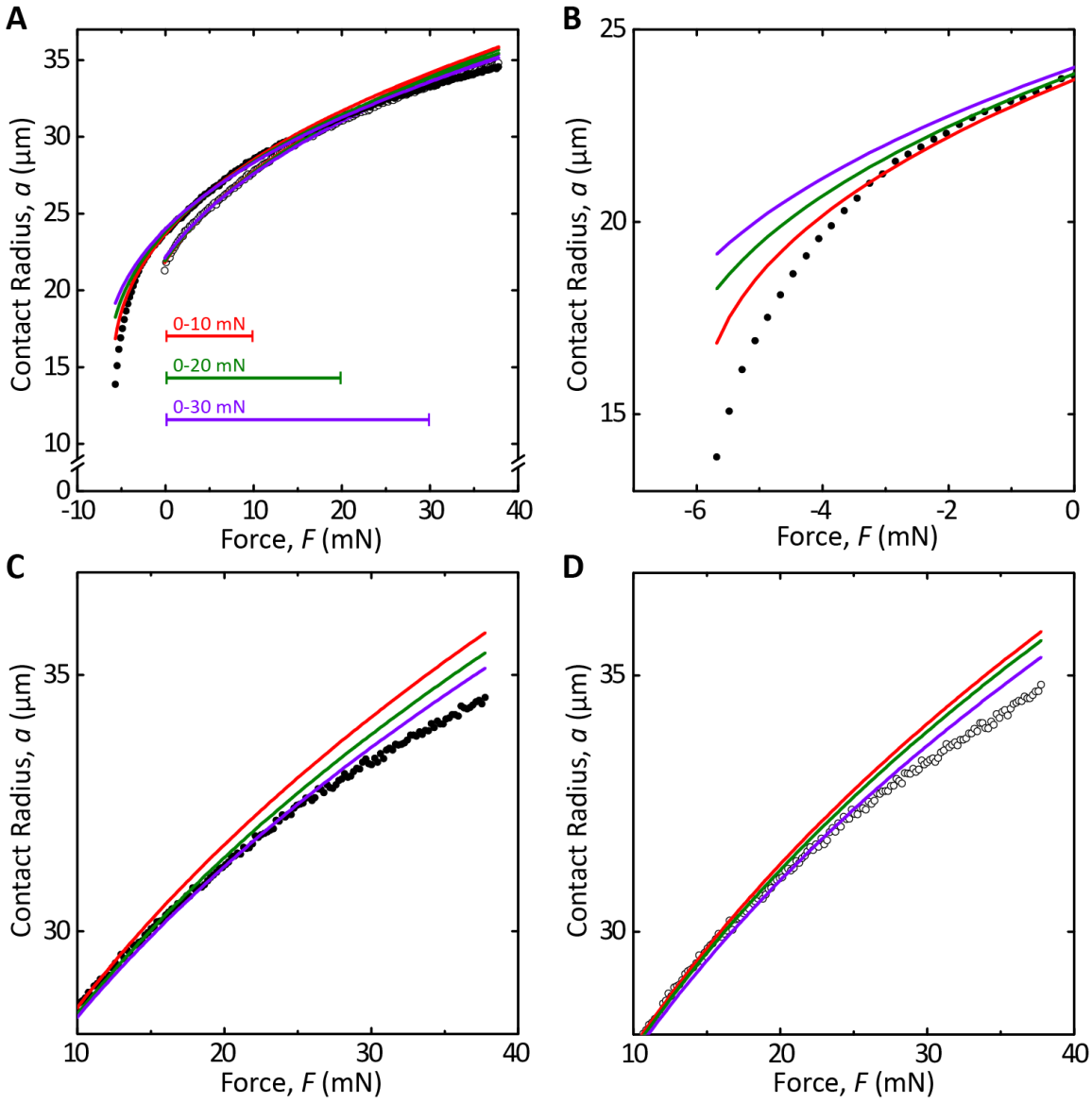

Figure A8.11. The fits of contact radius vs. applied load using Equation 5.2 overpredict the measured contact radii at tensile loads, although the fit over the force range 0-10 mN is closer to the measured data than the fits over 0-20 and 0-30 mN. (B), (C), and (D) show specific regions of the data and fits shown in (A).

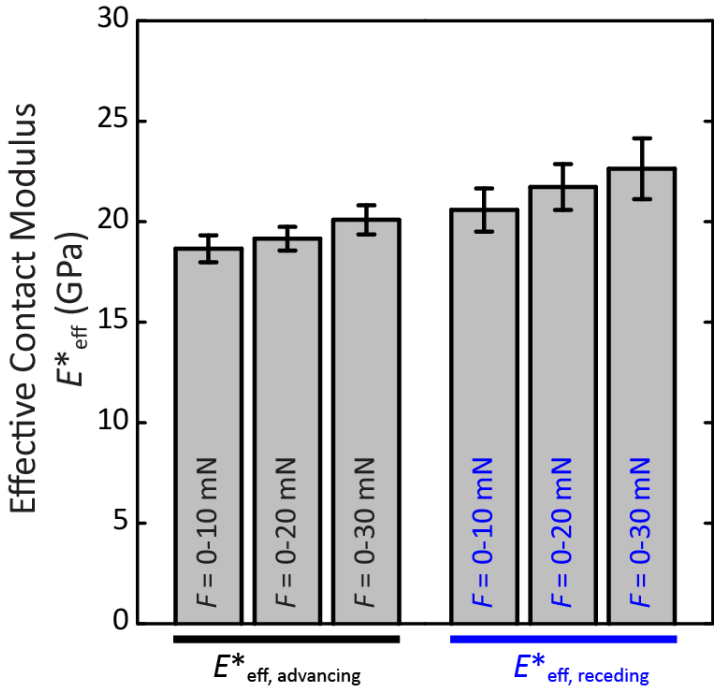

Figure A8.12. The fitting range influences the values of effective contact moduli predicted by Equation 5.2 for compression (advancing) and separation (receding) of high-MW PS films. Values are averages of the data shown in Figure A8.9. Error bars show one standard deviation.

Appendix 9. Hydrogel Film Preparation, Confocal Microscopy, and Supporting SFA Information

A layer of silver (thickness 46-50 nm) was deposited onto two cylindrical glass disks (radius of curvature $R = 2$ cm) via thermal evaporation. Gels of thickness 32 and 68 μm were cast directly on the silver surface. For the gel film of thickness 11 μm, additional surface preparation was used to prevent wrinkling during swelling. One of the silvered disks was functionalized with a cysteamine monolayer[208] via immersion in a 20mM aqueous cysteamine (Sigma-Aldrich) solution for 5 min. The concentration and incubation time were chosen to enable sufficient coverage of cysteamine[209] but avoid dissolution of the silver film. The surface was rinsed with ultrapure water (Millipore), then immersed in a 5 wt% aqueous glutaraldehyde (Sigma-Aldrich) solution for 5 min to covalently attach glutaraldehyde to the cysteamine monolayer,[210] and finally immersed in ultrapure water for 5 min.

To cast the hydrogel on cylindrical surfaces, a mold was prepared from two pieces of single-sided tape applied to a freshly cleaved mica strip (approximately 1 x 2.5 cm) forming a channel down the long axis (main text, Figure 6.1A). Tape thicknesses included 5 μm (Nitto Denko Corporation, UTS-5BSL), 10 μm (Nitto Denko Corporation, UTS-10BAF), and 30 μm (3M Scotch). The tape surfaces were coated with a hydrophobic pen to limit fluid leakage during casting (Daido Sangyo Co. Ltd). Hydrogels were polymerized from the following components in the specified mass ratios: acrylamide monomer (AAm, 7.5%, Sigma-Aldrich), N,N'-methylenebisacrylamide (MBAm, 0.3%, Sigma-Aldrich), N,N,N′,N′-tetramethylethylenediamine (TEMED, 0.15%, Sigma-Aldrich), ammonium persulfate (APS, 0.15%, Sigma-Aldrich), and ultrapure water. Special care was taken when handling the toxic acrylamide monomer and when disposing of waste. Immediately after mixing the hydrogel solution, 10 μL was deposited onto the cylinder and compressed with the mold for 5 min. The mold was then removed from the polymerized gel, which was then immersed in ultrapure water for at least 24 h. A new mold was prepared for each film. When preparing the molds, special care was taken to avoid wrinkling of the tape. The 5 μm thick tape was particularly susceptible to wrinkling upon application to the mica, and the presence of wrinkles greatly increased the thickness of the resulting gel film. With careful tape application, gels of swollen volume between 7 and 12 the 5 μm were cast using the 5 μm tape.

To assess film uniformity, 28.5 μL of 0.005 vol% solution of fluorescent beads (Fluoro-Max Red Fluorescent Microspheres, $\lambda_{\text{excitation}} = 542$ nm, $d = 490$ nm) in ultrapure water was mixed with 21.5 μL PAAm solution to yield 50 μL 7.5 wt% PAAm solution. 10 μL of this solution was cast between the bottom of a glass bottom petri dish and a freshly cleaved mica sheet. Strips of 5 μm thick tape (Nitto Denko Corporation, UTS-5BSL) were used as separators. To chemically attach the PAAm to glass, the glass surface was treated with UV/ozone (UVOCS T10x10/OES) for 10 min and then soaked in a 1:20 solution of 3-aminopropyl-triethoxysilane (APTES, 99.7%) in ultrapure water for 5 min. After rinsing with ultrapure water, the glass was soaked in a 1:20 solution of glutaraldehyde (Sigma Aldrich, 50 wt% in H2O) in ultrapure water for 5 min and then rinsed again with ultrapure water. Gels were prepared with and without the glutaraldehyde treatment of the surfaces.

A confocal microscope (Nikon Eclipse Ti2-E, A1R-HD) was used to measure the film thickness. The z-stacks were obtained with a 488 nm laser and step size of 0.5 μm. The polymerized film was analyzed before and after equilibration in water. Equilibration resulted in swelling of the gel, which took less than 5 min. This equilibration time is consistent with

the equilibration time predicted by polymer scaling[177]: $t \cong L^2/D$ where L is the characteristic size of the gel and D is the diffusion coefficient. Taking L as the film thickness (~10 μm) and a typical value of diffusion coefficient[177,211] $L = 10^{-11}$ m^2/s yields $t \approx 10$ s. The number of beads per stack was detected utilizing the NIS-Elements software and plotted against z position (Figure A9.1). Film thickness was determined from the width of the resulting curves.

We note that because the thicker gels were cast directly on the silver surface, they may have wrinkled upon swelling in water. We assumed that wrinkles would be flattened during compression and that after the gel was flattened, the compressive forces would be similar to those of a flat gel. This flattening is expected to result in relatively long-ranged repulsive forces. Since the film thickness was determined by fitting the poroelastic model to the compression forces, these long-ranged forces did not substantially affect the determination of the film thickness, since they accounted for a small percentage of the total forces. However, since the compression depth was calculated using the film thickness, a consequence of the fitting procedure and long-ranged forces is that repulsive forces appear at zero compression depth, as seen for the 32 μm film in Figure 6.2B in the main text.

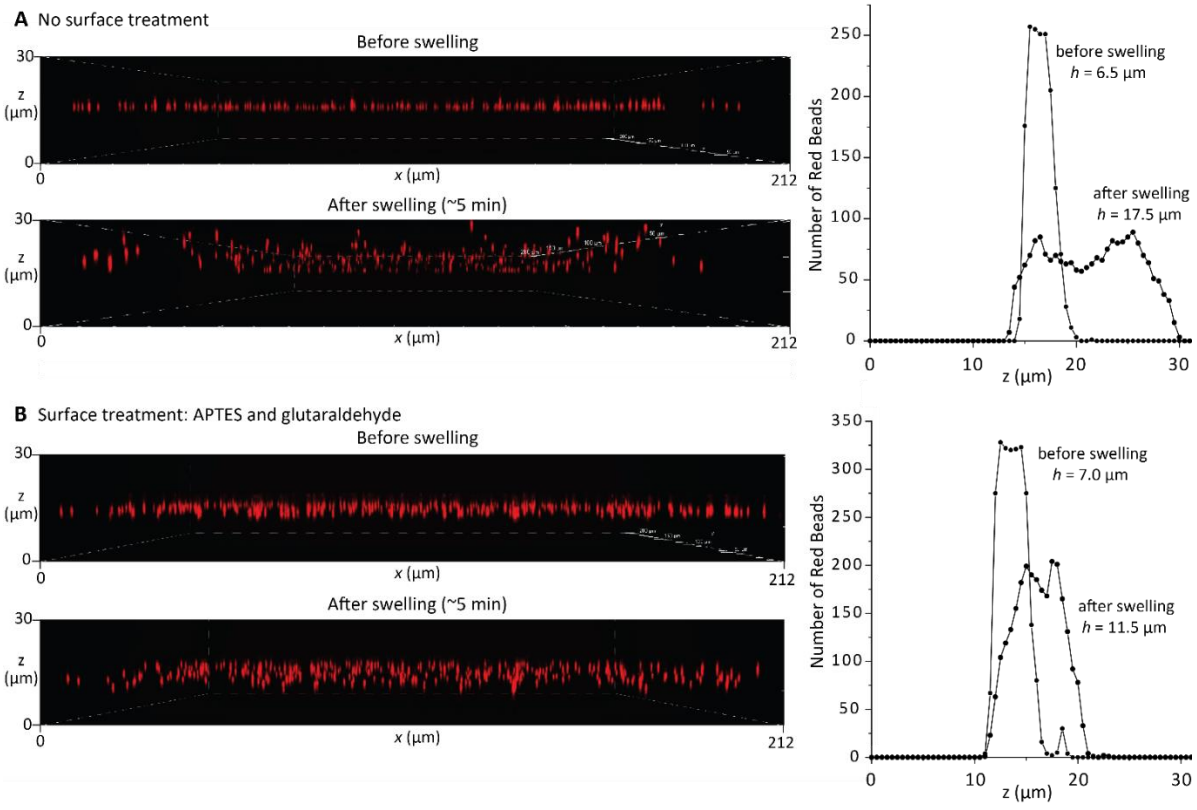

Figure A9.1. Confocal microscopy of gel films incorporating fluorescent beads. Images show fluorescence as a function of depth z and horizontal position x in the gel film. Plots show the total number of fluorescent beads as a function of z, where the width of the nonzero region corresponds to the film thickness. A) Gels deposited directly on glass show variations in the locations of the fluorescent beads in the z direction, indicating wrinkling of the film. B) Gels deposited on glass functionalized with APTES/glutaraldehyde. The consistent locations of the fluorescent beads in the z direction indicate the gels swell uniformly with minimal wrinkling.

Distance Measurement

In the SFA (SFA2000, SurForce LLC), white light multiple beam interferometry gave the distance D between the silver surfaces as follows. The hydrogel film was compressed between silver layers on each glass cylinder, forming a one-layer interferometer. Following Israelachvili,[212] D is related to the wavelengths of constructive interference λ_{n} and fringe order n by the following

$$D = \frac{n\lambda_{\mathrm{n}}}{2\mu} \tag{A9.1}$$

The refractive index μ in Equation A9.1 was equal to the refractive index μ_{gel} of the compressed hydrogel, calculated as a mass weighted average of the polymer refractive index[213] (1.5) and the refractive index of the solution μ_{sol}, which was either the dispersive refractive index of water[214] or non-dispersive refractive index of the ethanol/water solution.[203] We ignore the phase change at the silver-gel interface and dispersion of the polymer and ethanol/water solutions. The fringe order is calculated from the wavelengths of adjacent fringes as follows:

$$\frac{1}{n} = 1 - \frac{\mu_{\mathrm{n-1}}\lambda_{\mathrm{n}}}{\mu_{\mathrm{n}}\mu_{\mathrm{n-1}}} \tag{A9.2}$$

With the surfaces out of contact, a two-layer interferometer was formed, with a layer of solution adjacent to the gel layer. The refractive index μ in Equation A9.1 was then approximated as a weighted average of the refractive indices of the gel and solution layers,

$$\mu = \frac{h\mu_{\mathrm{gel}} + (D-h)\mu_{\mathrm{sol}}}{D} \tag{A9.3}$$

where h is the thickness of the gel layer. To measure the wavelengths of the interference fringes for gels of thicknesses greater than 7 μm, a diffraction grating of 1200 grooves/mm was used. For film thicknesses below 7 μm, the large spacing between interference fringes necessitated the use of gratings with 600 grooves/mm and 100 grooves/mm.

Interference fringes were recorded with a camera at 2 frames per second. A MATLAB script was written to determine the pixel locations of pairs of adjacent interference fringes. Gaussian fitting was used to find the pixel location of maximum intensity at the apex of the interference fringes (lowest wavelength), corresponding to the point of closest approach between the silver surfaces. The pixel locations were converted to wavelengths λ_{n} and $\lambda_{\mathrm{n-1}}$ by comparing to the locations of reference wavelengths produced by a mercury lamp. As the surfaces moved, the fringes shifted and eventually left the field of view, at which point the software automatically found a new pair of fringes. The orders of the fringes were determined to greater accuracy by averaging n^{-1} from Equation A9.2. The average was then inverted and rounded to the nearest whole number. Plotting D as a function of frame number revealed instances where the fringe order calculation was incorrect. In that case, the fringe order was manually incremented or decremented to maintain continuity of D. The fringe order rarely had to be altered by more than one, and most commonly not at all.

Force Measurement

A schematic of the SFA is shown in Figure A9.2A. The cylinder bearing the gel film was suspended on a double cantilever spring of spring constant K = 1000-1200 N/m. The base of the cantilever was translated with a motorized micrometer at constant velocity 10-70 nm/s, corresponding to the initial compression velocity of the surfaces immediately before contact, $\mathrm{d}(d)/\mathrm{d}t|_{d=0}$. As a result of compressing the surfaces with a spring, the compression velocity was less than the initial velocity: $\mathrm{d}(d)/\mathrm{d}t < \mathrm{d}(d)/\mathrm{d}t|_{d=0}$. Velocity was determined from the

change in D over time t with the surfaces out of contact, where D varies linearly with t (Figure A9.2B). The gel film was brought into contact with a bare silver-coated cylindrical glass surface ($R = 2$ cm) in a crossed cylinder configuration, equivalent to a rigid sphere ($R = 2$ cm) compressing a film on a rigid flat substrate.[1] The film was immersed in a capillary meniscus of solution between the surfaces. A solution reservoir in the sealed SFA chamber prevented evaporation of the meniscus. With the surfaces in contact ($D < h$), deviations from linearity of D corresponded to deflections of the spring Δx due to interactions between the surfaces. The normal force F was calculated from the spring deflection via Hooke's law, $F = K\Delta x$. To avoid errors in surface detection,[215] the film thickness h was determined by fitting the poroelastic[164] and Winkler[97] models to the measured forces. The compression depth was calculated as $d = h - D$. The compression velocity was calculated as $\mathrm{d}(d)/\mathrm{d}t = \Delta d/\Delta t$, where Δ indicates the change between adjacent data points ($\Delta t = 0.5$ s). Contact radius a was estimated as the base radius of a spherical cap of radius R and height d, where $a = \sqrt{2Rd}$ for $d \ll R$. Dividing the force by the contact area gives the average pressure $P_{\mathrm{avg}} = F/\pi a^2 = F/2\pi Rd$. The poroelastic[164] and Winkler[97] models give the same expression for the maximum pressure at the center of the contact area: $P_{\mathrm{max}} = 2P_{\mathrm{avg}}$. In all experiments, the maximum pressure was kept below the predicted osmotic pressure of the gel (27 kPa).[216] We assumed that possible changes in polymer concentration due to compression of the gels at these relatively low loads and small strains did not strongly influence the gel elastic modulus. Limiting the maximum pressure also avoided extensive drainage of the gel that would be expected at pressures above the osmotic pressure.[216] Such drainage might correspond to a discontinuous change in compression velocity at high loads which was not observed in our experiments.

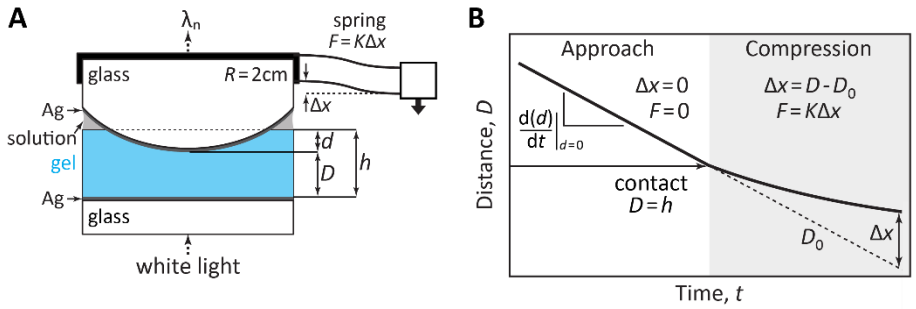

Figure A9.2. (A) Schematic of a hydrogel film compressed in a surface forces apparatus. For simplicity, the diagram shows a side view of a sphere-on-flat configuration, instead of the true crossed cylinder configuration of the SFA shown in Figure 6.1B of the main text. The surfaces are shown in compression, and the double cantilever spring is correspondingly deflected by distance Δx. Film thickness h, separation distance D, and compression depth d are indicated. (B) Measurement of initial velocity $\mathrm{d}(d)/\mathrm{d}t|_{d=0}$ and normal force F.

Crossed cylinder force derivation

Consider an isotropic linear elastic film compressed between crossed cylinders, where the axis of the upper cylinder is aligned with the x_1-axis, that of the lower cylinder is aligned with the x_2-axis, and the thickness direction in the film is aligned with the x_3-axis. The film thickness is h and the radius of each cylinder is R. We assume that $h \ll R$ and that the film is much larger than the contact region. The surface of the upper cylinder is given by

$$x_3 = \left(\frac{h}{2} - \frac{d}{2} + R - \sqrt{R^2 - x_2^2}\right) \tag{A9.4}$$

where d is the distance the film is compressed at the center of the contact region, here called the compression depth. Since $h \ll R$, the surface profile of the cylinder within the contact region can be approximated as a parabola and Equation A9.4 can be rewritten as

$$x_3 = \left(\frac{h}{2} - \frac{d}{2} + \frac{x_2^2}{2R}\right) \tag{A9.5}$$

Similarly, the surface of the lower cylinder within the contact region is approximated by

$$x_3 = -\left(\frac{h}{2} - \frac{d}{2} + \frac{x_1^2}{2R}\right) \tag{A9.6}$$

Adding Equations A9.5 and A9.6 yields the distance D between the cylinder surfaces

$$D = h - d + \frac{x_1^2 + x_2^2}{2R} = h - d + \frac{r^2}{2R} \tag{A9.7}$$

where r is the radial distance from the center of the contact region ($x_1 = x_2 = 0$). At the edge of the contact region, $D = h$, and therefore the radius a of the contact region is

$$a = \sqrt{2Rd} \tag{A9.8}$$

The strain in the film ε_{ij} at mechanical equilibrium can be expressed as

$$\varepsilon_{ij} = \frac{1}{2}\left(\frac{\partial u_i}{\partial x_j} + \frac{\partial u_j}{\partial x_i}\right) = \frac{1+\nu}{E}\sigma_{ij} - \frac{\nu}{E}\sigma_{kk}\delta_{ij} \tag{A9.9}$$

where x_i is the position of a material point, u_i is the displacement of a material point, σ_{ij} is the stress in the film, E is the Young's modulus, ν is the Poisson's ratio, and δ_{ij} is the Kronecker delta. Following Johnson,[97] we ignore lateral stress in the film, and assume frictionless compression. With $\sigma_{11} = \sigma_{22} = 0$, Equation A9.9 gives the following expression for normal stress in the film:

$$\sigma_{33} = E\frac{\partial u_3}{\partial x_3} \tag{A9.10}$$

The strain in the vertical direction is calculated from Equation A9.7 as

$$\frac{\partial u_3}{\partial x_3} = \left(-\frac{d}{h} + \frac{r^2}{2hR}\right) \tag{A9.11}$$

Combining Equations A9.10 and A9.11 yields

$$\sigma_{33} = E\left(-\frac{d}{h} + \frac{r^2}{2hR}\right) \tag{A9.12}$$

The compressive force applied by the cylinders is

$$F = -2\pi\int_0^{\sqrt{2Rd}} r\sigma_{33}\mathrm{d}r = 2\pi E\int_0^{\sqrt{2Rd}}\left(\frac{dr}{h} - \frac{r^3}{2hR}\right)\mathrm{d}r = \frac{\pi R E d^2}{h} \tag{A9.13}$$

This expression matches the Winkler model derived by Johnson[97] for a sphere compressing a flat gel, and justifies the use of the poroelasticity equation derived by Delavoipière et al. for a sphere-flat geometry[164] (Equation A11.15).

Appendix 10. Theoretical estimation of permeability

For a random isotropic network, the permeability k can be calculated from the characteristic size of the polymer chains a and the solid volume fraction ϕ as follows[217]

$$k = a^2 \frac{3}{20\phi}(-\ln(\phi) - 0.931) \quad \text{(A10.1)}$$

For 7.5 wt% hydrogels, the as-cast volume fraction ϕ_0 can be estimated from the density of water (1 g/ml) and solid polyacrylamide (1.19 g/ml), giving $\phi_0 = 0.064$. From the confocal microscopy images shown in Figure A9.1B, the gel thickness increases by approximately 64 % due to swelling from thickness 7 to 11.5 μm. We assume that the gels swell in only one dimension due to the glutaraldehyde surface treatment, and therefore that the volume increases 64 %, resulting in a volume fraction $\phi = 0.039$ of the swollen gel. This assumption is supported by the lack of wrinkling observed in Figure A9.1B and by the swelling study shown in Figure A11.4. Taking a as the diameter of the polyacrylamide chains (~0.5 nm)[218] yields $k \approx 2$ nm^2.

Appendix 11. Poroelastic Model, Algorithm for Force Calculation, and Supporting Figures

The poroelastic equation presented here combines Biot Theory and Darcy's law. Biot Theory[219] relates the force compressing a fluid-filled porous material to elasticity and fluid pressure, and Darcy's law relates fluid flow through a porous medium to the pressure gradient. The equations have been previously derived for compression of a gel between parallel plates[220,221] and for a sphere-flat geometry with a thin film approximation.[164] As shown in Appendix 9, the crossed cylinder geometry is expected to yield the same forces as the sphere-on-flat geometry. For a rigid sphere compressing a thin film on a rigid flat surface, the normal force F can be expressed as

$$F = \frac{\pi R d^2}{h}\left(E + \frac{\eta R}{2k}\frac{\mathrm{d}(d)}{\mathrm{d}t}\right) \quad \text{(A11.1)}$$

where R is the radius of curvature of the sphere, h is the thickness of the gel under zero load, η is the dynamic viscosity of the fluid, k is the permeability of the gel, d is the compression depth, and $\mathrm{d}(d)/\mathrm{d}t$ is the compression velocity.

For a gel film compressed to a force F_0 and compression depth d_0, if the motor driving the surfaces together is stopped, the surfaces will continue approaching each other until equilibrium is reached and the surfaces stop moving. Because force is applied with a spring, as the surfaces relax and approach each other, the normal force decreases. The normal force therefore depends on the compression depth d as follows:

$$F = F_0 - K(d - d_0) \quad \text{(A11.2)}$$

where K is the spring constant. Equation A11.1 be rearranged to solve for $\mathrm{d}(d)/\mathrm{d}t$:

$$\mathrm{d}(d)/\mathrm{d}t = \frac{2k}{\eta R}\left(\frac{hF}{\pi R d^2} - E\right) \quad \text{(A11.3)}$$

Combining Equations A11.2 and A11.3 yields

$$\mathrm{d}(d)/\mathrm{d}t = \frac{2k}{\eta R}\left(\frac{h(F_0 - K(d - d_0))}{\pi R d^2} - E\right) \quad \text{(A11.4)}$$

which can be fit to the measured $\mathrm{d}(d)/\mathrm{d}t$ as shown in Figure 6.2C in the main text.

The force needed to compress a thin poroelastic film was also modeled. Driving the base of the cantilever spring at constant velocity $\mathrm{d}(d)/\mathrm{d}t|_{d=0}$ results in the following relationship between force and compression depth:

$$F = K(t\,\mathrm{d}(d)/\mathrm{d}t|_{d=0} - d) \quad \text{(A11.5)}$$

where t is the time since contact ($t = 0$ at $d = 0$). Equation A11.4 can be written in discrete form and rearranged as:

$$\Delta d = \frac{2k\Delta t}{\eta R}\left(\frac{hK(t\mathrm{d}(d)/\mathrm{d}t|_{d=0} - d)}{\pi R d^2} - E\right) \quad \text{(A11.6)}$$

The compression force F can then be calculated with the following algorithm:

Choose Δt and tolerance
Set initial values ($i = 0$): $t_0 = 0$, $d_0 = 0$, $F_0 = 0$
For $i = 1$ to N [
    $t_i = t_{i-1} + \Delta t$
    guess $\Delta d_i = 0$
    $d_i = d_{i-1} + \Delta d_i$
    Calculate $\Delta d_{i,calc}$ with Equation A11.6
    While $|\Delta d_{i,calc} - \Delta d_i|$ < tolerance {
        Update guess for Δd_i
        $d_i = d_{i-1} + \Delta d_i$
        Calculate $\Delta d_{i,calc}$ with Equation A11.6
    }
    $d(d_i)/dt = \dfrac{d_i - d_{i-1}}{\Delta t}$
    Calculate F_i with Equation A11.1
]

The guess for Δd_i was updated by a factor that progressively decreased until Δd_i was within the desired tolerance of $\Delta d_{i,calc}$. Δt was chosen to be 0.1 s. Tolerance was chosen as 10^{-6} µm.

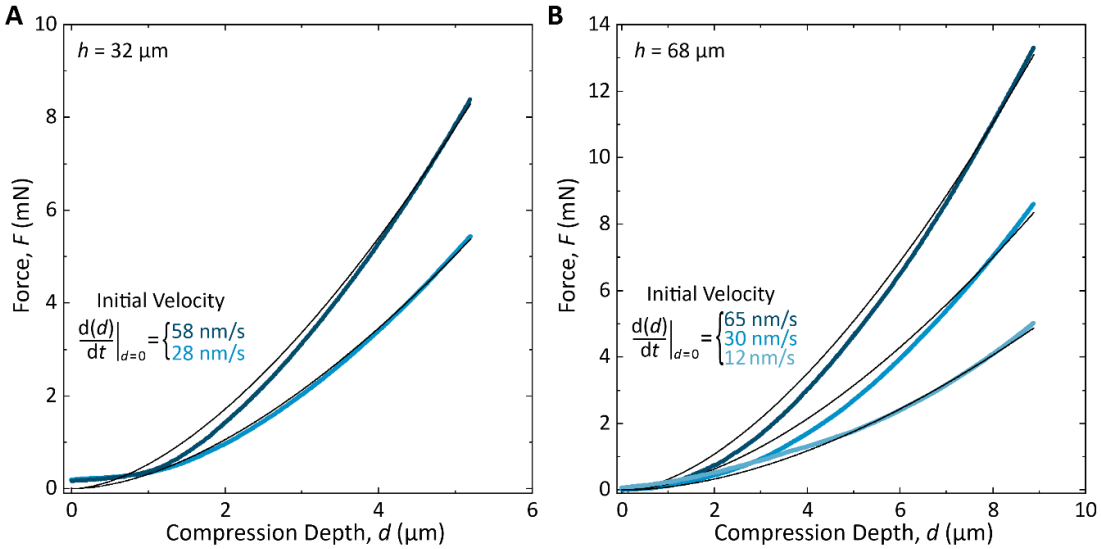

Figure A11.1. Normal force F vs. compression depth d measured for gel films of different thicknesses compressed at different velocities. (A) Film thickness $h = 32$ µm and (B) $h = 68$ µm. Black curves show the calculations using the poroelastic model. The film thickness h was determined from a one-parameter fit of Equation A11.1 to the measured forces, using the measured values of $d(d)/dt$. E and k were determined from the relaxation experiments described in the main text. The agreement between the model and the measured forces supports the accuracy of the values of E and k and suggests that the model could calculate compression forces for films of arbitrary thickness provided that the thin-film assumption of the model holds.

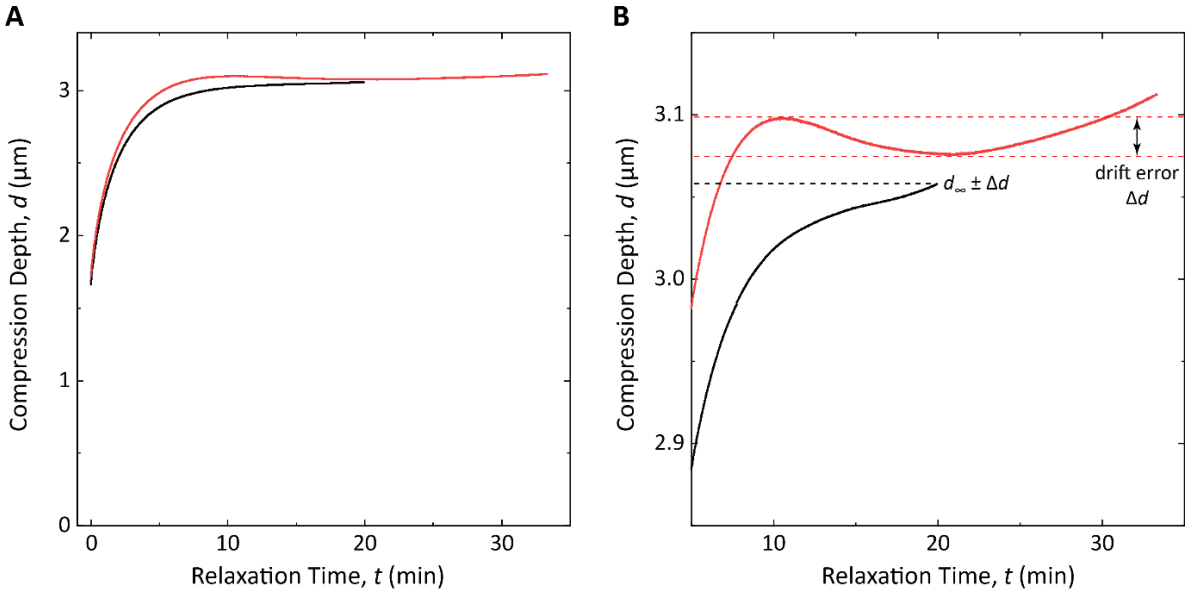

Figure A11.2. (A) Compression depth d vs. relaxation time t measured during sequential relaxation periods lasting 20 min (black) and 60 min (red). The 60-min relaxation period is truncated. While the 1-, 5-, and 20-min relaxations shown in Figure 6.2C in the main text follow the same trajectory, the 60-min relaxation reaches larger compression depths more quickly, possibly due to fluid drainage or microstructural changes of the gel occurring during the 20-min relaxation. (B) The data from (A) replotted to show the variations in the limiting value, likely due to thermal drift. The peak-to-peak variation over the first 20 min of the 60-min relaxation was taken as an approximate error of d_∞ for the 20-min relaxation.

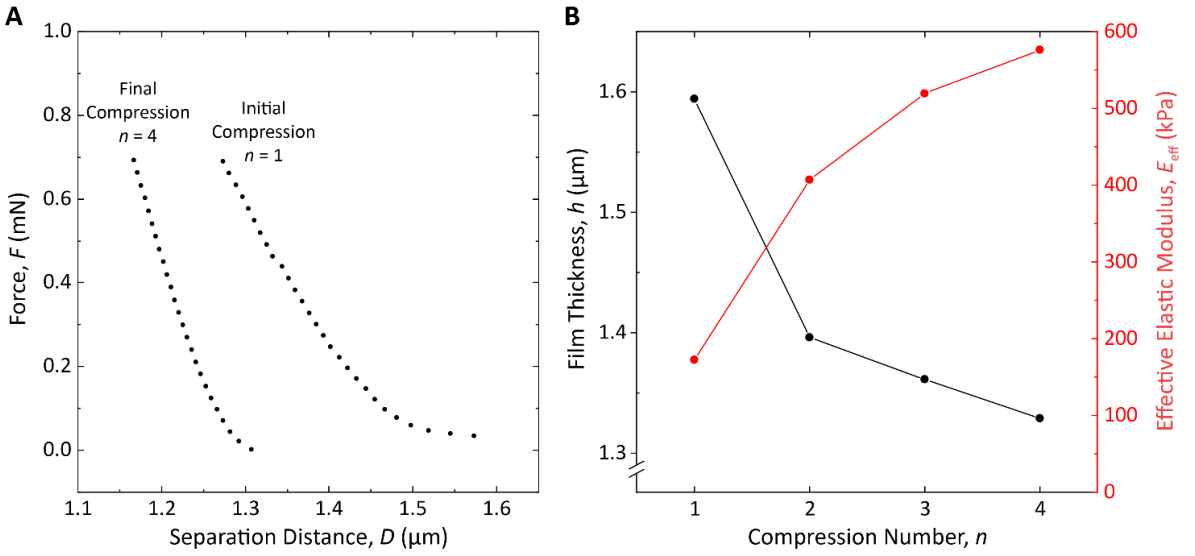

Figure A11.3. (A) Force F vs. separation distance D measured after addition of 100% ethanol. Four compressions were conducted, where the first ($n = 1$) and last ($n = 4$) are shown. (B) Film thickness h (black circles) and effective modulus E_{eff} (red circles) vs. compression number n. Lines are included to guide the eye.

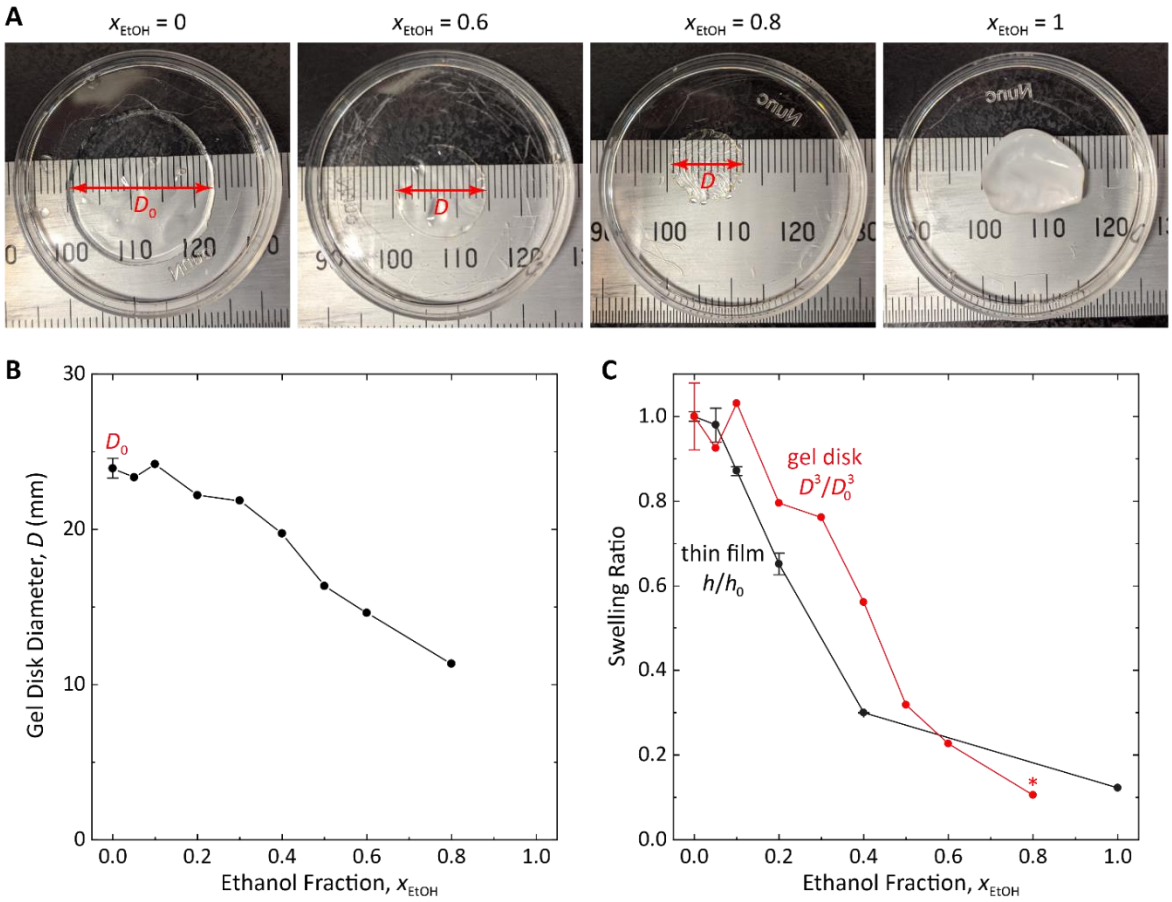

Figure A11.4. Hydrogel swelling ratios in ethanol solutions. Macroscopic gel disks of as-cast diameter 22 mm were swollen in water for 24 h to an initial swollen diameter D_0. The gels were then immersed in ethanol/water solutions of ethanol fraction x_{EtOH} and equilibrated for 48 h. (A) Images of gel disks equilibrated in different ethanol concentrations ($x_{\mathrm{EtOH}} = 0$, 0.6, 0.8, 1.0. Not shown: $x_{\mathrm{EtOH}} = 0.05$, 0.1, 0.2, 0.3, 0.4, 0.5). (B) Gel disk diameter D vs. x_{EtOH}. (C) Swelling ratio calculated from the ratio of final volume to initial. Since the gels collapse in ethanol, the ratio is less than 1. Red circles show the swelling ratios calculated for the macroscopic gel disks. The disks were unconstrained in the ethanol solutions, and therefore the collapse was assumed to be isotropic for $x_{\mathrm{EtOH}} < 1$, and the swelling ratio was calculated as the ratio of cubed diameter of the disk in ethanol solution to the cubed diameter of the disk in water (D^3/D_0^3). The asterisk for the data point at $x_{\mathrm{EtOH}} = 0.8$ indicates that the value is an underestimate of the swelling ratio, because the wrinkling of the gel shown in (A) lowered the measured value of D. For $x_{\mathrm{EtOH}} = 1$, the collapse occurred within the first minute of immersion, presumably fast enough to result in anisotropic collapse, and the diameter for $x_{\mathrm{EtOH}} = 1$ was not measured. For comparison, black circles show the swelling ratios calculated for a thin gel film from the film thicknesses plotted in the inset of Figure 6.3A in the main text. As stated in the main text, because the thin gel film was chemically attached to the silver surface, the film was assumed to collapse in only one dimension. Therefore, the swelling ratio for the thin film was calculated from the ratio of the film thickness in ethanol solution to the film thickness in water (h/h_0).

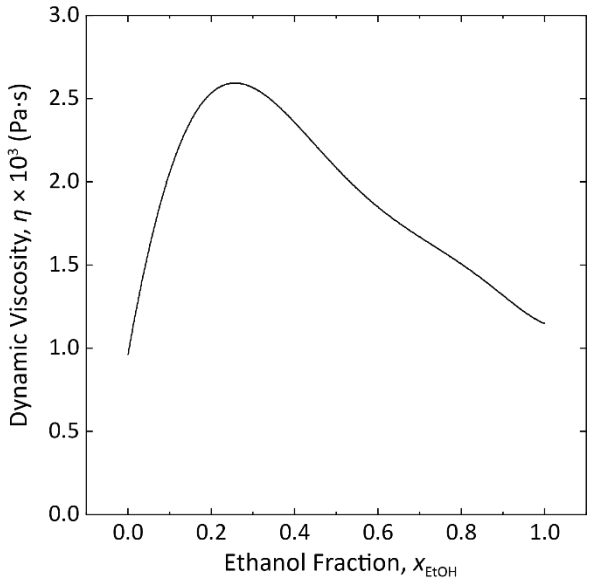

Figure A11.5. Dynamic viscosity η of ethanol/water solution vs. ethanol fraction x_{EtOH}.[222]

References

(1) Israelachvili, J. N. *Intermolecular and Surface Forces*, 3rd ed.; Academic Press, 2011.

(2) Waite, J. H. Mussel Adhesion – Essential Footwork. *J. Exp. Biol.* **2017**, *220* (4), 517–530.

(3) Lee, B. P.; Messersmith, P. B.; Israelachvili, J. N.; Waite, J. H. Mussel-Inspired Adhesives and Coatings. *Annu. Rev. Mater. Res.* **2011**, *41* (1), 99–132.

(4) Valois, E.; Mirshafian, R.; Waite, J. H. Phase-Dependent Redox Insulation in Mussel Adhesion. *Sci. Adv.* **2020**, *6* (23), eaaz6486.

(5) Monnier, C. A.; DeMartini, D. G.; Waite, J. H. Intertidal Exposure Favors the Soft-Studded Armor of Adaptive Mussel Coatings. *Nat. Commun.* **2018**, *9* (1), 1–9.

(6) Danner, E. W.; Kan, Y.; Hammer, M. U.; Israelachvili, J. N.; Waite, J. H. Adhesion of Mussel Foot Protein Mefp-5 to Mica: An Underwater Superglue. *Biochemistry* **2012**, *51* (33), 6511–6518.

(7) Lin, Q.; Gourdon, D.; Sun, C.; Holten-Andersen, N.; Anderson, T. H.; Waite, J. H.; Israelachvili, J. N. Adhesion Mechanisms of the Mussel Foot Proteins Mfp-1 and Mfp-3. *Proc. Natl. Acad. Sci. U. S. A.* **2007**, *104* (10), 3782–3786.

(8) Li, Y.; Cao, Y. The Molecular Mechanisms Underlying Mussel Adhesion. *Nanoscale Adv.* **2019**, *1* (11), 4246–4257.

(9) Lu, Q.; Danner, E.; Waite, J. H.; Israelachvili, J. N.; Zeng, H.; Hwang, D. S. Adhesion of Mussel Foot Proteins to Different Substrate Surfaces. *J. R. Soc. Interface* **2012**, *10* (79), 20120759–20120759.

(10) Yu, J.; Kan, Y.; Rapp, M.; Danner, E.; Wei, W.; Das, S.; Miller, D. R.; Chen, Y.;

Waite, J. H.; Israelachvili, J. N. Adaptive Hydrophobic and Hydrophilic Interactions of Mussel Foot Proteins with Organic Thin Films. *Proc. Natl. Acad. Sci. U. S. A.* **2013**, *110* (39), 15680–15685.

(11) Guo, Q.; Chen, J.; Wang, J.; Zeng, H.; Yu, J. Recent Progress in Synthesis and Application of Mussel-Inspired Adhesives. *Nanoscale* **2020**, *12* (3), 1307–1324.

(12) Waite, J. H.; Qin, X. Polyphosphoprotein from the Adhesive Pads of Mytilus Edulis. *Biochemistry* **2001**, *40* (9), 2887–2893.

(13) Lee, H.; Dellatore, S. M.; Miller, W. M.; Messersmith, P. B. Mussel-Inspired Surface Chemistry for Multifunctional Coatings. *Science* **2007**, *318*.

(14) Hong, S.; Na, Y. S.; Choi, S.; Song, I. T.; Kim, W. Y.; Lee, H. Non-Covalent Self-Assembly and Covalent Polymerization Co-Contribute to Polydopamine Formation. *Adv. Funct. Mater.* **2012**, *22* (22), 4711–4717.

(15) Liebscher, J.; Mrówczyński, R.; Scheidt, H. A.; Filip, C.; Haìdade, N. D.; Turcu, R.; Bende, A.; Beck, S. Structure of Polydopamine: A Never-Ending Story? *Langmuir* **2013**, *29* (33), 10539–10548.

(16) Delparastan, P.; Malollari, K. G.; Lee, H.; Messersmith, P. B. Direct Evidence for the Polymeric Nature of Polydopamine. *Angew. Chemie - Int. Ed.* **2019**, *58* (4), 1077–1082.

(17) Ryu, J. H.; Messersmith, P. B.; Lee, H. Polydopamine Surface Chemistry: A Decade of Discovery. *ACS Appl. Mater. Interfaces* **2018**, *10* (9), 7523–7540.

(18) Kim, K. K.; Kim, K. K.; Ryu, J. H.; Lee, H. Chitosan-Catechol: A Polymer with Long-Lasting Mucoadhesive Properties. *Biomaterials* **2015**, *52* (1), 161–170.

(19) Shin, M.; Park, S. G.; Oh, B. C.; Kim, K.; Jo, S.; Lee, M. S.; Oh, S. S.; Hong, S. H.;

Shin, E. C.; Kim, K. S.; Kang, S. W.; Lee, H. Complete Prevention of Blood Loss with Self-Sealing Haemostatic Needles. *Nat. Mater.* **2017**, *16* (1), 147–152.

(20) Ryu, J. H.; Hong, S.; Lee, H. Bio-Inspired Adhesive Catechol-Conjugated Chitosan for Biomedical Applications: A Mini Review. *Acta Biomater.* **2015**, *27*, 101–115.

(21) Lee, H.; Park, T. G.; Messersmith, P. B.; Lee, Y.; Statz, A. R.; Rho, J. Substrate-Independent Layer-by-Layer Assembly by Using Mussel-Adhesive-Inspired Polymers. *Adv. Mater.* **2008**, *20* (9), 1619–1623.

(22) Kim, E.; Song, I. T.; Lee, S.; Kim, J. S.; Lee, H.; Jang, J. H. Drawing Sticky Adeno-Associated Viruses on Surfaces for Spatially Patterned Gene Expression. *Angew. Chemie - Int. Ed.* **2012**, *51* (23), 5598–5601.

(23) Statz, A. R.; Meagher, R. J.; Barron, A. E.; Messersmith, P. B. New Peptidomimetic Polymers for Antifouling Surfaces. *J. Am. Chem. Soc.* **2005**, *127* (22), 7972–7973.

(24) Ahn, B. K.; Das, S.; Linstadt, R.; Kaufman, Y.; Martinez-Rodriguez, N. R.; Mirshafian, R.; Kesselman, E.; Talmon, Y.; Lipshutz, B. H.; Israelachvili, J. N.; et al. High-Performance Mussel-Inspired Adhesives of Reduced Complexity. *Nat. Commun.* **2015**, *6*, 8663.

(25) Chirdon, W. M.; O'Brien, W. J.; Robertson, R. E. Adsorption of Catechol and Comparative Solutes on Hydroxyapatite. *J. Biomed. Mater. Res. - Part B Appl. Biomater.* **2003**, *66* (2), 532–538.

(26) Li, Y.; Qin, M.; Li, Y.; Cao, Y.; Wang, W. Single Molecule Evidence for the Adaptive Binding of DOPA to Different Wet Surfaces. *Langmuir* **2014**, *30* (15), 4358–4366.

(27) Fortelny, R. H.; Petter-Puchner, A. H.; Walder, N.; Mittermayr, R.; Öhlinger, W.;

Heinze, A.; Redl, H. Cyanoacrylate Tissue Sealant Impairs Tissue Integration of Macroporous Mesh in Experimental Hernia Repair. *Surg. Endosc. Other Interv. Tech.* **2007**, *21* (10), 1781–1785.

(28) Kocherov, S.; Lev, G.; Chertin, B. Use of BioGlue Surgical Adhesive in Hypospadias Repair. *Curr. Urol.* **2014**, *7* (3), 132–135.

(29) Montanaro, L.; Arciola, C. R.; Cenni, E.; Ciapetti, G.; Savioli, F.; Filippini, F.; Barsanti, L. A. Cytotoxicity, Blood Compatibility and Antimicrobial Activity of Two Cyanoacrylate Glues for Surgical Use. *Biomaterials* **2000**, *22* (1), 59–66.

(30) Fürst, W.; Banerjee, A. Release of Glutaraldehyde from an Albumin-Glutaraldehyde Tissue Adhesive Causes Significant in Vitro and in Vivo Toxicity. *Ann. Thorac. Surg.* **2005**, *79* (5), 1522–1528.

(31) Klimo, P.; Khalil, A.; Slotkin, J. R.; Smith, E. R.; Scott, R. M.; Goumnerova, L. C. Wound Complications Associated with the Use of Bovine Serum Albumin-Glutaraldehyde Surgical Adhesive in Pediatric Patients. *Neurosurgery* **2007**, *60* (4 SUPPL. 2), 305–309.

(32) Saiz-Poseu, J.; Mancebo-Aracil, J.; Nador, F.; Busqué, F.; Ruiz-Molina, D. The Chemistry behind Catechol-Based Adhesion. *Angew. Chemie - Int. Ed.* **2019**, *58* (3), 696–714.

(33) Maier, G. P.; Rapp, M. V; Waite, J. H.; Israelachvili, J. N.; Butler, A. Adaptive Synergy between Catechol and Lysine Promotes Wet Adhesion by Surface Salt Displacement. *Science* **2015**, *349* (6248), 625–628.

(34) Rapp, M. V; Maier, G. P.; Dobbs, H. A.; Higdon, N. J.; Waite, J. H.; Butler, A.; Israelachvili, J. N. Defining the Catechol-Cation Synergy for Enhanced Wet

Adhesion to Mineral Surfaces. *J. Am. Chem. Soc.* **2016**, *138* (29), 9013–9016.

(35) Li, Y.; Wang, T.; Xia, L.; Wang, L.; Qin, M.; Li, Y.; Wang, W.; Cao, Y. Single Molecule Study of the Synergistic Effects of Positive Charges and Dopa for Wet Adhesion. *J. Mater. Chem. B* **2017**, *5*, 4416–4420.

(36) Sandy, M.; Butler, A. Chrysobactin Siderophores Produced by Dickeya Chrysanthemi Ec16. *J. Nat. Prod.* **2011**, *74* (5), 1207–1212.

(37) Paria, S.; Khilar, K. C. A Review on Experimental Studies of Surfactant Adsorption at the Hydrophilic Solid-Water Interface. *Adv. Colloid Interface Sci.* **2004**, *110* (3), 75–95.

(38) Halperin, A. Polymer Brushes That Resist Adsorption of Model Proteins: Design Parameters. *Langmuir* **1999**, *15* (7), 2525–2533.

(39) Ramachandran, G. N.; Ramakrishnan, C.; Sasisekharan, V. Stereochemistry of Polypeptide Chain Configurations. *J. Mol. Biol.* **1963**, *7* (1), 95–99.

(40) Gebbie, M. A.; Wei, W.; Schrader, A. M.; Cristiani, T. R.; Dobbs, H. A.; Idso, M.; Chmelka, B. F.; Waite, J. H.; Israelachvili, J. N. Tuning Underwater Adhesion with Cation–π Interactions. *Nat. Chem.* **2017**, *9*, 473–479.

(41) Hong, S.; Wang, Y.; Park, S. Y.; Lee, H. Progressive Fuzzy Cation- Assembly of Biological Catecholamines. *Sci. Adv.* **2018**, *4* (9), eaat7457.

(42) Wei, W.; Yu, J.; Gebbie, M. A.; Tan, Y.; Martinez Rodriguez, N. R.; Israelachvili, J. N.; Waite, J. H. Bridging Adhesion of Mussel-Inspired Peptides: Role of Charge, Chain Length, and Surface Type. *Langmuir* **2015**, *31* (3), 1105–1112.

(43) Bell, G. I. Models for the Specific Adhesion of Cells to Cells. *Science* **1978**, *200*, 618–627.

(44) Petrone, L.; Kumar, A.; Sutanto, C. N.; Patil, N. J.; Kannan, S.; Palaniappan, A.; Amini, S.; Zappone, B.; Verma, C.; Miserez, A. Mussel Adhesion Is Dictated by Time-Regulated Secretion and Molecular Conformation of Mussel Adhesive Proteins. *Nat. Commun.* **2015**, *6* (4), 8737.

(45) Li, Y.; Liang, C.; Gao, L.; Li, S.; Zhang, Y.; Zhang, J.; Cao, Y. Hidden Complexity of Synergistic Roles of Dopa and Lysine for Strong Wet Adhesion. *Mater. Chem. Front.* **2017**, *1* (12), 2664–2668.

(46) Degen, G. D.; Stow, P. R.; Lewis, R. B.; Andresen Eguiluz, R. C.; Valois, E.; Kristiansen, K.; Butler, A.; Israelachvili, J. N. Impact of Molecular Architecture and Adsorption Density on Adhesion of Mussel-Inspired Surface Primers with Catechol-Cation Synergy. *J. Am. Chem. Soc.* **2019**, *141* (47), 18673–18681.

(47) Shin, M.; Shin, J. Y.; Kim, K.; Yang, B.; Han, J. W.; Kim, N. K.; Cha, H. J. The Position of Lysine Controls the Catechol-Mediated Surface Adhesion and Cohesion in Underwater Mussel Adhesion. *J. Colloid Interface Sci.* **2020**, *563*, 168–176.

(48) Mu, Y.; Mu, P.; Wu, X.; Wan, X. The Two Facets of the Synergic Effect of Amine Cation and Catechol on the Adhesion of Catechol in Underwater Conditions. *Appl. Surf. Sci.* **2020**, *530*, 146973.

(49) Tiu, B. D. B.; Delparastan, P.; Ney, M. R.; Gerst, M.; Messersmith, P. Cooperativity of Catechols and Amines in High Performance Dry/Wet Adhesives. *Angew. Chemie Int. Ed.* **2020**, *59* (38), 16616–16624.

(50) Li, Y.; Cheng, J.; Delparastan, P.; Wang, H.; Sigg, S. J.; DeFrates, K. G.; Cao, Y.; Messersmith, P. B. Molecular Design Principles of Lysine-DOPA Wet Adhesion. *Nat. Commun.* **2020**, *11* (1), 1–8.

(51) Wang, J.; Tahir, M. N.; Kappl, M.; Tremel, W.; Metz, N.; Barz, M.; Theato, P.; Butt, H. J. Influence of Binding-Site Density in Wet Bioadhesion. *Adv. Mater.* **2008**, *20* (20), 3872–3876.

(52) Bilotto, P.; Labate, C.; De Santo, M. P.; Deepankumar, K.; Miserez, A.; Zappone, B. Adhesive Properties of Adsorbed Layers of Two Recombinant Mussel Foot Proteins with Different Levels of DOPA and Tyrosine. *Langmuir* **2019**, *35* (48), 15481–15490.

(53) Lee, B. P.; Chao, C. Y.; Nelson Nunalee, F.; Motan, E.; Shull, K. R.; Messersmith, P. B. Rapid Gel Formation and Adhesion in Photocurable and Biodegradable Block Copolymers with High DOPA Content. *Macromolecules* **2006**, *39* (5), 1740–1748.

(54) Anderson, T. H.; Yu, J.; Estrada, A.; Hammer, M. U.; Herbert Waite, J.; Israelachvili, J. N. The Contribution of DOPA to Substrate–Peptide Adhesion and Internal Cohesion of Mussel-Inspired Synthetic Peptide Films. *Adv Funct Mater* **2010**, *8* (2023), 4196–4205.

(55) Yu, J.; Wei, W.; Danner, E.; Israelachvili, J. N.; Herbert Waite, J.; Waite, J. H. Effects of Interfacial Redox in Mussel Adhesive Protein Films on Mica. *Adv Mater* **2011**, *23* (20), 2362–2366.

(56) Yu, J.; Wei, W.; Danner, E.; Ashley, R. K.; Israelachvili, J. N.; Waite, J. H. Mussel Protein Adhesion Depends on Interprotein Thiol-Mediated Redox Modulation. *Nat. Chem. Biol.* **2011**, *7* (9), 588–590.

(57) Wonderly, W. R.; Cristiani, T. R.; Cunha, K. C.; Degen, G. D.; Shea, J. E.; Waite, J. H. Dueling Backbones: Comparing Peptoid and Peptide Analogues of a Mussel Adhesive Protein. *Macromolecules* **2020**, *53* (16), 6767–6779.

(58) Ou, X.; Xue, B.; Lao, Y.; Wutthinitikornkit, Y.; Tian, R.; Zou, A.; Yang, L.; Wang,

W.; Cao, Y.; Li, J. Structure and Sequence Features of Mussel Adhesive Protein Lead to Its Salt-Tolerant Adhesion Ability. *Sci. Adv.* **2020**, *6* (39), eabb7620.

(59) Fan, H.; Wang, J.; Tao, Z.; Huang, J.; Rao, P.; Kurokawa, T.; Gong, J. P. Adjacent Cationic–Aromatic Sequences Yield Strong Electrostatic Adhesion of Hydrogels in Seawater. *Nat. Commun.* **2019**, *10* (1), 1–8.

(60) Kanyalkar, M.; Srivastava, S.; Coutinho, E. Conformation of a Model Peptide of the Tandem Repeat Decapeptide in Mussel Adhesive Protein by NMR and MD Simulations. *Biomaterials* **2002**, *23* (2), 389–396.

(61) Levine, Z. A.; Rapp, M. V; Wei, W.; Mullen, R. G.; Wu, C.; Zerze, G. H.; Mittal, J.; Waite, J. H.; Israelachvili, J. N.; Shea, J.-E. Surface Force Measurements and Simulations of Mussel-Derived Peptide Adhesives on Wet Organic Surfaces. *Proc. Natl. Acad. Sci. U. S. A.* **2016**, *113* (16), 4332–4337.

(62) Anand, P. P.; Vardhanan, Y. S. Computational Modelling of Wet Adhesive Mussel Foot Proteins (Bivalvia): Insights into the Evolutionary Convolution in Diverse Perspectives. *Sci. Rep.* **2020**, *10* (1), 1–24.

(63) Chen, A. B.; Shao, Q.; Hall, C. K. Molecular Simulation Study of 3,4-Dihydroxyphenylalanine in the Context of Underwater Adhesive Design. *J. Chem. Phys.* **2021**, *154* (14), 144702.

(64) Wei, W.; Yu, J.; Broomell, C.; Israelachvili, J. N.; Waite, J. H. Hydrophobic Enhancement of Dopa-Mediated Adhesion in a Mussel Foot Protein. *J. Am. Chem. Soc.* **2013**, *135* (1), 377–383.

(65) Papov, V. V.; Diamond, T. V.; Biemann, K.; Waite, J. H. Hydroxyarginine-Containing Polyphenolic Proteins in the Adhesive Plaques of the Marine Mussel

Mytilus Edulis. *J. Biol. Chem.* **1995**, *270* (34), 20183–20192.

(66) Wei, W.; Petrone, L.; Tan, Y.; Cai, H.; Israelachvili, J. N.; Miserez, A.; Waite, J. H. An Underwater Surface-Drying Peptide Inspired by a Mussel Adhesive Protein. *Adv. Funct. Mater.* **2016**, *26* (20), 3496–3507.

(67) Marumo, K.; Waite, J. H. Optimization of Hydroxylation of Tyrosine and Tyrosine-Containing Peptides by Mushroom Tyrosinase. *Biochim. Biophys. Acta* **1986**, *872*, 98–103.

(68) Derjaguin, B. V.; Muller, V. M.; Toporov, Y. P. Effect of Contact Deformations on the Adhesion of Particles. *J. Colloid Interface Sci.* **1975**, *53* (2), 314–326.

(69) Berendsen, H.J.C., Postma, J.P.M., Van Gunsteren, W.F. and Hermans, J. Interaction Models for Water in Relation to Protein Hydration. In *Intermolecular Forces*; Pullman, B., Ed.; Reidel Publishing Company: Dordrecht, 1981.

(70) Van Der Spoel, D.; Lindahl, E.; Hess, B.; Groenhof, G.; Mark, A. E.; Berendsen, H. J. C. GROMACS: Fast, Flexible, and Free. *J. Comput. Chem.* **2005**, *26* (16), 1701–1718.

(71) Oostenbrink, C.; Villa, A.; Mark, A. E.; Van Gunsteren, W. F. A Biomolecular Force Field Based on the Free Enthalpy of Hydration and Solvation: The GROMOS Force-Field Parameter Sets 53A5 and 53A6. *J. Comput. Chem.* **2004**, *25* (13), 1656–1676.

(72) Beauchamp, K. A.; Lin, Y. S.; Das, R.; Pande, V. S. Are Protein Force Fields Getting Better? A Systematic Benchmark on 524 Diverse NMR Measurements. *J. Chem. Theory Comput.* **2012**, *8* (4), 1409–1414.

(73) Wang, J.; Wolf, R. M.; Caldwell, J. W.; Kollman, P. A.; Case, D. A. Development and Testing of a General Amber Force Field. *J. Comput. Chem.* **2004**, *25* (9), 1157–

1174.

(74) Jorgensen, W. L.; Chandrasekhar, J.; Madura, J. D.; Impey, R. W.; Klein, M. L. Comparison of Simple Potential Functions for Simulating Liquid Water. *J. Chem. Phys.* **1983**, *79* (2), 926–935.

(75) Das, S.; Lee, B. H.; Linstadt, R. T. H.; Cunha, K.; Li, Y.; Kaufman, Y.; Levine, Z. A.; Lipshutz, B. H.; Lins, R. D.; Shea, J. E.; Heeger, A. J.; Kollbe Ahn, B. Molecularly Smooth Self-Assembled Monolayer for High-Mobility Organic Field-Effect Transistors. *Nano Lett.* **2016**, *16* (10), 6709–6715.

(76) Hoover, W. G. Canonical Dynamics: Equilibrium Phase-Space Distributions. *Phys. Rev. A* **1985**, *31* (3), 1695–1697.

(77) Hess, B.; Bekker, H.; Berendsen, H. J. C.; Fraaije, J. G. E. M. LINCS: A Linear Constraint Solver for Molecular Simulations. *J. Comput. Chem.* **1997**, *18* (12), 1463–1472.

(78) Miyamoto, S.; Kollman, P. A. Settle: An Analytical Version of the SHAKE and RATTLE Algorithm for Rigid Water Models. *J. Comput. Chem.* **1992**, *13* (8), 952–962.

(79) Hockney, R. W. The Potential Calculation and Some Applications. In *Methods in Computational Physics, Vol. 9*; Alder, B., Fernbach, S., Rotenberg, M., Eds.; Academic Press: New York/London, 1970; Vol. 9, pp 135–211.

(80) Darden, T.; York, D.; Pedersen, L. Particle Mesh Ewald: An N·log(N) Method for Ewald Sums in Large Systems. *J. Chem. Phys.* **1993**, *98* (12), 10089–10092.

(81) Páll, S.; Hess, B. A Flexible Algorithm for Calculating Pair Interactions on SIMD Architectures. *Comput. Phys. Commun.* **2013**, *184* (12), 2641–2650.

(82) Berendsen, H. J. C.; Postma, J. P. M.; Van Gunsteren, W. F.; Dinola, A.; Haak, J. R. Molecular Dynamics with Coupling to an External Bath. *J. Chem. Phys.* **1984**, *81* (8), 3684–3690.

(83) Dequidt, A.; Devémy, J.; Malfreyt, P. Confined KCl Solution between Two Mica Surfaces: Equilibrium and Frictional Properties. *J. Phys. Chem. C* **2015**, *119* (38), 22080–22085.

(84) Heinz, H.; Koerner, H.; Anderson, K. L.; Vaia, R. A.; Farmer, B. L. Force Field for Mica-Type Silicates and Dynamics of Octadecylammonium Chains Grafted to Montmorillonite. *Chem. Mater.* **2005**, *17* (23), 5658–5669.

(85) Daura, X.; Gademann, K.; Schäfer, H.; Jaun, B.; Seebach, D.; Van Gunsteren, W. F. The β-Peptide Hairpin in Solution: Conformational Study of a β-Hexapeptide in Methanol by NMR Spectroscopy and MD Simulation. *J. Am. Chem. Soc.* **2001**, *123* (10), 2393–2404.

(86) Kabsch, W.; Sander, C. Dictionary of Protein Secondary Structure: Pattern Recognition of Hydrogen-bonded and Geometrical Features. *Biopolymers* **1983**, *22* (12), 2577–2637.

(87) Touw, W. G.; Baakman, C.; Black, J.; Te Beek, T. A. H.; Krieger, E.; Joosten, R. P.; Vriend, G. A Series of PDB-Related Databanks for Everyday Needs. *Nucleic Acids Res.* **2015**, *43* (D1), D364–D368.

(88) Humphrey, W.; Dalke, A.; Schulten, K. VMD: Visual Molecular Dynamics. *J. Mol. Graph.* **1996**, *14* (1), 33–38.

(89) Counterman, A. E.; Clemmer, D. E. Volumes of Individual Amino Acid Residues in Gas-Phase Peptide Ions. *J. Am. Chem. Soc.* **1999**, *121* (16), 4031–4039.

(90) Kamino, K. Mini-Review: Barnacle Adhesives and Adhesion. *Biofouling* **2013**, *29* (6), 735–749.

(91) Zhao, H.; Sun, C.; Stewart, R. J.; Waite, J. H. Cement Proteins of the Tube-Building Polychaete. *J. Biol. Chem.* **2005**, *280* (52), 42938–42944.

(92) Tiu, B. D. B.; Delparastan, P.; Ney, M. R.; Gerst, M.; Messersmith, P. B. Enhanced Adhesion and Cohesion of Bioinspired Dry/Wet Pressure-Sensitive Adhesives. *ACS Appl. Mater. Interfaces* **2019**, *11* (31), 28296–28306.

(93) Hwang, D. S.; Zeng, H.; Masic, A.; Harrington, M. J.; Israelachvili, J. N.; Waite, J. H. Protein- and Metal-Dependent Interactions of a Prominent Protein in Mussel Adhesive Plaques. *J. Biol. Chem.* **2010**, *285* (33), 25850–25858.

(94) Yu, J.; Wei, W.; Menyo, M. S.; Masic, A.; Waite, J. H.; Israelachvili, J. N. Adhesion of Mussel Foot Protein-3 to TiO_2 Surfaces: The Effect of PH. *Biomacromolecules* **2013**, *14* (4), 1072–1077.

(95) Israelachvili, J. N. Thin Film Studies Using Multiple-Beam Interferometry. *J. Colloid Interface Sci.* **1973**, *44* (2), 259–272.

(96) Schwenzfeier, K. A.; Erbe, A.; Bilotto, P.; Lengauer, M.; Merola, C.; Cheng, H. W.; Mears, L. L. E.; Valtiner, M. Optimizing Multiple Beam Interferometry in the Surface Forces Apparatus: Novel Optics, Reflection Mode Modeling, Metal Layer Thicknesses, Birefringence, and Rotation of Anisotropic Layers. *Rev. Sci. Instrum.* **2019**, *90* (4), 043908.

(97) Johnson, K. L. *Contact Mechanics*; Cambridge University Press: Cambridge, 1985.

(98) Schweigert, N.; Zehnder, A. J. B.; Eggen, R. I. L. Chemical Properties of Catechols and Their Molecular Modes of Toxic Action in Cells, from Microorganisms to

Mammals. *Environ. Microbiol.* **2001**, *3* (2), 81–91.

(99) Zhou, Y. Z.; Alany, R. G.; Chuang, V.; Wen, J. Studies of the Rate Constant of L-DOPA Oxidation and Decarboxylation by HPLC. *Chromatographia* **2012**, *75* (11–12), 597–606.

(100) Maier, G. P.; Bernt, C. M.; Butler, A. Catechol Oxidation: Considerations in the Design of Wet Adhesive Materials. *Biomater. Sci.* **2018**, *6* (2), 332–339.

(101) Gallivan, J. P.; Dougherty, D. A. A Computational Study of Cation-π Interactions vs Salt Bridges in Aqueous Media: Implications for Protein Engineering. *J. Am. Chem. Soc.* **2000**, *122* (5), 870–874.

(102) Faghihnejad, A.; Zeng, H. Hydrophobic Interactions between Polymer Surfaces: Using Polystyrene as a Model System. *Soft Matter* **2012**, *8* (9), 2746.

(103) Faghihnejad, A.; Zeng, H. Interaction Mechanism between Hydrophobic and Hydrophilic Surfaces: Using Polystyrene and Mica as a Model System. *Langmuir* **2013**, *29* (40), 12443–12451.

(104) Mangipudi, V. S.; Tirrell, M. Contact-Mechanics-Based Studies of Adhesion between Polymers. *Rubber Chem. Technol.* **1998**, *71* (3), 407–448.

(105) Robertson, R. E. The Fracture Energy of Low Molecular Weight Fractions of Polystyrene. In *Toughness and Brittleness of Plastics*; UTC, 1976; Vol. 19, pp 89–96.

(106) Li, L.; Mangipudi, V. S.; Tirrell, M.; Pocius, A. V. Direct Measurement of Surface and Interfacial Energies of Glassy Polymers and Pdms. In *Fundamentals of Tribology and Bridging the Gap Between the Macro- and Micro/Nanoscales*; Springer Netherlands: Dordrecht, 2012; pp 305–329.

(107) Ruths, M. Characterization of Molecularly Thin Polymer Layers with the Surface

Forces Apparatus (SFA). In *Functional Polymer Films*; 2011; pp 745–769.

(108) Tirrell, M. Measurement of Interfacial Energy at Solid Polymer Surfaces. *Langmuir* **1996**, *12* (19), 4548–4551.

(109) Maeda, N.; Chen, N.; Tirrell, M.; Israelachvili, J. N. Adhesion and Friction Mechanisms of Polymer-on-Polymer Surfaces. *Science* **2002**, *297* (5580), 379–382.

(110) Chen, N.; Maeda, N.; Tirrell, M.; Israelachvili, J. Adhesion and Friction of Polymer Surfaces: The Effect of Chain Ends. *Macromolecules* **2005**, *38* (8), 3491–3503.

(111) Zeng, H.; Maeda, N.; Chen, N.; Tirreh, M.; Israelachvili, J. Adhesion and Friction of Polystyrene Surfaces around T G. *Macromolecules* **2006**, *39* (6), 2350–2363.

(112) Zeng, H.; Tirrell, M.; Israelachvili, J. Limit Cycles in Dynamic Adhesion and Friction Processes: A Discussion. *J. Adhes.* **2006**, *82* (9), 933–943.

(113) Zeng, H.; Zhao, B.; Israelachvili, J. N.; Tirrell, M. Liquid- to Solid-like Failure Mechanism of Thin Polymer Films at Micro- and Nanoscales. *Macromolecules* **2010**, *43* (1), 538–542.

(114) Zeng, H.; Huang, J.; Tian, Y.; Li, L.; Tirrell, M. V.; Israelachvili, J. N. Adhesion and Detachment Mechanisms between Polymer and Solid Substrate Surfaces: Using Polystyrene-Mica as a Model System. *Macromolecules* **2016**, *49* (14), 5223–5231.

(115) Klein, J. The Interdiffusion of Polymers. *Science* **1990**, *250* (4981), 640–646.

(116) Chennevière, A.; Drockenmuller, E.; Damiron, D.; Cousin, F.; Boué, F.; Restagno, F.; Léger, L. Quantitative Analysis of Interdigitation Kinetics between a Polymer Melt and a Polymer Brush. *Macromolecules* **2013**, *46* (17), 6955–6962.

(117) Geoghegan, M.; Clarke, C. J.; Boué, F.; Menelle, A.; Russ, T.; Bucknall, D. G. The Kinetics of Penetration of Grafted Polymers into a Network. *Macromolecules* **1999**,

32 (15), 5106–5114.

(118) Lee, L.-H. Adhesion of High Polymers. I. Influence of Diffusion, Adsorption, and Physical State on Polymer Adhesion. *J. Polym. Sci. Part A-2 Polym. Phys.* **1967**, *5* (4), 751–760.

(119) Keddie, J. L.; Jones, R. A. L.; Cory, R. A. Interface and Surface Effects on the Glass-Transition Temperature in Thin Polymer Films. *Faraday Discuss.* **1994**, *98*, 219–230.

(120) Sharp, J. S.; Forrest, J. A. Free Surfaces Cause Reductions in the Glass Transition Temperature of Thin Polystyrene Films. *Phys. Rev. Lett.* **2003**, *91* (23).

(121) Z. Fakhraai; Forrest, J. A. Measuring the Surface Dynamics of Glassy Polymers. *Science* **2008**, *319* (5863), 600–604.

(122) Mansfield, K. F.; Theodorou, D. N. Molecular Dynamics Simulation of a Glassy Polymer Surface. *Macromolecules* **1991**, *24* (23), 6283–6294.

(123) Boiko, Y. M. Interdiffusion of Polymers with Glassy Bulk. *Colloid Polym. Sci.* **2011**, *289* (17–18), 1847–1854.

(124) Boiko, Y. M. Is Adhesion between Amorphous Polymers Sensitive to the Bulk Glass Transition? *Colloid Polym. Sci.* **2013**, *291* (9), 2259–2262.

(125) Israelachvili, J.; Min, Y.; Akbulut, M.; Alig, A.; Carver, G.; Greene, W.; Kristiansen, K.; Meyer, E.; Pesika, N.; Rosenberg, K.; Zeng, H. Recent Advances in the Surface Forces Apparatus (SFA) Technique. *Reports Prog. Phys.* **2010**, *73* (3), 036601.

(126) Israelachvili, J. N.; Alcantar, N. A.; Maeda, N.; Mates, T. E.; Ruths, M. Preparing Contamination-Free Mica Substrates for Surface Characterization, Force Measurements, and Imaging. *Langmuir* **2004**, *20* (9), 3616–3622.

(127) *Physical Properties of Polymers Handbook*; Mark, J. E., Ed.; Springer, 2007.

(128) Bailey, A. I.; Kay, S. M. Measurement of Refractive Index and Dispersion of Mica, Employing Multiple Beam Interference Techniques. *Br. J. Appl. Phys.* **1965**, *16* (1), 39–44.

(129) Keddie, J. L.; Jones, R. A. L.; Cory, R. A. Size-Dependent Depression of the Glass Transition Temperature in Polymer Films. *EPL* **1994**, *27* (1), 59–64.

(130) Tabor, D. Surface Forces and Surface Interactions. *J. Colloid Interface Sci.* **1977**, *58* (1), 2–13.

(131) McGuiggan, P. M.; Wallace, J. S.; Smith, D. T.; Sridhar, I.; Zheng, Z. W.; Johnson, K. L. Contact Mechanics of Layered Elastic Materials: Experiment and Theory. *J. Phys. D. Appl. Phys.* **2007**, *40* (19), 5984–5994.

(132) Zhang, G.; Wei, Z.; Ferrell, R. E.; Guggenheim, S.; Cygan, R. T.; Luo, J. Evaluation of the Elasticity Normal to the Basal Plane of Non-Expandable 2:1 Phyllosilicate Minerals by Nanoindentation. *Am. Mineral.* **2010**, *95* (5–6), 863–869.

(133) Christensen, N. I. Poisson's Ratio and Crustal Seismology. *J. Geophys. Res.* **1996**, *101* (B2), 3139–3156.

(134) Wool, R. P.; O'Connor, K. M. Craze Healing in Polymer Glasses. *Polym. Eng. Sci.* **1981**, *21* (14), 970–977.

(135) Prager, S.; Tirrell, M. The Healing Process at Polymer-Polymer Interfaces. *J. Chem. Phys.* **1981**, *75* (10), 5194–5198.

(136) Gent, A. N.; Lai, S.-M. Adhesion and Autohesion of Rubber Compounds: Effect of Surface Roughness. *Rubber Chem. Technol.* **1995**, *68* (1), 13–25.

(137) Padhye, N.; Parks, D. M.; Trout, B. L.; Slocum, A. H. A New Phenomenon: Sub-T g, Solid-State, Plasticity-Induced Bonding in Polymers. *Sci. Rep.* **2017**, *7*, 46405.

(138) Barus, C. Isothermals, Isopiestics and Isometrics Relative to Viscosity. *Am. J. Sci.* **1893**, *45* (266), 87–96.

(139) Kadijk, S. E.; Van Den Brule, B. H. A. A. On the Pressure Dependency of the Viscosity of Molten Polymers. *Polym. Eng. Sci.* **1994**, *34* (20), 1535–1546.

(140) Sedlacek, T.; Zatloukal, M.; Filip, P.; Boldizar, A.; Saha, P. On the Effect of Pressure on the Shear and Elongational Viscosities of Polymer Melts. In *Polymer Engineering and Science*; John Wiley & Sons, Ltd, 2004; Vol. 44, pp 1328–1337.

(141) Reynolds, C.; Thompson, R.; Mcleish, T. Pressure and Shear Rate Dependence of the Viscosity and Stress Relaxation of Polymer Melts. **2018**, *62*, 631–642.

(142) Ruths, M.; Granick, S. Rate-Dependent Adhesion between Polymer and Surfactant Monolayers on Elastic Substrates. *Langmuir* **1998**, *14* (7), 1804–1814.

(143) Horn, R. G.; Israelachvili, J. N.; Pribac, F. Measurement of the Deformation and Adhesion of Solids in Contact. *J. Colloid Interface Sci.* **1987**, *115* (2), 480–492.

(144) Rubinstein, M.; Colby, R. H. *Polymer Physics*; Oxford University Press, 2003.

(145) Fetters, L. J.; Lohse, D. J.; Colby, R. H. Chain Dimensions and Entanglement Spacings. In *Physical Properties of Polymers Handbook*; Springer New York: New York, NY, 2007; pp 447–454.

(146) Teshima, R.; Otsuka, T.; Takasu, N.; Yamagata, N.; Yamamoto, K. Structure of the Most Superficial Layer of Articular Cartilage. *J. Bone Jt. Surg. - Ser. B* **1995**, *77* (3), 460–464.

(147) Crockett, R.; Roos, S.; Rossbach, P.; Dora, C.; Born, W.; Troxler, H. Imaging of the Surface of Human and Bovine Articular Cartilage with ESEM and AFM. *Tribol. Lett.* **2005**, *19* (4), 311–317.

(148) Fujioka, R.; Aoyama, T.; Takakuwa, T. The Layered Structure of the Articular Surface. *Osteoarthr. Cartil.* **2013**, *21* (8), 1092–1098.

(149) Reitsma, S.; Slaaf, D. W.; Vink, H.; Van Zandvoort, M. A. M. J.; Oude Egbrink, M. G. A. The Endothelial Glycocalyx: Composition, Functions, and Visualization. *Pflugers Arch. Eur. J. Physiol.* **2007**, *454* (3), 345–359.

(150) Hodges, R. R.; Dartt, D. A. Tear Film Mucins: Front Line Defenders of the Ocular Surface; Comparison with Airway and Gastrointestinal Tract Mucins. *Exp. Eye Res.* **2013**, *117*, 62–78.

(151) Hattrup, C. L.; Gendler, S. J. Structure and Function of the Cell Surface (Tethered) Mucins. *Annu. Rev. Physiol.* **2008**, *70* (1), 431–457.

(152) Atuma, C.; Strugala, V.; Allen, A.; Holm, L. The Adherent Gastrointestinal Mucus Gel Layer: Thickness and Physical State in Vivo. *Am. J. Physiol. - Gastrointest. Liver Physiol.* **2001**, *280* (5), G922–G929.

(153) Caló, E.; Khutoryanskiy, V. V. Biomedical Applications of Hydrogels: A Review of Patents and Commercial Products. *Eur. Polym. J.* **2015**, *65*, 252–267.

(154) Peppas, N. A.; Bures, P.; Leobandung, W.; Ichikawa, H. Hydrogels in Pharmaceutical Formulations. *Eur. J. Pharm. Biopharm.* **2000**, *50* (1), 27–46.

(155) Kirschner, C. M.; Anseth, K. S. Hydrogels in Healthcare: From Static to Dynamic Material Microenvironments. *Acta Mater.* **2013**, *61* (3), 931–944.

(156) Galli, M.; Oyen, M. L. Spherical Indentation of a Finite Poroelastic Coating. *Appl. Phys. Lett.* **2008**, *93* (3), 31911.

(157) Oyen, M. L. Mechanical Characterisation of Hydrogel Materials. *Int. Mater. Rev.* **2014**, *59* (1), 44–59.

(158) Chan, E. P.; Hu, Y.; Johnson, P. M.; Suo, Z.; Stafford, C. M. Spherical Indentation Testing of Poroelastic Relaxations in Thin Hydrogel Layers. *Soft Matter* **2012**, *8* (5), 1492–1498.

(159) Galli, M.; Comley, K. S. C.; Shean, T. A. V.; Oyen, M. L. Viscoelastic and Poroelastic Mechanical Characterization of Hydrated Gels. *J. Mater. Res.* **2009**, *24* (3), 973–979.

(160) Hu, Y.; Zhao, X.; Vlassak, J. J.; Suo, Z. Using Indentation to Characterize the Poroelasticity of Gels. *Appl. Phys. Lett.* **2010**, *96* (12), 121904.

(161) Reale, E. R.; Dunn, A. C. Poroelasticity-Driven Lubrication in Hydrogel Interfaces. *Soft Matter* **2017**, *13* (2), 428–435.

(162) Esteki, M. H.; Alemrajabi, A. A.; Hall, C. M.; Sheridan, G. K.; Azadi, M.; Moeendarbary, E. A New Framework for Characterization of Poroelastic Materials Using Indentation. *Acta Biomater.* **2020**, *102*, 138–148.

(163) Kalcioglu, Z. I.; Mahmoodian, R.; Hu, Y.; Suo, Z.; Van Vliet, K. J. From Macro- to Microscale Poroelastic Characterization of Polymeric Hydrogels via Indentation. *Soft Matter* **2012**, *8* (12), 3393–3398.

(164) Delavoipière, J.; Tran, Y.; Verneuil, E.; Chateauminois, A. Poroelastic Indentation of Mechanically Confined Hydrogel Layers. *Soft Matter* **2016**, *12* (38), 8049–8058.

(165) Delavoipière, J.; Tran, Y.; Verneuil, E.; Heurtefeu, B.; Hui, C. Y.; Chateauminois, A. Friction of Poroelastic Contacts with Thin Hydrogel Films. *Langmuir* **2018**, *34* (33), 9617–9626.

(166) Ciapa, L.; Delavoipière, J.; Tran, Y.; Verneuil, E.; Chateauminois, A. Transient Sliding of Thin Hydrogel Films: The Role of Poroelasticity. *Soft Matter* **2020**, *16*,

6539–6548.

(167) Xiang, L.; Zhang, J.; Gong, L.; Zeng, H. Surface Forces and Interaction Mechanisms of Soft Thin Films under Confinement: A Short Review. *Soft Matter* **2020**, *16* (29), 6697–6719.

(168) Heuberger, M. The Extended Surface Forces Apparatus. Part I. Fast Spectral Correlation Interferometry. *Rev. Sci. Instrum.* **2001**, *72* (3), 1700–1707.

(169) Kristiansen, K.; Donaldson, S. H.; Berkson, Z. J.; Scott, J.; Su, R.; Banquy, X.; Lee, D. W.; De Aguiar, H. B.; McGraw, J. D.; Degen, G. D.; Israelachvili, J. N. Multimodal Miniature Surface Forces Apparatus (MSFA) for Interfacial Science Measurements. *Langmuir* **2019**, *35* (48), 15500–15514.

(170) Zappone, B.; Patil, N. J.; Lombardo, M.; Lombardo, G. Transient Viscous Response of the Human Cornea Probed with the Surface Force Apparatus. *PLoS One* **2018**, *13* (5), e0197779.

(171) Wang, K.; Andresen Eguiluz, R. C.; Wu, F.; Seo, B. R.; Fischbach, C.; Gourdon, D. Stiffening and Unfolding of Early Deposited-Fibronectin Increase Proangiogenic Factor Secretion by Breast Cancer-Associated Stromal Cells. *Biomaterials* **2015**, *54*, 63–71.

(172) Shoaib, T.; Yuh, C.; Wimmer, M. A.; Schmid, T. M.; Espinosa-Marzal, R. M. Nanoscale Insight into the Degradation Mechanisms of the Cartilage Articulating Surface Preceding OA. *Biomater. Sci.* **2020**, *8*, 3944–3955.

(173) Meier, Y. A.; Zhang, K.; Spencer, N. D.; Simic, R. Linking Friction and Surface Properties of Hydrogels Molded against Materials of Different Surface Energies. *Langmuir* **2019**, *35* (48), 15805–15812.

(174) Schulze, K. D.; Hart, S. M.; Marshall, S. L.; O'Bryan, C. S.; Urueña, J. M.; Pitenis, A. A.; Sawyer, W. G.; Angelini, T. E. Polymer Osmotic Pressure in Hydrogel Contact Mechanics. *Biotribology* **2017**, *11*, 3–7.

(175) Wu, S.; Shanks, R. A. Solubility Study of Polyacrylamide in Polar Solvents. *J. Appl. Polym. Sci.* **2004**, *93* (3), 1493–1499.

(176) Erfkamp, J.; Guenther, M.; Gerlach, G. Hydrogel-Based Piezoresistive Sensor for the Detection of Ethanol. *J. Sensors Sens. Syst.* **2018**, *7* (1), 219–226.

(177) de Gennes, P. G. *Scaling Concepts in Polymer Physics*; Cornell University Press: Ithaca, NY, 1979.

(178) Oloyede, A.; Flachsmann, R.; Broom, N. D. The Dramatic Influence of Loading Velocity on the Compressive Response of Articular Cartilage. *Connect. Tissue Res.* **1992**, *27* (4), 211–224.

(179) Moeendarbary, E.; Valon, L.; Fritzsche, M.; Harris, A. R.; Moulding, D. A.; Thrasher, A. J.; Stride, E.; Mahadevan, L.; Charras, G. T. The Cytoplasm of Living Cells Behaves as a Poroelastic Material. *Nat. Mater.* **2013**, *12* (3), 253–261.

(180) Masterton, S.; Ahearne, M. Mechanobiology of the Corneal Epithelium. *Exp. Eye Res.* **2018**, *177*, 122–129.

(181) Rodgers, S. J.; Lee, C. W.; Ng, C. Y.; Raymond, K. N. Ferric Ion Sequestering Agents. 15. Synthesis, Solution Chemistry, and Electrochemistry of a New Cationic Analogue of Enterobactin. *Inorg. Chem.* **1987**, *26* (10), 1622–1625.

(182) Persmark, M.; Expert, D.; Neilands, J. B. Isolation, Characterization, and Synthesis of Chrysobactin, a Compound with Siderophore Activity from Erwinia Chrysanthemi. *J. Biol. Chem.* **1989**, *264* (6), 3187–3193.

(183) Lu, C.; Buyer, J. S.; Okonya, J. F.; Miller, M. J. Synthesis of Optically Pure Chrysobactin and Immunoassay Development. *BioMetals* **1996**, *9* (4), 377–383.

(184) Dertz, E. A.; Xu, J.; Raymond, K. N. Tren-Based Analogues of Bacillibactin: Structure and Stability. *Inorg. Chem.* **2006**, *45* (14), 5465–5478.

(185) Perkin, S.; Chai, L.; Kampf, N.; Raviv, U.; Briscoe, W.; Dunlop, I.; Titmuss, S.; Seo, M.; Kumacheva, E.; Klein, J. Forces between Mica Surfaces, Prepared in Different Ways, Across Aqueous and Nonaqueous Liquids Confined to Molecularly Thin Films. *Langmuir* **2006**, *22* (14), 6142–6152.

(186) Sides, P. J.; Faruqui, D.; Gellman, A. J. Dynamics of Charging of Muscovite Mica: Measurement and Modeling. *Langmuir* **2009**, *25* (3), 1475–1481.

(187) Li, B.; Fujii, M.; Fukada, K.; Kato, T.; Seimiya, T. Time Dependent Anchoring of Adsorbed Cationic Surfactant Molecules at Mica/Solution Interface. *J. Colloid Interface Sci.* **1999**, *209* (1), 25–30.

(188) Chen, Y. L.; Chen, S.; Frank, C.; Israelachvili, J. N. Molecular Mechanisms and Kinetics during the Self-Assembly of Surfactant Layers. *J. Colloid Interface Sci.* **1992**, *1531* (1), 244–265.

(189) Weeks, J. R. The Dielectric Constant of Mica. *Phys. Rev.* **1922**, *19* (4), 319–322.

(190) Malmberg, C. G.; Maryott, A. A. Dielectric Constant of Water from 0 to 100 C. *J. Res. Natl. Bur. Stand. (1934).* **1956**, *56* (1).

(191) Teschke, O.; Ceotto, G.; de Souza, E. F. Interfacial Water Dielectric-Permittivity-Profile Measurements Using Atomic Force Microscopy. *Phys. Rev. E* **2001**, *64* (1), 10.

(192) Christenson, H. K.; Thomson, N. H. The Nature of the Air-Cleaved Mica Surface.

Surf. Sci. Rep. **2016**, *71* (2), 367–390.

(193) Schlegel, M. L.; Nagy, K. L.; Fenter, P.; Cheng, L.; Sturchio, N. C.; Jacobsen, S. D. Cation Sorption on the Muscovite (0 0 1) Surface in Chloride Solutions Using High-Resolution X-Ray Reflectivity. *Geochim. Cosmochim. Acta* **2006**, *70* (14), 3549–3565.

(194) Lee, S. S.; Fenter, P.; Nagy, K. L.; Sturchio, N. C. Monovalent Ion Adsorption at the Muscovite (001)-Solution Interface: Relationships among Ion Coverage and Speciation, Interfacial Water Structure, and Substrate Relaxation. *Langmuir* **2012**, *28* (23), 8637–8650.

(195) Kobayashi, K.; Liang, Y.; Murata, S.; Matsuoka, T.; Takahashi, S.; Nishi, N.; Sakka, T. Ion Distribution and Hydration Structure in the Stern Layer on Muscovite Surface. *Langmuir* **2017**, *33* (15), 3892–3899.

(196) Denoyel, R.; Durand, G.; Lafuma, F.; Audebert, R. Adsorption of Cationic Polyelectrolytes onto Montmorillonite and Silica: Microcalorimetric Study of Their Conformation. *J. Colloid Interface Sci.* **1990**, *139* (1), 281–290.

(197) Luckham, P. F.; Klein, J. Forces between Mica Surfaces Bearing Adsorbed Polyelectrolyte, Poly-L-Lysine, in Aqueous Media. *J. Chem. Soc. Faraday Trans. 1* **1984**, *80* (4), 865.

(198) Pasche, S.; De Paul, S. M.; Vörös, J.; Spencer, N. D.; Textor, M. Poly(l-Lysine)-Graft-Poly(Ethylene Glycol) Assembled Monolayers on Niobium Oxide Surfaces: A Quantitative Study of the Influence of Polymer Interfacial Architecture on Resistance to Protein Adsorption by ToF-SIMS and in Situ OWLS. *Langmuir* **2003**, *19* (22), 9216–9225.

(199) Degen, G. D.; Cristiani, T. R.; Cadirov, N.; Andresen Eguiluz, R. C.; Kristiansen, K.; Pitenis, A. A.; Israelachvili, J. N. Surface Damage Influences the JKR Contact Mechanics of Glassy Low-Molecular-Weight Polystyrene Films. *Langmuir* **2019**, *35* (48), 15674–15680.

(200) Israelachvili, J. N.; Adams, G. E. Measurement of Forces between Two Mica Surfaces in Aqueous Electrolyte Solutions in the Range 0-100 Nm. *J. Chem. Soc. Faraday Trans. 1 Phys. Chem. Condens. Phases* **1978**, *74* (0), 975.

(201) Rheims, J.; Köser, J.; Wriedt, T. Refractive-Index Measurements in the near-IR Using an Abbe Refractometer. *Meas. Sci. Technol.* **1997**, *8* (6), 601–605.

(202) Kohl, M.; Essenpreis, M.; Cope, M. The Influence of Glucose Concentration upon the Transport of Light in Tissue-Simulating Phantoms. *Phys. Med. Biol.* **1995**, *40* (7), 1267–1287.

(203) Scott, T. A. Refractive Index of Ethanol-Water Mixtures and Density and Refractive Index of Ethanol-Water-Ethyl Ether Mixtures. *J. Phys. Chem.* **1946**, *50* (5), 406–412.

(204) Wanless, E. J.; Christenson, H. K. Interaction between Surfaces in Ethanol: Adsorption, Capillary Condensation, and Solvation Forces. *J. Chem. Phys.* **1994**, *101* (5), 4260–4267.

(205) Pashley, R. M. Hydration Forces between Mica Surfaces in Aqueous Electrolyte Solutions. *J. Colloid Interface Sci.* **1981**, *80* (1), 153–162.

(206) Raviv, U.; Laurat, P.; Klein, J. Time Dependence of Forces between Mica Surfaces in Water and Its Relation to the Release of Surface Ions. *J. Chem. Phys.* **2002**, *116* (12), 5167–5172.

(207) Christenson, H. K.; Christenson, K. Adhesion and Surface Energy of Mica in Air and

Water. *J. Phys. Chem.* **1993**, *97* (46), 12034–12041.

(208) Kudelski, A.; Hill, W. Raman Study on the Structure of Cysteamine Monolayers on Silver. *Langmuir* **1999**, *15* (9), 3162–3168.

(209) Michota, A.; Kudelski, A.; Bukowska, J. Chemisorption of Cysteamine on Silver Studied by Surface-Enhanced Raman Scattering. *Langmuir* **2000**, *16* (26), 10236–10242.

(210) Xiao, Y.; Ju, H. X.; Chen, H. Y. Hydrogen Peroxide Sensor Based on Horseradish Peroxidase-Labeled Au Colloids Immobilized on Gold Electrode Surface by Cysteamine Monolayer. *Anal. Chim. Acta* **1999**, *391* (1), 73–82.

(211) Hoch, G.; Chauhan, A.; Radke, C. J. Permeability and Diffusivity for Water Transport through Hydrogel Membranes. *J. Memb. Sci.* **2003**, *214* (2), 199–209.

(212) Tadmor, R.; Chen, N.; Israelachvili, J. N. Thickness and Refractive Index Measurements Using Multiple Beam Interference Fringes (FECO). *J. Colloid Interface Sci.* **2003**, *264* (2), 548–553.

(213) Hecht, A. M.; Geissler, E. Dynamic Light Scattering from Polyacrylamide-Water Gels. *J. Phys.* **1978**, *39* (6), 631–638.

(214) Fernandez-Prini, R.; Dooley, R. B. Release on the Refractive Index of Ordinary Water Substance as a Function of Wavelength , Temperature and Pressure. *The International Association for the Properties of Water and Steam*. 1997, pp 1–7.

(215) Kaufman, J. D.; Klapperich, C. M. Surface Detection Errors Cause Overestimation of the Modulus in Nanoindentation on Soft Materials. *J. Mech. Behav. Biomed. Mater.* **2009**, *2* (4), 312–317.

(216) Bhattacharyya, A.; O'Bryan, C.; Ni, Y.; Morley, C. D.; Taylor, C. R.; Angelini, T. E.

Hydrogel Compression and Polymer Osmotic Pressure. *Biotribology* **2020**, *22*, 100125.

(217) Jackson, G. W.; James, D. F. The Permeability of Fibrous Porous Media. *Can. J. Chem. Eng.* **1986**, *64* (3), 364–374.

(218) Maurer, H. R. *Disc Electrophoresis and Related Techniques of Polyacrylamide Gel Electrophoresis*; De Gruyter: Berlin, 1978.

(219) Biot, M. A. General Theory of Three-Dimensional Consolidation. *J. Appl. Phys.* **1941**, *12* (2), 155–164.

(220) McCutchen, C. W. The Frictional Properties of Animal Joints. *Wear* **1962**, *5* (1), 1–17.

(221) Cederbaum, G.; Li, L.; Schulgasser, K. Analysis of Poroelastic Plates. In *Poroelastic Structures*; Elsevier Science Ltd, 2000; pp 111–134.

(222) González, B.; Calvar, N.; Gómez, E.; Domínguez, Á. Density, Dynamic Viscosity, and Derived Properties of Binary Mixtures of Methanol or Ethanol with Water, Ethyl Acetate, and Methyl Acetate at T = (293.15, 298.15, and 303.15) K. *J. Chem. Thermodyn.* **2007**, *39* (12), 1578–1588.